

**JAERI-Tech
2002-098**



JP0350041



**JAPANESE CONTRIBUTION TO THE DESIGN OF PRIMARY
MODULE OF SHIELDING BLANKET IN ITER-FEAT**

February 2003

**Toshimasa KURODA, Toshihisa HATANO, Nobuharu MIKI
Seiji HIROKI, Mikio ENOEDA, Junji OHMORI, Shinichi SATO
and Masato AKIBA**

**日本原子力研究所
Japan Atomic Energy Research Institute**

本レポートは、日本原子力研究所が不定期に公開している研究報告書です。

入手の問合わせは、日本原子力研究所研究情報部研究情報課（〒319-1195 茨城県那珂郡東海村）あて、お申し越しください。なお、このほかに財団法人原子力弘済会資料センター（〒319-1195 茨城県那珂郡東海村日本原子力研究所内）で複写による実費頒布をおこなっております。

This report is issued irregularly.

Inquiries about availability of the reports should be addressed to Research Information Division, Department of Intellectual Resources, Japan Atomic Energy Research Institute, Tokai-mura, Naka-gun, Ibaraki-ken 〒319-1195, Japan.

©Japan Atomic Energy Research Institute, 2003

編集兼発行 日本原子力研究所

Japanese Contribution to the Design of Primary Module of Shielding Blanket in ITER-FEAT

Toshimasa KURODA, Toshihisa HATANO, Nobuharu MIKI, Seiji HIROKI, Mikio ENOEDA,
Junji OHMORI⁺¹, Shinichi SATO^{*1} and Masato AKIBA

Department of Fusion Engineering Research
Naka Fusion Research Establishment
Japan Atomic Energy Research Institute
Naka-machi, Naka-gun, Ibaraki-ken

(Received November 12, 2002)

Japanese contributions to the design activity on the shielding blanket module consisting of the separable first wall and the shield block for ITER-FEAT are compiled. Temperature and stress distributions in the first wall and the shield block are analyzed and evaluated with 2-D and 3-D models for steady state and also for transient condition according to plasma ramp-up and ramp-down. While temperatures and stresses in the first wall satisfy their allowable values, those in a front part of the shield block exceed the allowable guideline. Based on this result, design improvements are suggested. Coolant flow and pressure distributions along the complicated coolant channel in the shield block are preliminary analyzed. Though heat removal is satisfactory in all coolant channels, back flows due to choking in coolant collectors are found. Design improvements to avoid the choking are suggested. Electromagnetic forces acting on blanket modules are analyzed with detailed 3-D models of solid elements for different disruption scenarios. The maximum moment around radial axis is 1.36 MNm on module #5 under fast upward VDE, and the maximum moment around vertical axis is 1.47 MNm on module #1 under fast downward VDE. The supporting beam of the first wall with welded attachment to the shield block is designed. Required welding thickness and support conditions to withstand electromagnetic forces are estimated. Strength of the shield block at the region mating the flexible cartridge is also estimated. Though the shield block surface attached by the flexible cartridge shows sufficient strength, the internal thread mating the Inconel bolt would need more length. In addition, water-to-water leak detection system in case main supply/return manifolds are located within the vacuum vessel is designed. By using Kr as the tracer material, the possibility of water-to-water leak detection and the concept of the detection system are shown. The design of the shielding blanket of ITER-FEAT has been examined in more detail and improved based on above results.

Keywords: ITER, Shielding Blanket, Design, Separable First Wall, Shield Block, Thermo-mechanical Analysis, Thermal-hydraulic Analysis, Electromagnetic Analysis, Structural Analysis, Water-to-water Leak Detection

⁺¹ Department of ITER Project

^{*1} Kawasaki Heavy Industries, Ltd.

ITER-FEAT 遮蔽ブランケット設計

日本原子力研究所那珂研究所核融合工学部

黒田 敏公・秦野 歳久・三木 信晴・廣木 成治・榎枝 幹男

大森 順次⁺¹・佐藤 真一^{*1}・秋場 真人

(2002 年 11 月 12 日受理)

本報告は、ITER-FEAT の遮蔽ブランケット設計における日本での検討事項をまとめたものである。ITER-FEAT において分離型となった第一壁及び遮蔽ブロックの温度・応力分布を定常時及びプラズマ立ち上げ・立ち下げを含む過渡時について解析した。第一壁では温度・応力共許容値を満足したが、遮蔽ブロックの前面端部で応力が許容値を上回り、前面に設置するヘッダー蓋板の肉厚を薄くする、あるいはコーナ一部を面取りする等の改善策を提案した。遮蔽ブロック内の流路における流量配分及び圧力損失等を求めるため 3 次元解析を実施した結果、各流路における除熱性能は確保され、前面端部を除いて十分許容温度以下に冷却されているものの、一部狭隘な箇所があることから逆流を生じている流路があることが判明した。これに基づき、狭隘箇所の流路断面積拡大等について改善策を提案した。つぎに、遮蔽ブランケットモジュールに作用する電磁力を求めるため、詳細な 1 モジュールモデル及び部分的に詳細なモジュールを含む 1 セクターモデル等を用い、種々のディスラプションシナリオに対する解析を実施した。その結果、半径方向モーメントの最大値 1.36 MNm が上側 VDE の際に No. 5 モジュールに、またポロイダル方向モーメントの最大値 1.47 MNm が下側 VDE の際に No. 1 モジュールに働くことがわかった。また、分離型第一壁と遮蔽ブロック及び遮蔽ブロックと真空容器の各接続部分に関し、前者については第一壁支持脚固定部の溶接構造検討、後者についてはモジュール固定用のフレキシブルカートリッジ/ボルトと当たる面での遮蔽ブロック強度の概略評価を実施した。その結果、必要となる第一壁支持脚溶接厚さを提案すると共にフレキシブルカートリッジ固定用ボルトの雌ねじとなる遮蔽ブロック部分の詳細検討が必要であることを指摘した。さらに、ブランケットへの主給水/排水配管が真空容器内部に設置された一体構造の場合に必要な水-水リーク検出システムの設計検討を行い、Kr をトレーサーとしたシステムが有効となる可能性を示した。尚、これらの成果に基づき、ITER-FEAT においてさらに詳細な検討及び設計改善がなされた。

那珂研究所：〒311-0193 茨城県那珂郡那珂町向山 801-1

⁺¹ ITER 開発室

^{*1} 川崎重工業株式会社

Contents

1. Introduction	1
2. Thermo-mechanical Analysis of First Wall and Shield Block	3
2.1 First Wall	3
2.1.1 Analysis Model and Conditions	3
2.1.2 Steady State Analysis	3
2.1.3 Transient Analysis	4
2.2 Shield Block	4
2.2.1 Analysis Model and Conditions	4
2.2.2 Stress Due to Coolant Pressure	4
2.2.3 Steady State Analysis	5
2.2.4 Transient Analysis	5
2.2.5 Discussion	5
3. Thermal-hydraulic Analysis of Shield Block	20
3.1 Analysis Model and Conditions	20
3.2 Analysis Results and Discussions	37
3.2.1 Coolant Velocity and Flow Distribution	37
3.2.2 Pressure Profile	42
3.2.3 Temperature Profile	44
3.3 Conclusions	47
4. Electromagnetic Analysis of Shielding Blanket	48
4.1 Preliminary EM Analysis Using One Module Model	48
4.1.1 Analysis Conditions	48
4.1.2 Analysis Results	49
4.2 Centered Disruption (CD)	54
4.2.1 One Sector Model with 17 Module Model	54
4.2.2 One Sector Model with Fine Mesh Model of Module 5	76
4.3 Fast Downward VDE (VDE/F-D)	79
4.3.1 Analysis Method	79
4.3.2 Analysis Results	80
4.4 Fast Upward VDE (VDE/F-U)	97
4.4.1 Analysis Method	97
4.4.2 Analysis Results	97
4.5 Conclusions	106
5. Design and Structural Analysis on First Wall and Shield Block Attachments	107
5.1 First Wall Supporting Beam	107

5.1.1 Supporting Beam for Separable First Wall	107
5.1.2 Basic Design	107
5.1.3 EM Loads and Calculation Method	108
5.1.4 Calculation Results	109
5.1.5 Basic Layout of FW Supporting Beams	117
5.1.6 Conclusions	119
5.2 Strength Evaluation of Shield Block Region Attached by Flexible Cartridge	119
5.2.1 EM Pushing Force	119
5.2.2 EM Pulling Force	120
6. Design of Water-to-water Leak Detection System for Integrated Cooling Manifold Concept	122
6.1 Background	122
6.2 Design Requirements	122
6.2.1 Candidate Tracer Materials	122
6.2.2 Target Leak Rate and Sampling Duration	122
6.2.3 Cooling Water Conditions	123
6.2.4 Other Conditions	123
6.3 Evaluation of Lower Detectable Limit	123
6.3.1 Na-24	123
6.3.2 D ₂ O	124
6.3.3 He	124
6.3.4 Kr	125
6.4 Impact of Tracer Materials on Components and Removal of Tracers	126
6.4.1 Na-24	126
6.4.2 D ₂ O	126
6.4.3 He	127
6.4.4 Kr	127
6.5 Assessment of Candidate Tracer Materials	127
6.6 Conceptual Design of Water-to-water Leak Detection System Using Kr Tracer	129
6.6.1 Experiment on Diffusion Efficiency of Kr by Diffusion Column	129
6.6.2 Design of Water-to-water Leak Detection System	131
6.7 Summary	133
7. Conclusions	134
Acknowledgement	136
References	136

目 次

1. はじめに	1
2. 第一壁/遮蔽ブロック熱・応力解析	3
2.1 第一壁	3
2.1.1 解析モデル及び解析条件	3
2.1.2 定常状態	3
2.1.3 過渡状態	4
2.2 遮蔽ブロック	4
2.2.1 解析モデル及び解析条件	4
2.2.2 冷却材圧力による応力	4
2.2.3 定常状態	5
2.2.4 過渡状態	5
2.2.5 考察	5
3. 遮蔽ブロック熱・流力解析	20
3.1 解析モデル及び解析条件	20
3.2 解析結果及び考察	37
3.2.1 冷却水流速及び流量配分	37
3.2.2 圧力分布	42
3.2.3 温度分布	44
3.3 結論	47
4. 電磁力解析	48
4.1 1モジュールモデルによる解析	48
4.1.1 解析条件	48
4.1.2 解析結果	49
4.2 定位置ディスラプション	54
4.2.1 1セクタモデル (プランケット17モジュールを含む)	54
4.2.2 1セクタモデル (詳細メッシュのプランケット5モジュールを含む)	76
4.3 下側VDE	79
4.3.1 解析方法	79
4.3.2 解析結果	80
4.4 上側VDE	97
4.4.1 解析方法	97
4.4.2 解析結果	97
4.5 結論	106
5. 第一壁及び遮蔽ブロック支持部設計と強度評価	107
5.1 第一壁支持脚	107

5.1.1 分離型第一壁の支持脚	107
5.1.2 基本設計	107
5.1.3 電磁力荷重及び解析方法	108
5.1.4 解析結果	109
5.1.5 第一壁支持脚の基本的レイアウト	117
5.1.6 結論	119
5.2 フレキシブルカートリッジに対面する遮蔽ブロック部分の強度評価	119
5.2.1 電磁力押付荷重	119
5.2.2 電磁力引張荷重	120
6. 冷却水マニホールド一体型概念用水-水リーク探知システムの設計	122
6.1 背景	122
6.2 設計への要求事項	122
6.2.1 トレーサー候補材	122
6.2.2 探知目標リーク量とサンプリング間隔	122
6.2.3 冷却水条件	123
6.2.4 その他の条件	123
6.3 検出下限値の評価	123
6.3.1 ナトリウム-24	123
6.3.2 重水	124
6.3.3 ヘリウム	124
6.3.4 クリプトン	125
6.4 トレーサー材の冷却水機器への影響と除去法	126
6.4.1 ナトリウム-24	126
6.4.2 重水	126
6.4.3 ヘリウム	127
6.4.4 クリプトン	127
6.5 トレーサー候補材の評価	127
6.6 クリプトントレーサーを用いた水-水リーク探知システムの概念設計	129
6.6.1 放散塔におけるクリプトンの放散効率に関する実験	129
6.6.2 水-水リーク探知システムの設計	131
6.7 まとめ	133
7. 総括	134
謝辞	136
参考文献	136

1. Introduction

The design of the shielding blanket for ITER-FEAT has been modified to employ a first wall separable from a shield block to reduce radioactive wastes in case of unexpected excessive damage of the first wall and also to reduce the fabrication cost. The separable first wall is mounted on the shield block as shown in Fig. 1-1. Both of the first wall and the shield block are designed to incorporate many slots to decrease the eddy current, i.e. finally to decrease the electromagnetic force acting on them, during plasma disruption. The dimensions of the shielding blanket module are approximately 1.4-m-wide, 1.1-m-high and 0.45-m-deep based on the revisited segmentation shown in Fig. 1-2 [1].

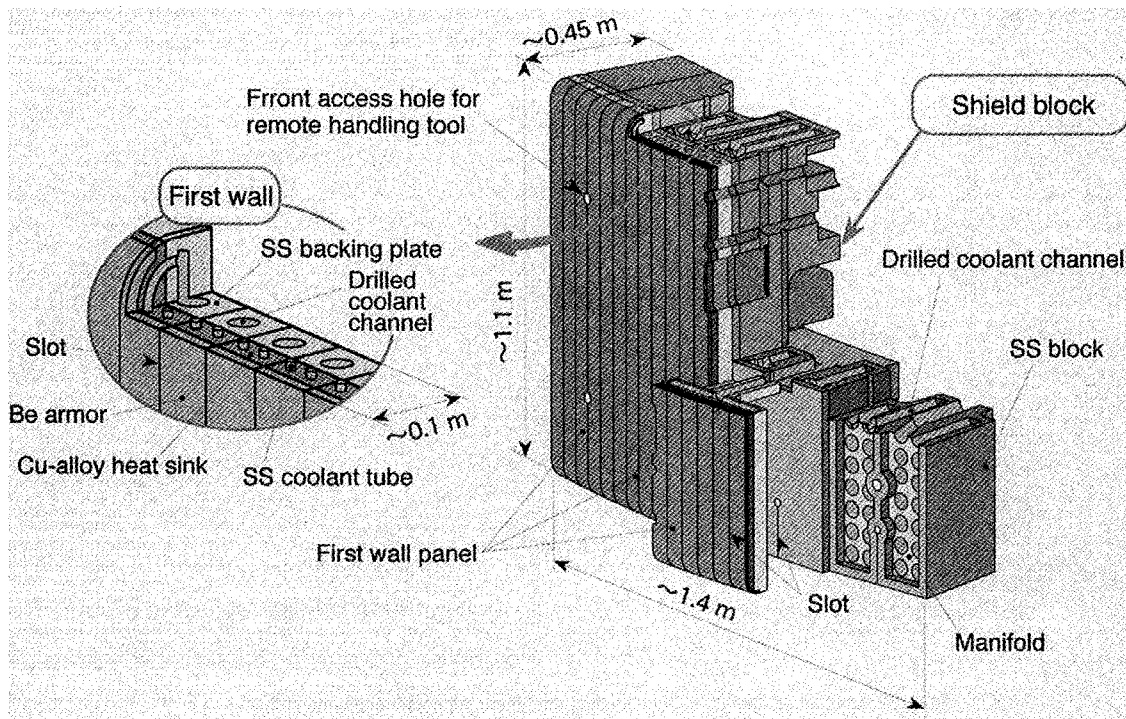
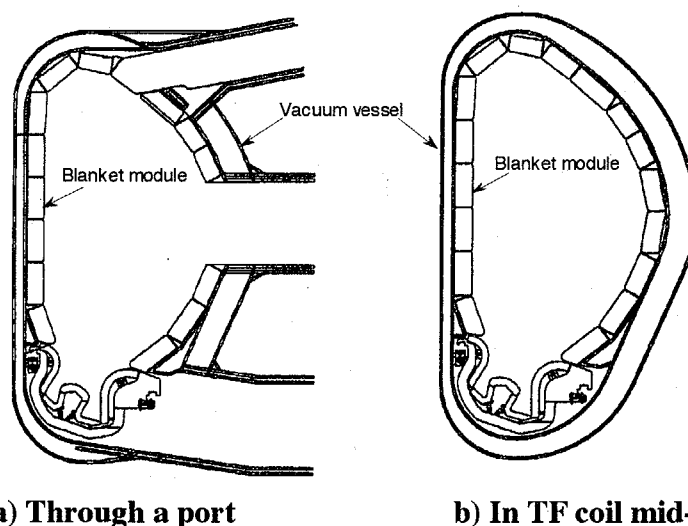


Fig. 1-1 Shielding blanket module with separable first wall



a) Through a port **b) In TF coil mid-plane**
Fig. 1-2 Blanket module segmentation (poloidal cross-section) [1]

Four first wall panels are mounted on one shield block. The first wall panel is provided with poloidal slots which penetrate the Be armor and the Cu-alloy heat sink dividing it into six separate strips. The slots also pass through the SS backing plate except in its central part where the toroidal inlet/outlet coolant collectors are located. Front access holes (mainly circular hole of 30 mm in diameter) are also provided for remote handling tools to access the blanket module mechanical, hydraulic and electrical connections to the vacuum vessel.

Coolant channels in the shield block are oriented in radial direction. By the insertion of a guide tube into the radial channel, coaxial counter-flow returning at the bottom (rear in the shield block) is formed in the individual channel as shown in Fig. 1-3. Coolant manifolds and collectors connecting sections of the shield block are provided in its front region.

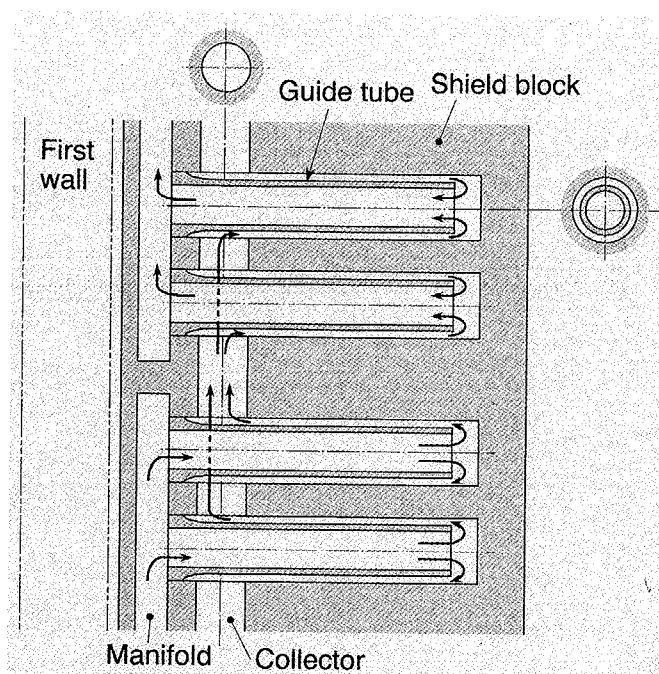


Fig. 1-3 Concept of the radial flow in the shield block

This report compiles Japanese contributions to the design activity on the shielding blanket module consisting of the separable first wall and the shield block for ITER-FEAT. In Chapter 2, temperature and stress distributions in the first wall and the shield block are analyzed and evaluated with 2-D and 3-D models for steady state and also for transient condition according to plasma ramp-up and ramp-down. Coolant flow and pressure distributions along the complicated coolant channel in the shield block are preliminarily analyzed with a 3-D model in Chapter 3. Electromagnetic forces acting on blanket modules are analyzed with detailed 3-D models of solid elements for different disruption scenarios in Chapter 4. In Chapter 5, the supporting beam of the first wall is designed with estimates of stress at the fixing points, and stresses in the shield block at the region mating the flexible cartridge are estimated. In addition, water-to-water leak detection system is designed, in Chapter 6, in case main supply/return manifolds are located within the vacuum vessel.

2. Thermo-mechanical Analysis of First Wall and Shield Block

2.1 First wall

2.1.1 Analysis model and conditions

The separable first wall (FW) panel is about 350 mm in toroidal width and further stripped by poloidal slotting into six strips of which toroidal width is about 50 mm each except for the poloidally central part. At the poloidally central part, the depth of the slot is up to the bottom of Cu-alloy heat sink. Thus only Be armor and Cu-alloy are castellated in this part and the SS backing plate remains unslotted to contain water coolant collectors. The pitch of SS tubes embedded within the Cu-alloy heat sink is 24.2 mm in the basic configuration as shown in Fig. 2-1. On the other hand, the pitch is 15 mm and SS tubes are put to one side in the strip with the front access hole for remote handling, also as shown in Fig. 2-1, in order to avoid their interference.

For thermo-mechanical analysis, a toroidal-radial cross-section of a strip of the first wall is modeled. Sizes of two cross-sections and finite element models are shown in Figs. 2-1 and 2-2, respectively. ABAQUS version 5.8 is used as the analysis code with first order 4-node-elements in thermal analysis and generalized plane strain elements (with free condition for the bending and displacement in Z direction) in thermo-mechanical analysis. Temperature dependent material properties are taken from the ITER Material Properties Handbook [2]. Irradiation effects on the material properties are not taken into account.

In steady state analysis, surface heat flux of 0.5 MW/m^2 and neutron flux of 0.78 MW/m^2 are given to be constant. Coolant flow rate is 4 kg/s for one FW panel, thus 0.67 kg/s for one strip. Thermal load conditions are shown in Table 2-1. Volumetric heating rates are obtained by 1-D neutronic calculation, and considered uniform in the Be armor and in the Cu-alloy heat sink because of low attenuation within relatively thin these materials while radial attenuation in the thicker SS region is taken into account. Heat transfer coefficients in the cooling channels are estimated by using Dittus-Boelter's correlation. The stress free temperature is set to the room temperature (20°C). For transient thermal analysis, the heat load evolution during one thermal cycle is considered as shown in Table 2-2.

2.1.2 Steady state analysis

Steady state thermal analysis is carried out to evaluate the temperature distribution before transient analysis. Temperature distribution and temperature range in both FW strips are shown in Fig. 2-3 and Table 2-3, respectively. Maximum temperatures are 269°C at the top of Be armor in the basic configuration and 304°C at the back of SS backing plate in the configuration with the front access hole.

A structural analysis is carried out considering the temperature distribution of steady state. Deformations of both fingers are shown in Fig. 2-4. The strip with basic configuration symmetrically deforms. On the other hand, the strip with the front access hole deforms asymmetrically as shown in the figure. Displacements at the corners are also noted in Fig. 2-4. The stress distributions are shown in Figs. 2-5 through 2-8. The maximum Tresca stresses with allowable values ($3S_m$) are summarized in Table 2-4. All the stresses satisfy

the allowable limits.

2.1.3 Transient analysis

Transient thermal analysis is carried out to evaluate the temperature distribution during one thermal cycle assuming 400-sec-burn time followed by dwell time up to 1800 sec from the start of plasma burn. Figure 2-9 shows the resulting transient temperature behavior plotted up to 800 sec from the start of plasma burn. Temperatures in both FW strips reach steady state within the burn time (400 sec). Temperatures of Be armor and Cu-alloy heat sink follow the heat load evolution with a time constant less than 100 seconds. Temperature of the SS backing plate in the strip with the front access hole spends about 300 seconds to reach steady state. The maximum and minimum temperatures in Be, Cu-alloy and SS region are naturally the same as those obtained in steady state analysis (see Table 2-3).

With respect to the stress transient, Fig. 2-10 shows the calculated stress response on the basis of the transient thermal analysis. As can be seen from the figure, overshooting of stresses, especially in Be armor and SS backing plate is observed. However, the stresses satisfy the acceptable criteria (3Sm) summarized in Table 2-4.

2.2 Shield block

2.2.1 Analysis model and conditions

The shield block consists of four forged sub-blocks welded together at their rear side. Within one sub-block, two poloidal-radial slots (0.16-m-deep) are machined to reduce EM loads, i.e. one from the top and another from the bottom. For thermo-mechanical analysis, one eighth of the shield block, i.e. one fourth of the sub-block, is modeled with holes for the insertion of FW supporting beam and for front access of remote handling tools as shown in Fig. 2-11. ABAQUS version 5.8 is used as the analysis code with four-node tetrahedron elements.

In thermal analysis, nuclear heating rate distribution corresponding to the neutron flux of 0.78 MW/m² at FW shown in Fig 2-12 is applied. For transient thermal analysis, the heat load evolution during one thermal cycle was considered as shown in Table 2-5. Heat transfer coefficients in coolant channels are shown in Table 2-6.

Temperature dependent material properties are taken from the ITER Material Properties Handbook [2].

2.2.2 Stress due to coolant pressure

At first, a structural analysis is carried out for coolant pressure load. Von Mises stress distribution is shown in Fig. 2-13. The maximum von Mises stress is 28 MPa which is significantly lower than the allowable stress 1.5Sm (220 MPa).

2.2.3 Steady state analysis

Steady state thermal analysis is carried out to evaluate the temperature distribution before transient analysis. Temperatures on the corners of the analysis model and temperature distributions on the outer surface and internal cross-sections are shown in Table 2-7, and Figs. 2-14 and 2-15, respectively. The maximum temperature is 419 °C at the corner of the sub-block and satisfies the allowable limit (450 °C).

Thermal stress distributions on outer surface and internal cross-sections of the shield block are shown in Figs. 2-16 and 2-17, respectively. The maximum von Mises stress is 450 MPa at the plasma side edge of the front access hole. Since this maximum stress exceeds 3Sm, i.e. 348 MPa at 325 °C, more detail stress evaluation (including fatigue) and measures to reduce the stress will be required.

2.2.4 Transient analysis

Transient thermal analysis was performed based on the heat load evolution shown in Table 2-5. Temperature distribution at the end of burn time (at 430 sec from the start) is shown in Fig. 2-18 and Table 2-8. Maximum temperature is 396 °C at the same location as in the steady state analysis. Temperature responses at the location of A and B in Fig. 2-11 are plotted in Fig. 2-19. Because of large heat capacity, temperatures in the shield block are still rising and do not reach steady state.

Thermal stress distribution of the shield block at the end of burn time is shown in Fig. 2-20. The maximum von Mises stress is 357 MPa at the same location as in the steady state analysis. This maximum stress exceeds 3Sm (339 MPa at 348 °C). Therefore, detail stress evaluation and measures to reduce the stress are necessary.

2.2.5 Discussion

Thermo-mechanical analyses are performed on the SS shield block. High thermal stresses due to local high temperatures are resulted, especially on the corner surface and the edge of the front access hole but not in the shield block. Since these stresses are peaked at the surface and the edge, beveling of the corner and the edge will be effective to reduce these stresses. Before that, decrease of the header cover plate thickness will be also effective to reduce the stress and the temperature. Since the stress in the header cover plate due to coolant pressure is far below the allowable value, the latter measure could be first conducted.

Table 2-1 Thermal load and cooling conditions

Heat flux [MW/m ²]	0.5
Nuclear heating rate [MW/m ³]	
Be armor	7.6
Cu-alloy (DSCu AL-25) heat sink	11.2
SS tube and backing plate	$16.241e^{-0.0113x*}$
Coolant	
Temperature [°C]	150
Velocity	
Channel within Cu-alloy heat sink (10 mm in diameter) [m/s]	3.64
Channel within SS backing plate (24 mm in diameter) [m/s]	1.26
Pressure [MPa]	3

*:x = distance from first wall surface facing plasma [mm]

Table 2-2 Thermal load evolution

Time [s]	Heat flux [MW/m ²]	Nuclear heating rate [%]
0	0.11	0
0 - 30	0.11 - 0.5 (linear increase)	0 - 100 (linear increase)
30 - 430	0.5	100
430 - 490	0.5 - 0 (linear decrease)	100 - 0 (linear decrease)
490 - 1800	0	0

Table 2-3 Temperature range in FW strips

Location	Temperature range [°C]		Allowable limit [°C]
	Basic configuration	With front access hole	
Be armor	269 - 230	295 - 259	-
Cu-alloy heat sink	230 - 220	258 - 229	-
SS tube	220 - 178	229 - 182	450
SS backing plate	260 - 166	304 - 166	450

Table 2-4 Maximum Tresca stresses at steady state

	Location	Max. Tresca stress [MPa]	T [°C]	Sm [MPa]	3Sm [MPa]
Basic configuration	Be tile	133	230		
	Cu-alloy heat sink	229	98	106	318
	SS tube	185	186	143	429
	SS backing plate	249	169	148	444
With front access hole	Be tile	234	231		
	Cu-alloy heat sink	107	201	112	336
	SS tube	260	170	147	441
	SS backing plate	286	177	146	438

Table 2-5 Heat load evolution

Time [s]	Volumetric heating rate [%]
0 - 30	0 - 100 (linear increase)
30 - 430	100
430 - 490	100 - 0 (linear decrease)
490 - 1800	0

Table 2-6 Heat transfer coefficient

Location	Radial coolant channel		Front header
	Side surface	Bottom surface	
Heat transfer coefficient [W/m ² K]	8310	4910	4480

Table 2-7 Temperatures on the surface of shield block at steady state

Location*	A	B	C	D
Temperature [°C]	419	413	361	368

* : See Fig.2-11.

Table 2-8 Temperatures on the surface of the shield block at the end of burn time

Location*	A	B	C	D
Temperature [°C]	396	392	351	357

* : See Fig. 2-11.

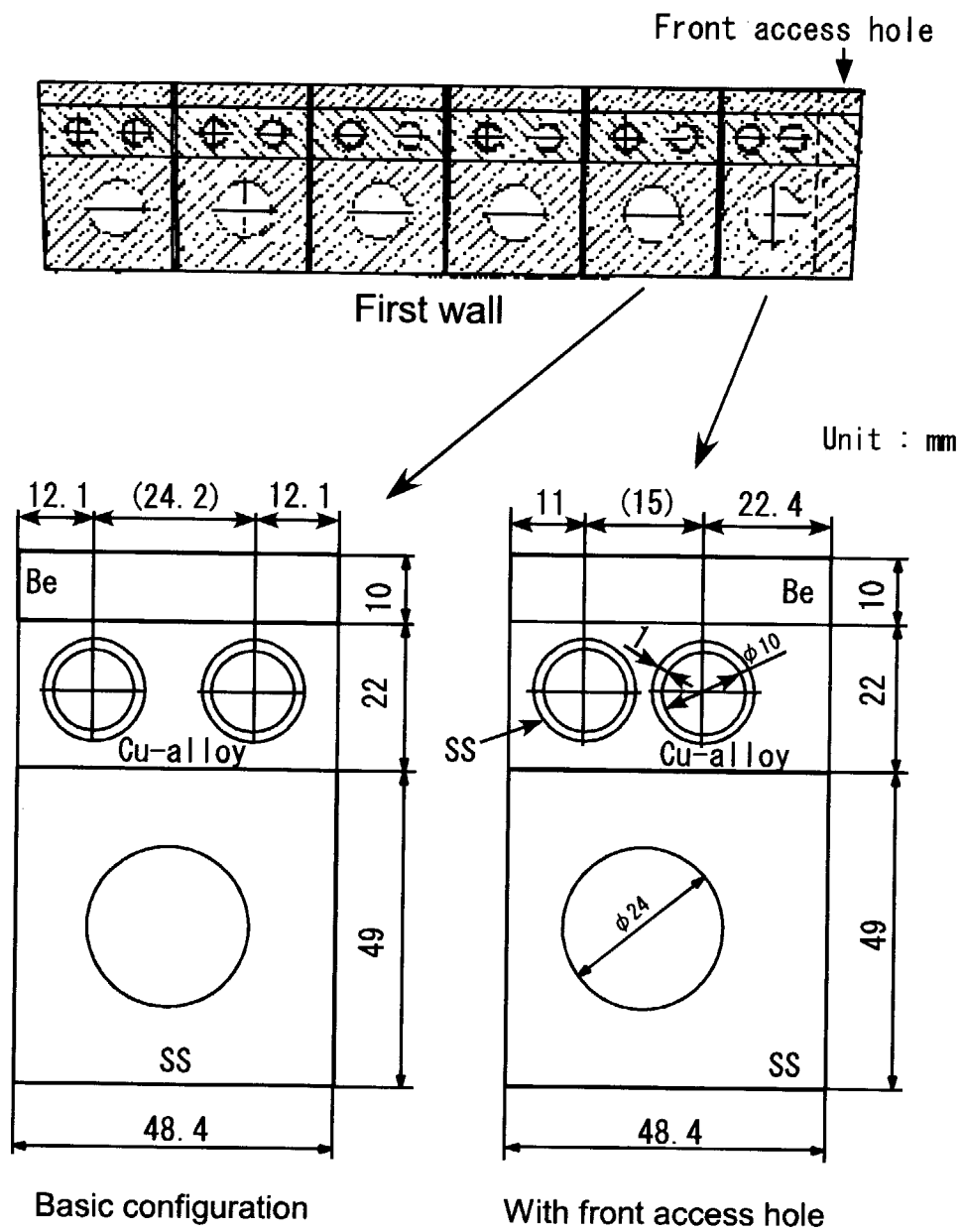


Fig. 2-1 Cross-section of FW strips

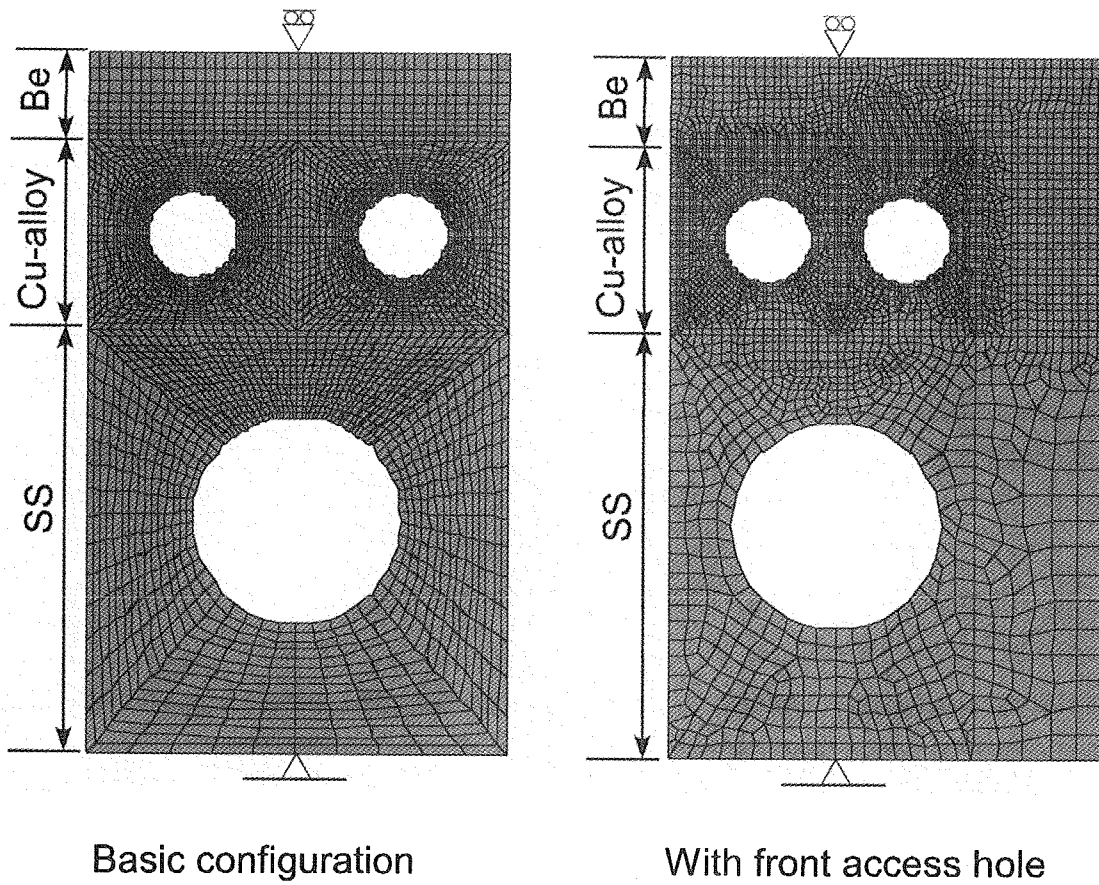


Fig. 2-2 Two-dimensional FW analysis model

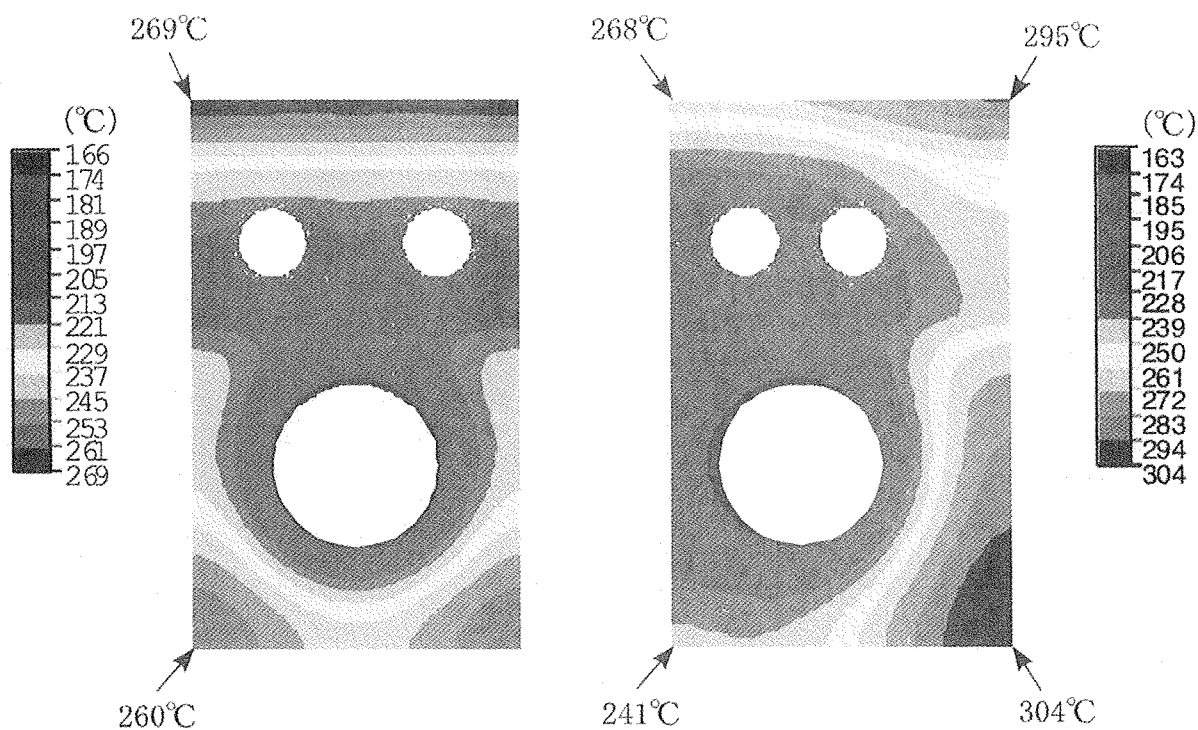
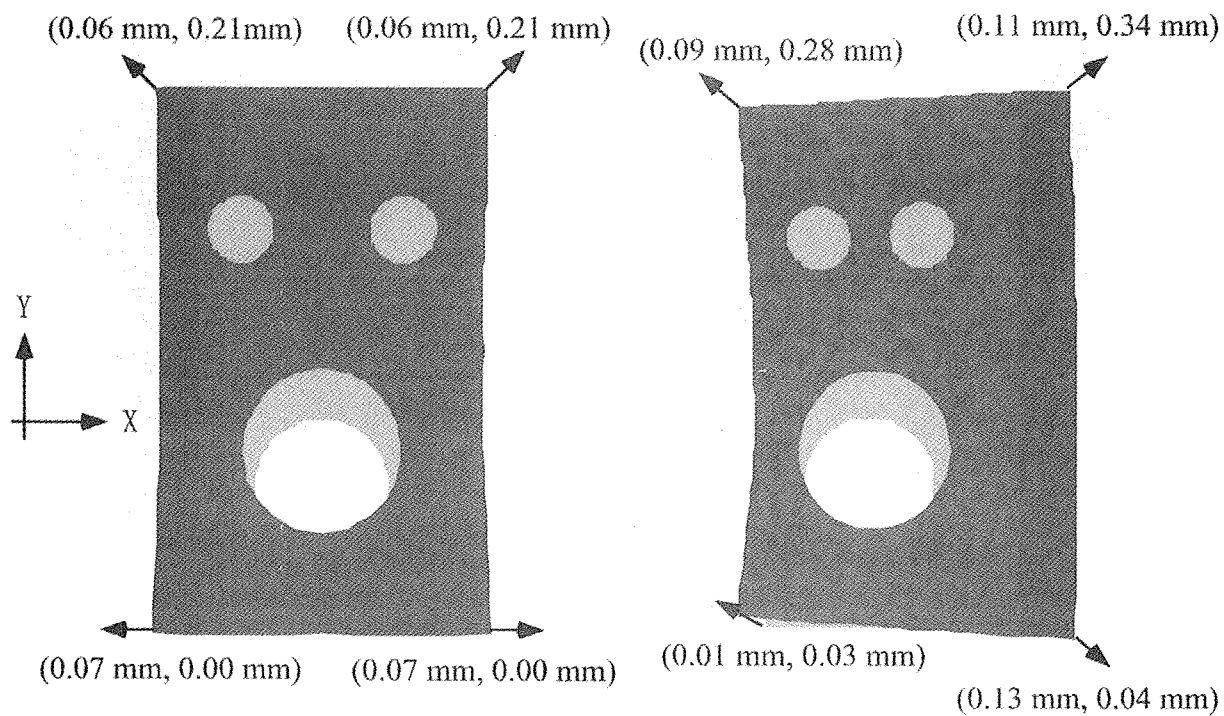


Fig. 2-3 Temperature distribution at steady state



Digital values: deformation (X,Y) from initial locations

Fig. 2-4 Deformation due to temperature distribution at steady state

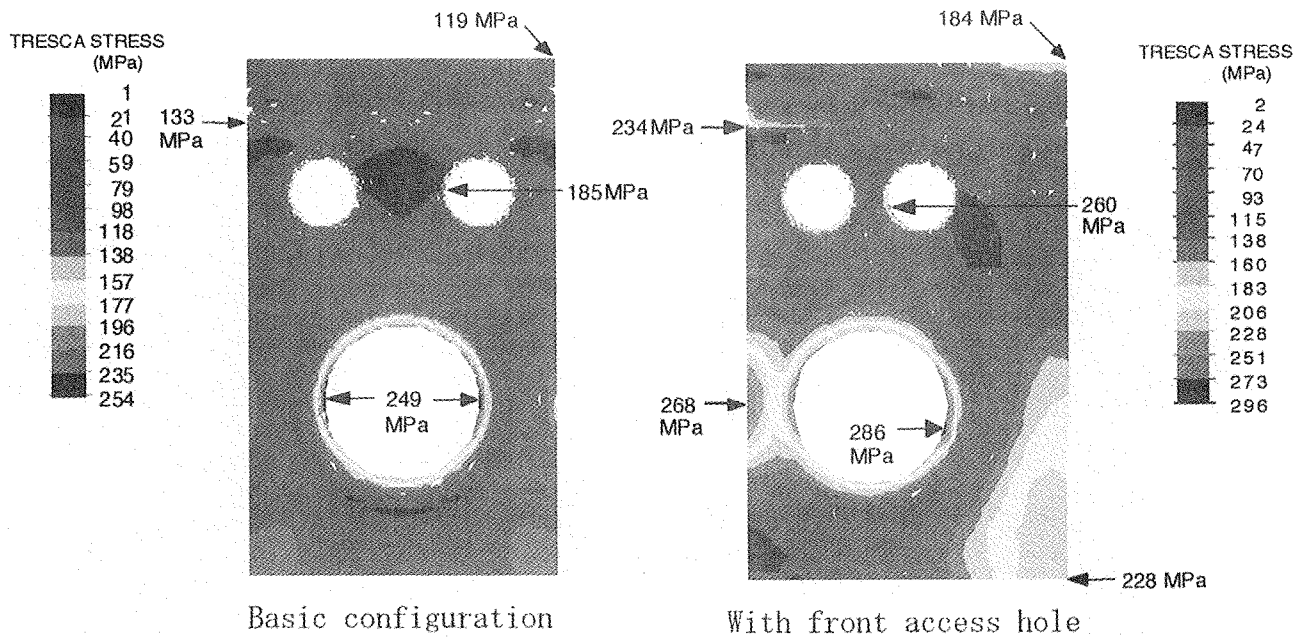


Fig.2-5 Tresca stress distribution at steady state

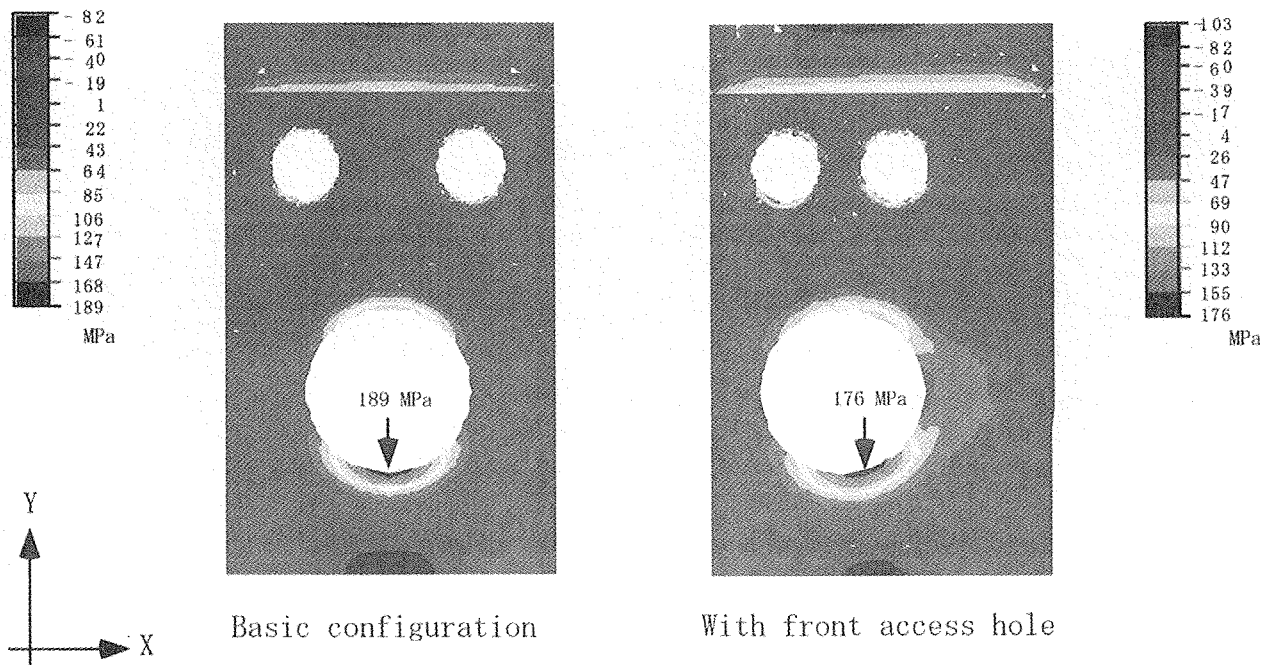


Fig.2-6 Stress component in X direction at steady state

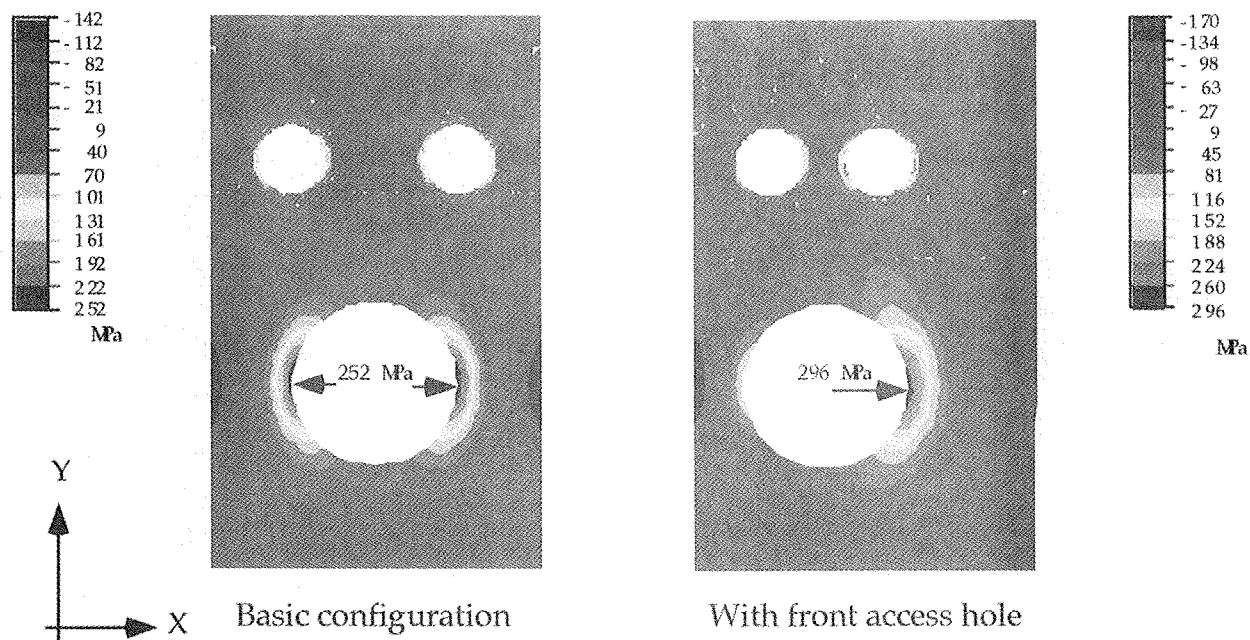


Fig. 2-7 Stress component in Y direction at steady state

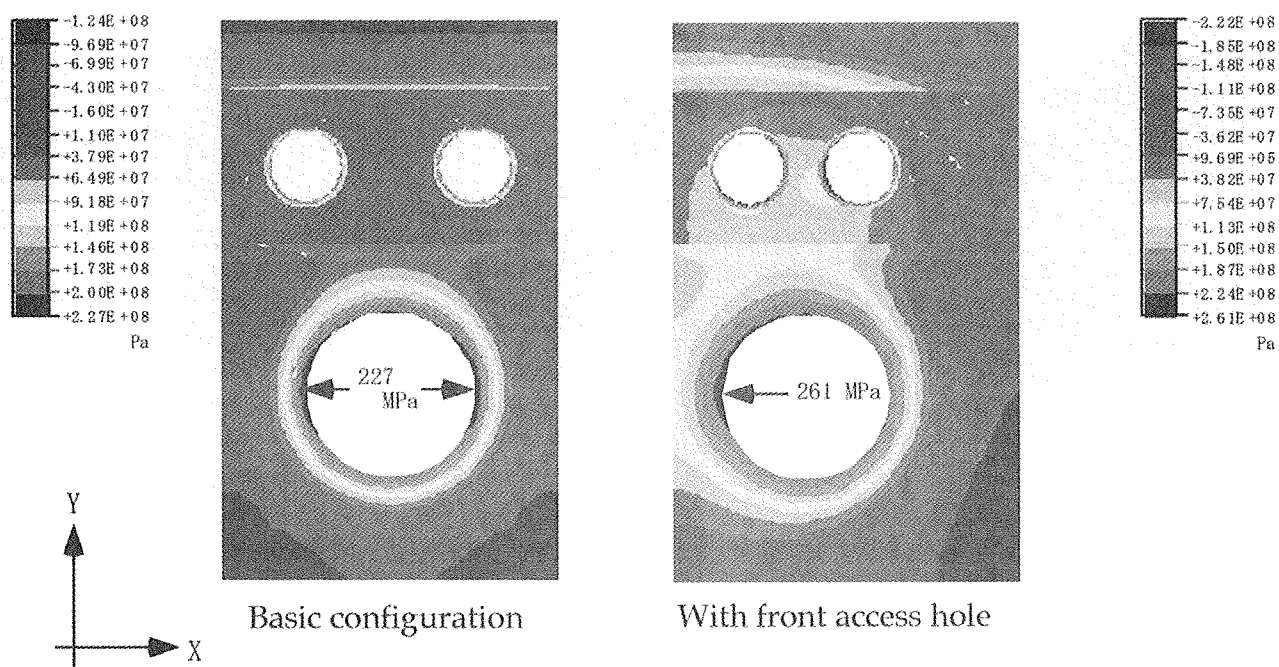
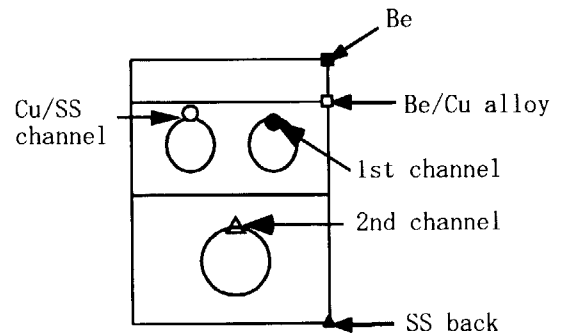
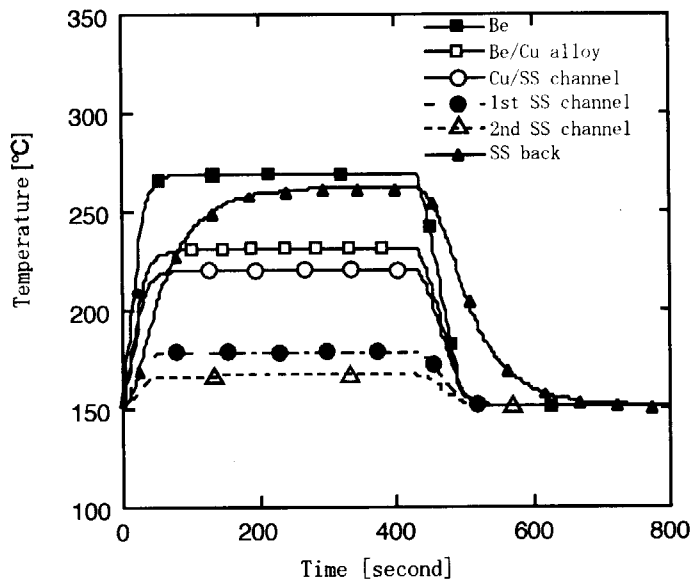
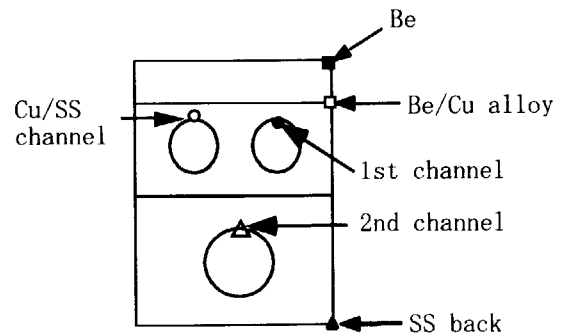
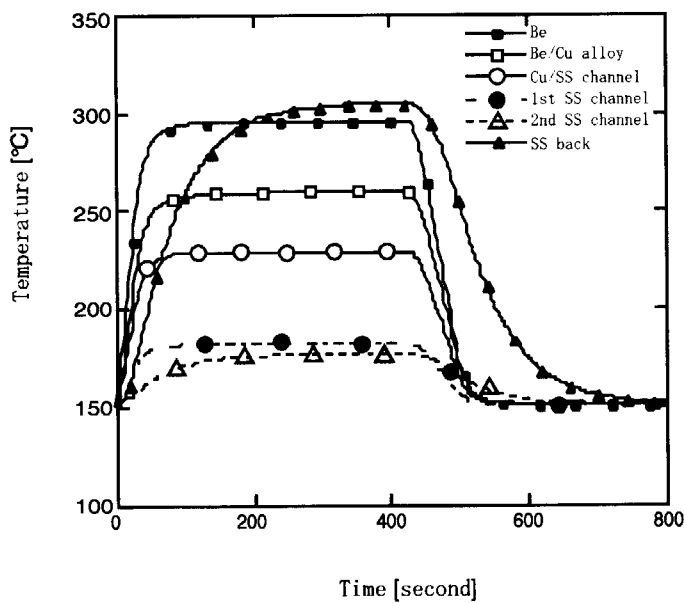


Fig. 2-8 Stress component in Z direction at steady state



Locations in the figure

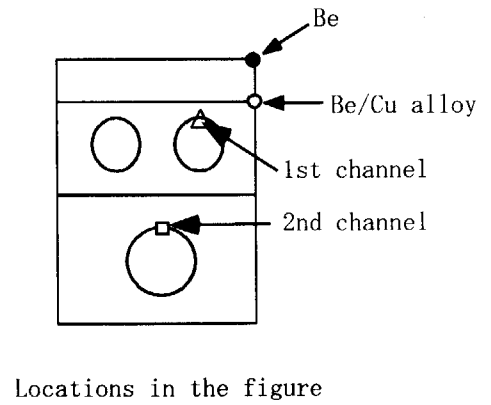
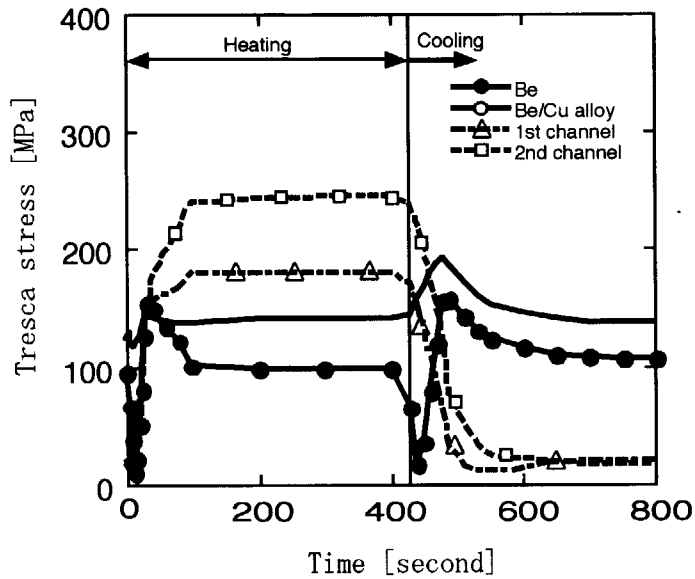
a) Basic configuration



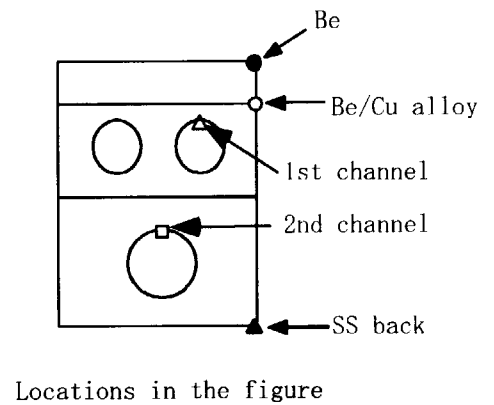
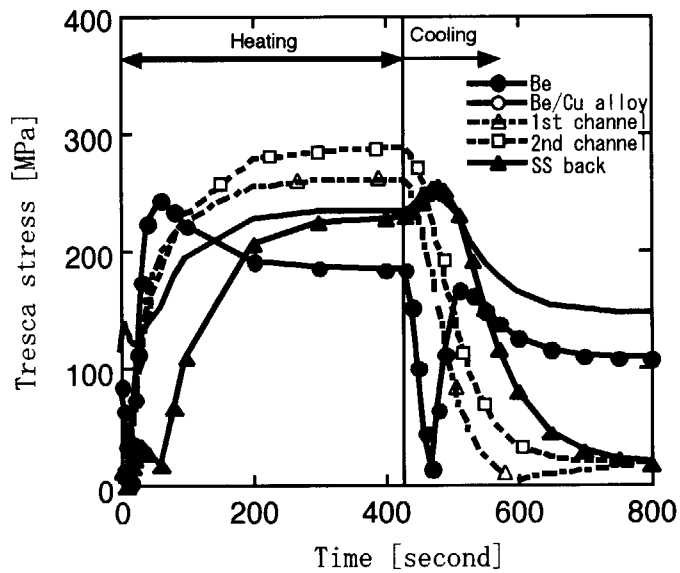
Locations in the figure

b) With front access hole

Fig. 2-9 Temperature response in FW strips



a) Basic configuration



b) With front access hole

Fig. 2-10 Stress response during thermal cycle

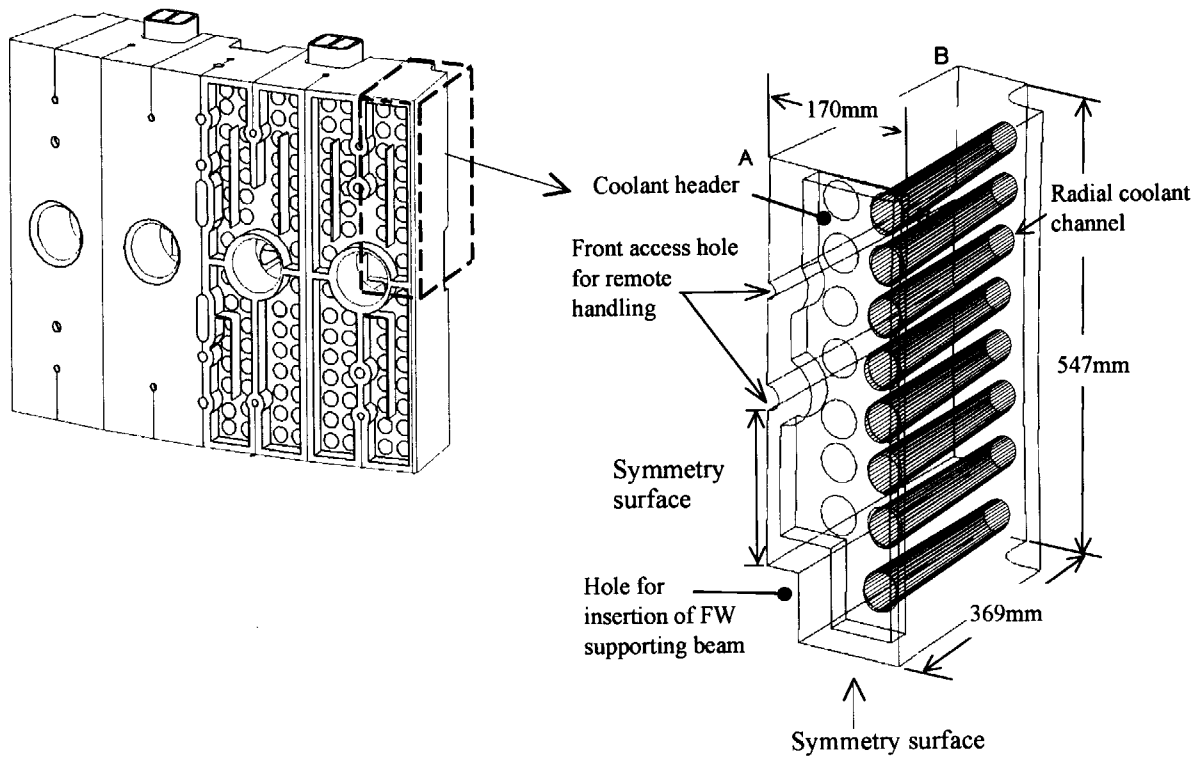


Fig. 2-11 FEM analysis model of 1/8 shield block

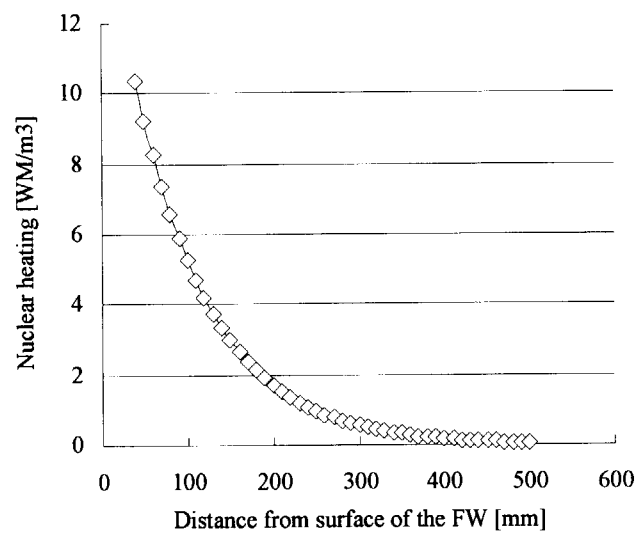


Fig. 2-12 Nuclear heating rate in SS shield block

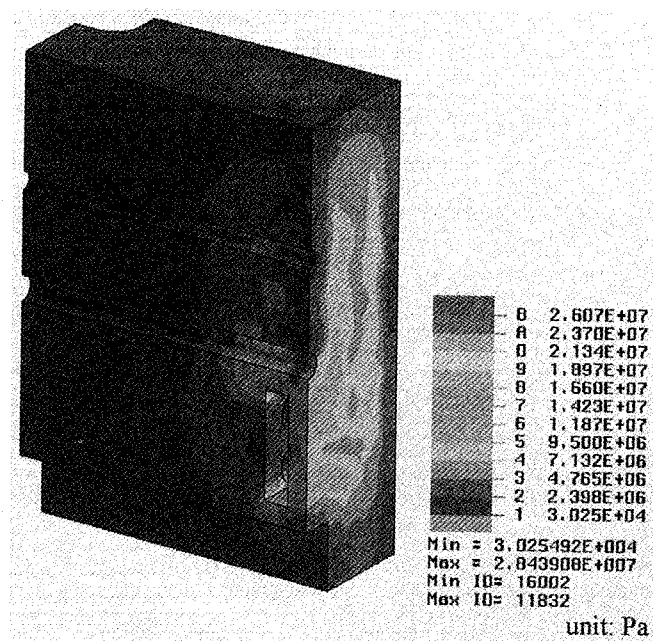


Fig. 2-13 Von Mises stress distribution due to coolant pressure

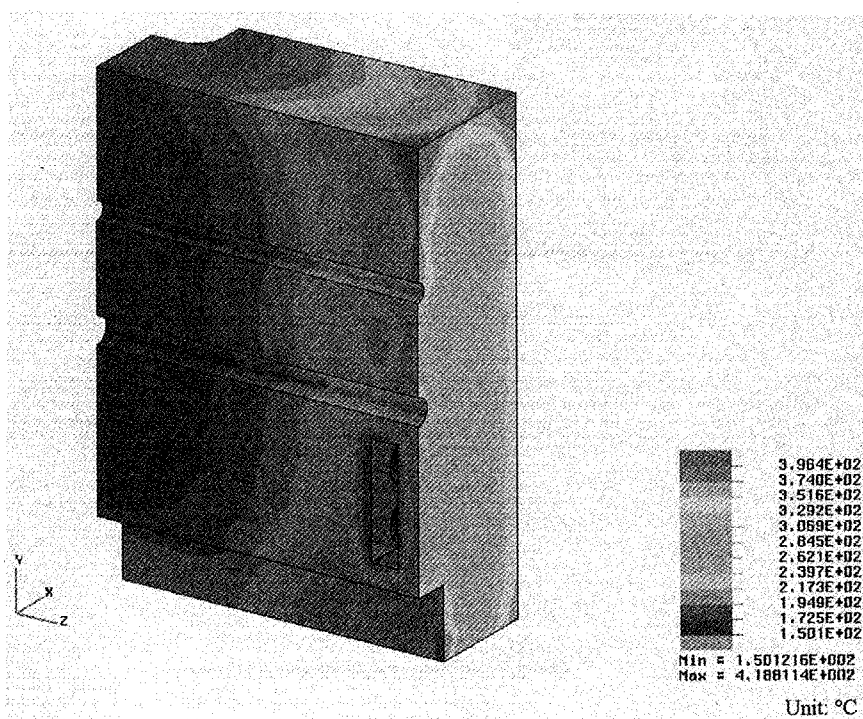


Fig. 2-14 Temperature distribution at steady state

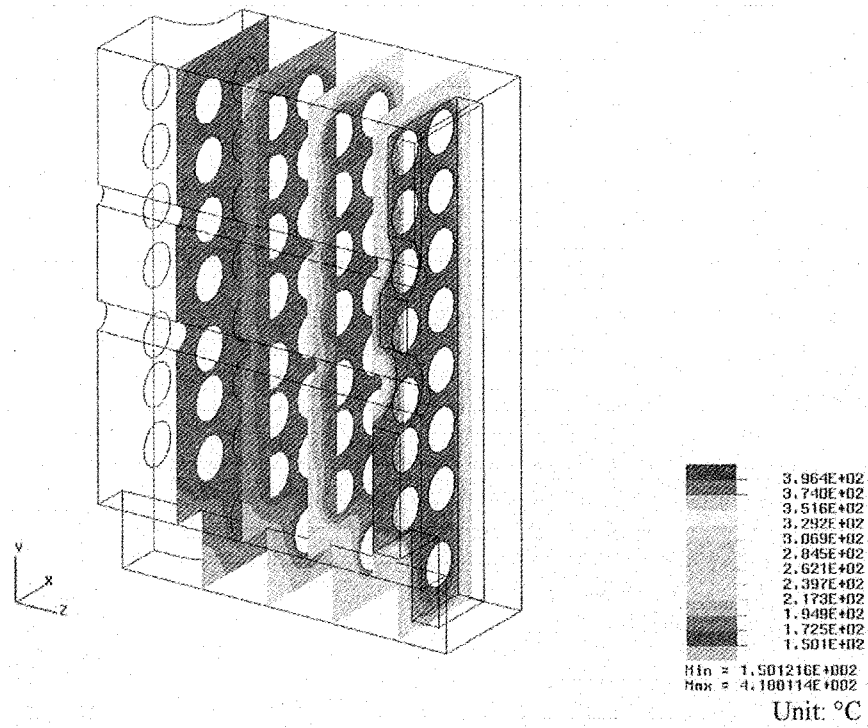


Fig. 2-15 Temperature distribution on cross-sections at steady state

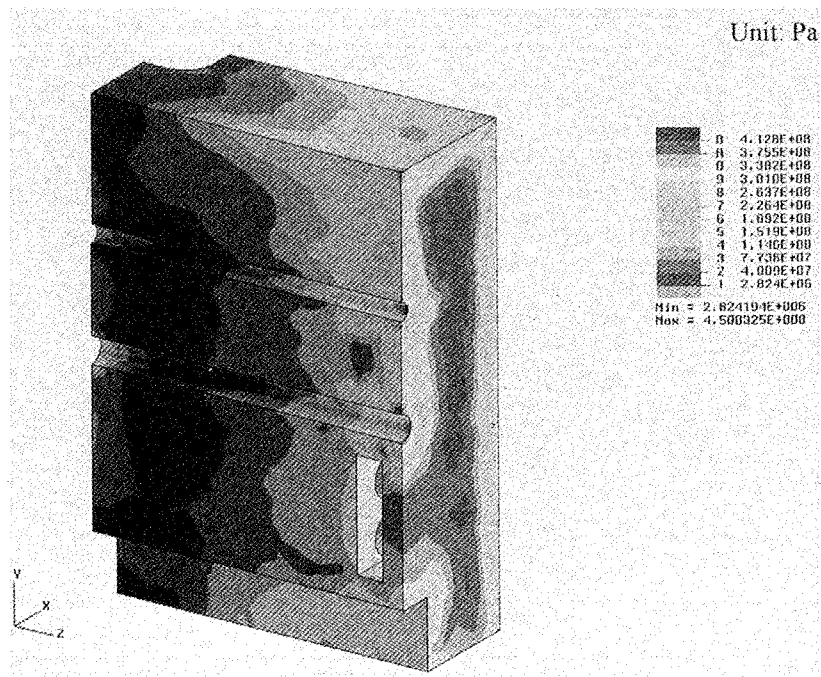


Fig.2-16 Von Mises stress distribution at steady state

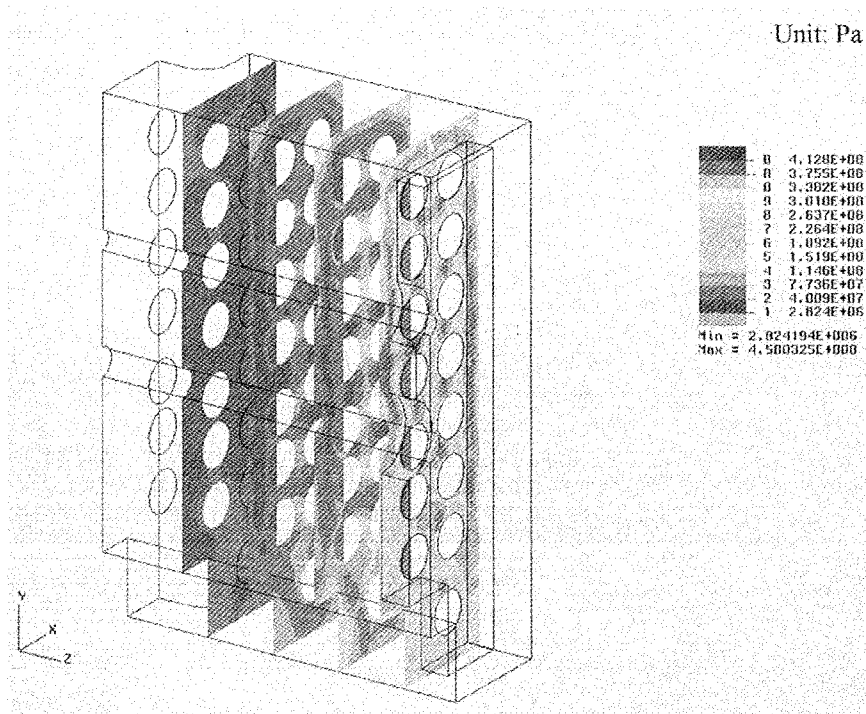


Fig.2-17 Von Mises stress distribution on cross-sections at steady state

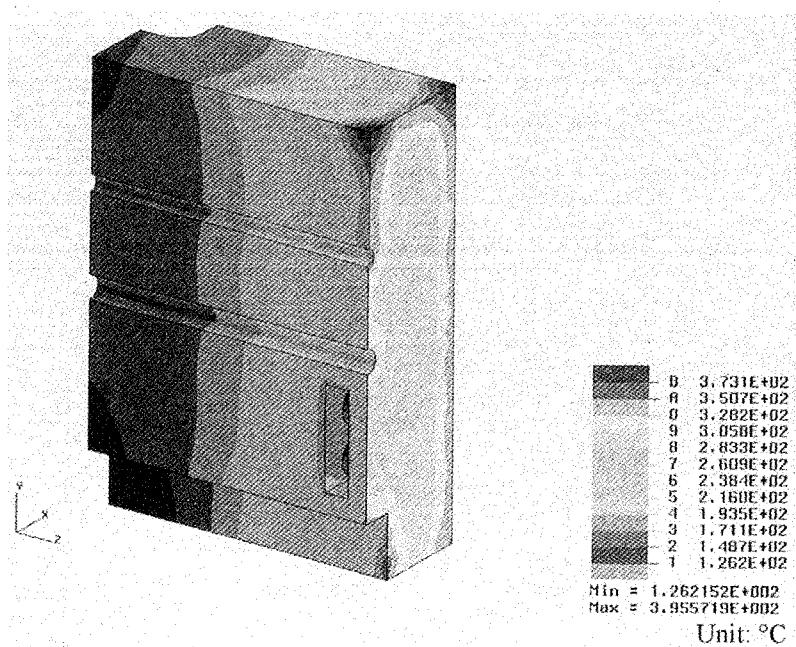


Fig. 2-18 Temperature distribution at the end of burn time

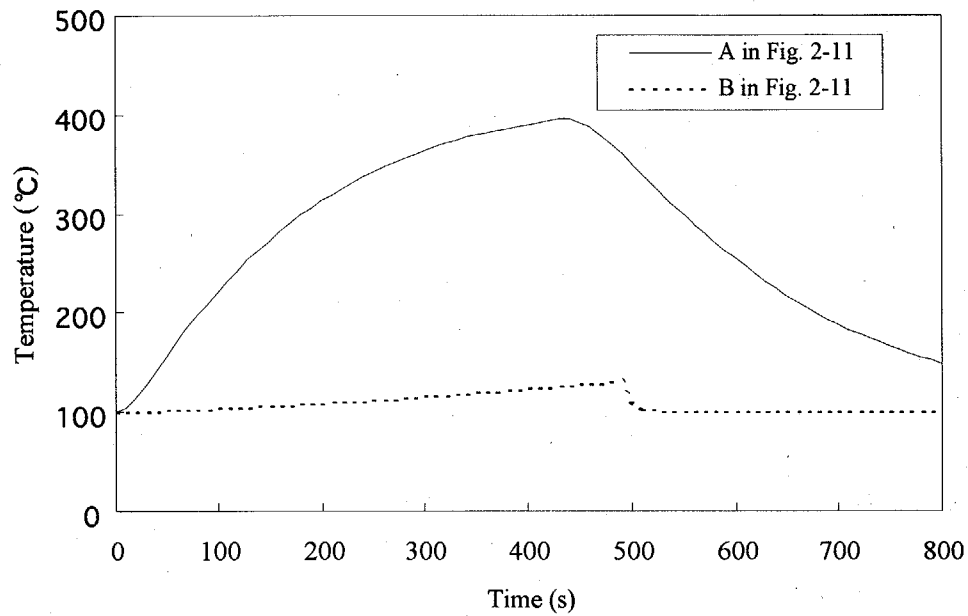


Fig. 2-19 Temperature responses at the corners of 1/8 shield block analysis model

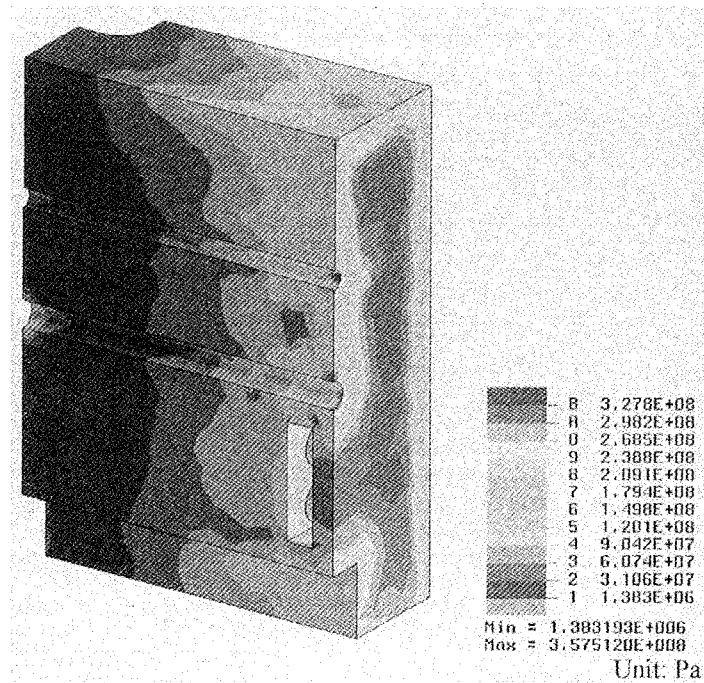


Fig. 2-20 Thermal stress distribution at the end of burn time

3. Thermal-hydraulic Analysis of Shield Block

The shield block includes a lot of concentric radial coolant channels and also long poloidal and short toroidal channels to connect the radial channels. Thus, the internal configuration due to the coolant routing of the shield block is complicated. To investigate the coolant pressure loss, flow distribution and heat removal performance of the shield block, a detailed 3-D thermal-hydraulic analysis has been performed.

3.1 Analysis model and conditions

The mechanical configuration of the shield block module is shown in Fig. 3.1-1. One of horizontal cross-sections of a toroidal half block is shown in Fig. 3.1-2. Since the coolant routing is designed to divide the coolant flow into two toroidal half blocks, the 3-D analysis model corresponding to one half block is generated. Isometric views and cross-sections of the generated model are compiled in Figs. 3.1-3 through 3.1-30. The model devotedly follows the design except for recesses at the back of the shield block. The recess to accommodate to the external manifolds and the recess at the toroidal end are only included. Since the lengths of radial channels strictly follow the design, the stainless steel structure is thicker than the design in some back regions. The number of elements composing the analysis model is 2,925,550 in total (about 1,340,000 and 1,590,000 for water and steel structure parts, respectively). The computer code used for the analysis is STAR-CD ver. 3.10A in which k- ϵ model is preliminary applied to solve the coolant turbulent flow.

Table 3.1-1 summarizes physical properties used in the analysis. Nuclear heating rates in the structural material corresponding to the neutron wall loading of 0.78 MW/m^2 are listed in Table 3.1-2. As for inlet coolant conditions, temperature 130°C , pressure 4 MPa and flow rate 4.0 kg/s are given.

Table 3.1-1 Physical properties of coolant and structural material

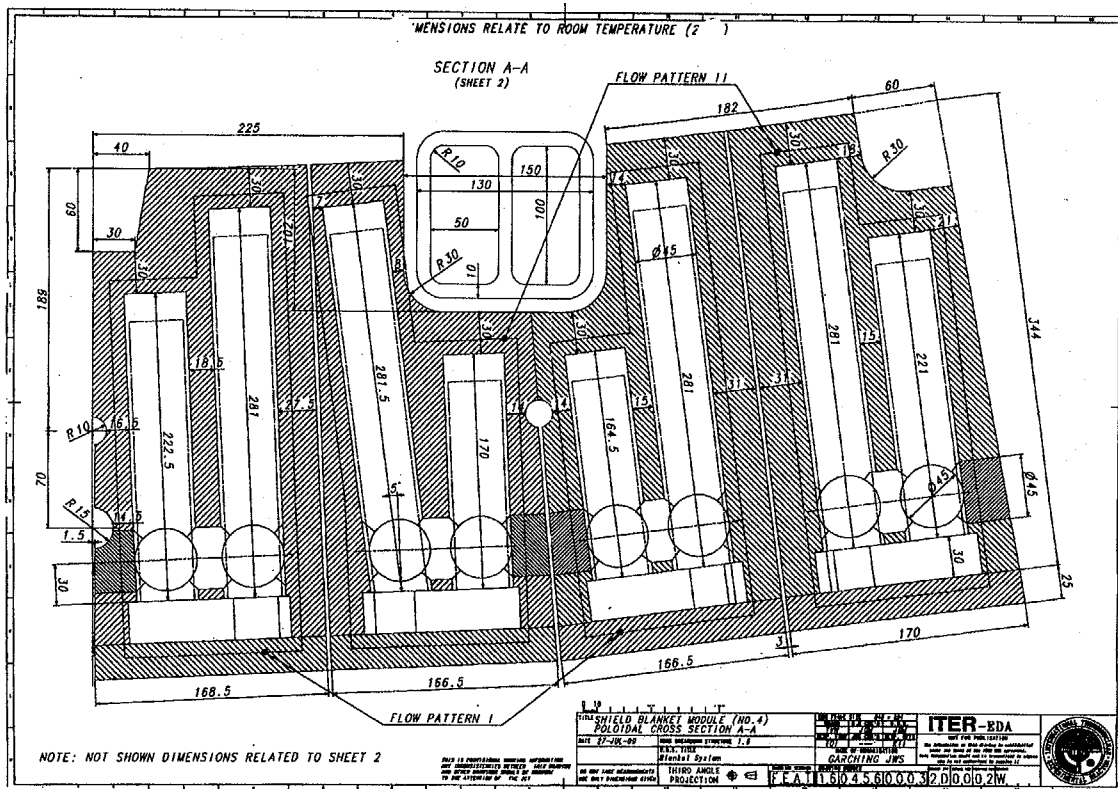
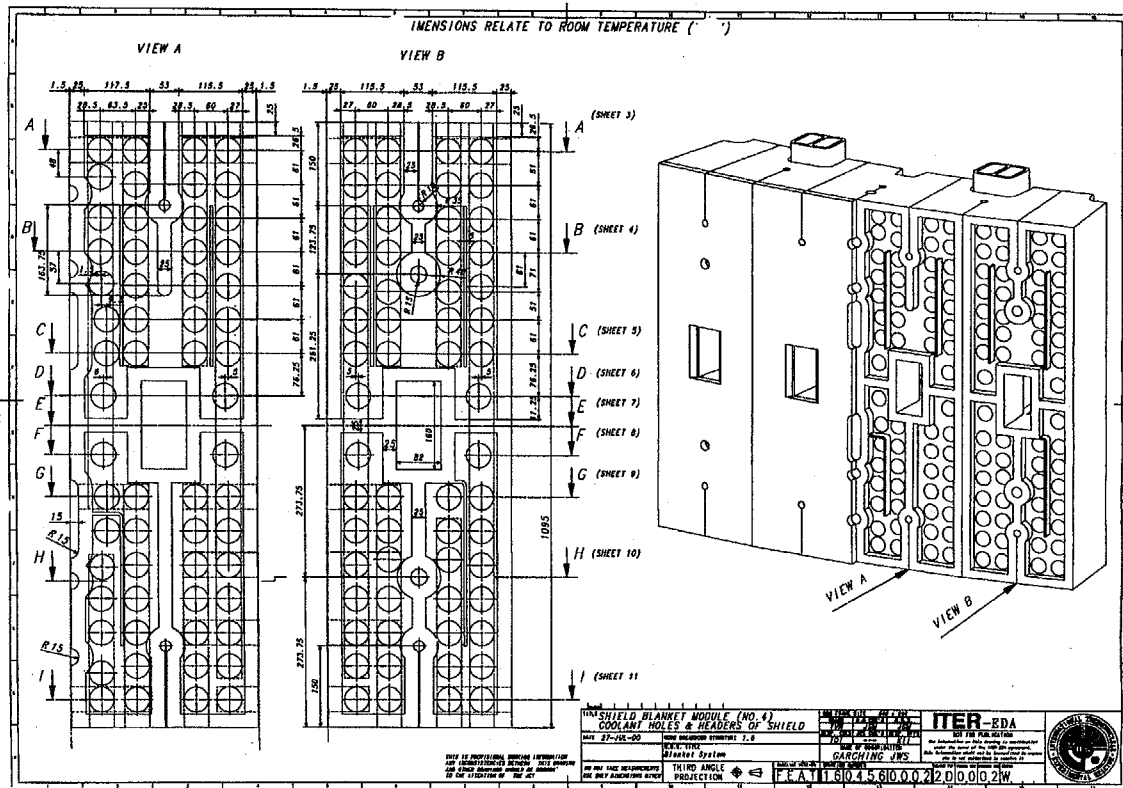
Material	Coolant	Structure
	H ₂ O*	SS316L(N)-IG
Density [kg/m ³]	927.9	7914
Viscosity [Pa·s]	6.864×10^{-4}	-
Thermal conductivity [W/m/K]	198.4	$13.651 + 0.01434T$
Specific heat [J/kg/K]	4275	$4.6549 + 0.21045T + 8.6641 \times 10^{-7} T^2$

* at 140°C , 4 MPa

T: temperature in $^\circ\text{C}$

Table 3.1-2 Nuclear heating rates distribution in shield block (SS structure)

Distance from shield block surface [mm]	Nuclear heating rate [MW/m ³]
4	5.76
14	5.27
24	4.79
34	4.34
44	3.94
54	3.55
64	3.21
74	2.87
84	2.59
94	2.32
104	2.07
114	1.86
124	1.66
134	1.48
144	1.32
154	1.18
164	1.05
174	0.931
184	0.826
194	0.734
204	0.652
214	0.578
224	0.512
264	0.454
244	0.402
254	0.356
264	0.316
274	0.278
284	0.246
695.6	0.252
309	0.222
322.3	0.195
335.6	0.171
349	0.147
362.3	0.126



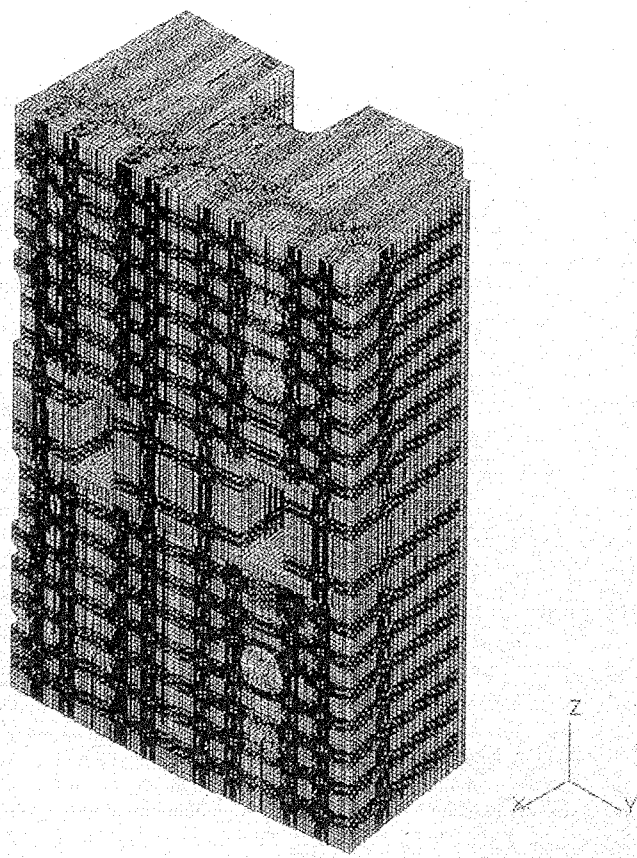


Fig. 3.1-3 Isometric front view of analysis model

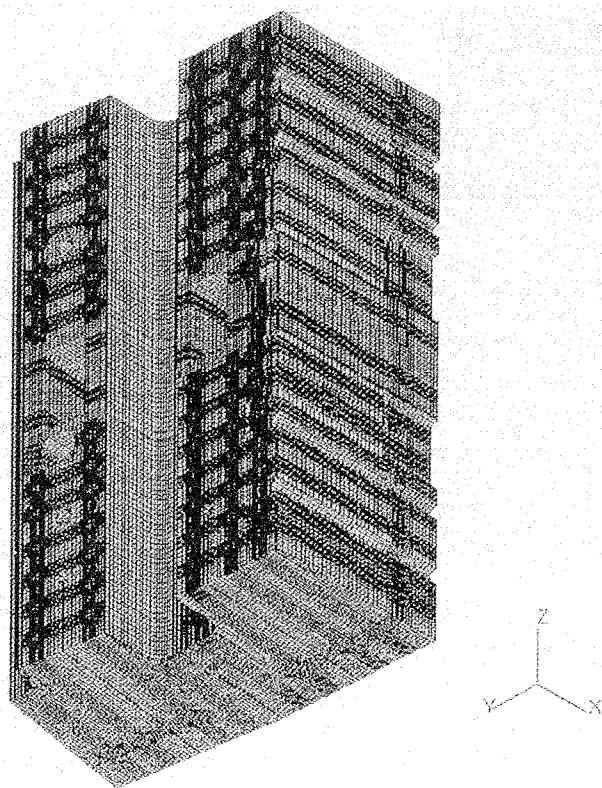


Fig. 3.1-4 Isometric back view of analysis model

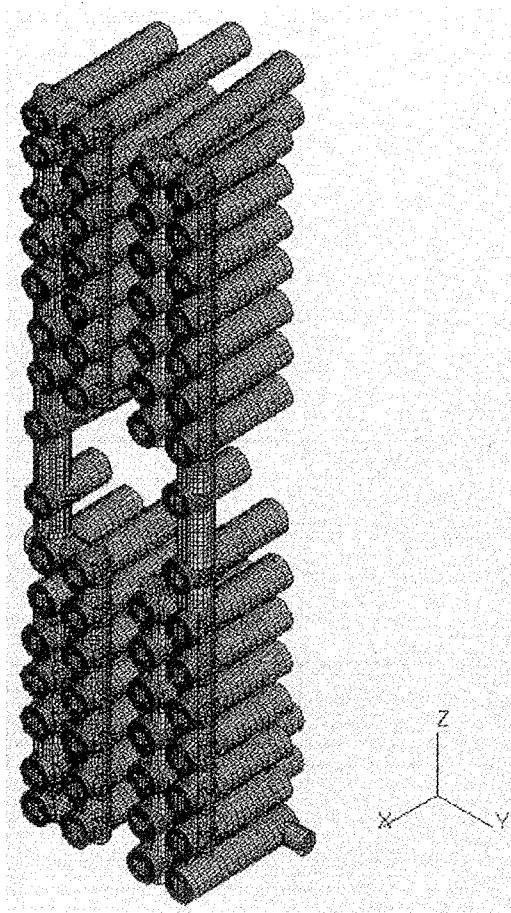


Fig. 3.1-5 Isometric view of coolant channels (module center side)

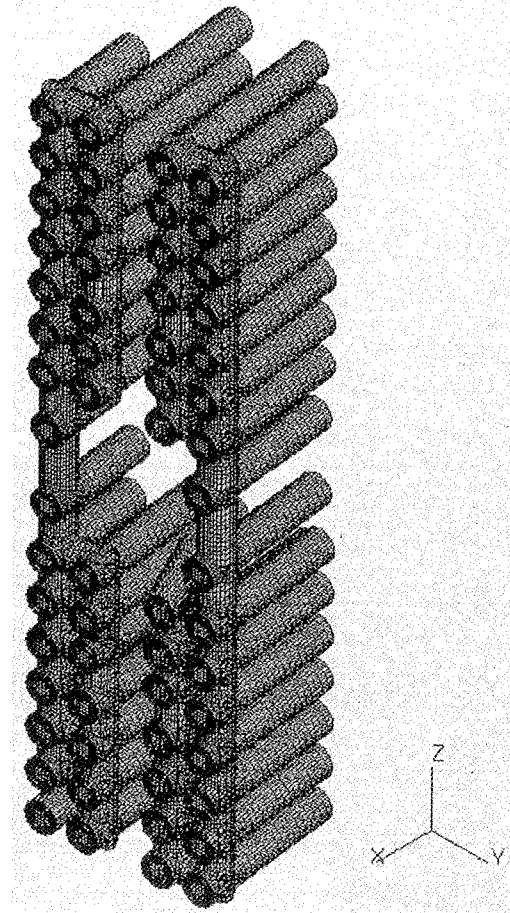


Fig. 3.1-6 Isometric view of coolant channels (module edge side)

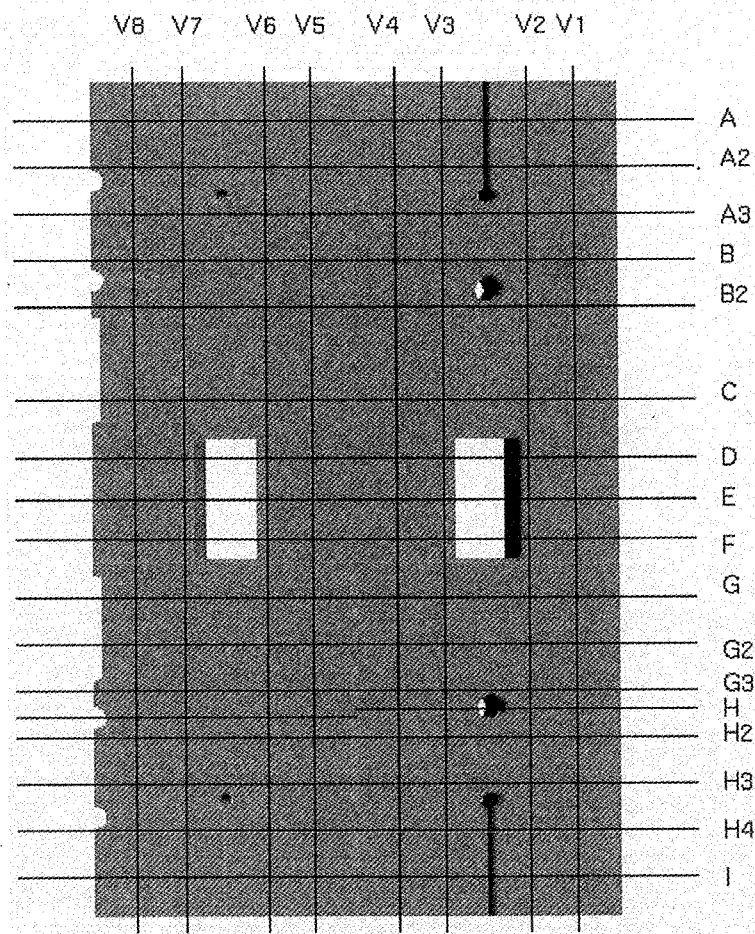


Fig. 3.1-7 Front view of analysis model

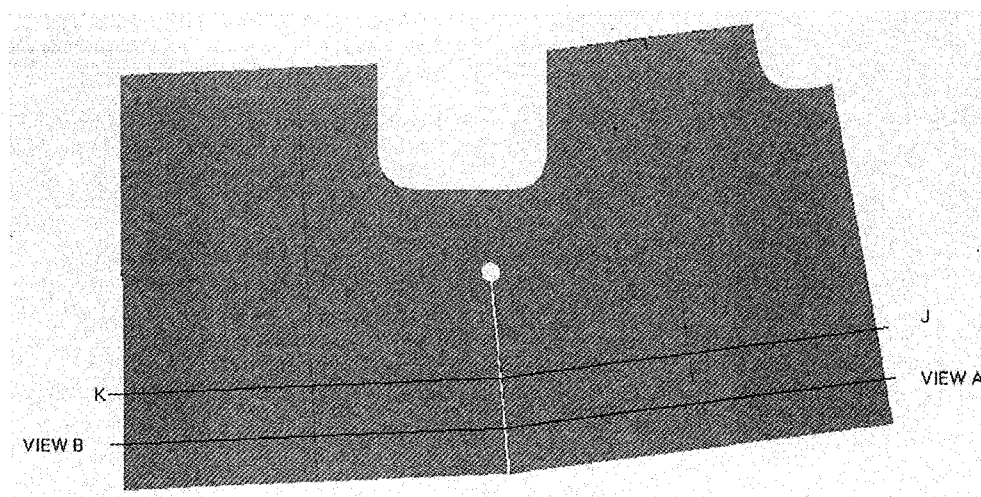


Fig. 3.1-8 Plan view of analysis model

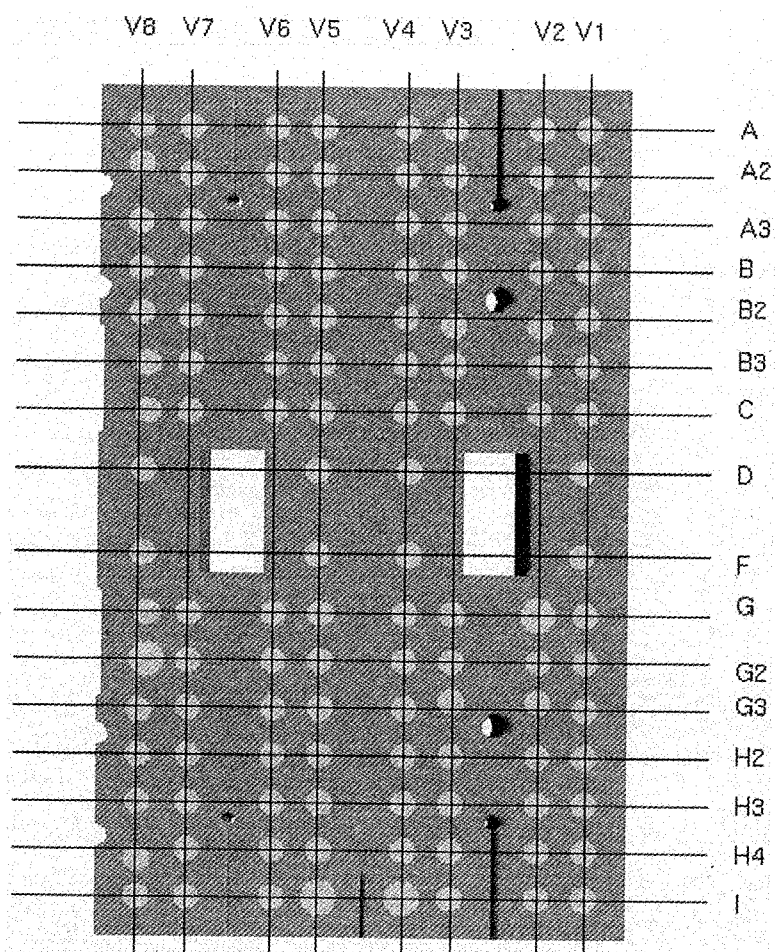


Fig. 3.1-9 Radial channels and cut lines for cross-sections

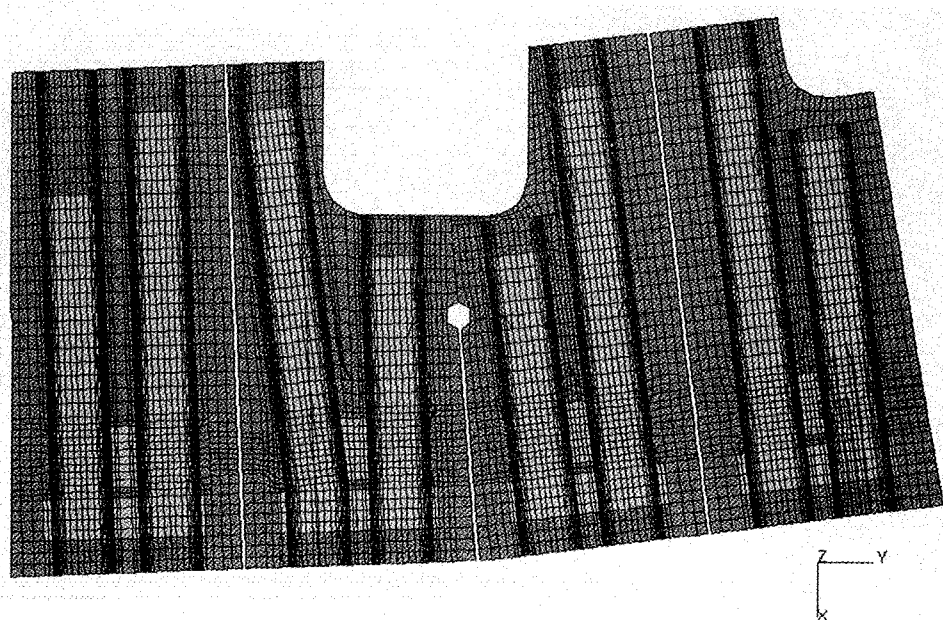


Fig. 3.1-10 Section A-A of analysis model

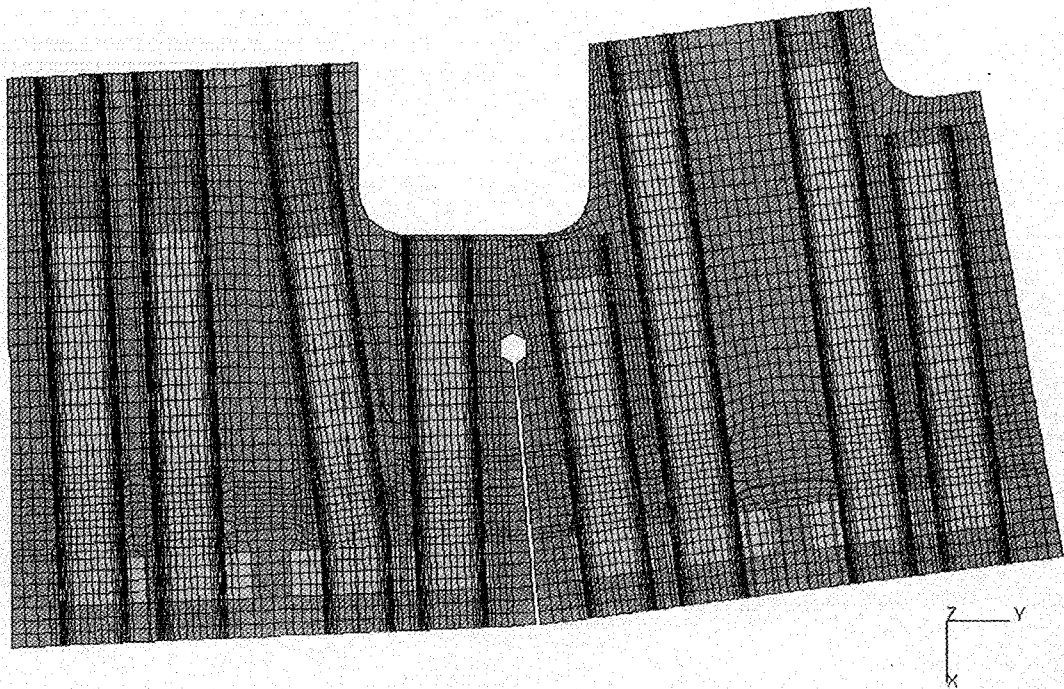


Fig. 3.1-11 Section B-B of analysis model

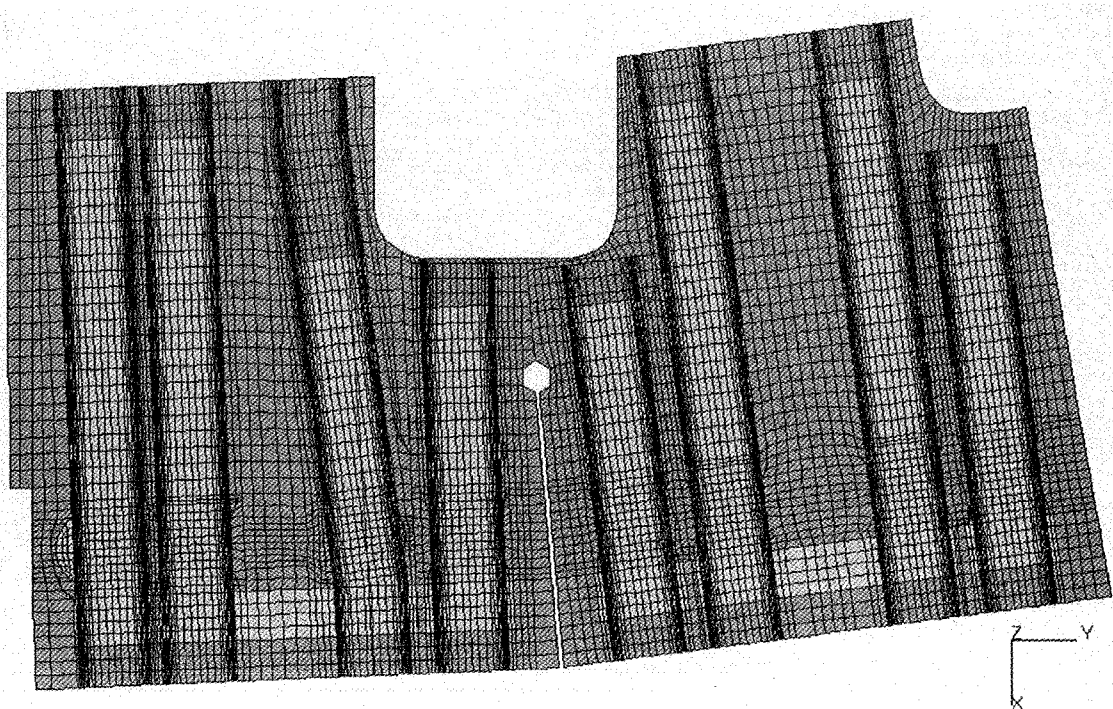


Fig. 3.1-12 Section C-C of analysis model

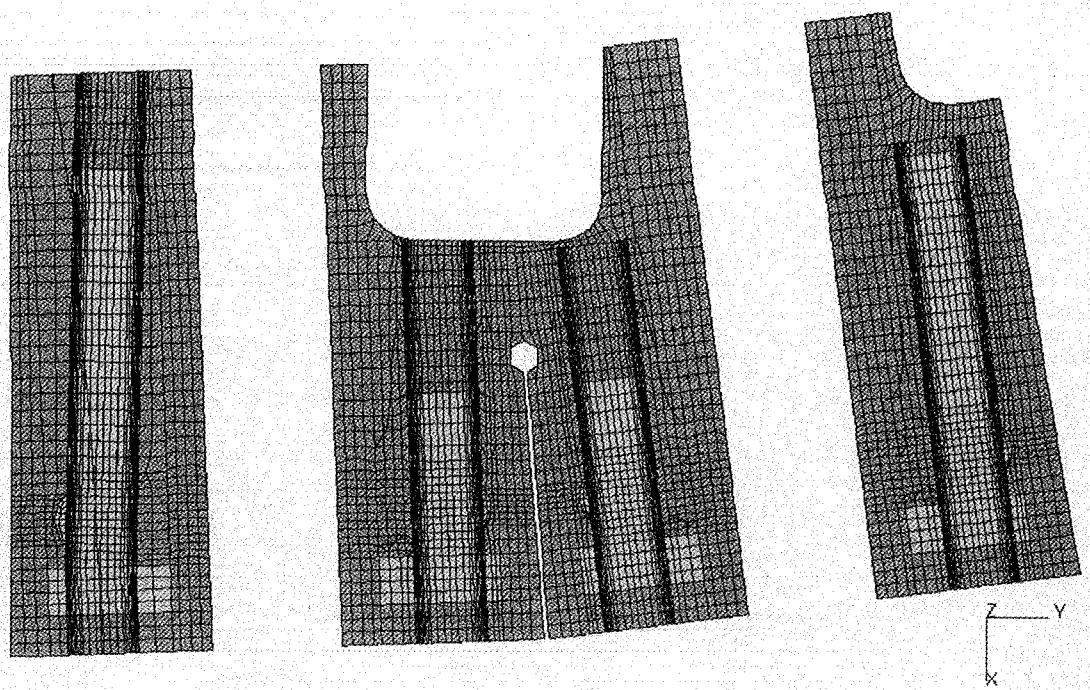


Fig. 3.1-13 Section D-D of analysis model

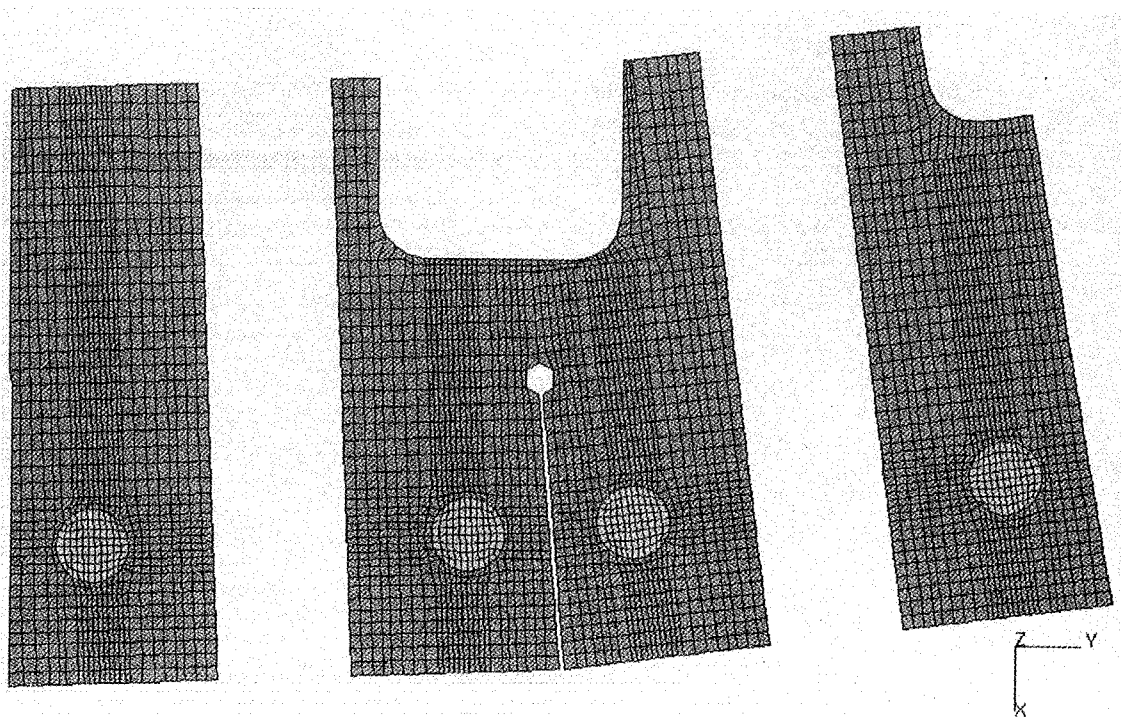


Fig. 3.1-14 Section E-E of analysis model

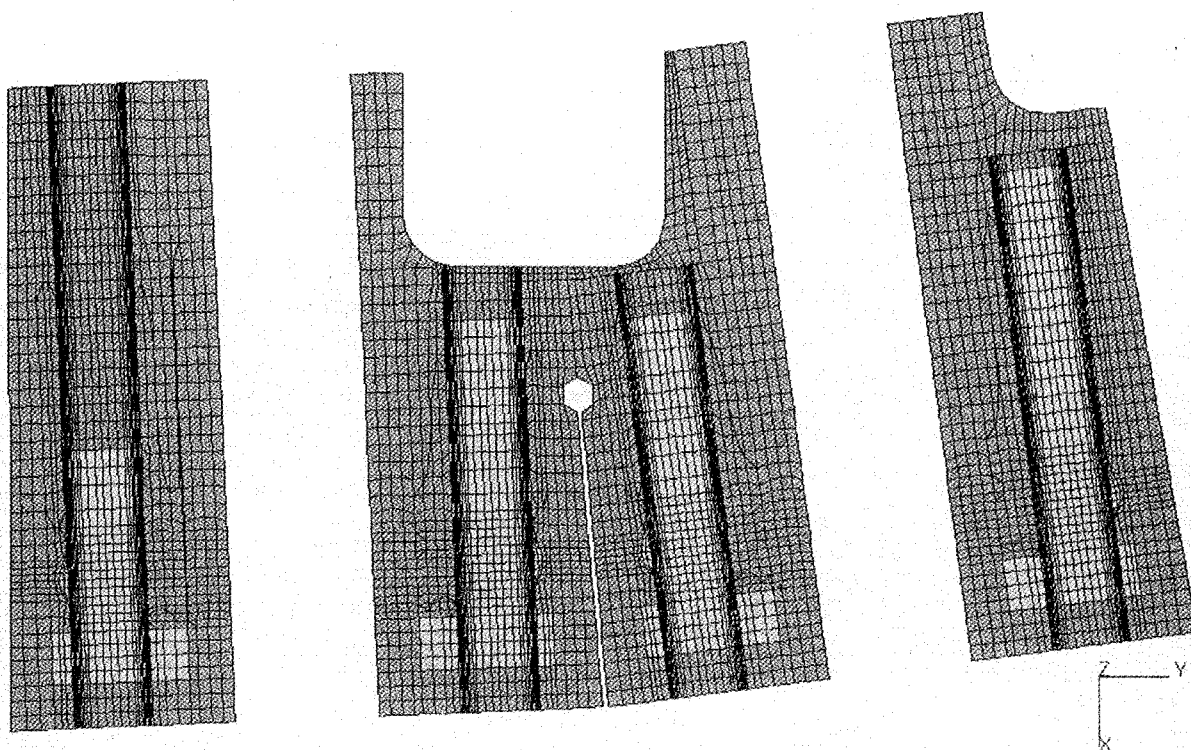


Fig. 3.1-15 Section F-F of analysis model

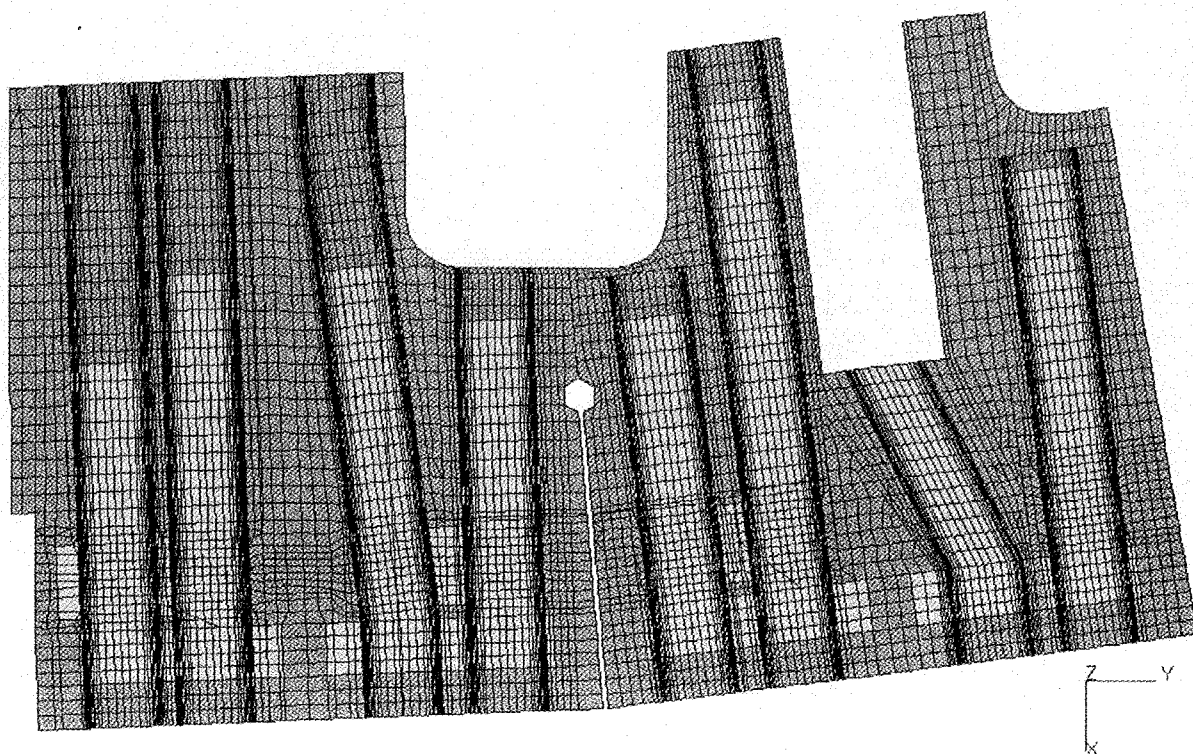


Fig. 3.1-16 Section G-G of analysis model

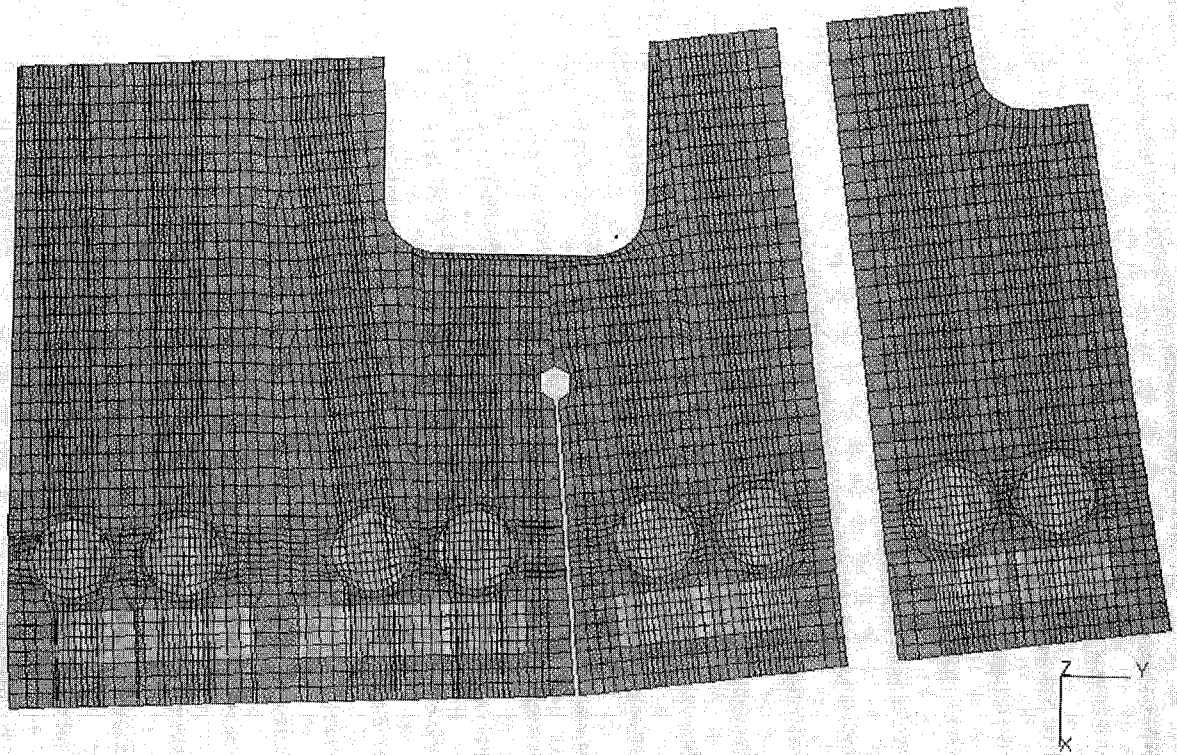


Fig. 3.1-17 Section H-H of analysis model

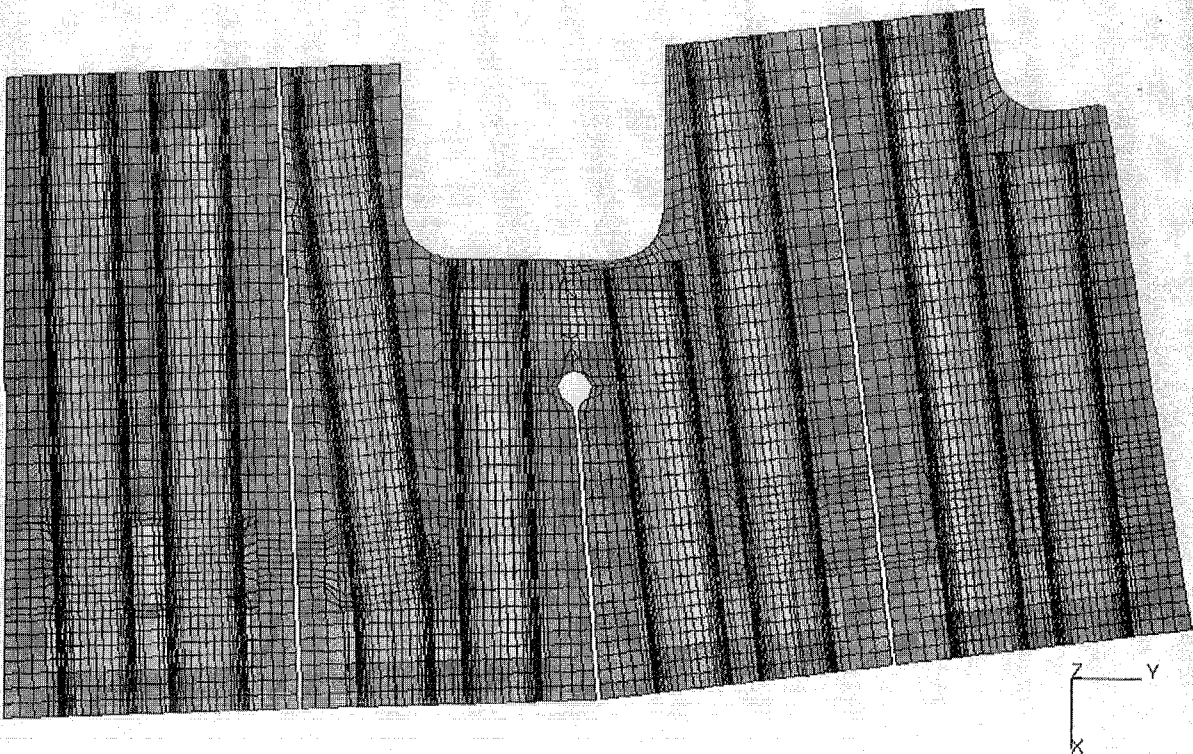


Fig. 3.1-18 Section I-I of analysis model

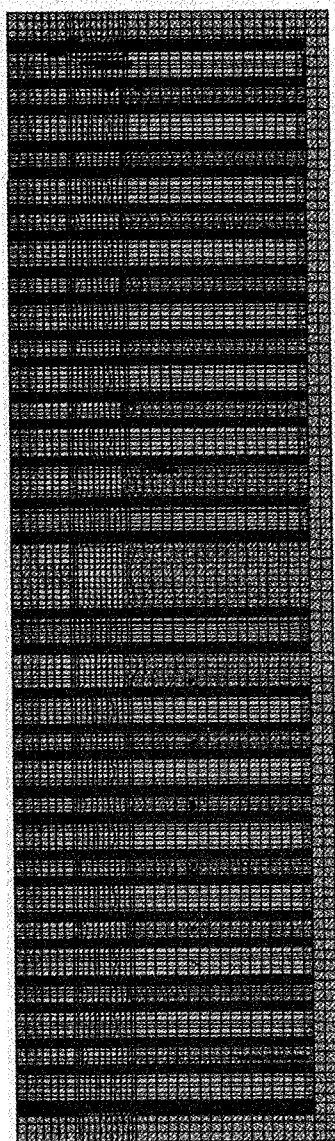


Fig. 3.1-19 Section V1-V1 of analysis model

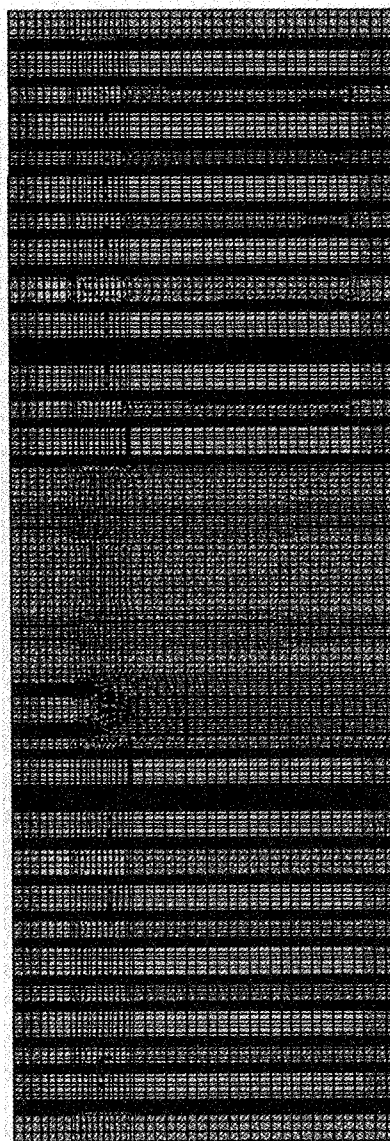


Fig. 3.1-20 Section V2-V2 of analysis model

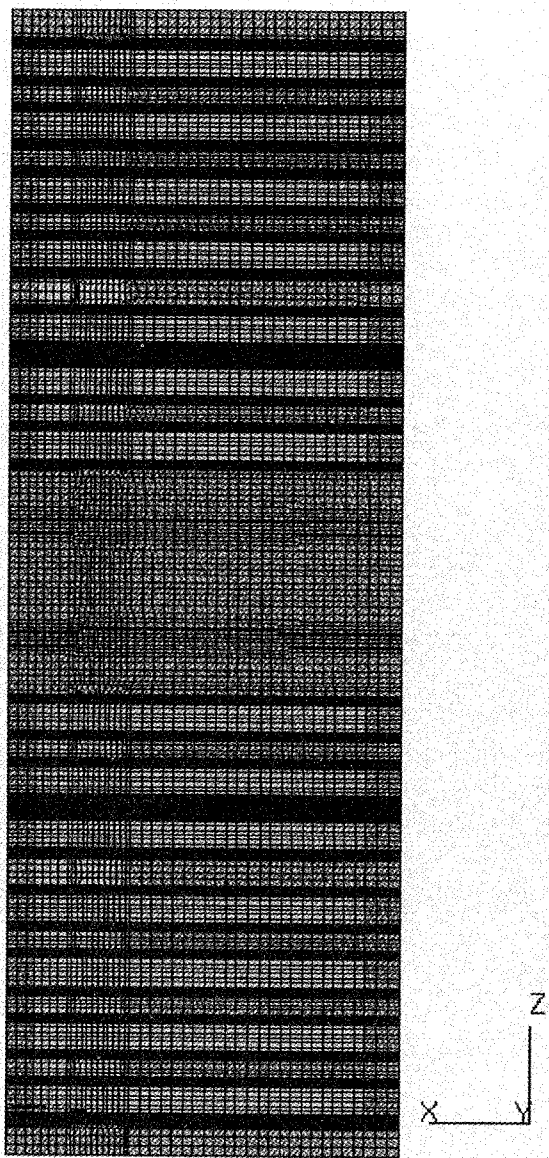


Fig. 3.1-21 Section V3-V3 of analysis model

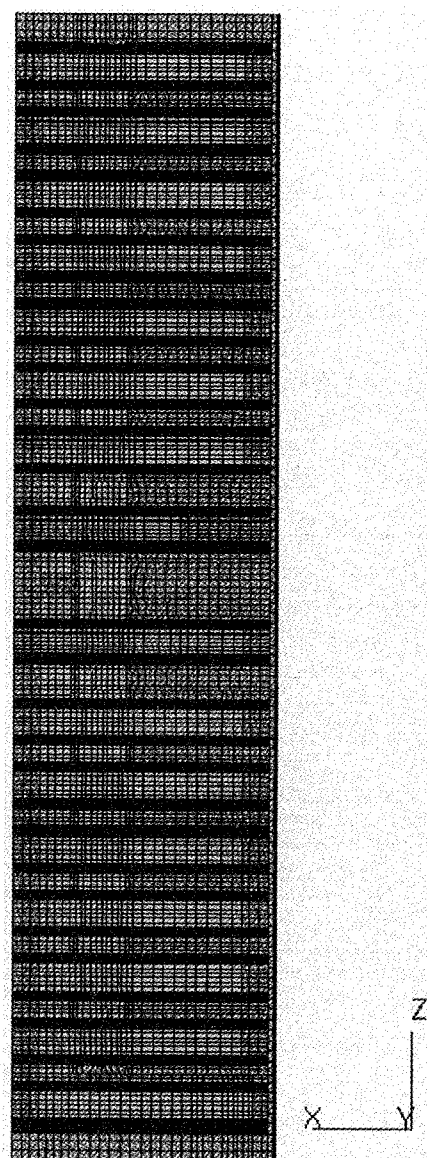


Fig. 3.1-22 Section V4-V4 of analysis model

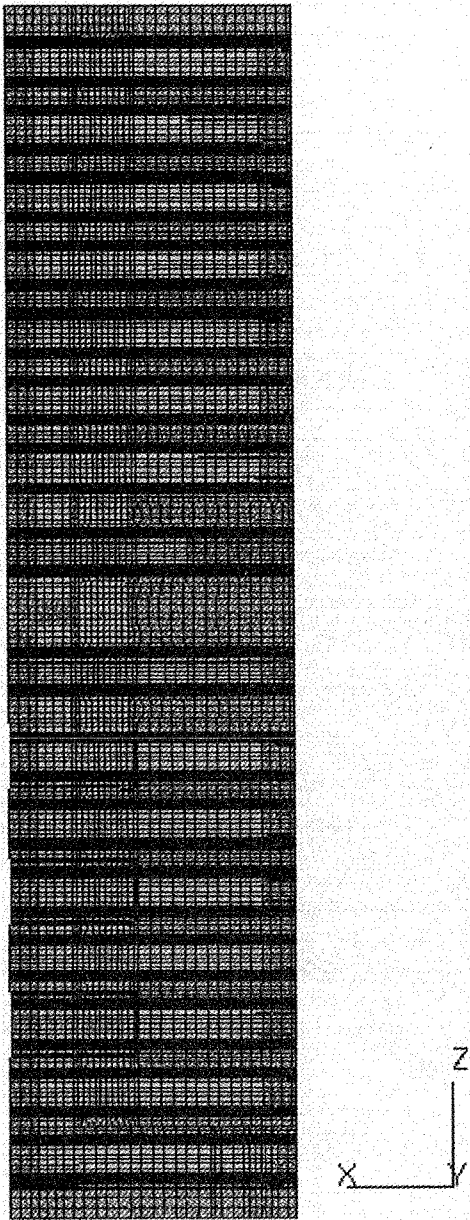


Fig. 3.1-23 Section V5-V5 of analysis model

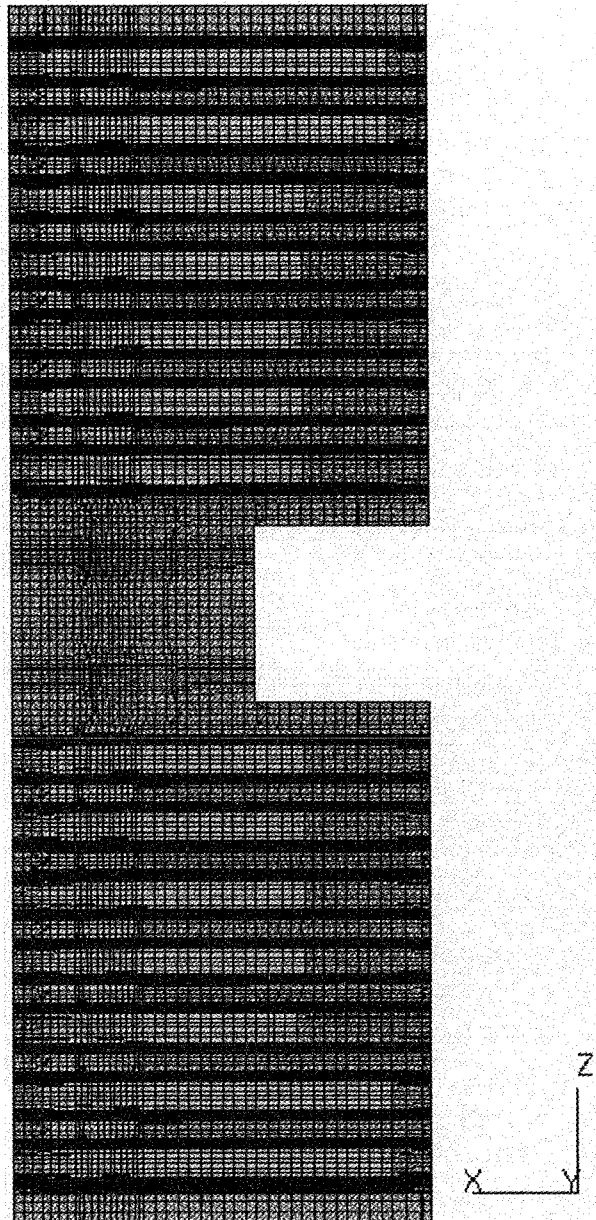


Fig. 3.1-24 Section V6-V6 of analysis model

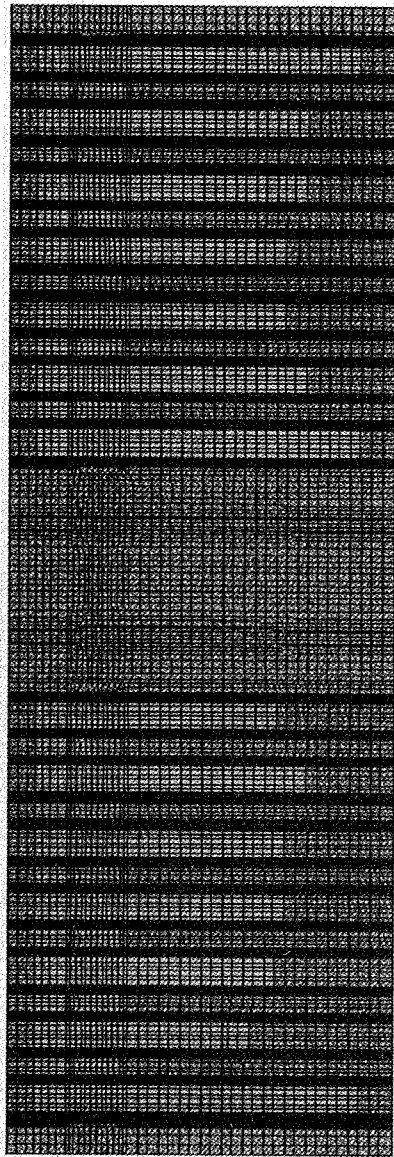


Fig. 3.1-25 Section V7-V7 of analysis model

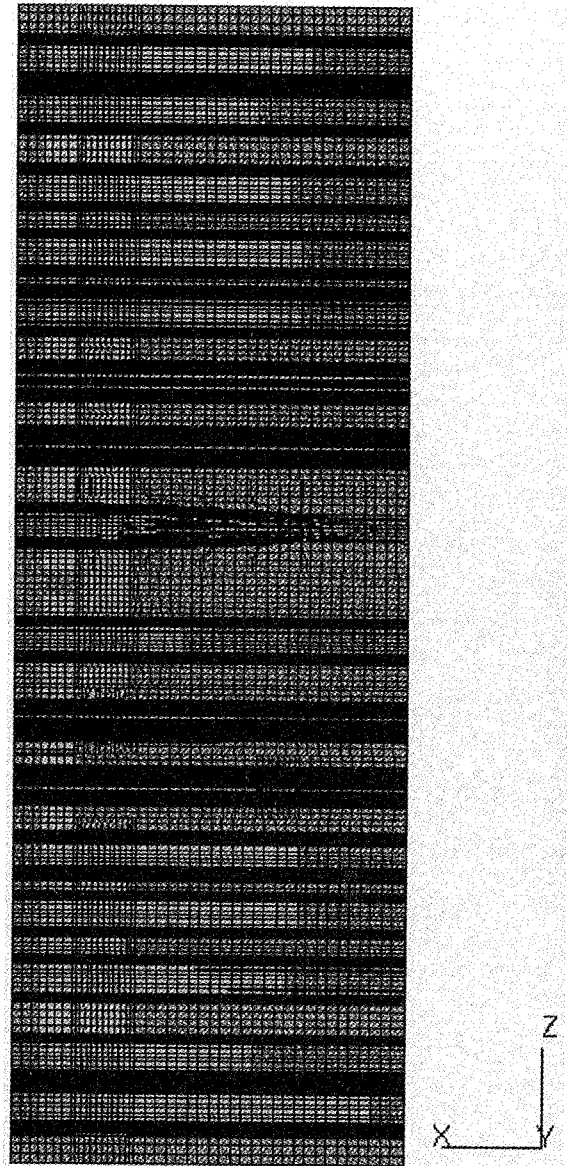


Fig. 3.1-26 Section V8-V8 of analysis model

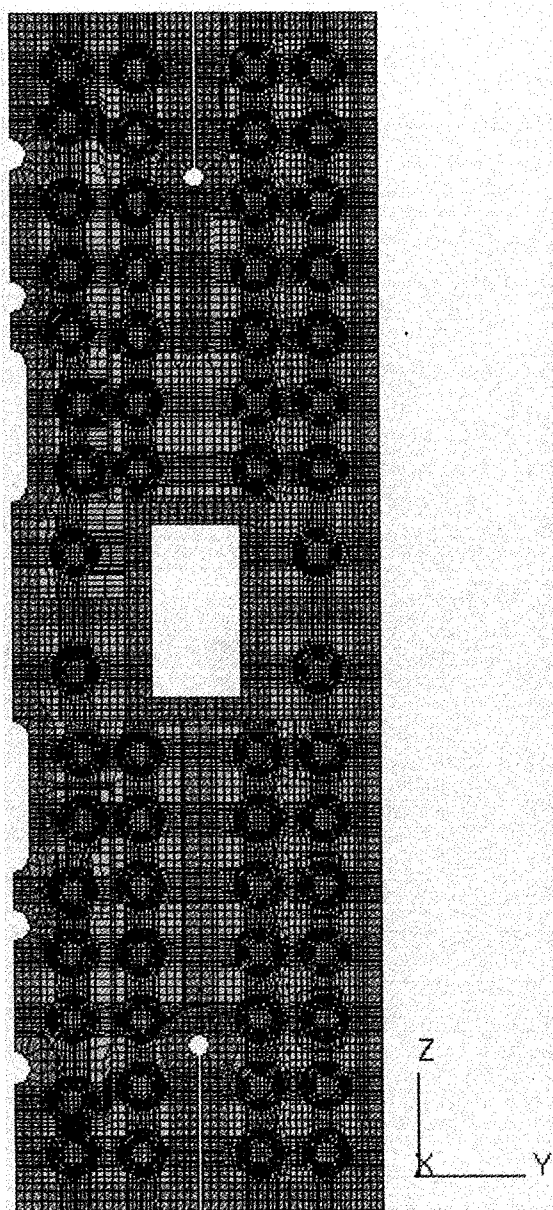


Fig. 3.1-27 View B of analysis model

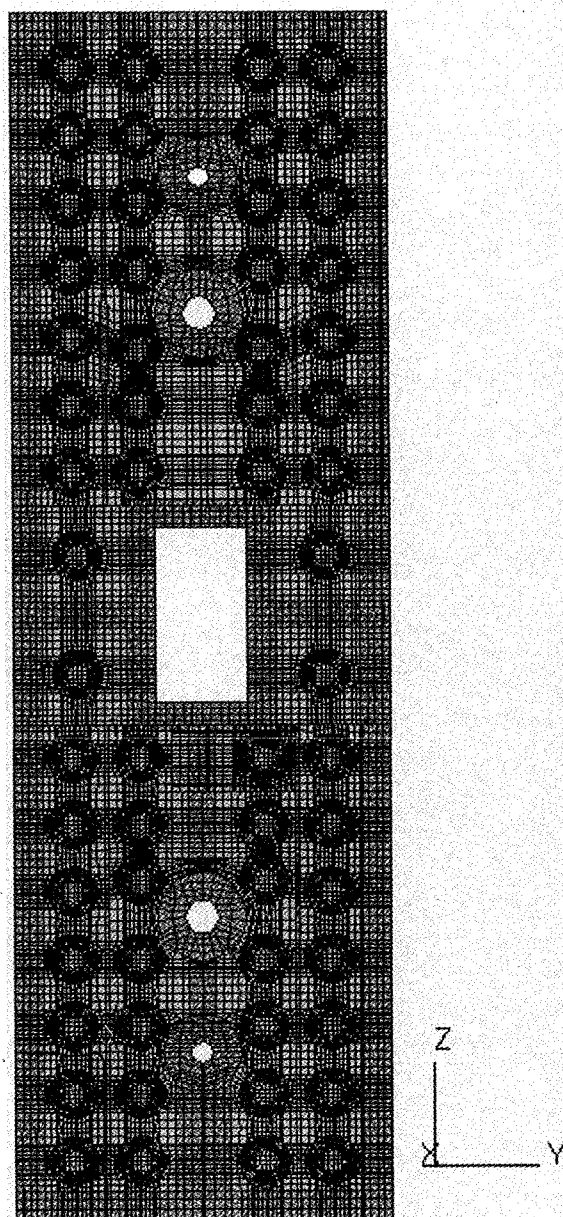


Fig. 3.1-28 View A of analysis model

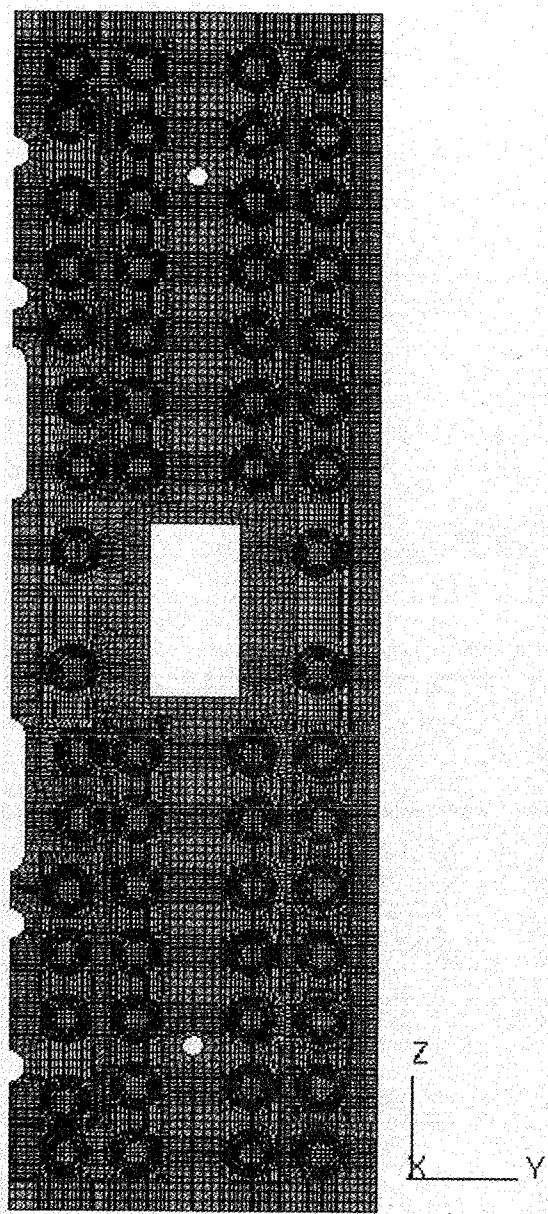


Fig. 3.1-29 Section K-K of analysis model

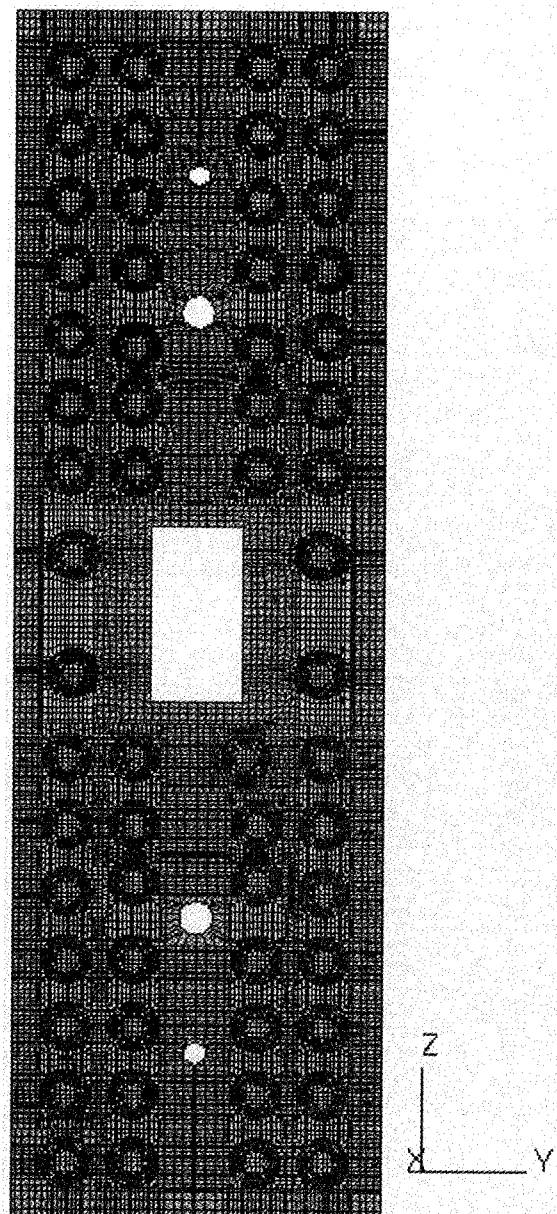


Fig. 3.1-30 Section J-J of analysis model

3.2 Analysis results and discussions

3.2.1 Coolant velocity and flow distribution

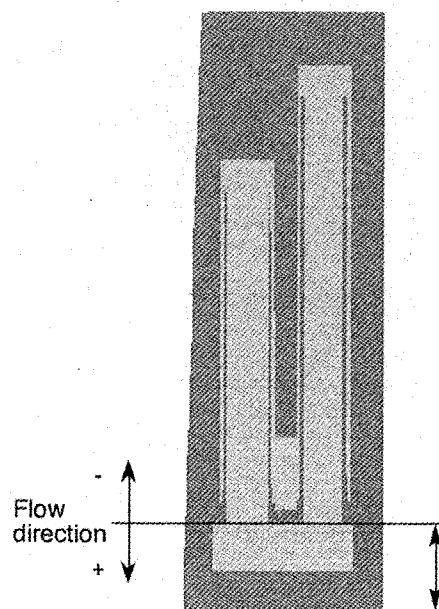
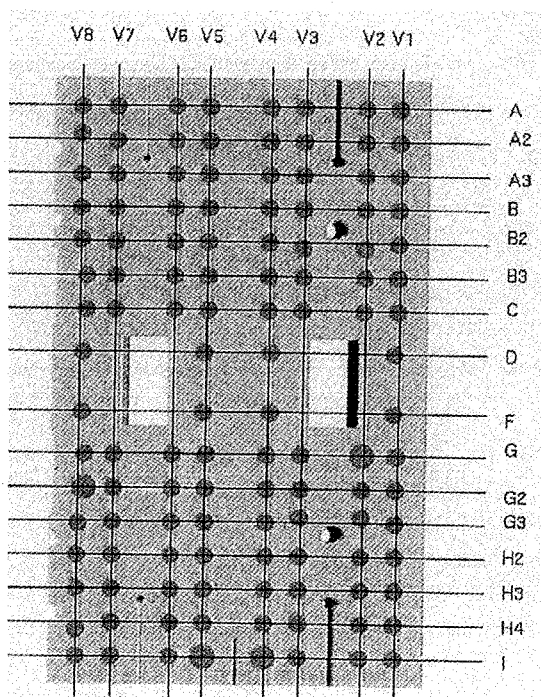
Velocity profiles in the headers are shown in Figs. 3.2-1 and 3.2-2. Owing to baffle plates, the coolant flows around well to distribute flow rates to radial channels. However, flow rates (velocities) seem a little low at top and bottom regions (see Fig. 3.2-1), it would be better for the baffle plates to be a little longer in order to supply more coolant flow to these regions.

Table 3.2-1 and Fig. 3.2-3 show flow rates in radial direction in the inner tube of the radial channel. As noted in the table, a plus sign '+' means the coolant flows into the header from the radial channel and a minus sign '-' the coolant flows out of the header to the radial channel. In Fig. 3.2-3, columns with black top are for flows out of the header (minus sign). Backward flow occurs in many channels. This backward flow would be due to the non-optimized baffle plate and an obstructed flow in the poloidal channel connecting the upper and lower radial channels. Figures 3.2-4 through 3.2-9 show velocity vectors including the obstructed parts. Figures 3.2-10 through 3.2-13 also show color contours of coolant velocity including same parts. In the poloidal channel beside the hole for the first wall support beam, the coolant velocity becomes very high as 14-16 m/s. The diameter of the poloidal channel is 45 mm, thus the cross-sectional area is 1590 mm^2 . However, at the location where the poloidal channel is interfered by the inner tube of the radial channel, the flow area is very small as about 190 mm^2 , which can be seen as a small crescent in Figs. 3.1-13 and 3.1-15, and thus causes high velocity.

To avoid or improve the flow obstruction in the poloidal channel, it is necessary to increase the poloidal channel diameter and/or to decrease the outer diameter of the inner tube for the concentric radial channel. Since little room is remained for enlarging the poloidal channel diameter in terms of the internal configuration of the shield block, the reduction of the inner tube diameter would be more realistic. However, even in this case, the effects of the inner tube diameter on the improvement on the backward flows, flow velocities and pressure losses should be carefully checked before its final decision.

Table 3.2-1 Coolant flow rates at radial channels

	V8	V7	V6	V5	V4	V3	V2	V1
A	-0.146	-0.0506	-0.185	-0.195	-0.247	-0.115	-0.194	-0.194
A2	-0.364	-0.0626	-0.140	0.154	-0.185	0.0141	-0.168	0.144
A3	0.322	0.0566	0.259	0.194	0.279	0.0489	0.248	0.187
B	-0.0114	0.105	0.0966	0.204	0.0337	0.107	0.0465	0.200
B2	-0.276	0.104	-0.0210	0.316	-0.203	-0.0945	0.113	0.313
B3	-0.747	-0.384	-0.0889	0.510	-0.470	-0.309	-0.116	0.515
C	-1.07	-0.0906	0.276	0.848	-1.03	0.104	0.282	0.964
D	-1.39			1.78	-1.94			1.77
F	1.64			-1.56	1.52			-1.75
G	0.939	0.501	-0.517	-0.678	0.568	0.345	4.01	-1.07
G2	-4.01	0.330	-0.279	-0.316	0.345	0.219	-0.209	-0.533
G3	0.376	0.194	-0.173	-0.177	0.167	0.149	-0.0808	-0.196
H2	0.219	0.0667	-0.105	-0.109	0.106	0.107	0.112	0.105
H3	0.471	0.243	0.0532	-0.0772	0.100	0.0850	0.135	0.411
H4	-0.506	-0.159	-0.00129	0.0658	0.190	0.133	-0.0207	-0.239
I	-0.225	-0.0845	-0.129	4.01	-4.01	-0.0258	-0.267	-0.398



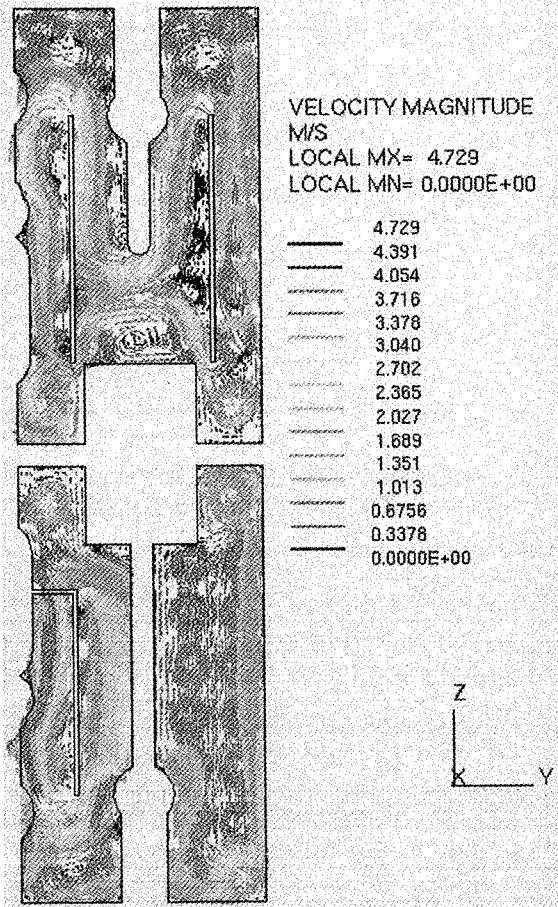


**Fig. 3.2-1 Velocity vectors at header
(view B)**

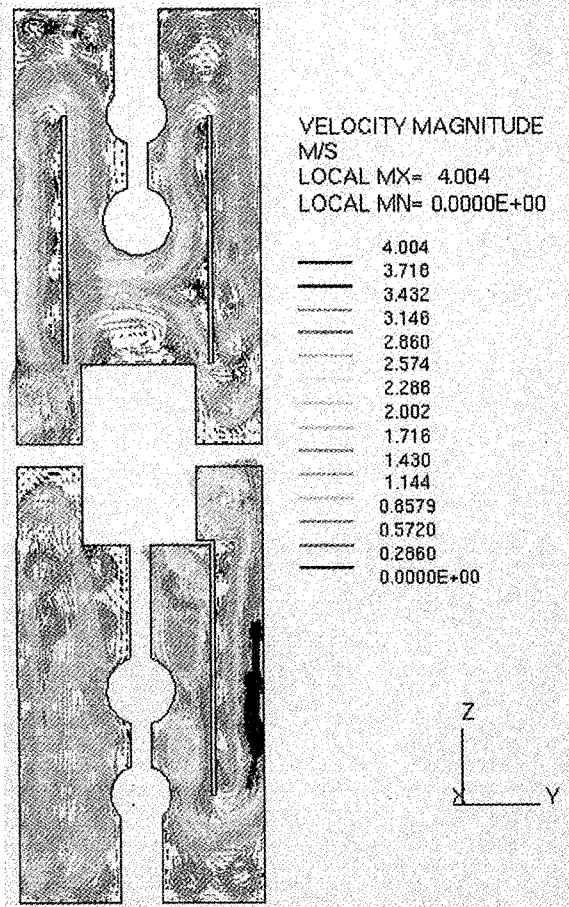


**Fig. 3.2-2 Velocity vectors at header
(view A)**

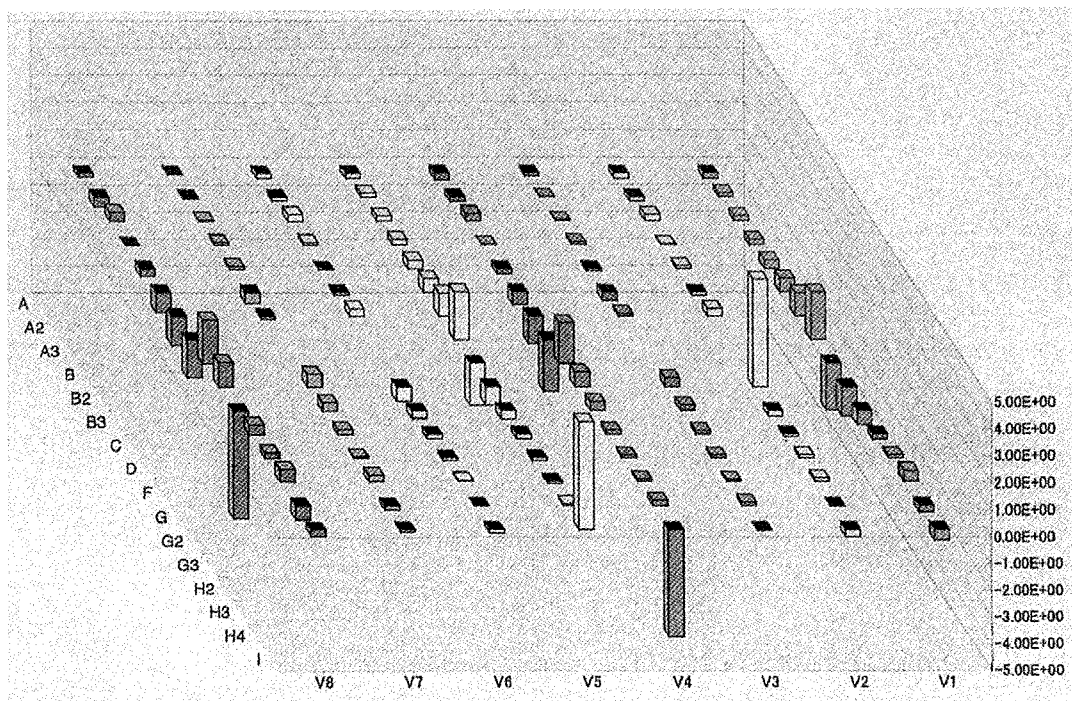


Fig. 3.2-3 Coolant flow rates at radial channels

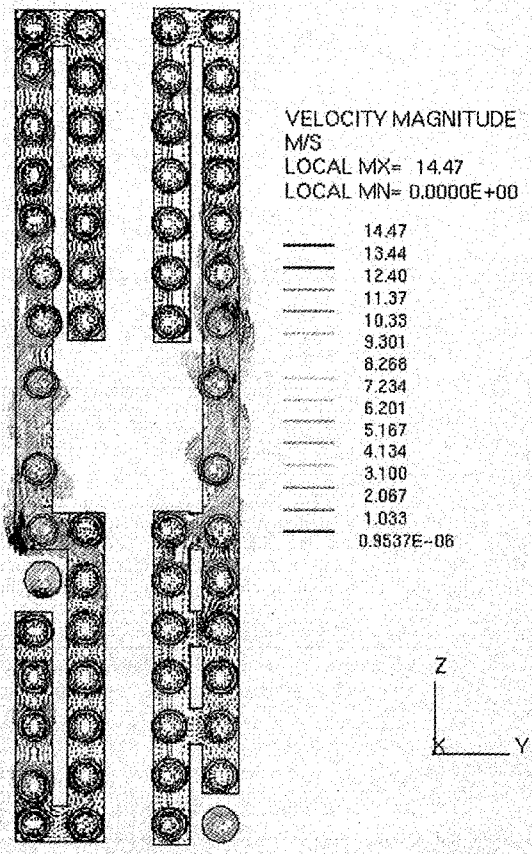


Fig. 3.2-4 Velocity vectors (section K-K)

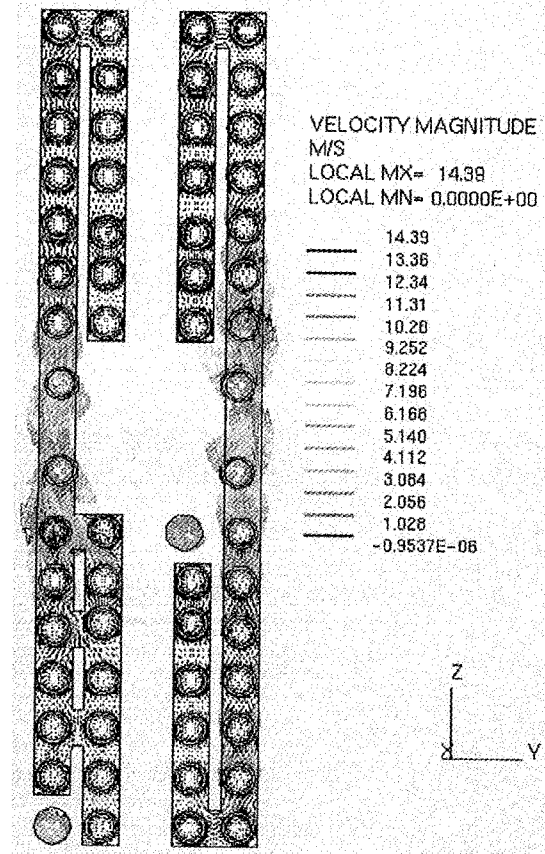


Fig. 3.2-5 Velocity vectors (section J-J)

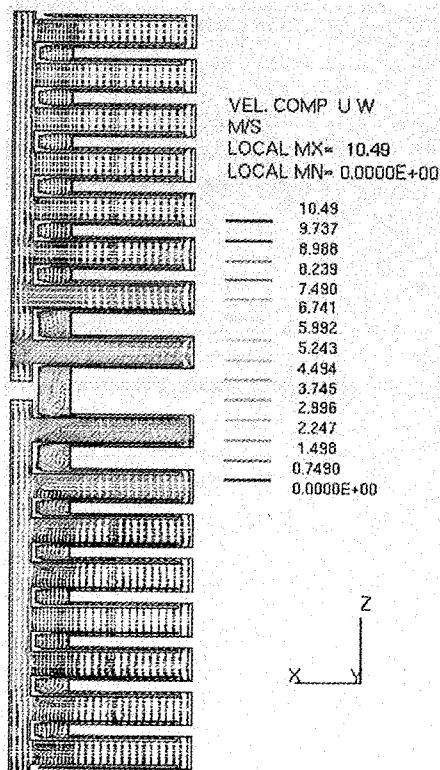


Fig. 3.2-6 Velocity vectors (section V1-V1)

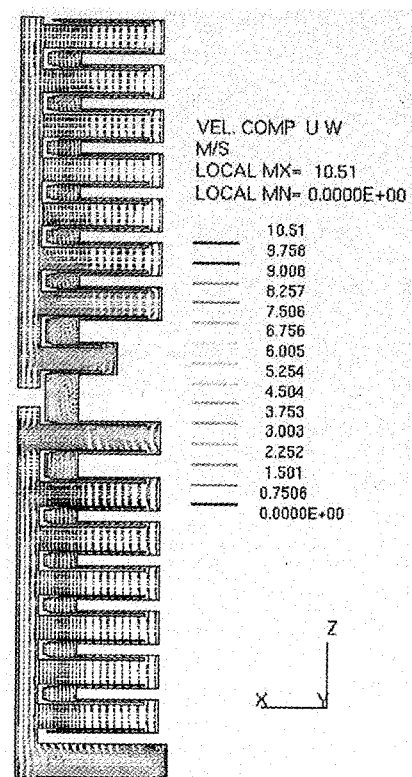


Fig. 3.2-7 Velocity vectors (section V4-V4)

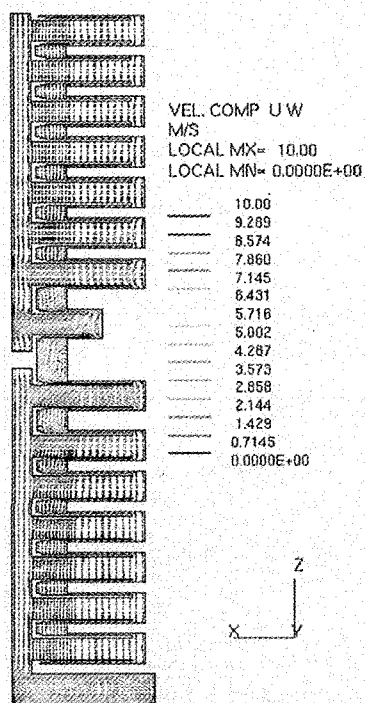


Fig. 3.2-8 Velocity vectors (section V5-V5)

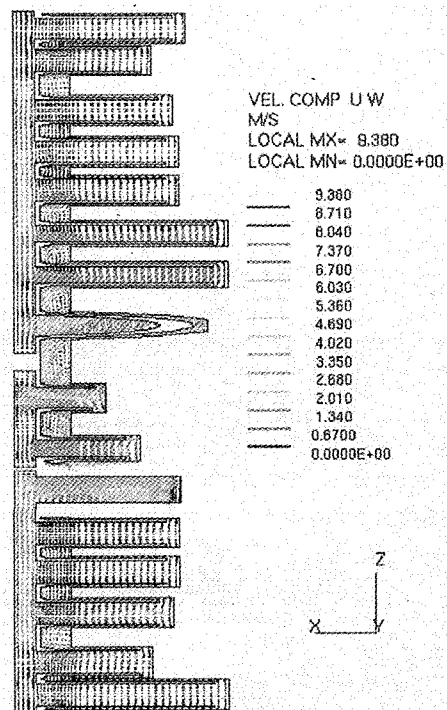


Fig. 3.2-9 Velocity vectors (section V8-V8)

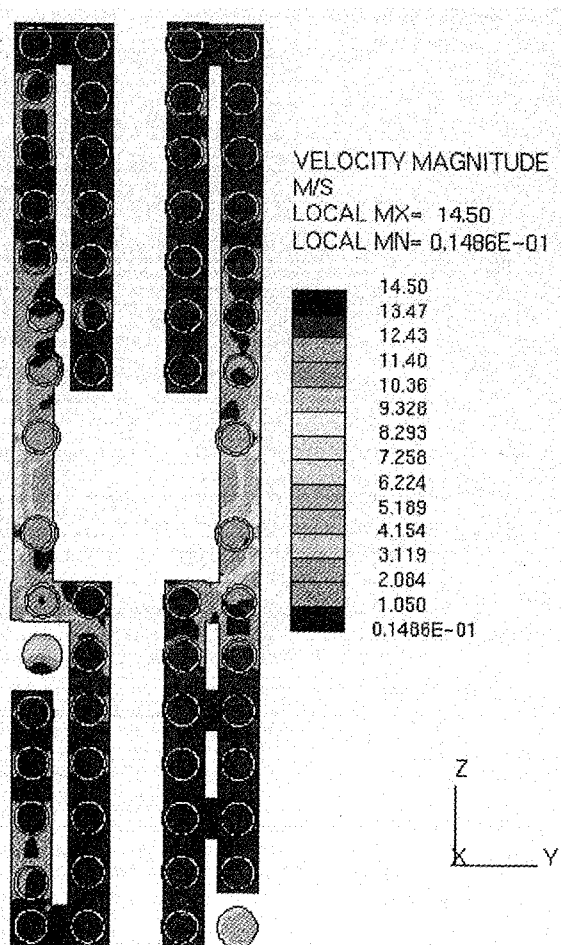


Fig. 3.2-10 Velocity contour (section K-K)

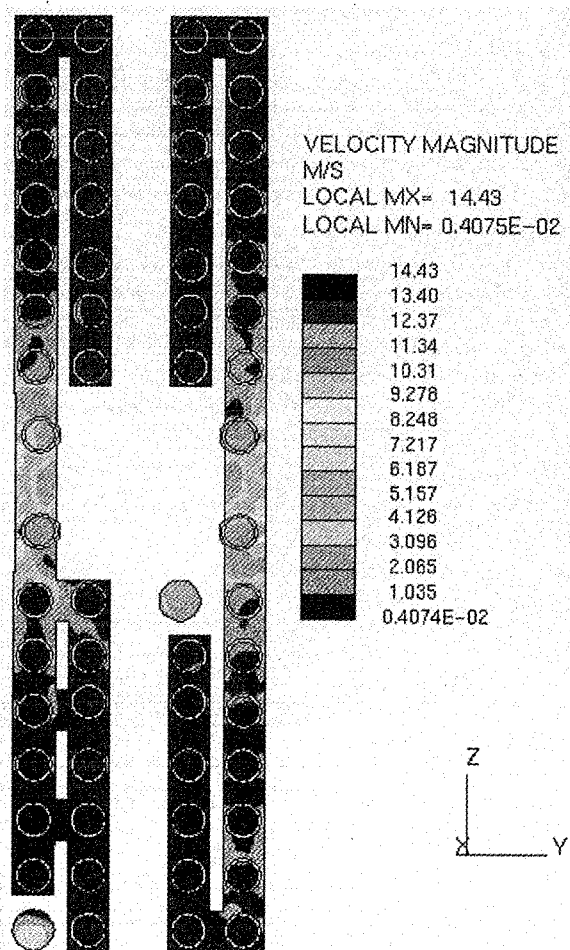


Fig. 3.2-11 Velocity contour (section J-J)

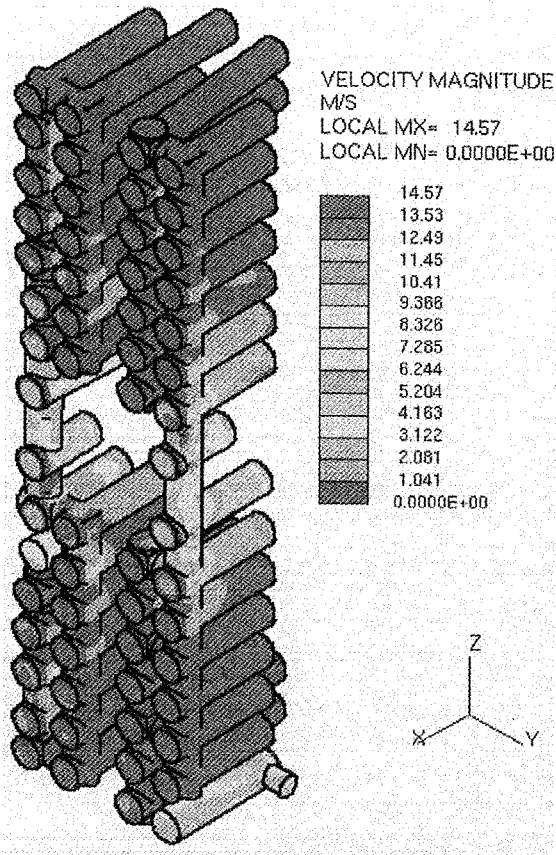


Fig. 3.2-12 Velocity contour (front view B)

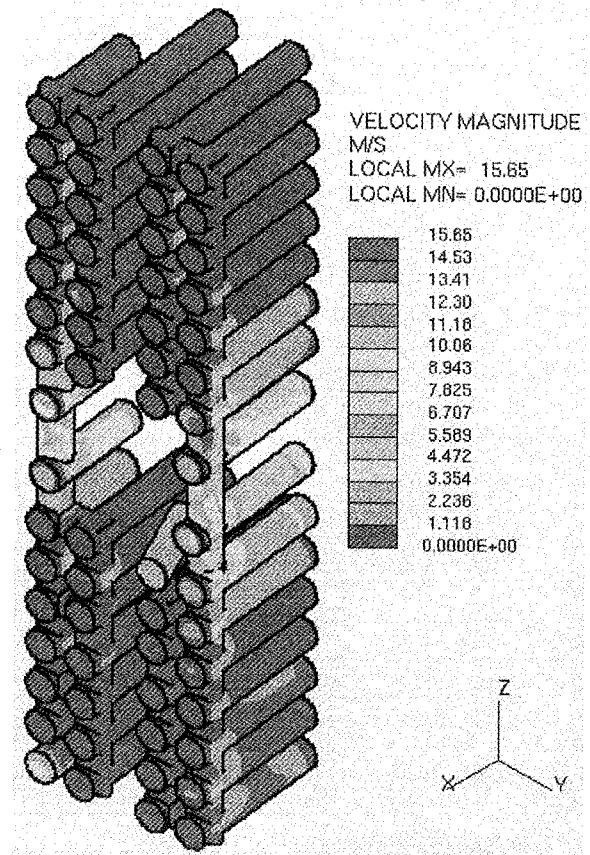


Fig. 3.2-13 Velocity contour (front view A)

3.2.2 Pressure profile

Pressure profiles are shown in Figs. 3.2-14 through 3.2-17. Figure 3.2-16 and 3.2-17 correspond to the annular region of the concentric radial channel. Total pressure drop from the inlet to the outlet of the shield block is 0.55 MPa. As seen from the figures, pressure losses are fairly low except for the above-mentioned small flow area parts in the poloidal channels. The pressure loss about 0.04-0.05 MPa is generated at each part. Since there are eight similar parts, total pressure loss of these parts reach 0.3-0.4 MPa. If the outer diameter (39 mm at present) of the inner tube for the radial channel can be reduced to 35 mm, 31 mm or 27 mm, the flow area (190 mm^2 at present) is increased to 260 mm^2 , 370 mm^2 or 490 mm^2 , respectively. As, in these cases, the flow area is increased by a factor of 1.4, 1.9 or 2.6, the pressure loss due to the eight parts would be reduced to 0.2 MPa, 0.1 MPa or 0.06 MPa, respectively. Therefore, including pressure losses in other regions of the shield block, the total pressure loss could be roughly estimated as 0.4 MPa, 0.3 MPa or 0.25 MPa, respectively.

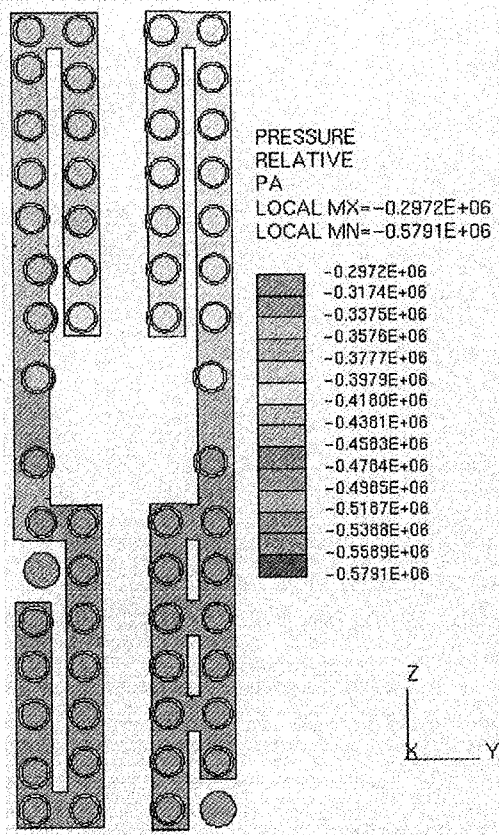


Fig. 3.2-14 Pressure profile (section K-K)

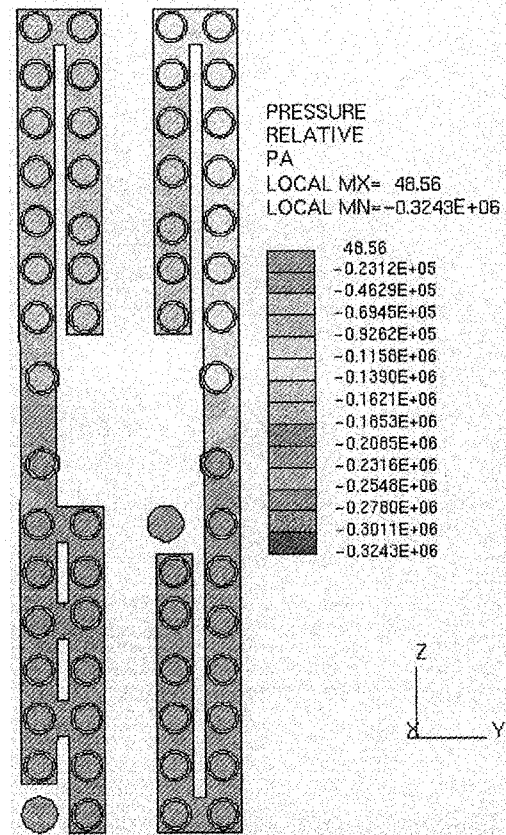


Fig. 3.2-15 Pressure profile (section J-J)

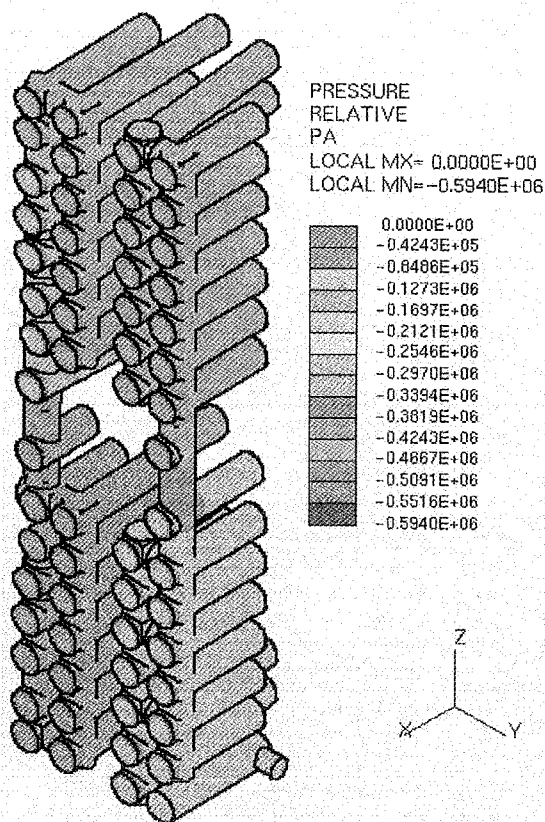


Fig. 3.2-16 Pressure profile (front view B)

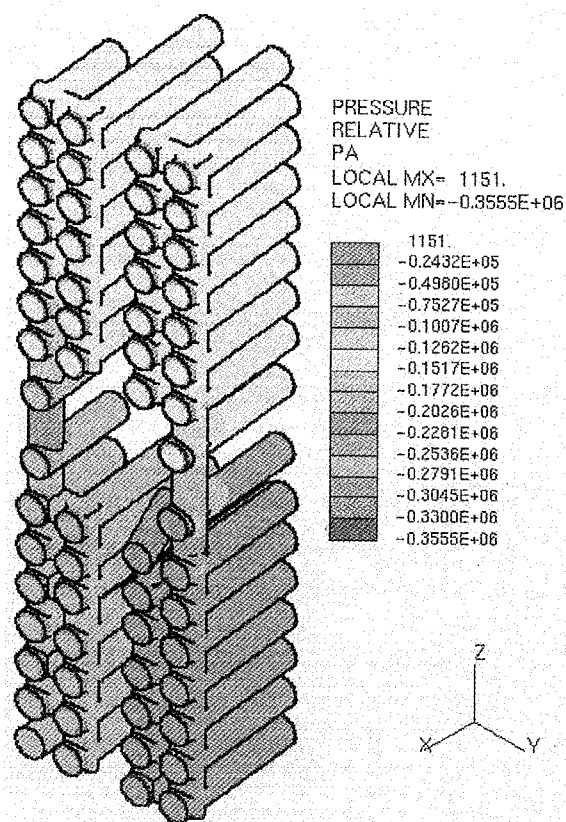
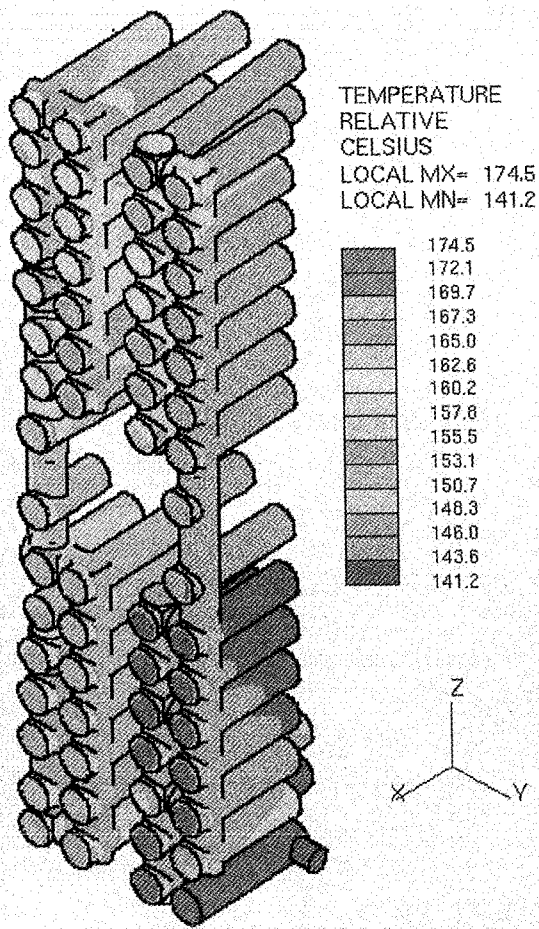


Fig. 3.2-17 Pressure profile (front view A)

3.2.3 Temperature profile

The average outlet temperature of the coolant is 153 °C while the inlet temperature is 130 °C. The outlet temperature is slightly over the design value, 148 °C, due to thicker structural materials in back region than the design and an uncertainty on the estimation of the inlet (the outlet of the first wall) temperature. Figures 3.2-18 and 3.2-19 show coolant temperature profiles. Though some hot spots up to 175 °C are observed, they would be improved by the modification to eliminate or reduce the flow obstruction in the poloidal channel and the rearrangement of the baffle plate in the header.

Temperature profiles of SS316L(N)-IG structural material are shown in Figs. 3.2-18 through 3.2-20. High temperatures up to the maximum temperature, 428 °C, are observed at the top and bottom edge regions of the front side. When these high temperatures are found to be unallowable, e.g., in terms of excessive thermal stress, they could be reduced by decreasing the thickness of the header cover plate (currently 25 mm thick) and/or beveling the edge parts. Temperatures in the back region are not so high even though some parts are thicker than the design. It is because the nuclear heating rates are sufficiently low in the back region.



**Fig. 3.2-18 Coolant temperature profile
(front view B)**

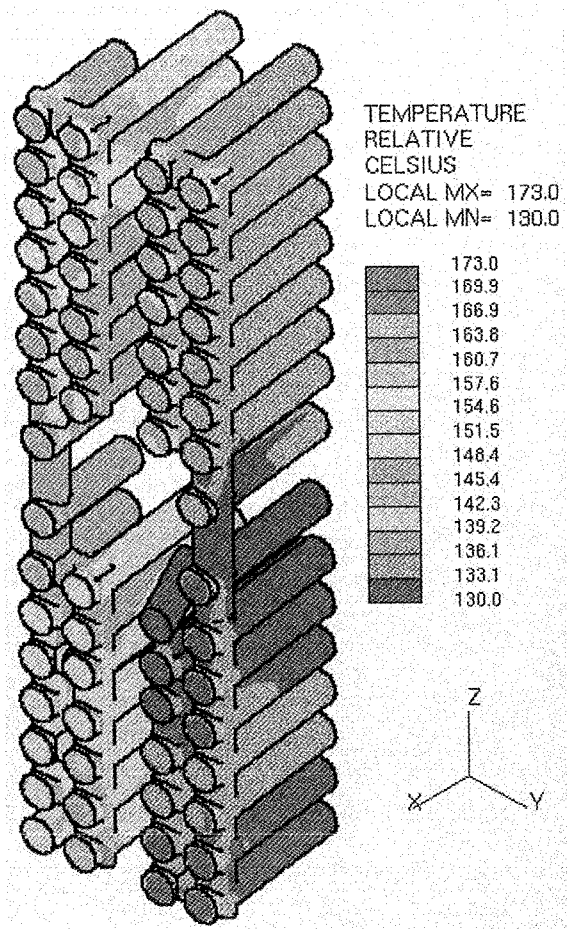


**Fig. 3.2-19 Coolant temperature profile
(front view A)**

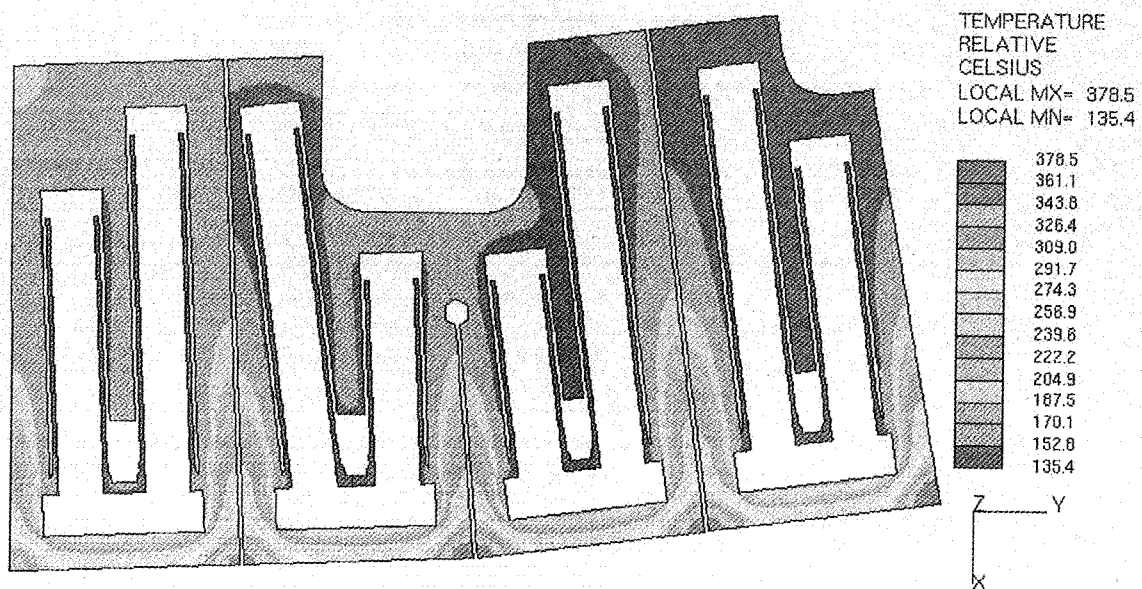


Fig. 3.2-20 Temperature profile of structural material (section A-A)

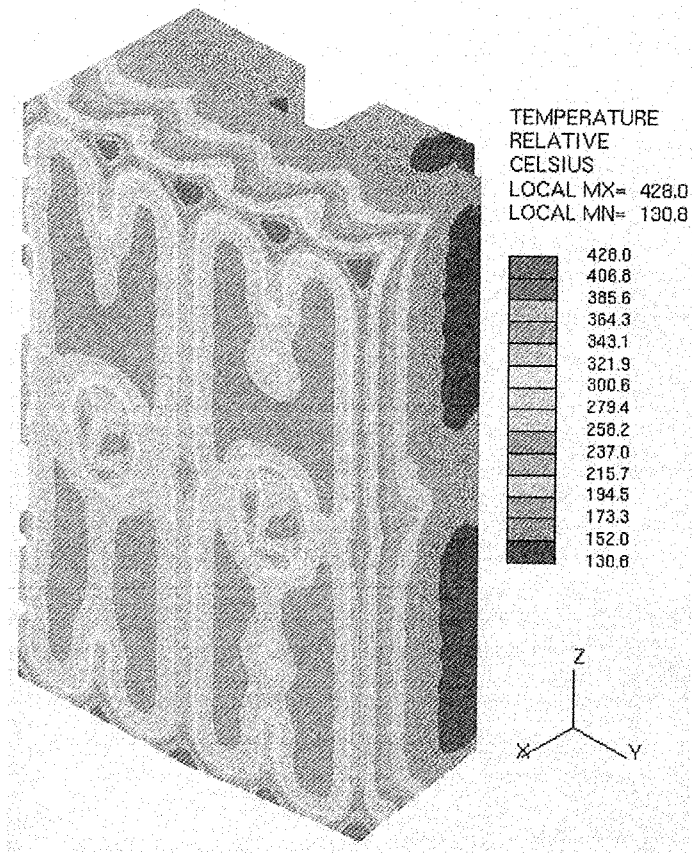


Fig. 3.2-21 Temperature profile of structural material (module front view)

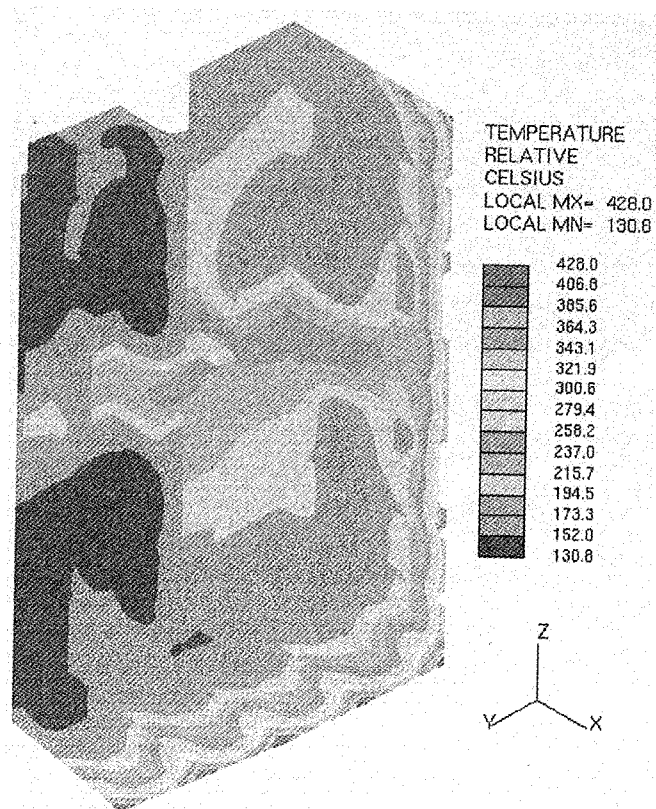


Fig. 3.2-22 Temperature profile of structural material (module back view)

3.3 Conclusions

A detailed 3-D thermal-hydraulic analysis of the shield block has been performed. From the results of the analysis, the following conclusions are derived:

- 1) By the baffle plates arranged in the header, the coolant tends to flow into each radial channel. However, further optimization of the baffle plates, especially on its length, is necessary to supply the coolant flow to the radial channels near the module top and bottom.
- 2) There are many backward flows in the radial channels, and thus the flow distribution into the radial channels is non-uniform. The flow obstruction in the poloidal channel by the inner tube of the radial channel seems major cause of this flow distribution. The coolant velocity in the smallest flow area interfered by the inner tube is 14-16 m/s. The improvement of this flow obstruction is required, e.g., by decreasing the inner tube diameter.
- 3) Total pressure loss from the inlet to the outlet of the shield block is 0.55 MPa. Since about 55-75 % of the total pressure loss is caused by the flow obstruction in the poloidal channel, the improvement of the flow obstruction will be effective to decrease the total pressure loss.
- 4) The outlet temperature of the coolant is 153 °C with the inlet temperature of 130 °C. Though some hot spots up to 175 °C in the coolant are observed, the structural material, SS316L(N)-IG are cooled well. The maximum temperature of the structural material is 428 °C at the top/bottom edge region of the front side. This temperature could be reduced by decreasing the thickness of the header cover plate and/or beveling the top/bottom edge region.

4. Electromagnetic Analysis of Shielding Blanket

4.1 Preliminary EM analysis using one module model

Electro-magnetic loads on FW and shield block are analyzed for centered disruption with 25 ms and 19 ms decay time. The latter case is assumed equivalent to the centered disruption including plasma movement effect. For disruption time of 25 ms, effect of slits is studied for EM load on FW by analyzing no slit and two slits cases in addition to standard five slits case.

4.1.1 Analysis conditions

4.1.1.1 Conditions for analysis of eddy current

Eddy current is analyzed by the method that base magnetic flux density applied on the FW or shield block is changed to zero according to the assumed disruption time.

- Code: A-f3D (A solid model code using boundary element method) [3]

- Base magnetic flux density [4]

Bp : 1.7 T
Br : 0.22 T

- Mesh model:

Mesh model of FW and shield block are shown in Fig. 4.1-1 and Fig. 4.1-2, respectively.

Boundary condition for the adjoining shield blocks is not taken into account in this analysis.

- Analysis case :

Four analysis cases are conducted for FW as shown in the next table.

Case	Disruption time	Number of slits	Comments
1	25 ms*	0	
2		2	Excluding center and edge slits in Fig. 4.1-1
3		5	Standard slits number
4	19 ms**	5	Standard slits number

Two analysis cases are conducted for shield block as shown in the next table.

Case	Disruption time	Number of slits	Comments
1	25 ms*	5	Standard slits number
2	19 ms**	5	Standard slits number

* : assumed decay time for centered disruption

** equivalent decay time for centered disruption including plasma moving effect

- Electrical resistance

Region	Resistance (Ω -m)	Comments
1) Be	8×10^{-1}	
2) DSCu	3.5×10^{-8}	
3) SS	8.6×10^{-7}	
4) Water	8×10^{-1}	
5) Slits	8×10^{-1}	
6) Homogenized coolant and SS region (see Fig. 4.1-2)	1.28×10^{-6}	Electrical resistance is volumetrically averaged.

4.1.1.2 Conditions for analysis of electro-magnetic force

Electro-magnetic force is calculated by multiplying the analyzed eddy current by the magnetic flux density at center of an equatorial module, which is analyzed for condition of ITER ODR [5]. Here B_p and B_r are neglected because they are much less than B_t as follows:

$$\begin{aligned} B_t &: 8.851 \text{ T} \\ B_p &: 0.0273 \text{ T} \\ B_r &: 0.0381 \text{ T} \end{aligned}$$

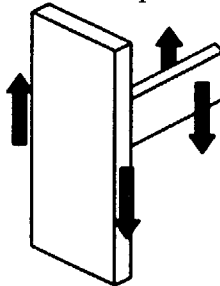
4.1.2 Analysis results

Eddy current and EM force on FW and shield block are shown in Figs. 4.1-3 to 4.1-6. Analyzed moments on FW and shield block are summarized in Table 4.1-1 and Table 4.1-2, respectively. M_r is a moment generated by change in B_p of 1.7 T, and M_p by change in B_r of 0.22 T. Relation between the moments on FW and number of slits is shown in Fig. 4.1-7. M_p is much reduced by slits, but M_r is slightly changed. Concerning effect of disruption time, M_r and M_p on FW for 19 ms case are larger about 30 percent than those for 25 ms case, and the increasing rate is nearly equal to decreasing rate of disruption time. However, as for shield block, increasing rate of M_r and M_p is less than decreasing rate of disruption time.

Table 4.1-1 Moment induced on FW (Solid model)

Case	Disruption time	Number of slits	Moment	
			M_r	M_p
1	25 ms	0	10.3 kNm	51.1 kNm
2		2	7.79 kNm	9.88 kNm
3		5	5.89 kNm	3.25 kNm
4	19 ms	5	7.64 kNm	4.24 kNm
Ratio of moment $M_{\text{Case4}}/M_{\text{Case3}}$			1.30	1.30

M_r due to ΔB_p of 1.7 T



M_p due to ΔB_r of 0.22 T

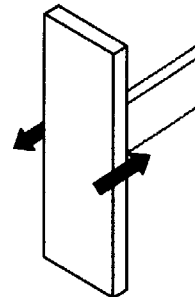
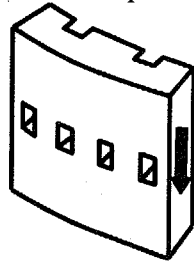
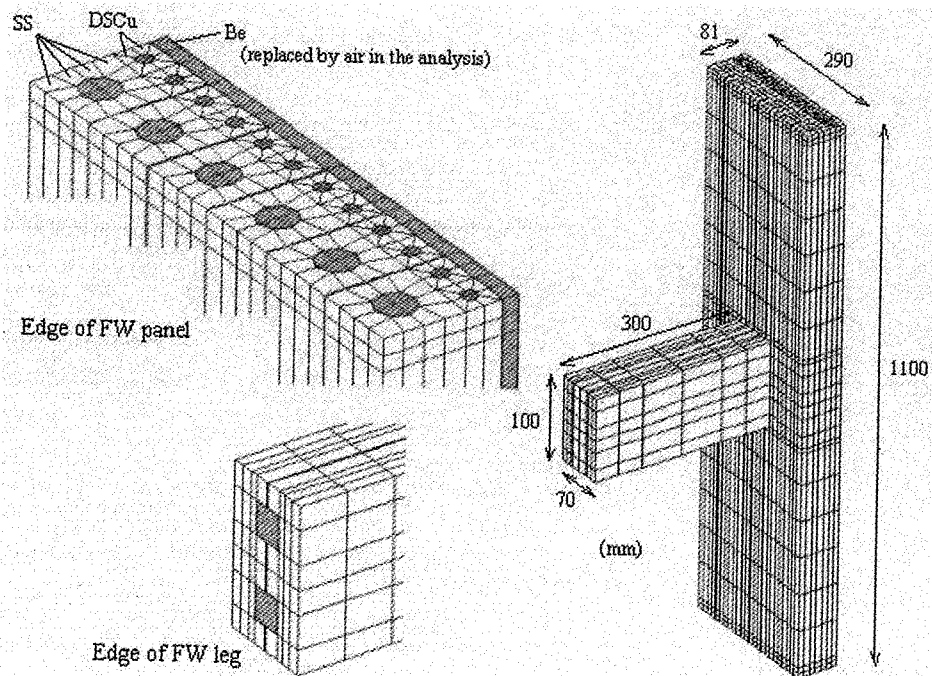
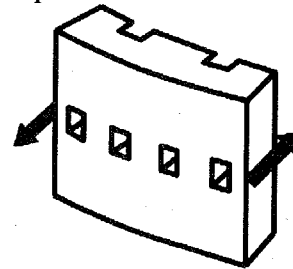


Table 4.1-2 Moment induced on shield block (Solid model)

Case	Disruption time	Moment	
		Mr	Mp
1	25 ms	0.69 MNm	0.64 MNm
2	19 ms	0.84 MNm	0.74 MNm
Ratio of moment $M_{\text{Case2}}/M_{\text{Case1}}$		1.22	1.16

Mr due to ΔB_p of 1.7 TMp due to ΔB_r of 0.22 T.**Fig. 4.1-1 Mesh model of the FW**

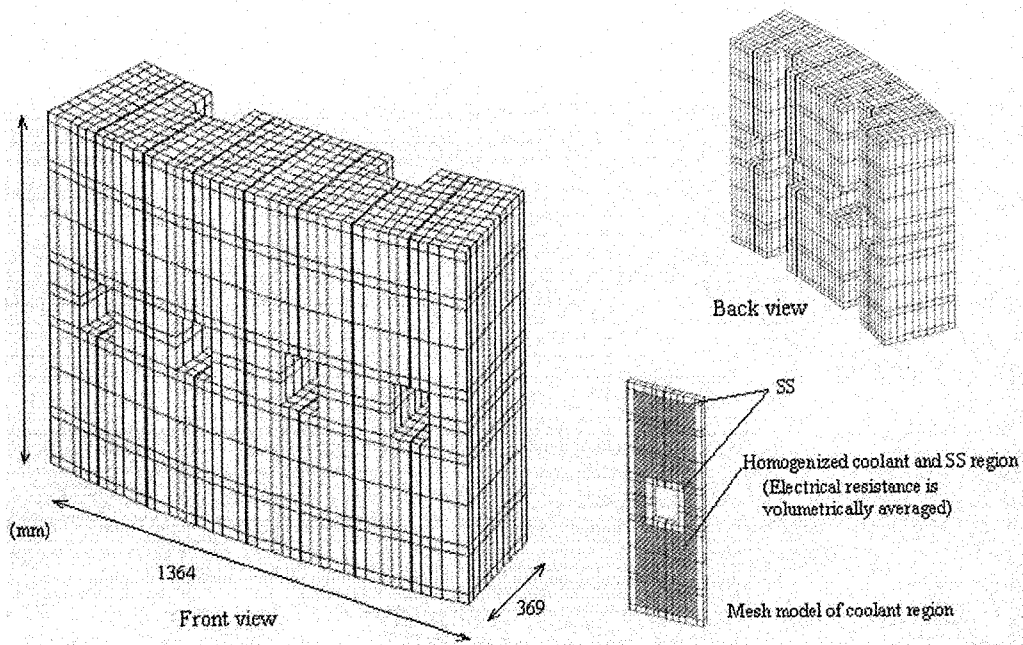
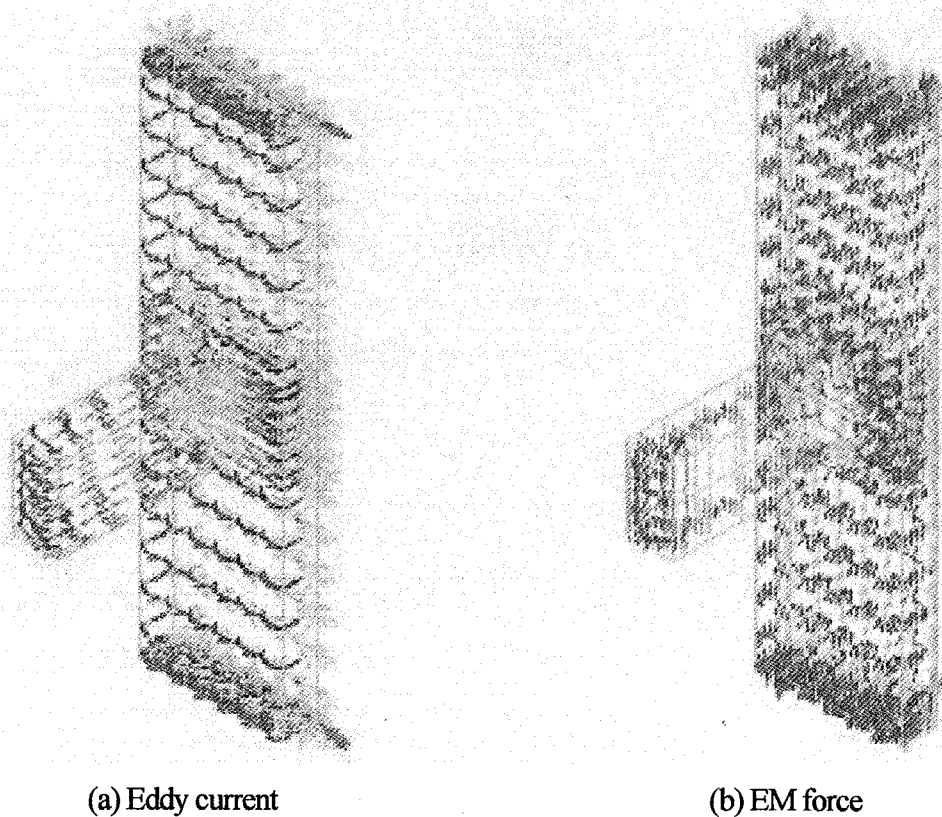


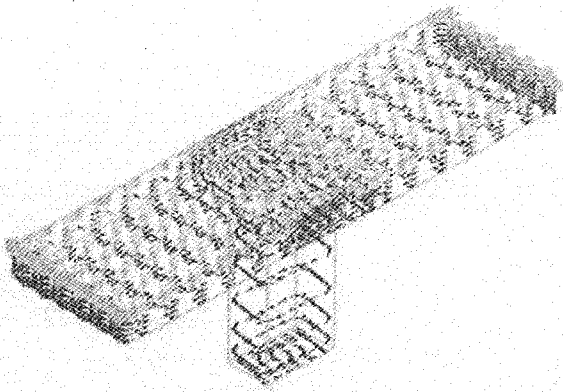
Fig. 4.1-2 Mesh model of the shield block



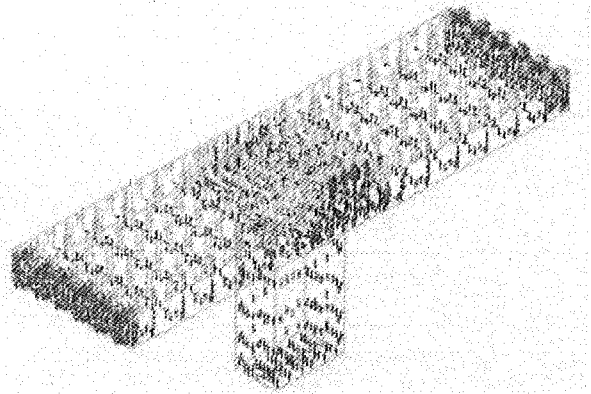
(a) Eddy current

(b) EM force

Fig. 4.1-3 EM load on FW with 5 slits under ΔB_p of 1T with 25 ms decay time



(a) Eddy current



(b) EM force

Fig. 4.1-4 EM load on FW with 5 slits under ΔB_r of 1T with 25 ms decay time

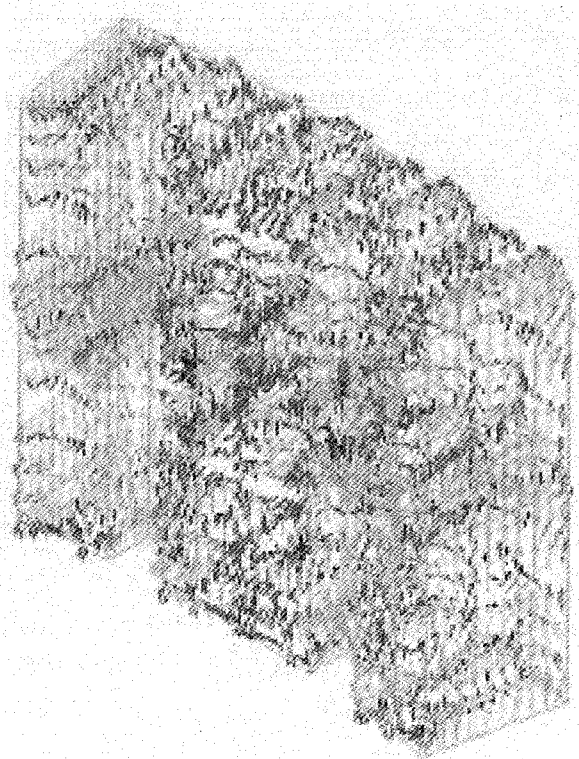
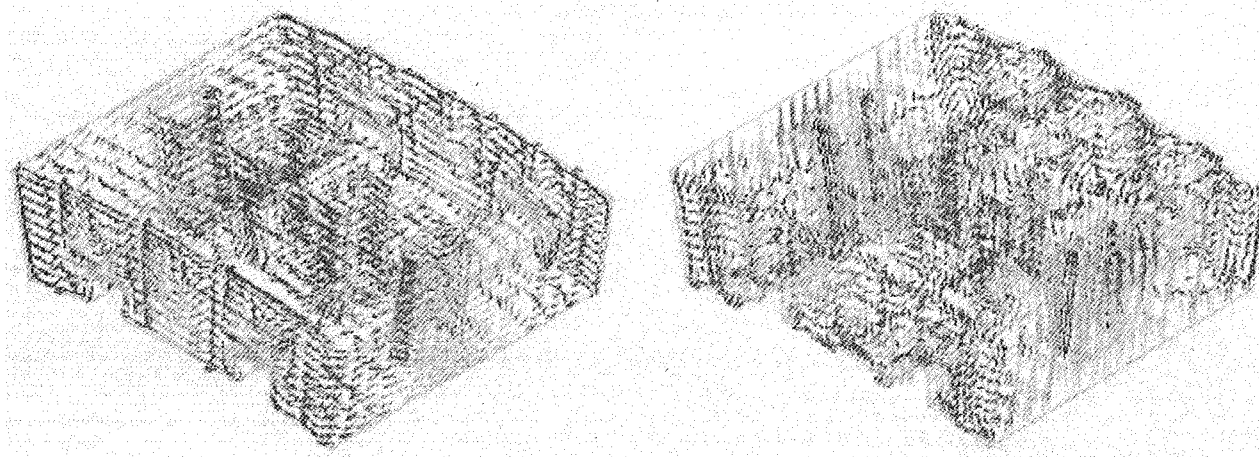
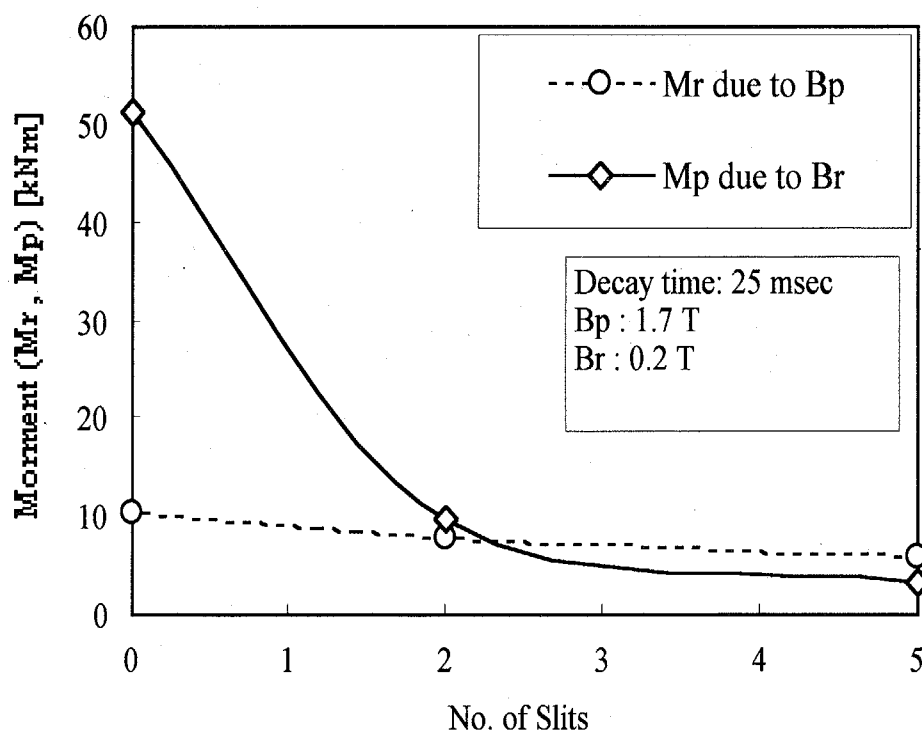


Fig. 4.1-5 EM load on shield block under ΔB_p of 1T with 25 ms decay time



(a) Eddy current

(b) EM force

Fig. 4.1-6 EM load on shield block under ΔB_r of 1T with 25 ms decay time**Fig. 4.1-7 Effect of slits on EM force of FW**

4.2 Centered disruption (CD)

4.2.1 One sector model with 17 module model

4.2.1.1 ITER-FEAT blanket modules and magnet system

The 17-fold segmentation of the shield modules in the poloidal direction is shown in Fig 4.2.1-1. The inboard module on the equatorial plane (modules #2-#5 counting clockwise from inboard-down to outboard) is about 1.3 m in width, about 1.1m in height and 0.45 m in depth as shown in Fig. 4.2.1-2. Fig. 4.2.1-3 shows the cross section of the shield block with many coolant channels in radial direction. The magnet system layout is shown in Fig. 4.2.1-4 and the specifications of TF and PF coils are listed in Tables 4.2.1-1 and 4.2.1-2.

Simulation analysis on the behaviors of plasma current and plasma movement during the centered disruption are performed for the case with fast current decay time, 27 ms, categorized as CD II [6]. In the CD II, plasma moves upward first during the disruption. The plasma current of 15 MA is kept constant during 10 ms as shown in Fig. 4.2.1-5 and increases up to 15.7 MA at 11 ms due to thermal quench. Then current quench occurs immediately and the plasma current decreases to 0 A at 38.5 ms. The plasma current densities during CD II are shown in Figs. 4.2.1-6 to 4.2.1-9. The plasma center position moves as shown in Figs. 4.2.1-10 and 4.2.1-11.

4.2.1.2 Analysis method

Eddy currents of 17 blanket modules in the poloidal cross section are analyzed by taking into account plasma movement during the disruption. Nine degrees for the blankets and vacuum vessel (VV) in toroidal direction is modeled in this analysis. EM analysis code used in the analysis is a solid element code, EM Solution [7] of Science Solutions International Lab., Inc.

Modeling of EM analysis is as follows:

- a. FW is neglected because the EM force in FW is much smaller than that of shield block.
- b. The area of 9 degrees in toroidal direction is analyzed. The inboard blankets are modeled for half a module and outboard blankets modeled for a full module, as shown in Fig. 4.2.1-12 and 4.2.1-13.
- c. The recess for branch pipe, flexible support and keys at rear surface of the shield block is considered in the blanket models. Detailed meshes are used for the blanket modules from #4 to #6 in order to calculate the correct eddy current due to plasma upward movement. Typical models are shown in Fig. 4.2.1-14 and 4.2.1-15 for inboard and Fig. 4.2.1-16 for outboard modules.
- d. Cooling channel region in the shield block is modeled as homogenous elements with equivalent electrical conductivity. Though the equivalent electrical conductivity has the dependence on the direction, as shown in Fig. 4.2.1-17, the ratio of 0.616 for the SS conductivity is used as the equivalent electrical conductivity for all directions. The equivalent electrical resistivity used in the analysis is $0.88\mu\Omega\text{m}/0.616 = 1.43\mu\Omega\text{m}$.
- e. Ribs of VV are neglected because no eddy current flows in the poloidal direction.
- f. Halo current is not included in the analysis.
- g. Vacuum vessel is also modeled by solid elements.

In the EM analysis, plasma current is assumed to keep 15 MA until 11ms without increasing the plasma current due to thermal quench, and to decrease from 15 MA at 11 ms to 0 MA at 38.5 ms (see Fig. 4.2.1-5). Movement of plasma current is simulated in the calculation model using current change of 7

meshes in the R direction and 14 meshes in the Z direction.

4.2.1.3 Analysis results

Magnetic flux density distributions are shown in Figs. 4.2.1-18 to 4.2.1-21 and eddy current distributions in Figs. 4.2.1-22 to 4.2.1-32. Total eddy current in the VV in toroidal direction is about 15 MA at the end of current quench, and this corresponds to 97% of that of the initial plasma current.

Moments induced in shield blankets during the disruption are shown in Tables 4.2.1-3 and 4.2.1-4. These moments are calculated for the rear surface center of shield block. Figs. 4.2.1-33 and 4.2.1-34 show the time history of moment around radial axis (M_r) and moment around vertical axis (M_p) on modules, respectively. Figs. 4.2.1-35 and 4.2.1-36 show the poloidal distribution of M_r and M_p on modules. The radial moment M_r on modules #3 and #4 exceed 1 MNm, at 16.5 ms. The vertical moment M_p on module #5 also exceeds 1 MNm at 16.5 ms. The maximum moment on each blanket module during the centered disruption is shown in Fig. 4.2.1-37. The maximum moments of both M_r and M_p do not occur at the end of disruption but at 16.5 ms from the start of the current quench. The reason for that is considered to be the plasma movement effect which causes the high magnetic flux density change.

Table 4.2.1-1 Parameters for TF and CS coils

	TF coil	CS coil	
		Central modules	End modules
Overall weight (including structures) (t)	290 x 18	840	
Coil current (MA)	9.13	24.2	21.9
Number of turns per TF coil / CS module:			
Radial	12	13	13
Toroidal / Vertical	14	42	38
Total	144	538	486
Conductor unit length (m)	820.8	821.7 (for six pancakes)	
Turn voltage (V)	34.7	18.6	20.5
Ground/Terminal voltage (kV) in normal operation	5 / 5 (two coils in series)	5 / 10	
Number of current lead pairs	9	6	

Table 4.2.1-2 Position, current and magnetic field of CS and PF coils

Coil	Rc (m)	Zc (m)	ΔR (m)	ΔZ (m)	Number of turns	I _{max} (MA _t)	I at EOB (MA _t)	B _{max} at IM(T)	B _{max} at EOB
CSU3	1.677	4.974	0.765	1.789	486	21.9	-1.52	13.5	12.8
CSU2	1.677	3.041	0.765	1.977	538	24.2	-20.05	13.5	12.8
CSU1	1.677	1.014	0.765	1.977	538	24.2	-23.90	13.5	12.8
CSL1	1.677	-1.014	0.765	1.977	538	24.2	-23.90	13.5	12.8
CSL2	1.677	-3.041	0.765	1.977	538	24.2	-17.92	13.5	12.8
CSL3	1.677	-4.974	0.765	1.789	486	21.9	-0.53	13.5	12.8
PF1	3.880	7.584	1.027	0.974	270	12.2	1.74	6.0	6.0
PF2	8.338	6.509	0.703	0.472	94	4.2	-1.94	5.0	5.0
PF3	12.014	3.055	0.820	1.262	220	8.7	-6.74	5.0	5.0
PF4	11.955	-2.465	0.703	1.119	164.5	6.3	-4.92	5.0	5.0
PF5	8.396	-6.748	0.820	0.945	220	9.9	-7.62	5.0	5.0
PF6	4.273	-7.559	1.813	0.852	416.5	18.7	15.00	6.0	6.0

Table 4.2.1-3 Moment Mr (kNm) on shield block for centered disruption II
(Starting current quench is shown as 0 ms)

Module No.	5.5 (ms)	11 (ms)	16.5 (ms)	22 (ms)	27.5 (ms)	Max
1	-238.1	-645.7	-480.5	-205.6	-85.1	-645.7
2	-294.3	-835.4	-756.5	-331.2	-130.5	-835.4
3	-286.1	-842.9	-1059.2	-520.1	-213.8	-1059.2
4	-153.3	-505.6	-1021.3	-708.5	-343.6	-1021.3
5	-10.5	-29.6	-462.6	-828.4	-563.7	-828.4
6	39.5	255.4	233.3	-575.9	-788.5	-788.5
7	28.4	231.6	377.5	-240.9	-701.2	-701.2
8	19.2	221.6	385.4	-204.6	-683.6	-683.6
9	0.7	110.3	101.6	-245.8	-303.4	-303.4
10	-69.4	5.0	-140.3	-355.8	-239.4	-355.8
11	-126.7	-105.0	-232.5	-215.2	-114.1	-232.5
12	-191.1	-180.0	-280.4	-185.9	-88.5	-280.4
13	-191.8	-190.9	-241.0	-134.7	-59.4	-241.0
14	-375.5	-416.3	-441.1	-230.9	-102.2	-441.1
15	-293.3	-358.4	-309.4	-138.4	-52.4	-358.4
16	-267.4	-399.2	-307.4	-138.8	-57.7	-399.2
17	-182.1	-338.8	-219.3	-81.9	-26.2	-338.8

Table 4.2.1-4 Moment M_p (kNm) on shield block for centered disruption II
 (Starting current quench is shown as 0 ms)

Module No.	5.5 (ms)	11 (ms)	16.5 (ms)	22 (ms)	27.5 (ms)	Max
1	99.4	250.6	134.3	55.4	18.3	250.6
2	-60.0	-220.6	-524.8	-470.8	-380.4	-524.8
3	84.1	250.1	-88.5	-220.6	-198.7	250.1
4	180.5	592.8	627.6	131.6	-14.6	627.6
5	124.7	548.1	1119.4	546.4	103.6	1119.4
6	14.5	120.9	534.6	662.5	277.5	662.5
7	1.5	74.0	217.1	135.4	-160.5	217.1
8	-9.8	69.1	106.1	-157.4	-269.2	-269.2
9	-32.6	-43.2	-161.1	-223.5	-78.0	-223.5
10	-112.7	-215.6	-400.6	-204.3	-49.4	-400.6
11	-75.6	-118.6	-141.7	-53.2	-25.9	-141.7
12	-74.8	-106.5	-99.2	-39.4	-21.3	-106.5
13	10.6	-5.0	30.2	36.9	26.9	36.9
14	-58.9	-133.0	-71.5	-20.7	-4.3	-133.0
15	72.9	51.0	92.8	84.6	74.6	92.8
16	93.8	82.3	126.7	122.8	113.4	126.7
17	3.7	-72.2	-20.2	20.6	36.5	-72.2

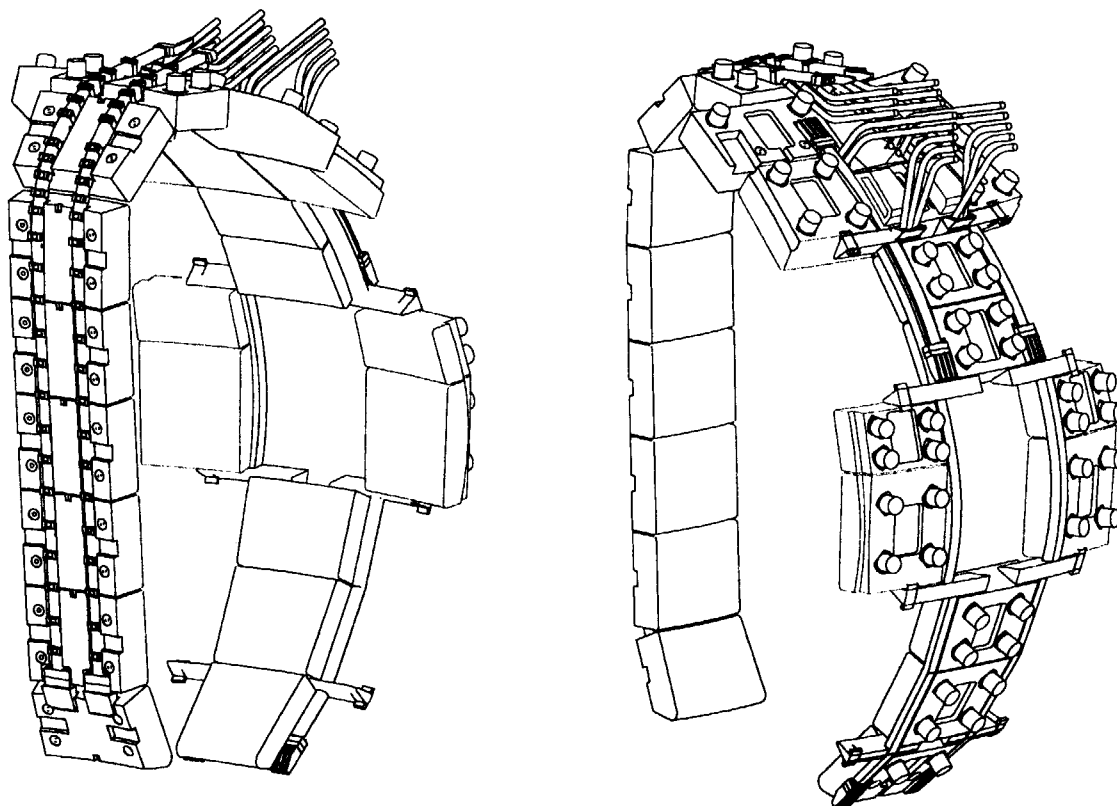


Fig. 4.2.1-1 Blanket module segmentation

DIMENSIONS RELATE TO ROOM TEMPERATURE (293K)

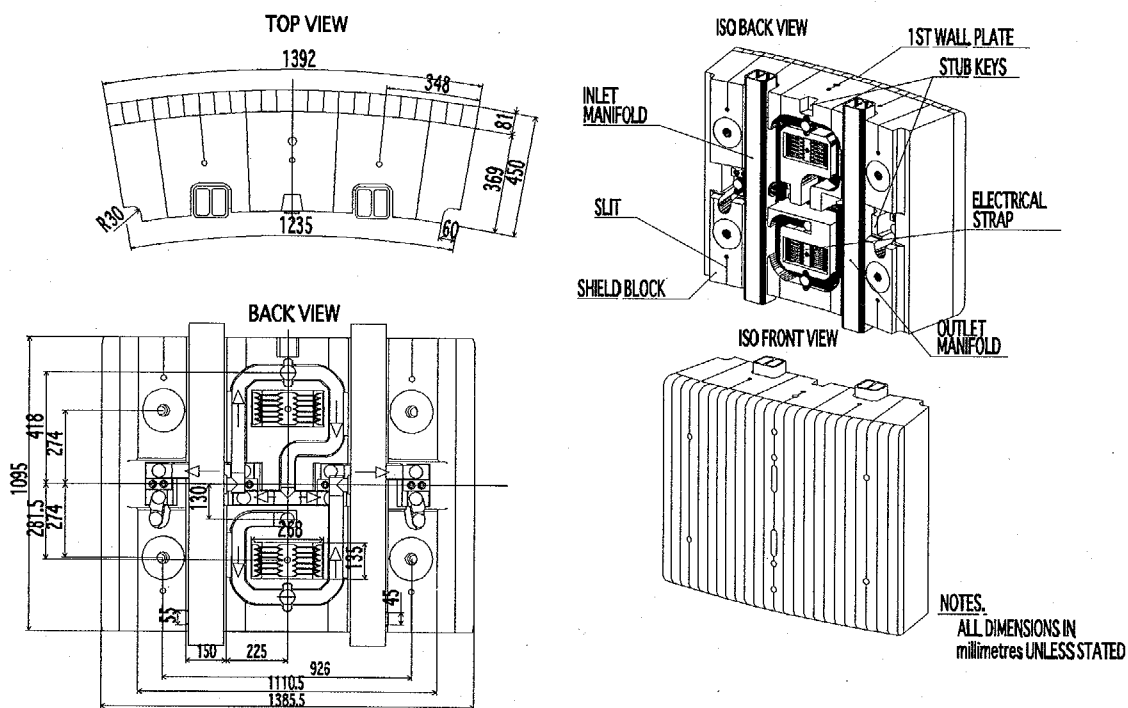


Fig. 4.2.1-2 Whole structures of shield block (#4 module)

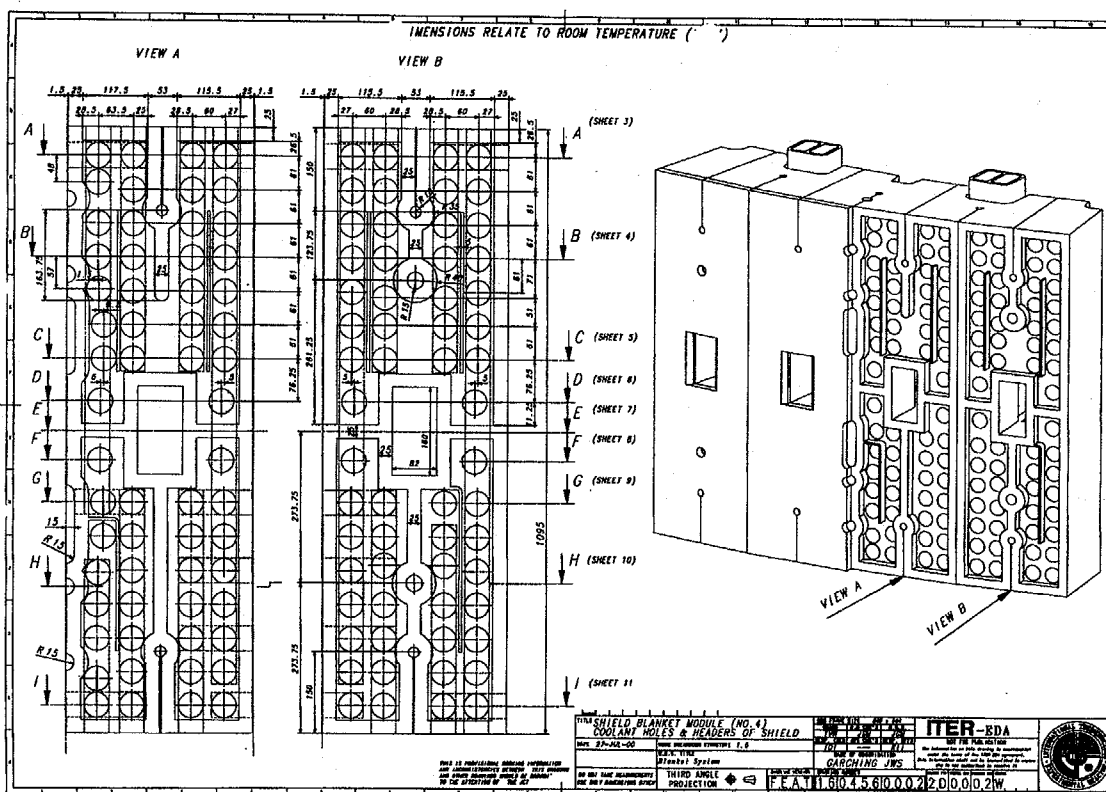


Fig. 4.2.1-3 Coolant holes and headers of shield block (#4 module)

Time (ms)	I_p (MA)	I_p used for EM analysis (MA)
0	15.0	15.0
10	15.0	15.0
12	16.0	15.5
16	12.5	12.0
22	9.5	9.0
27	6.5	6.2
33	3.0	3.0
38	0.0	0.0

— 59 —

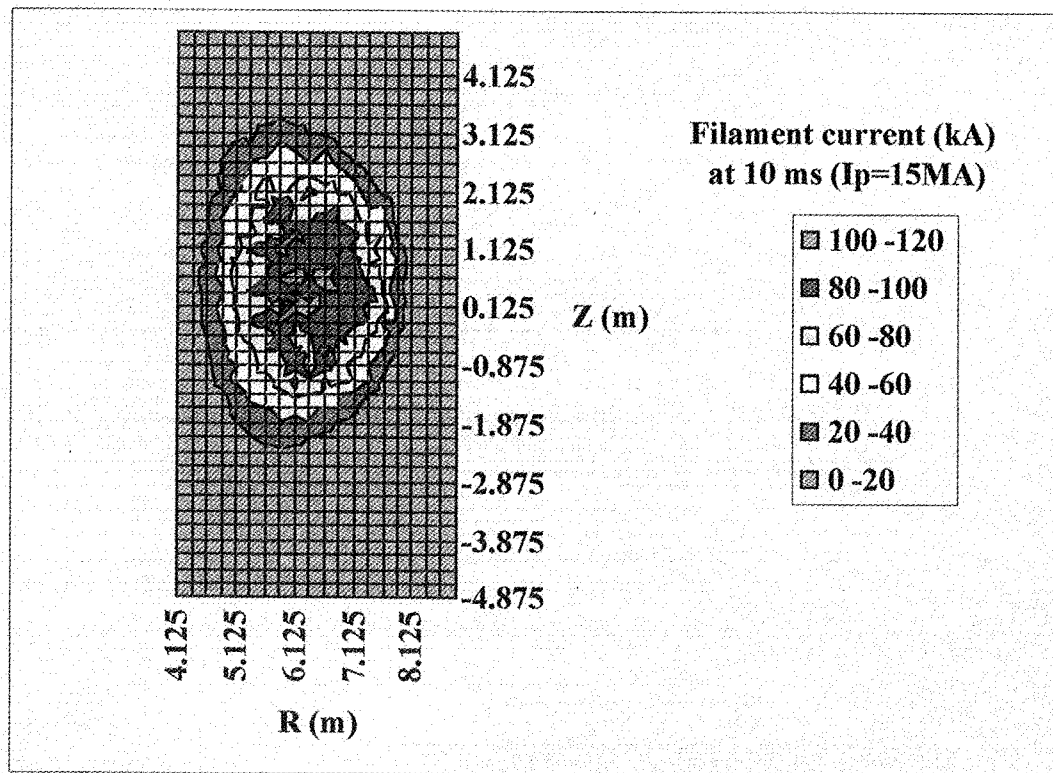


Fig. 4.2.1-6 Plasma current density before thermal quench under CDII

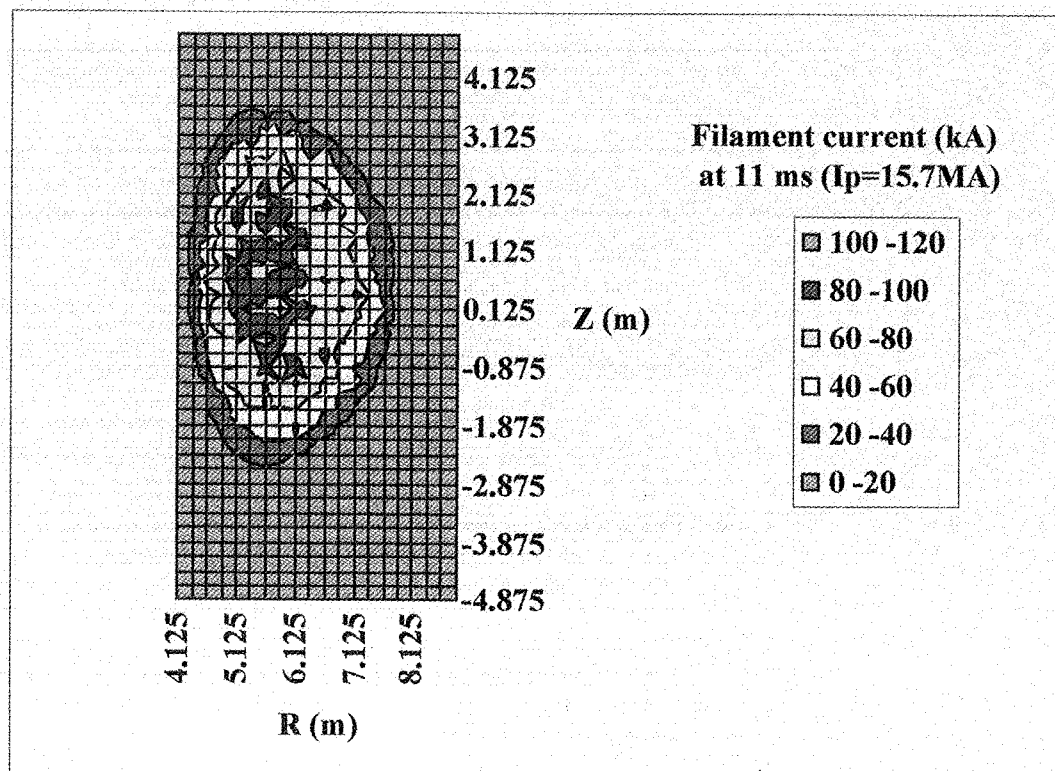


Fig. 4.2.1-7 Plasma current density just after thermal quench under CDII

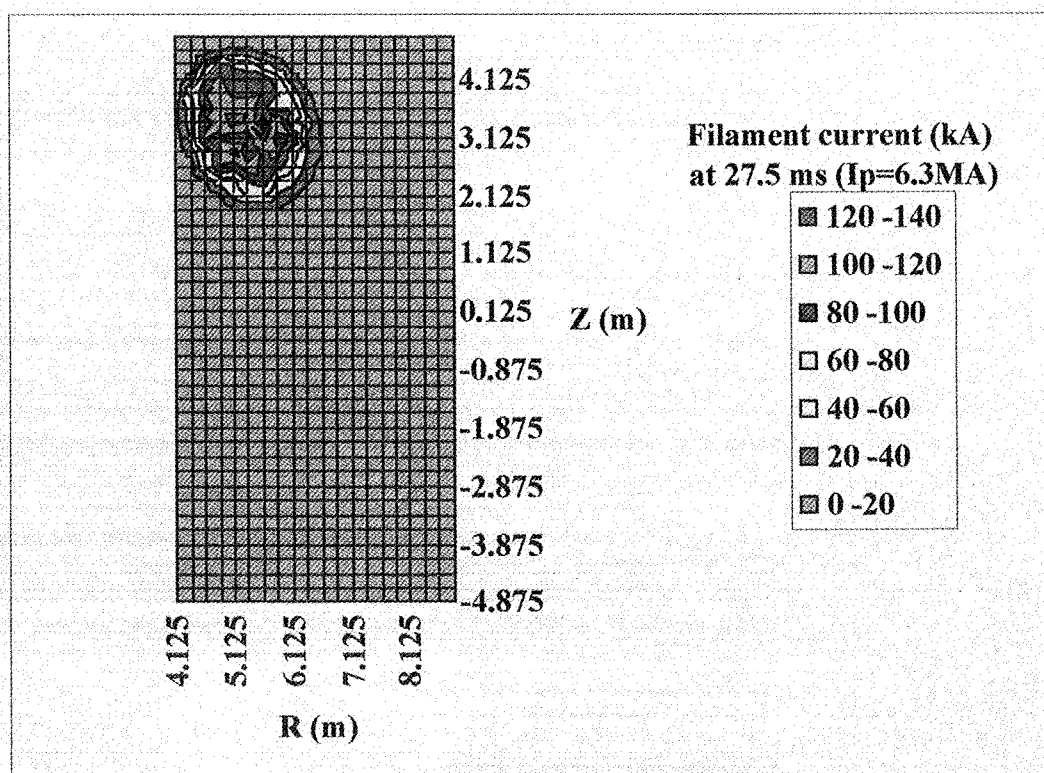


Fig. 4.2.1-8 Plasma current density at 16.5 ms during current quench under CDII

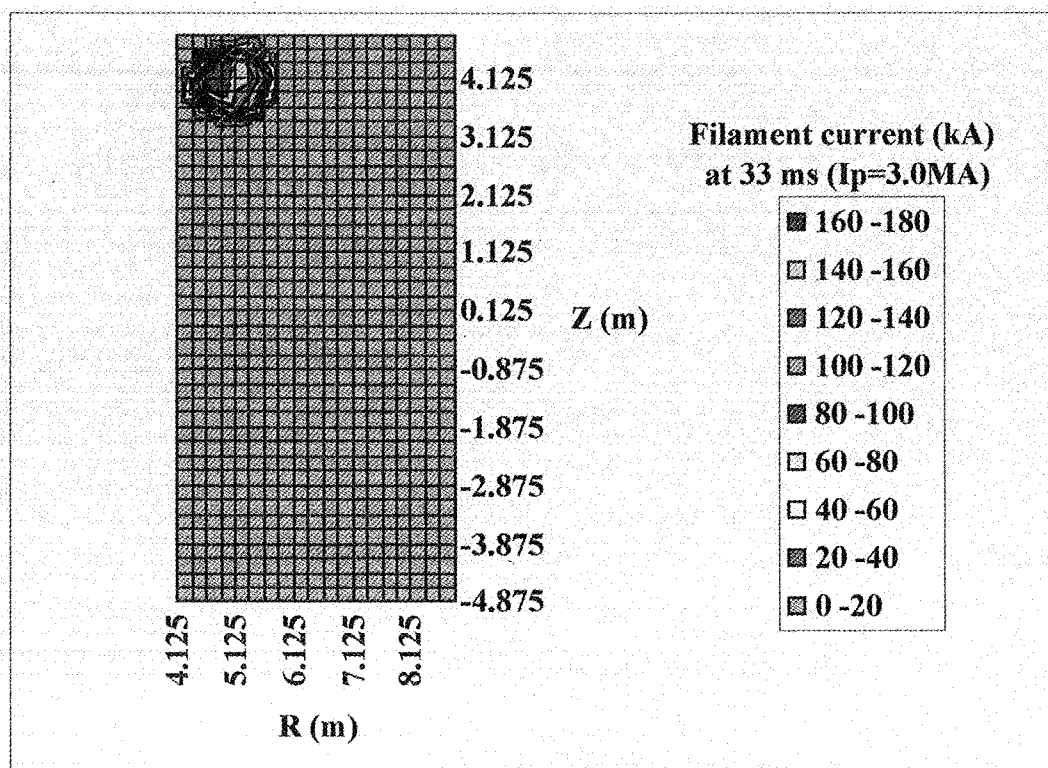


Fig. 4.2.1-9 Plasma current density at 22 ms during current quench under CDII

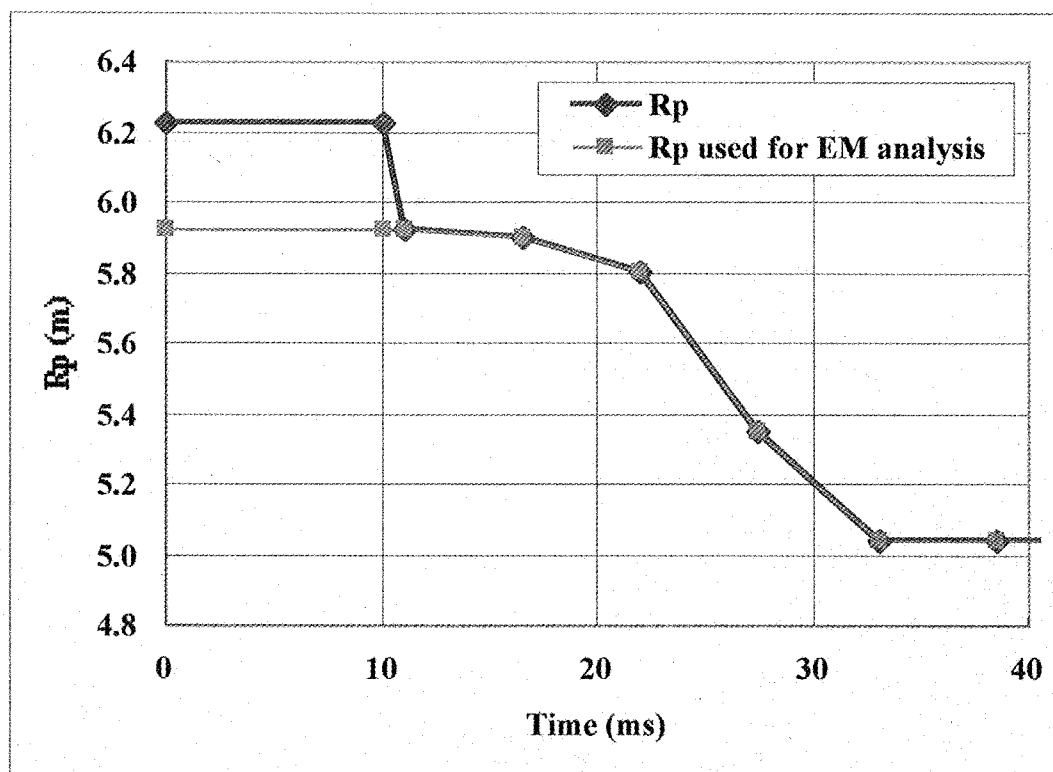


Fig. 4.2.1-10 Plasma position R_p under CD II (Starting current quench is 11 ms)

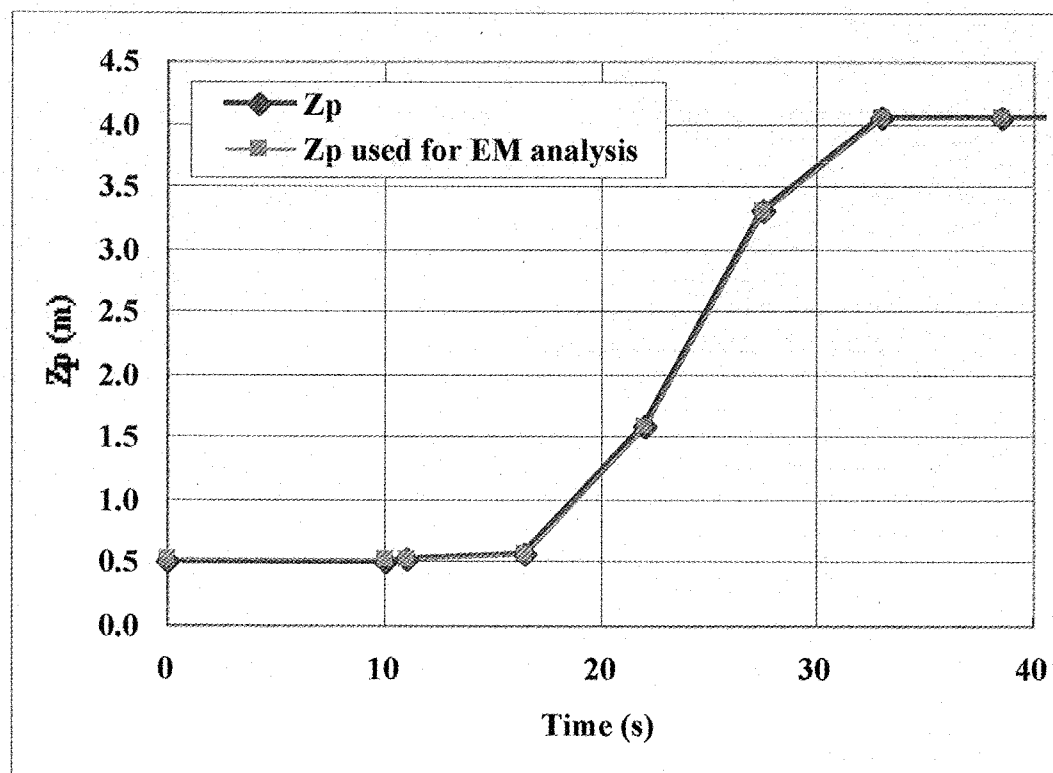


Fig. 4.2.1-11 Plasma position Z_p under CD II (Starting current quench is 11 ms)

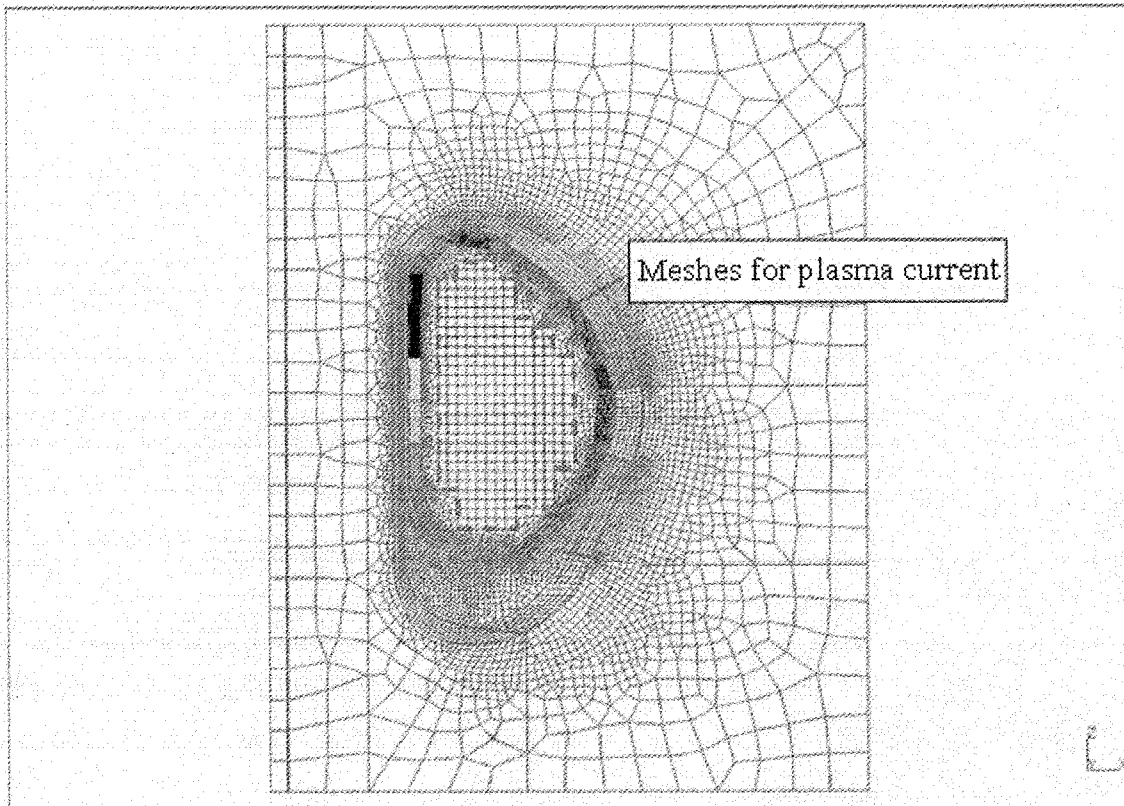


Fig. 4.2.1-12 Vertical cross section of mesh model

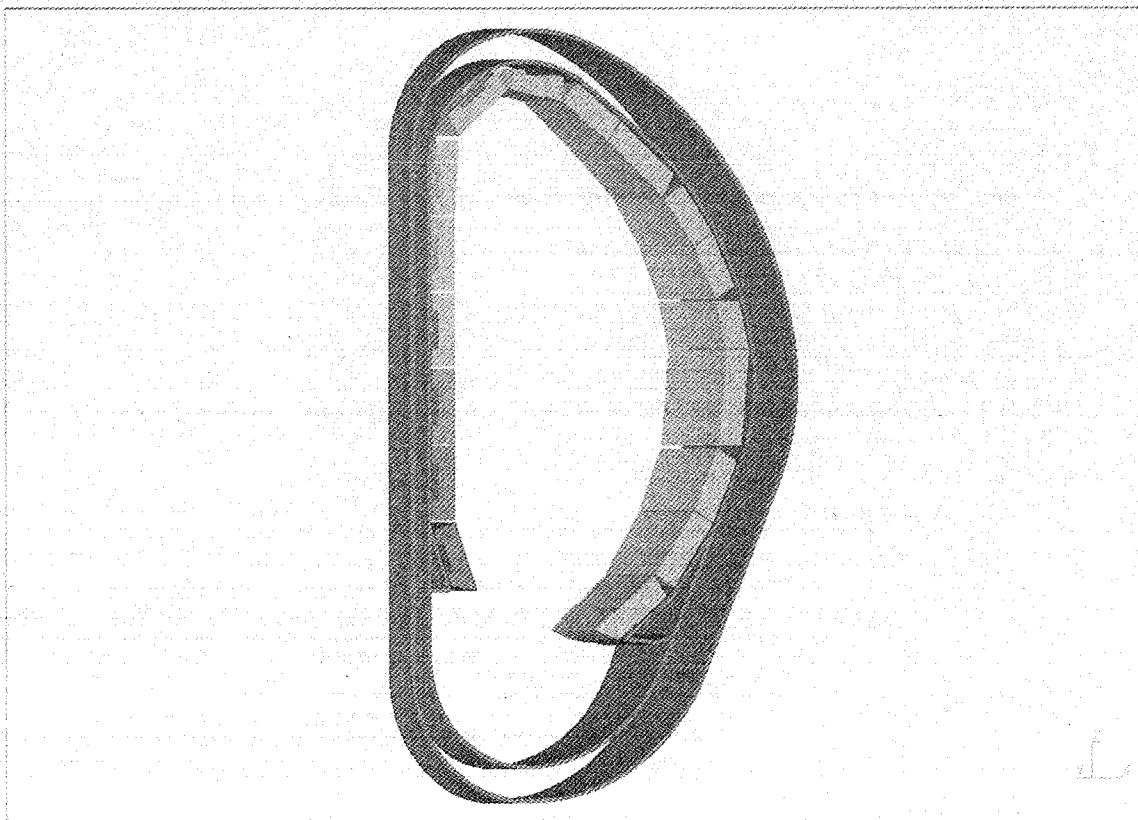


Fig. 4.2.1-13 3D model of EM analysis

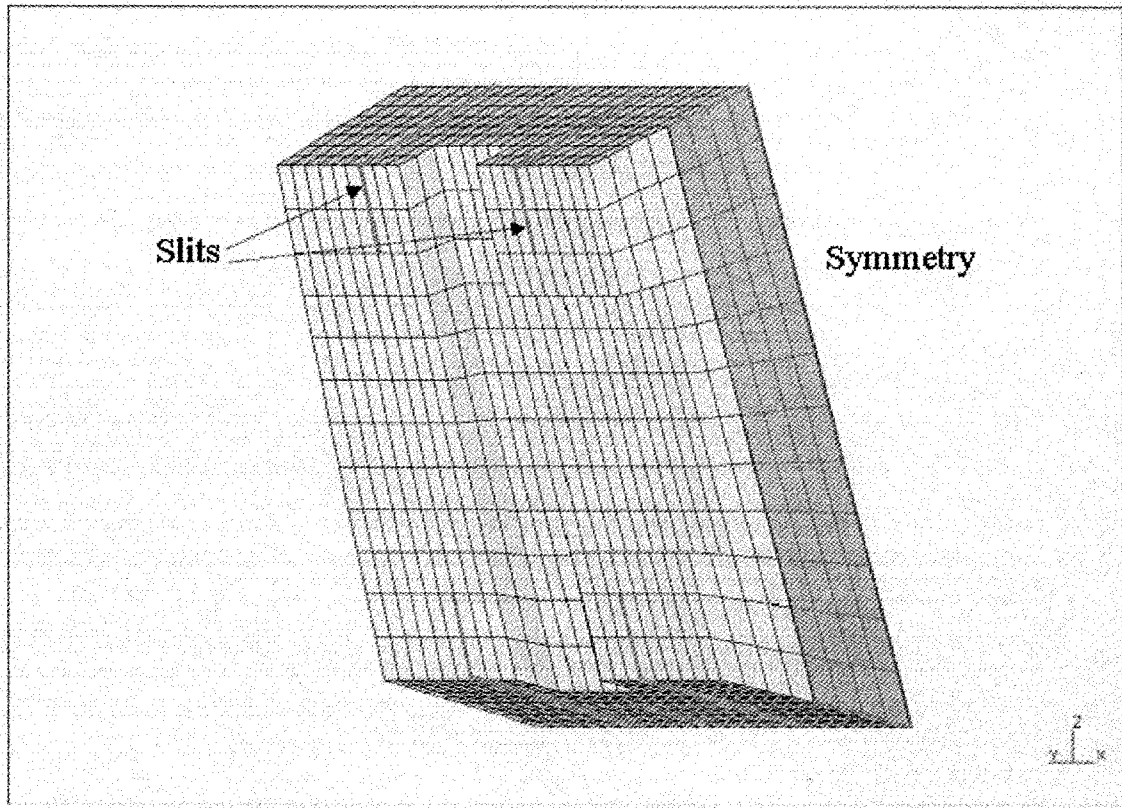


Fig. 4.2.1-14 Mesh model of module #1

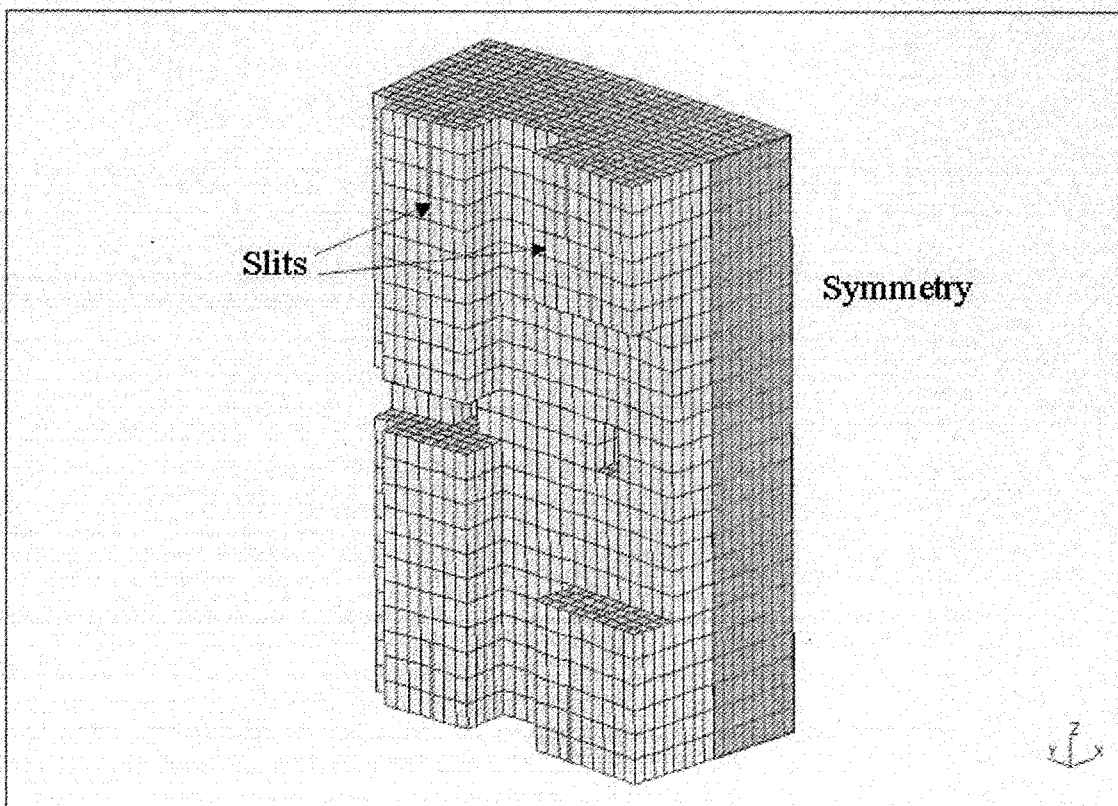


Fig. 4.2.1-15 Mesh model of module #5

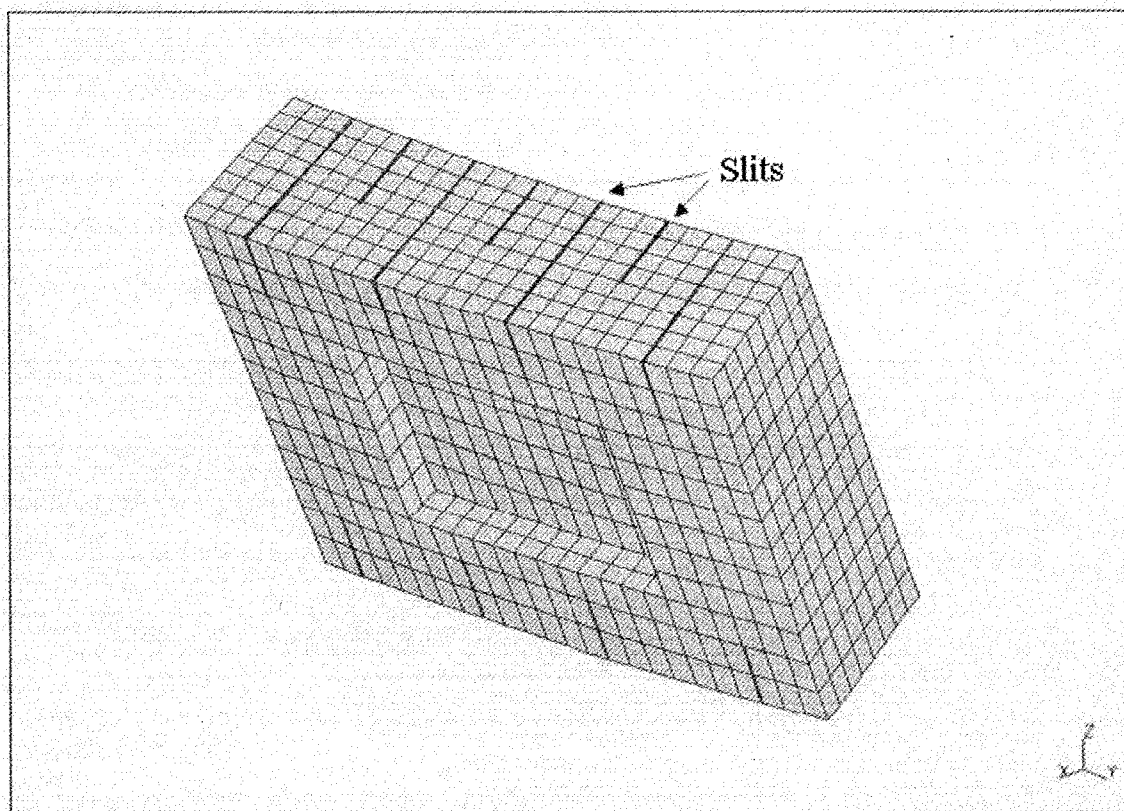


Fig. 4.2.1-16 Mesh model of outboard module #15

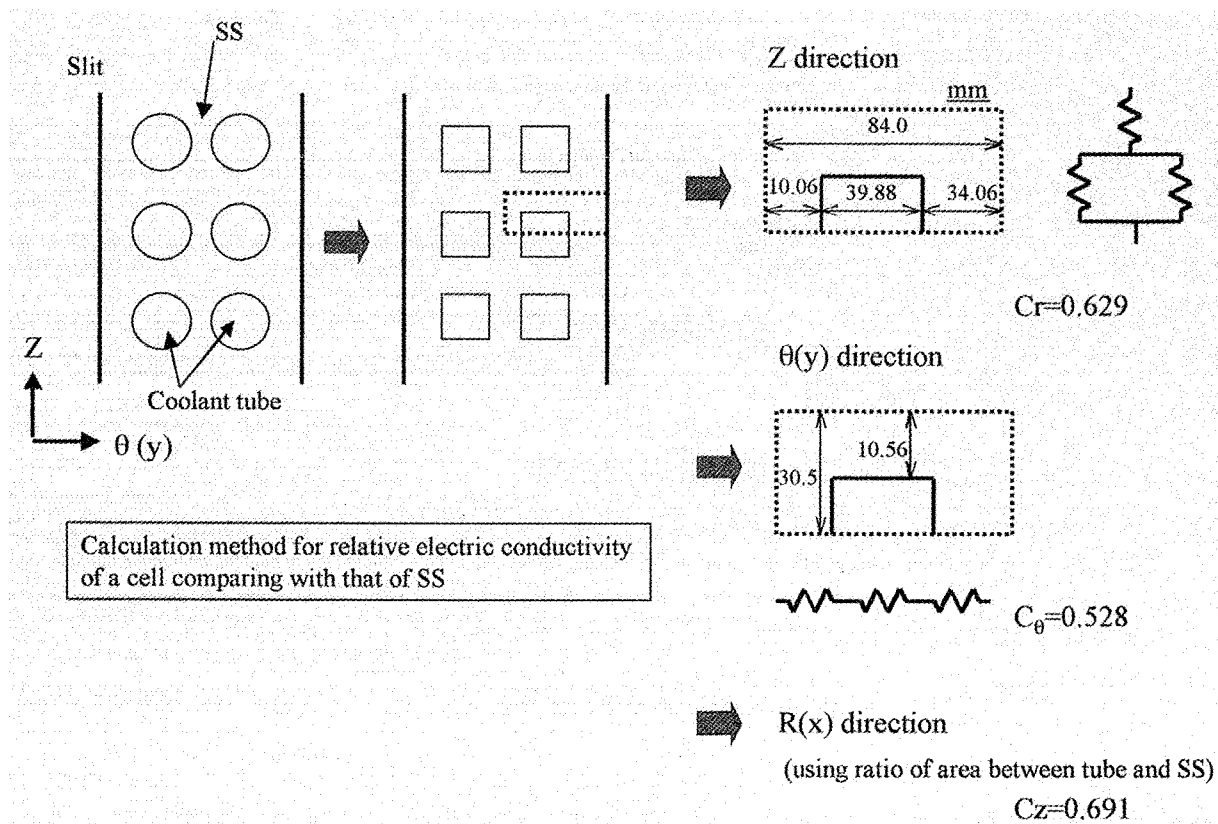


Fig.4.2.1-17 Equivalent conductivity

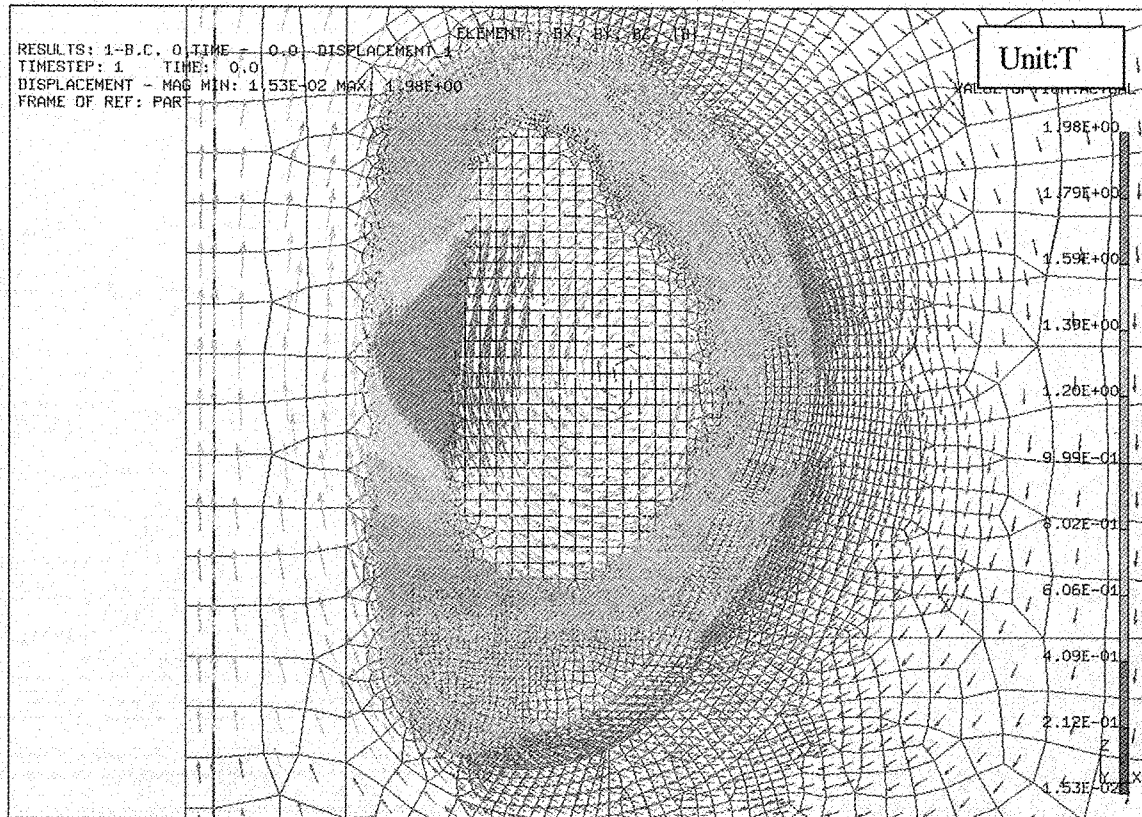


Fig. 4.2.1-18 Magnetic field due to plasma at the start of current quench under CDII

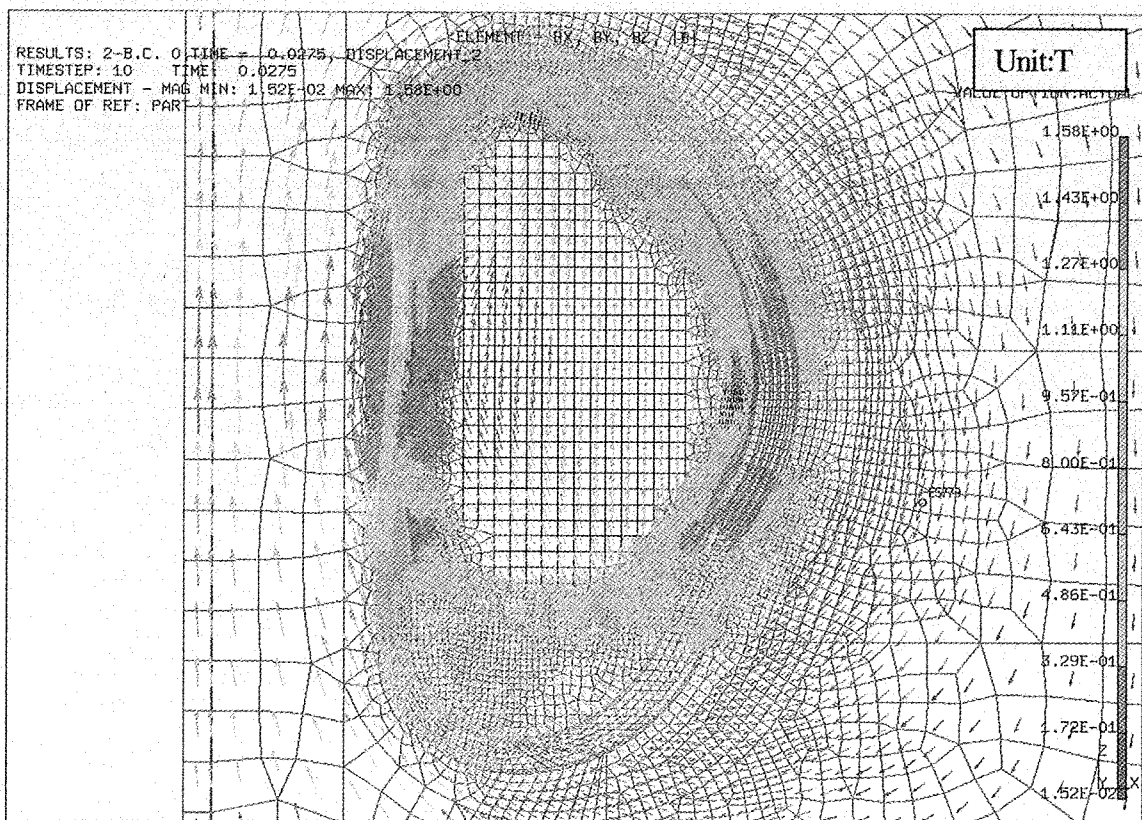


Fig. 4.2.1-19 Magnetic field due to eddy current at the end of disruption under CDII

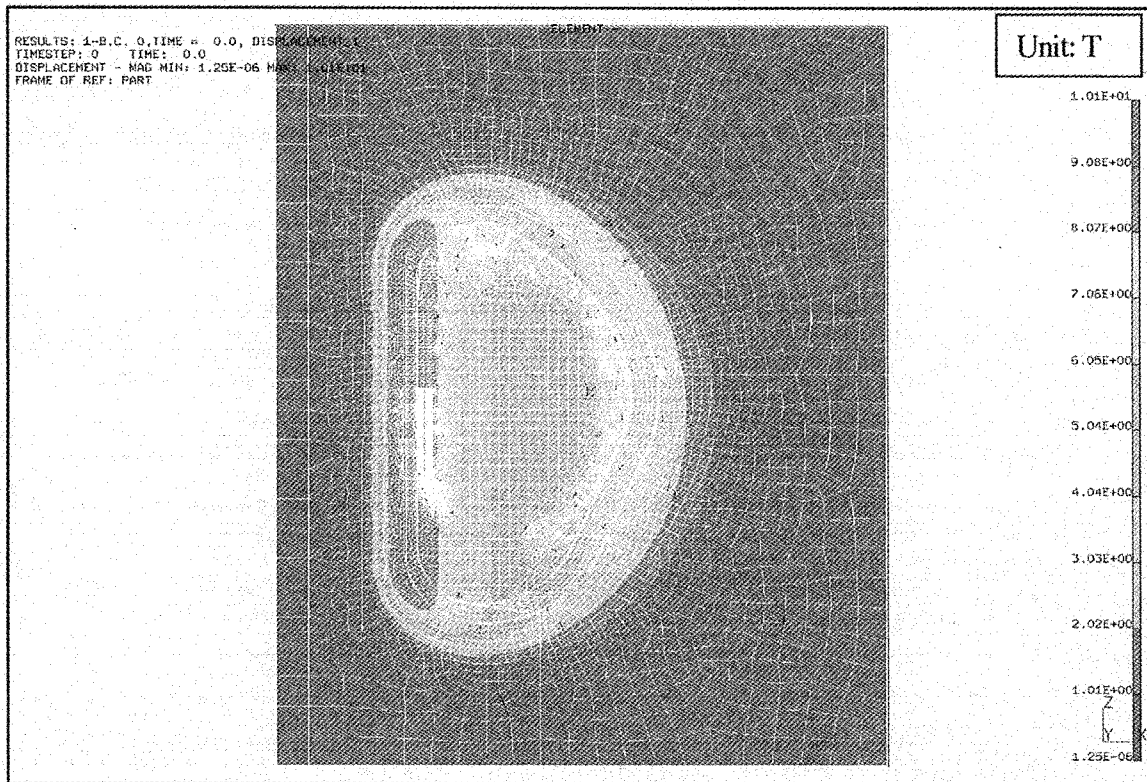


Fig. 4.2.1-20 Magnetic field induced by TF coils

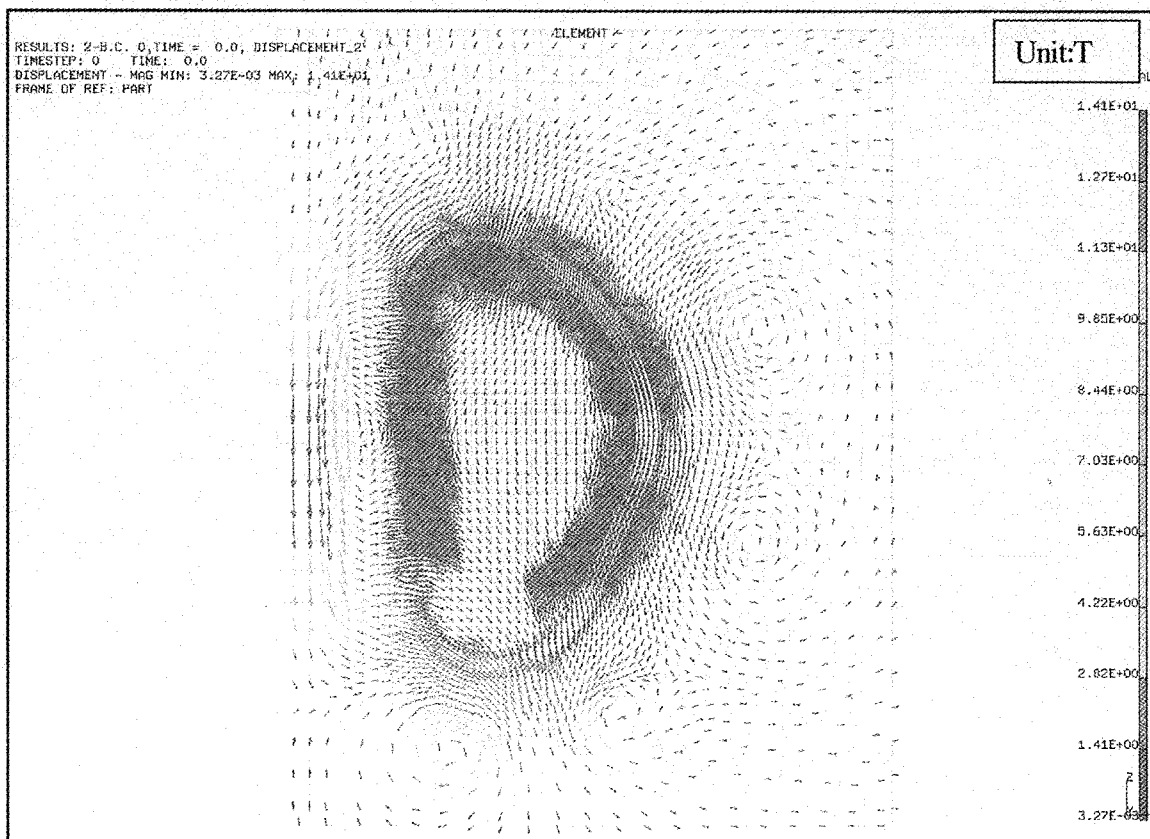


Fig. 4.2.1-21 Magnetic field induced by PF coils

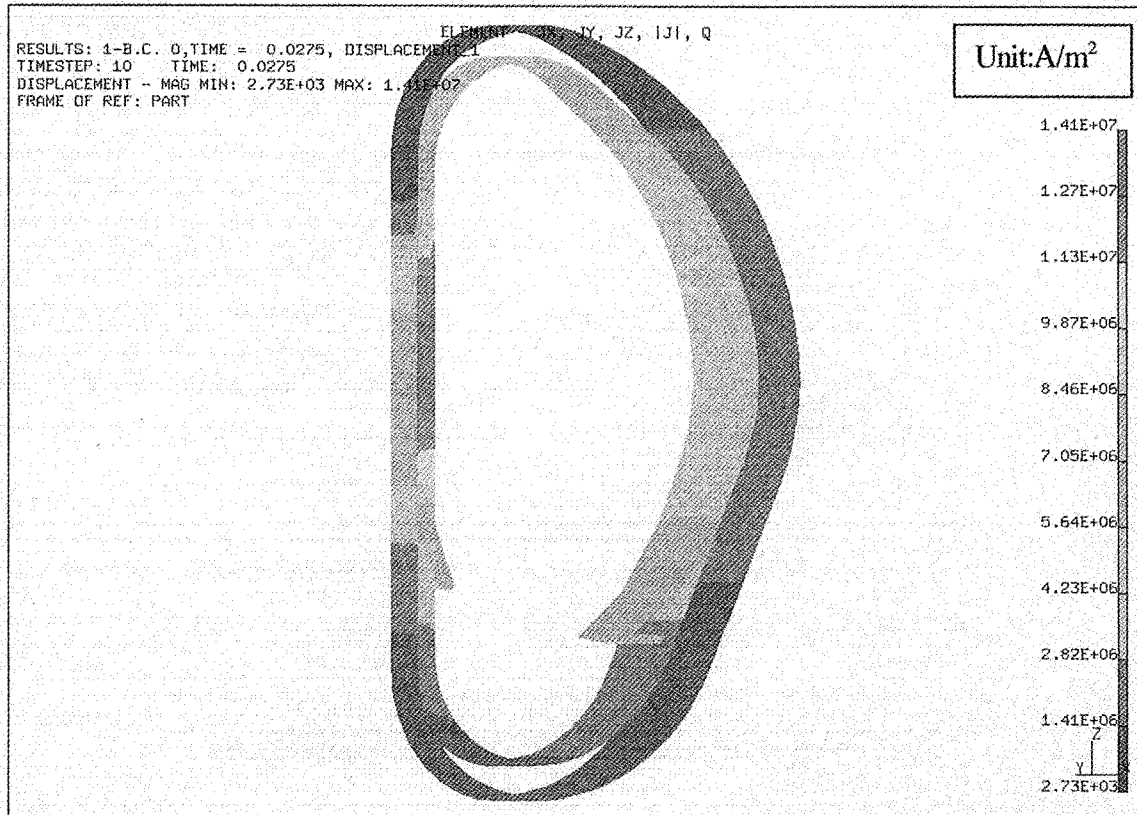


Fig. 4.2.1-22 Eddy current distribution on VV at the end of current quench under CDII

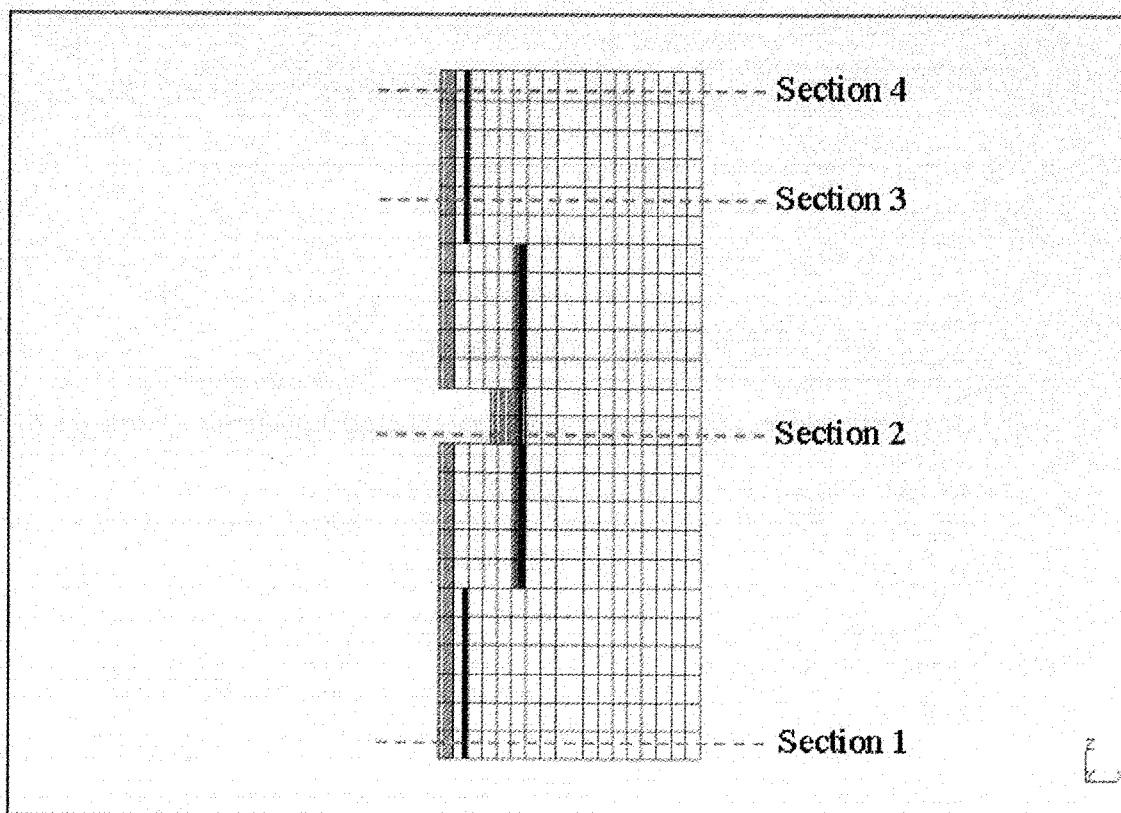


Fig. 4.2.1-23 Horizontal cross section of module #5 for drawing eddy current distribution

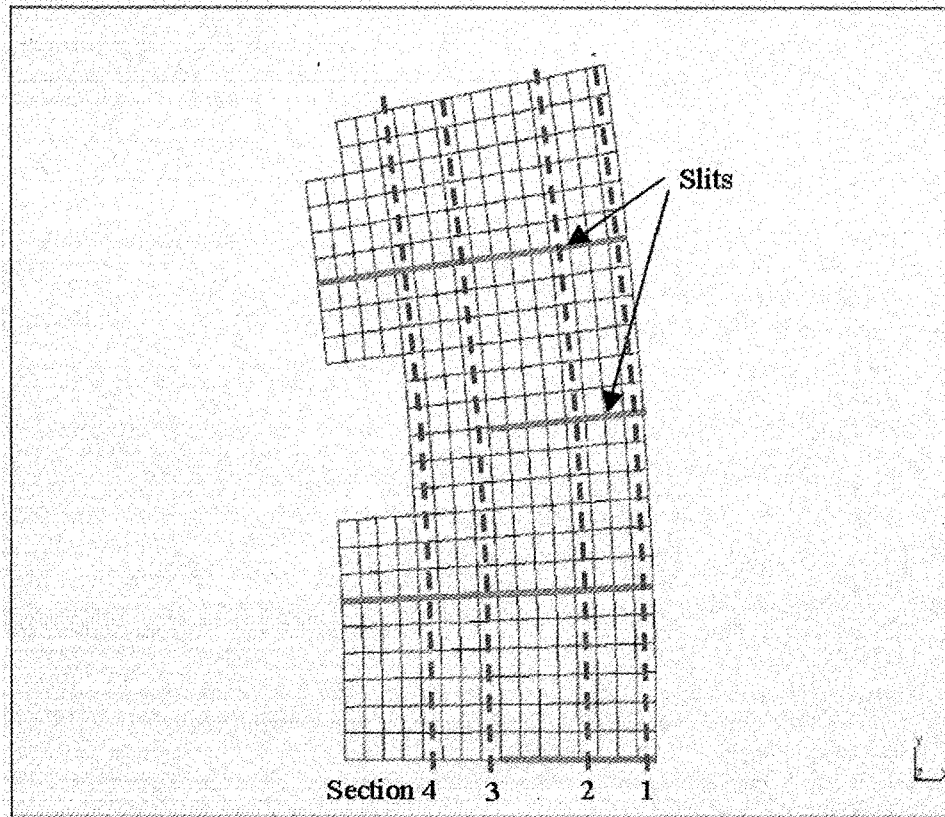


Fig. 4.2.1-24 Vertical cross section of module #5 for drawing eddy current distribution

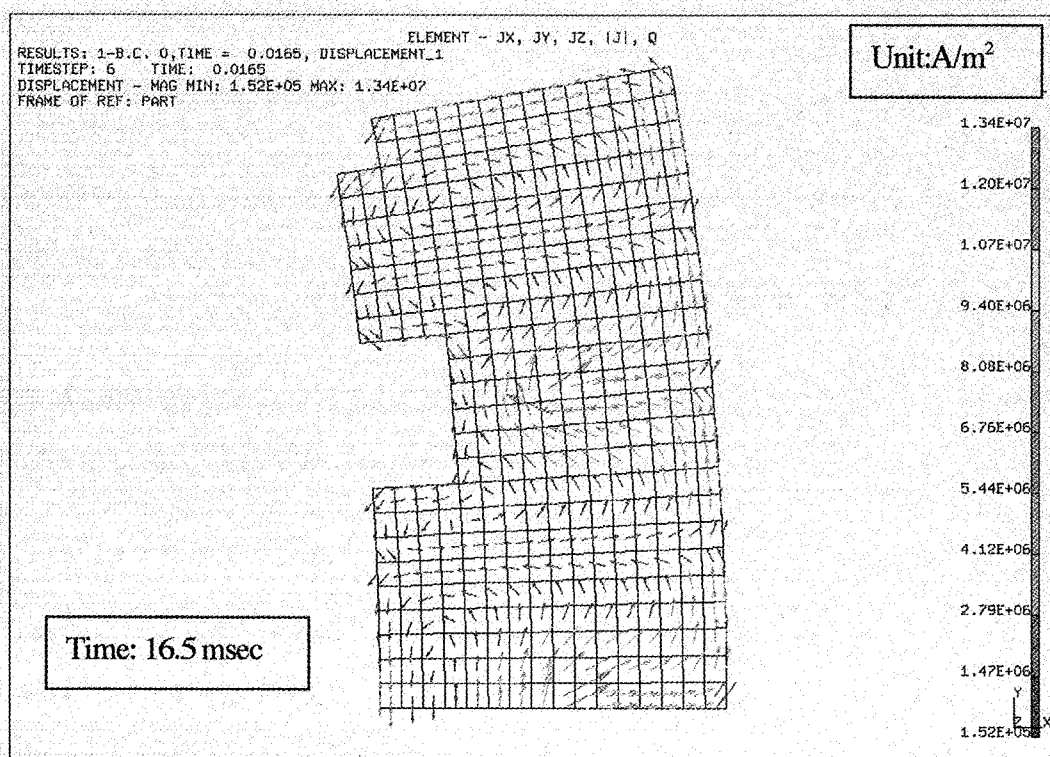


Fig. 4.2.1-25 Eddy current distribution on horizontal cross section 1 of module #5
 (Starting current quench is shown as 0 ms)

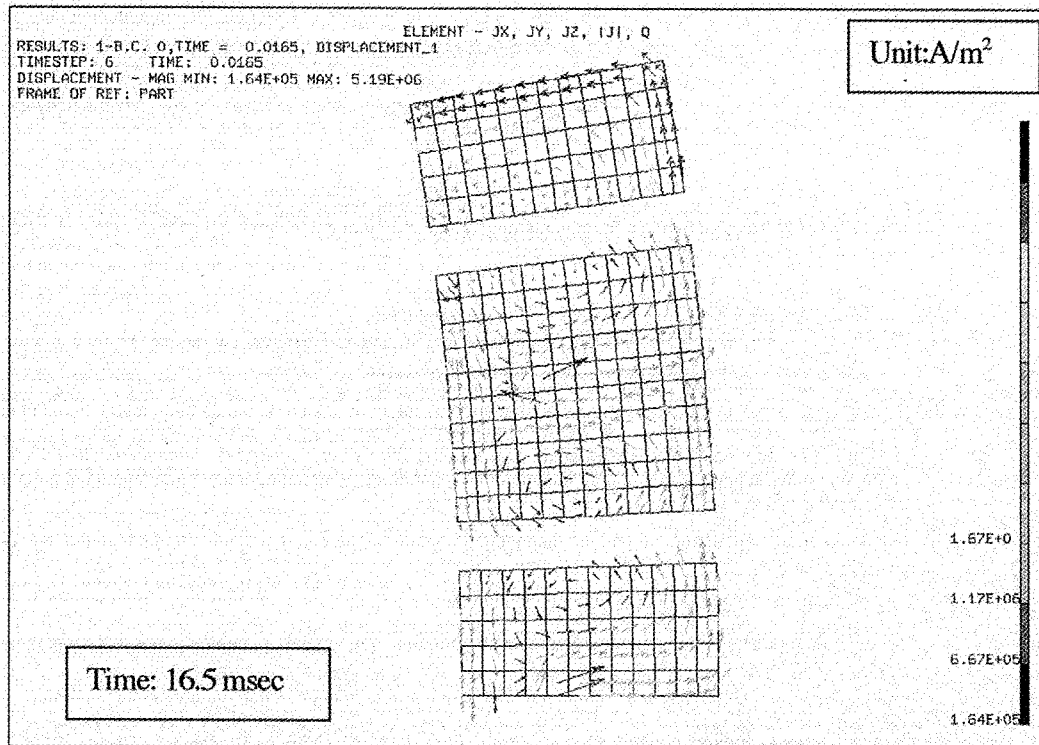


Fig. 4.2.1-26 Eddy current distribution on horizontal cross section 2 of module #5
 (Starting current quench is shown as 0 ms)

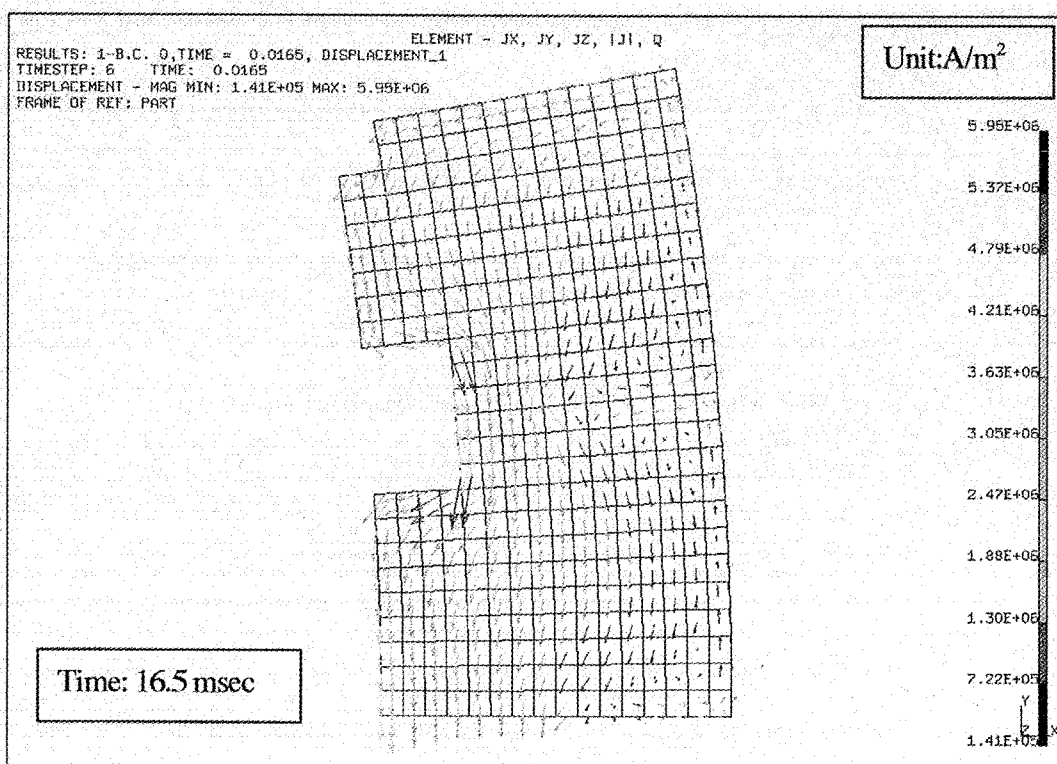


Fig. 4.2.1-27 Eddy current distribution on horizontal cross section 3 of module #5
 (Starting current quench is shown as 0 ms)

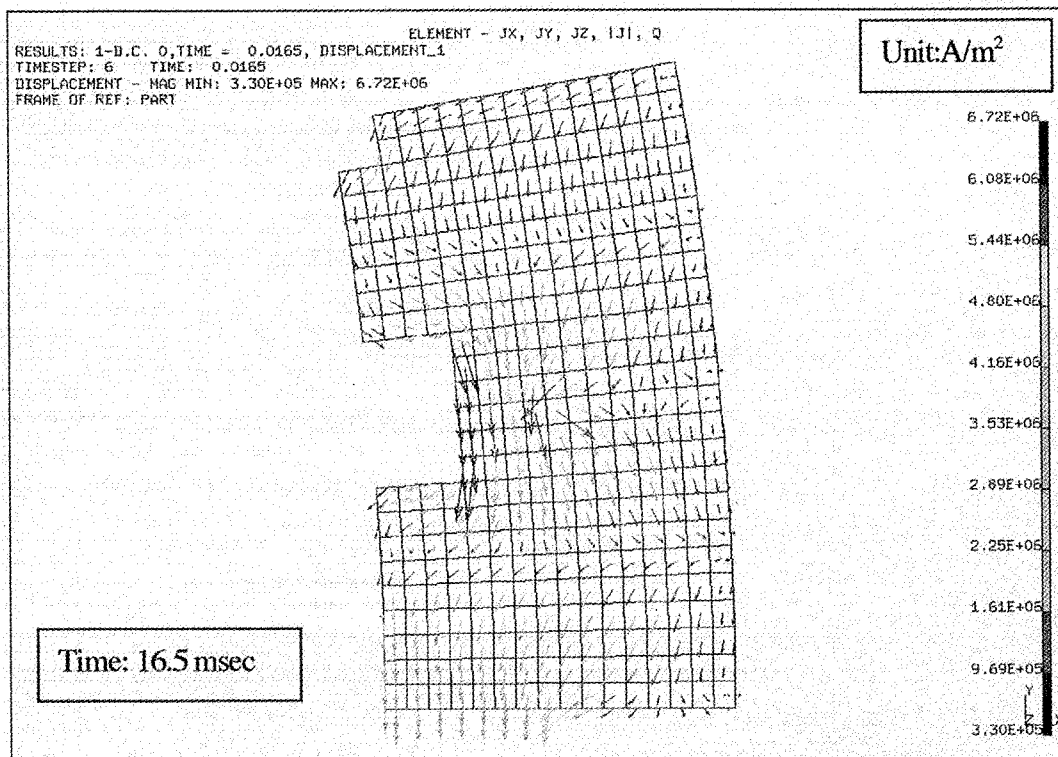


Fig. 4.2.1-28 Eddy current distribution on horizontal cross section 4 of module #5
 (Starting current quench is shown as 0 ms)

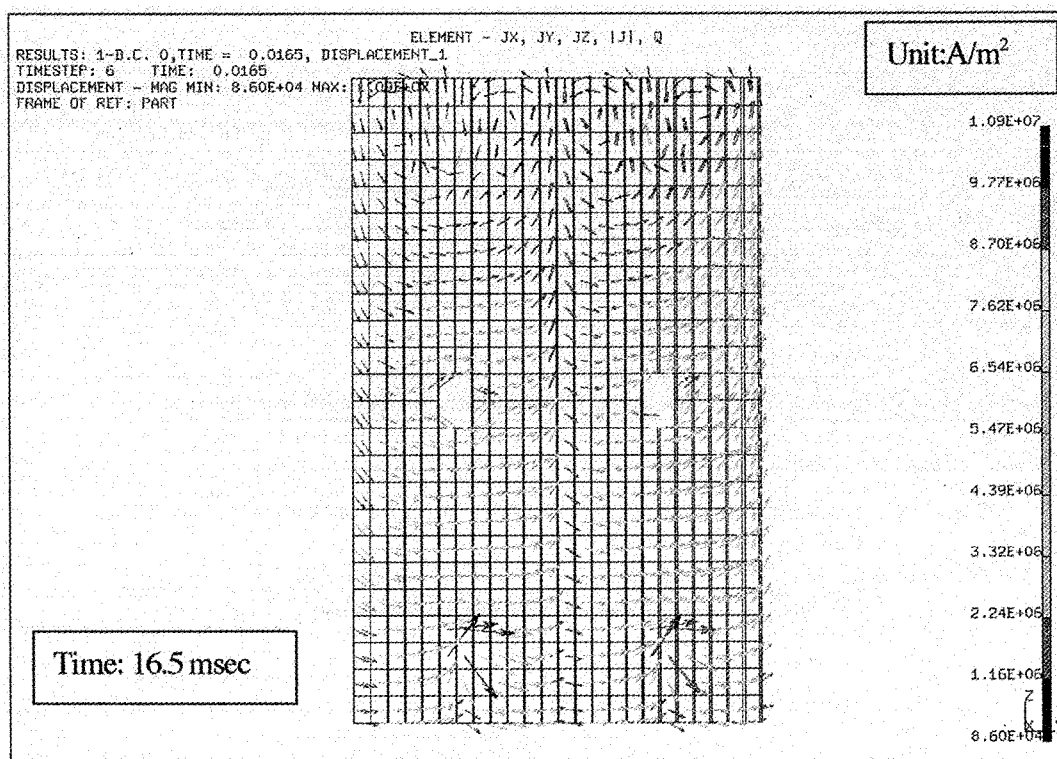


Fig. 4.2.1-29 Eddy current distribution on vertical cross section 1 of module #5
 (Starting current quench is shown as 0 ms)

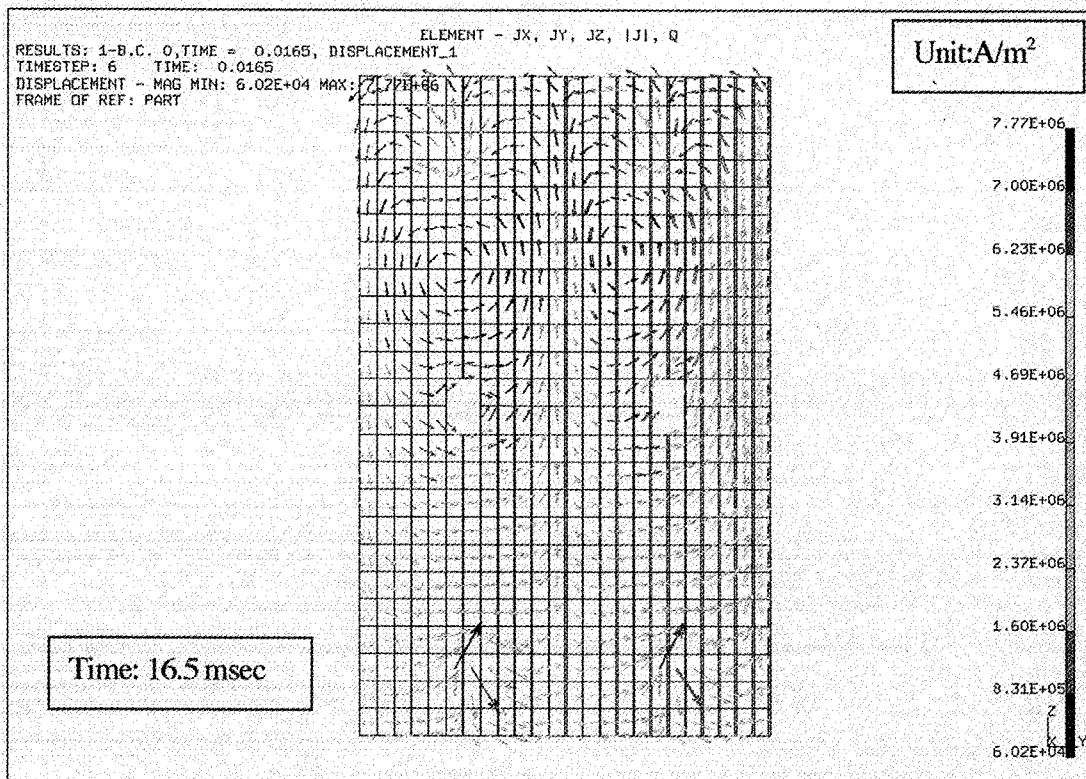


Fig. 4.2.1-30 Eddy current distribution on vertical cross section 2 of module #5
 (Starting current quench is shown as 0 ms)

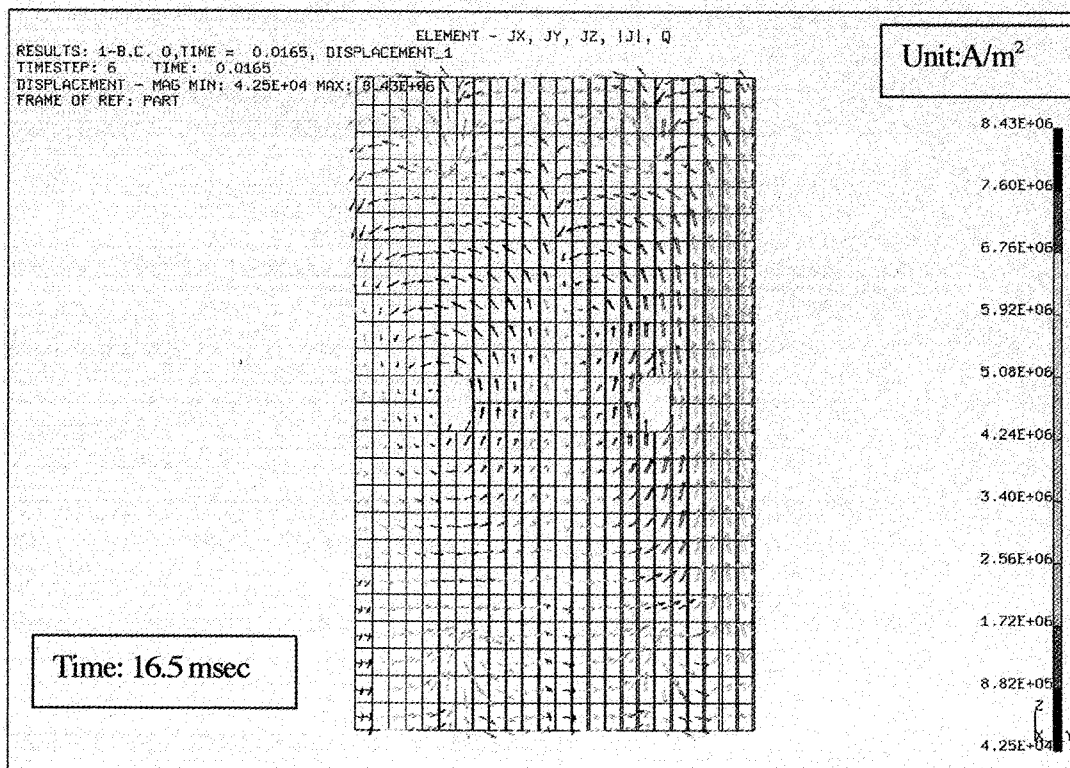


Fig. 4.2.1-31 Eddy current distribution on vertical cross section 3 of module #5
 (Starting current quench is shown as 0 ms)

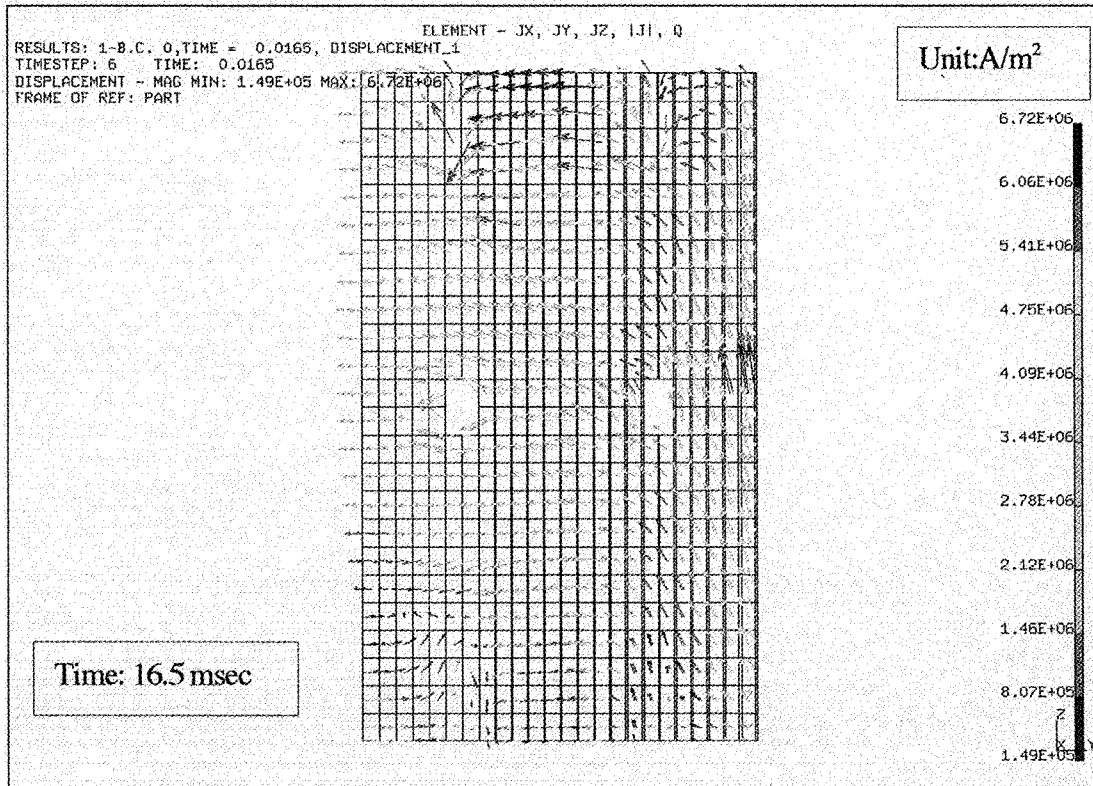


Fig. 4.2.1-32 Eddy current distribution on vertical cross section 4 of module #5
 (Starting current quench is shown as 0 ms)

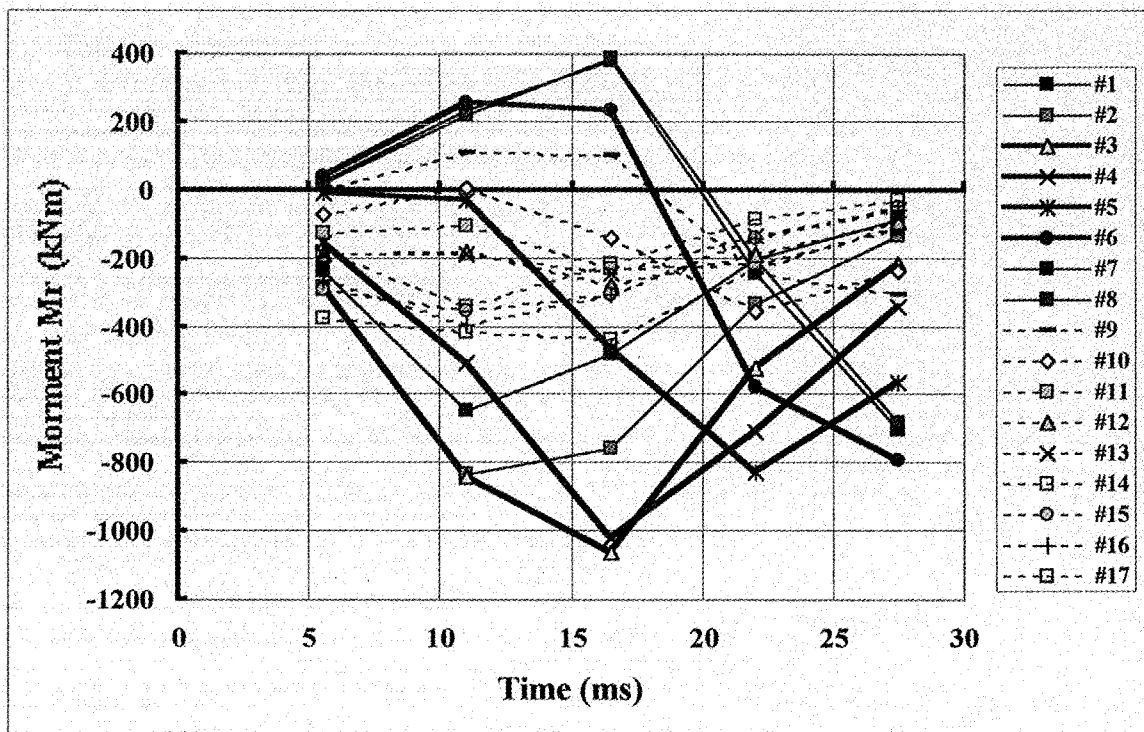


Fig. 4.2.1-33 Moment Mr on modules under CD II as a function of time
 (Starting current quench is shown as 0 ms)

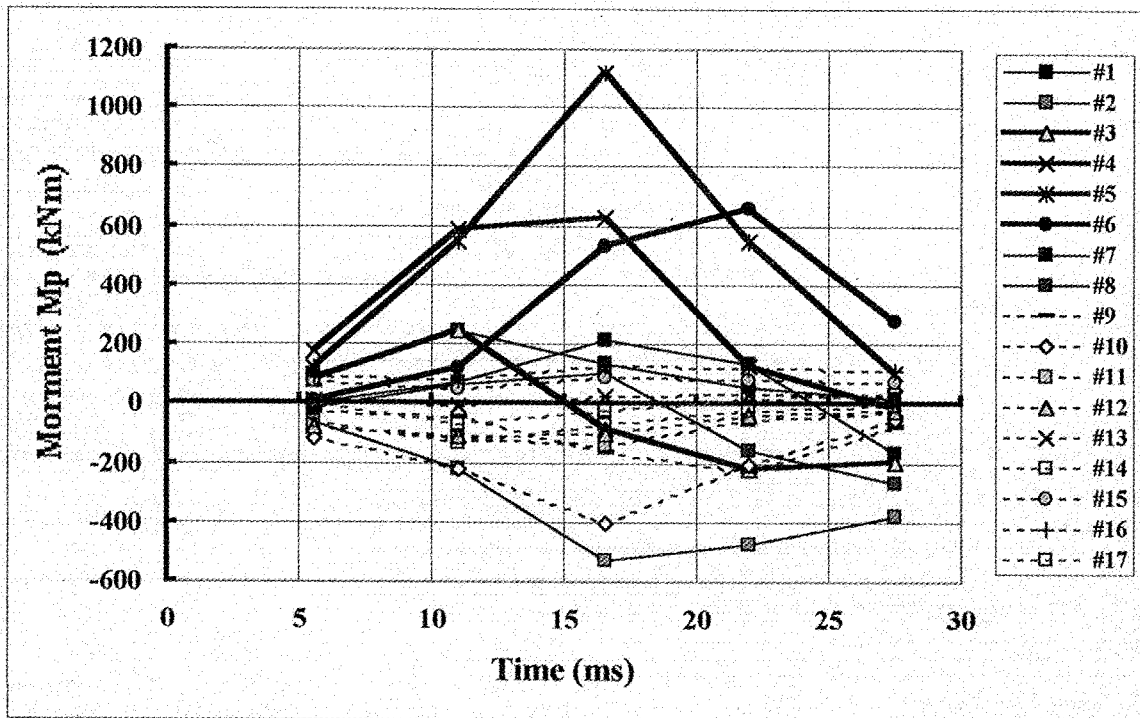


Fig. 4.2.1-34 Moment M_p on modules under CD II as a function of time
(Starting current quench is shown as 0 ms)

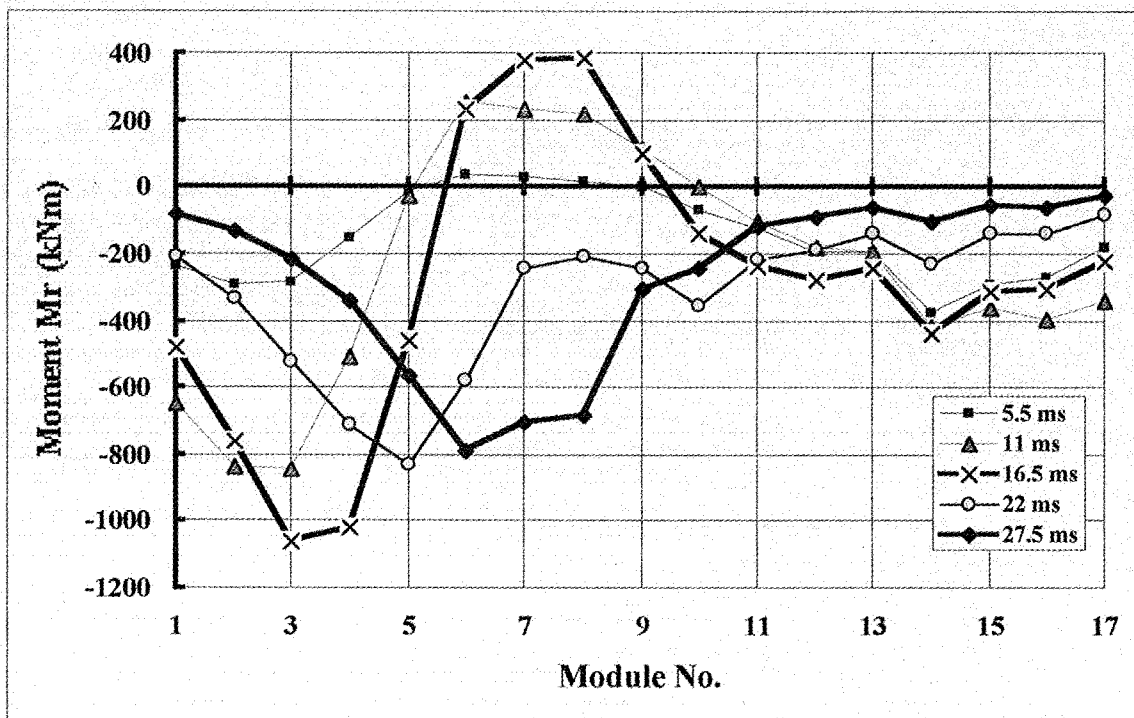


Fig. 4.2.1-35 Moment M_r on modules under CD II
(Starting current quench is shown as 0 ms)

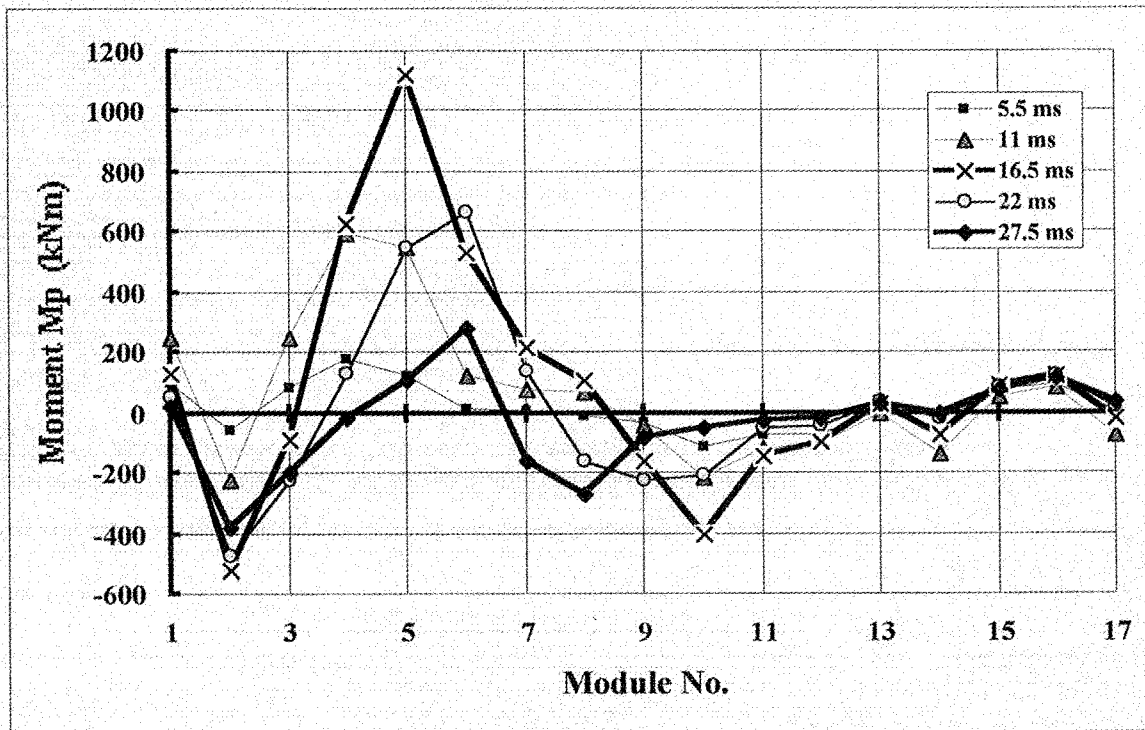


Fig. 4.2.1-36 Moment M_p on modules under CD II
(Starting current quench is shown as 0 ms)

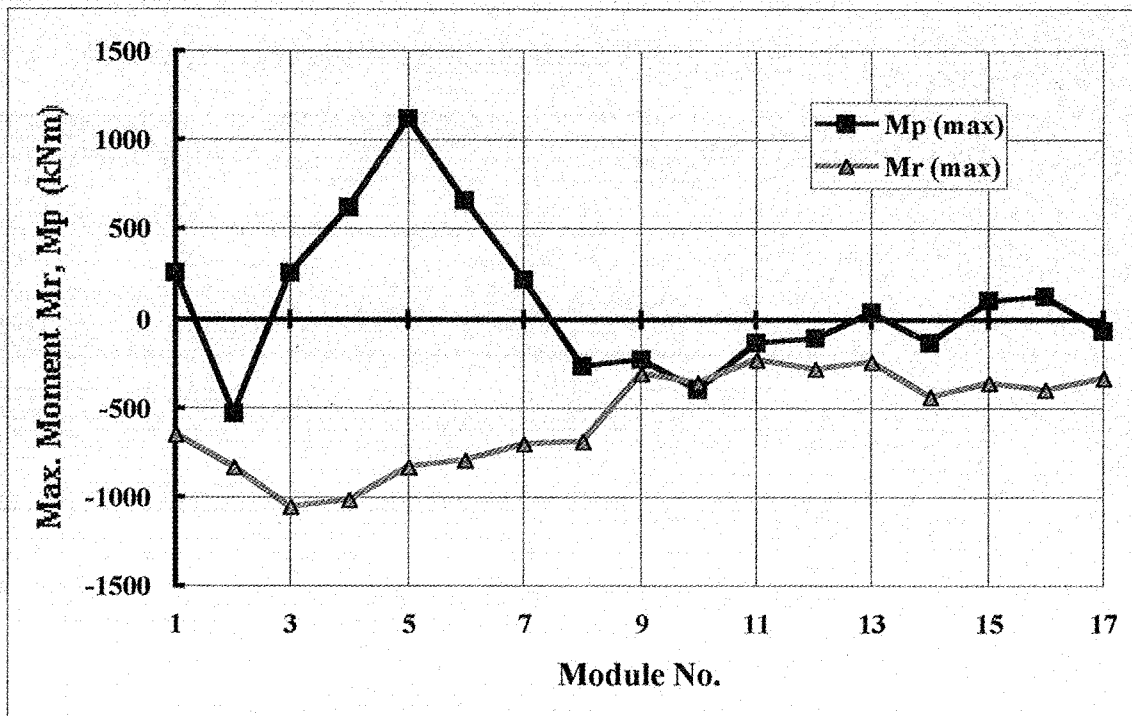


Fig. 4.2.1-37 Maximum moment on modules under CD II

4.2.2 One sector model with fine mesh model of module #5

A very fine solid mesh model of module #5 including rough vacuum vessel model has been developed to confirm the validity of coarse mesh model using equivalent material properties described in section 4.2.1. The Module #5 has the maximum EM torque M_p under CDII of 27 ms decay time, and has been selected in this analysis. The cooling tubes in the FW and shield block are precisely modeled.

4.2.2.1 Analysis method

Eddy current of module #5 is analyzed by using same solid element code EMSolution as that used in section 4.2.1. FW and the shield block of module #5 are modeled by detailed meshes as shown in Fig. 4.2.2-1. Two adjoining modules #4 and #6 are also included in this model in order to consider the effect of their eddy current. The modules #4 and #6 are modeled as boxes with wall thickness of 25 mm. The coolant channels for FW and shield block of module #5 are completely modeled as square tube with the same cross sectional area (see Fig. 4.2.2-2). Be tiles on FW is neglected because of small EM load, resulting from a lot of slits of Be tiles. Electrical resistances of the materials are as follows:

Region	Resistance ($\Omega\cdot m$)	Notes
1) Be	8×10^{-1}	Equivalent value including slits effect
2) DSCu	3.3×10^{-8}	
3) SS	8.8×10^{-7}	

The plasma current is kept under constant current of 15 MA during 10 ms, and then increases up to 15.7 MA at 11 ms. And then it decreases down to 0 A at 38.5 ms. In the EM analysis, plasma current is assumed to keep 15 MA until 11 ms without increasing the plasma current due to thermal quench, and to decrease from 15 MA at 11 ms to 0 MA at 38.5 ms (see Fig. 4.2.1-5).

4.2.2.2 Analysis results

Comparison of the moment for the fine mesh model with that for the 17-blanket model is shown in Table 4.2.2-1 and Fig. 4.2.2-3. Though the maximum moment M_r of the fine mesh model is slightly larger than that of the 17-blanket model, there is a good agreement between the two calculation results. It is concluded that the course mesh model using the equivalent resistivities can be applicable to calculate the EM loads on all modules under the CD and VDE.

Table 4.2.2-1 Comparison of EM load on module #5 under centered disruption II between fine mesh model and one sector model (Starting current quench is shown as 0 ms)

		5.5 (ms)	11 (ms)	16.5 (ms)	22 (ms)	27.5 (ms)	Max
M_r (kNm)	Fine mesh	-29.8	-57.9	-602.5	-978.1	-545.4	-978.1
	One sector	-10.5	-29.6	-462.6	-828.4	-563.7	-828.4
M_z (kNm)	Fine mesh	121.3	518.2	1038.3	442.4	107.7	1038.3
	One sector	124.7	548.1	1119.4	546.4	103.6	1119.4

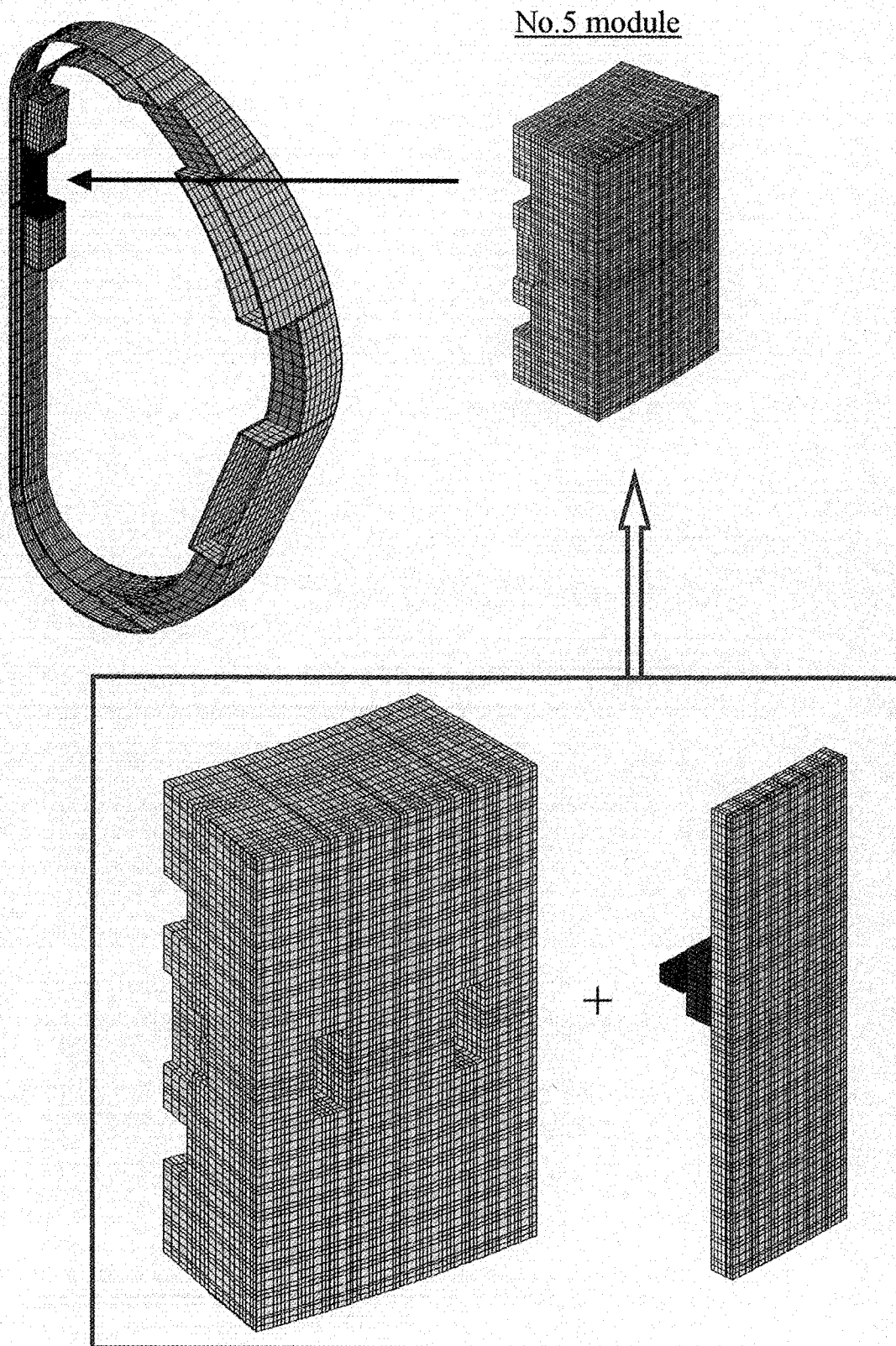
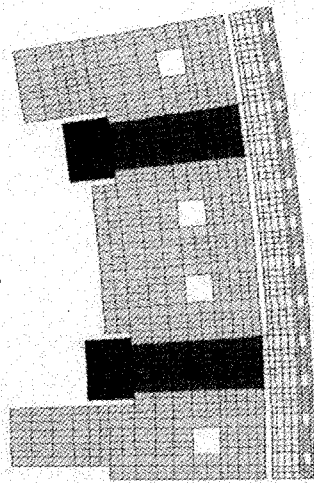
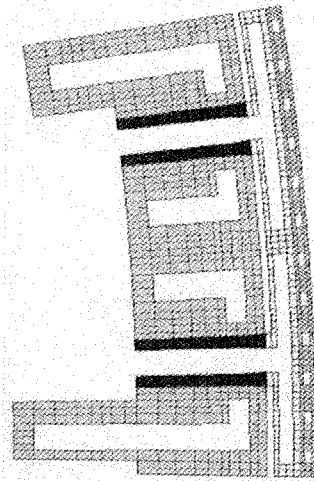


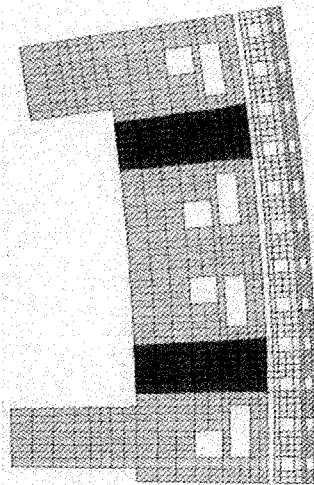
Fig. 4.2.2-1 Fine mesh model of module #5



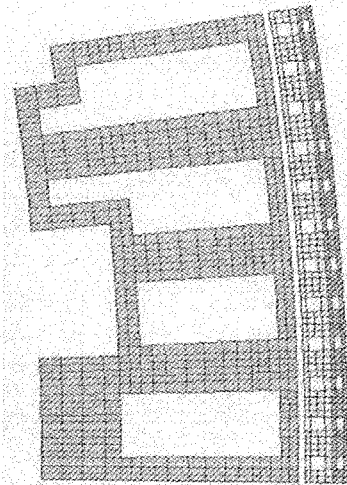
(a) Module at mid height ($z=2371\text{mm}$)



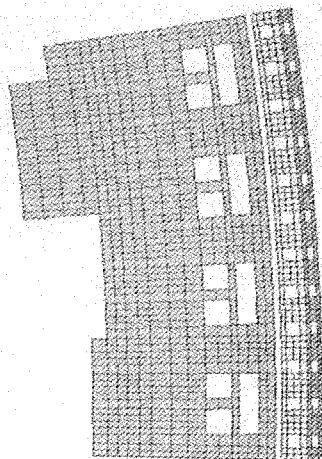
(b) Module at FW leg coolant tube ($z=2421\text{mm}$)



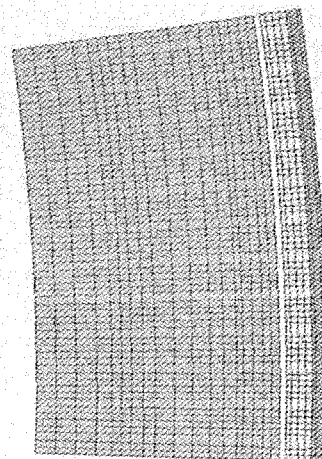
(c) FW leg upper position ($z=2439\text{mm}$)



(d) Shield block (SB) coolant tube ($z=2562\text{mm}$)



(e) Upper SB coolant manifold ($z=2593\text{mm}$)



(f) Module top ($z=2915\text{mm}$)

Fig. 4.2.2-2 Cross-section of mesh model for module #5

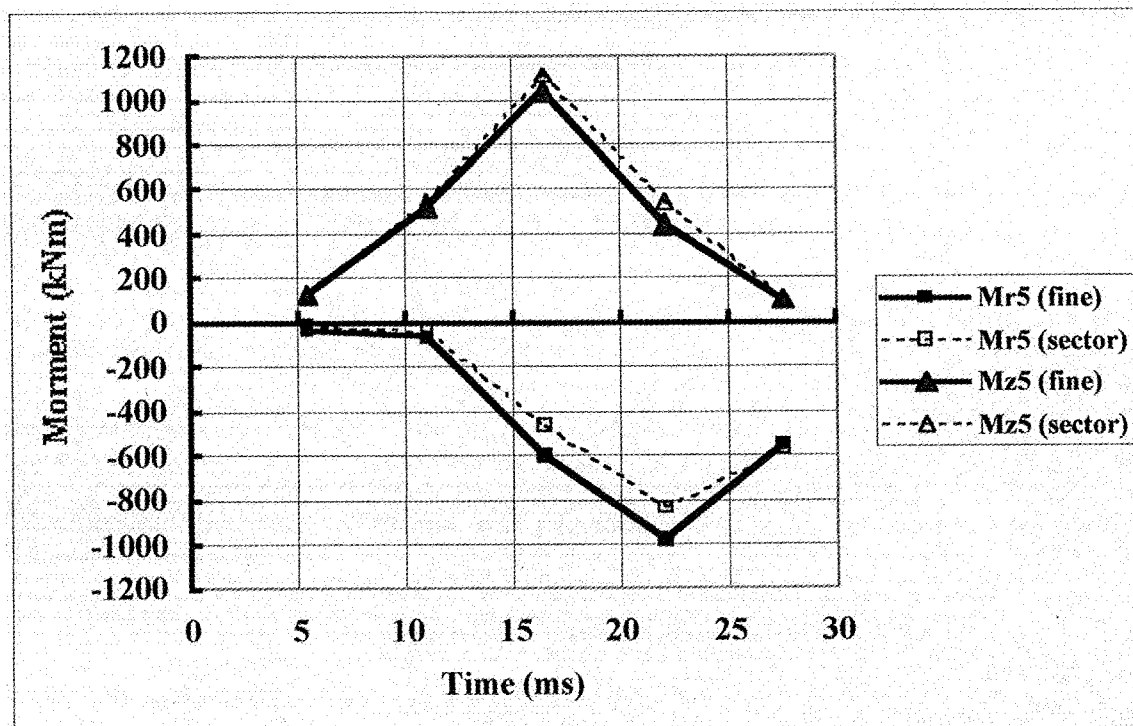


Fig. 4.2.2-3 Comparison of moment on module #5 under CD II between fine mesh model and one sector model (Starting current quench is shown as 0 ms)

4.3 Fast downward VDE (VDE/F-D)

4.3.1 Analysis method

4.3.1.1 Model of plasma movement

The plasma current of the fast downward VDE III (VDE/F-DIII) is shown in Fig. 4.3-1. According to the disruption scenario, the plasma starts to move downward, and then thermal quench occurs at 411 ms. The plasma current increases from 13.8 MA up to 15.7 MA at 414 ms due to thermal quench. The plasma current decreases to 0 MA at 441 ms. The plasma current densities during VDE/F-DIII are shown in Figs. 4.3-2 to 4.3-5. The plasma center position moves as shown in Figs. 4.3-6 and 4.3-7.

In the EM analysis, the plasma current change and movement before the current quench are not taken into account. Initial plasma current in the analysis is 15.7 MA at 414 ms just after thermal quench and decreases to 0 MA at 441 ms, resulting in the neglect of eddy current on the modules during the thermal quench. The plasma movement is simulated using the filament current change in the plasma area.

4.3.1.2 Mesh model

Mesh models for the fast downward VDE are shown in Figs. 4.3-8 to 4.3-13. Seventeen blankets in the poloidal cross section are modeled by the solid meshes basically same as the model for the centered disruption. Some detail meshes are used for the blanket modules from #1 to #3 in this analysis in order to calculate the correct eddy current due to plasma downward movement (see Fig. 4.3-10 and 4.3-11). The recess for the branch pipes and electrical straps has been modeled in the back of all modules. The

recess for cooling manifolds and key has also modeled in detail meshes of modules #1 to #3.

4.3.2 Analysis results

Magnetic flux density distributions are shown in Figs. 4.3-14 and 4.3-15 and eddy current distributions are shown in Figs. 4.3-16 to 4.3-26. Toroidal component of eddy current flowing in the VV is about 15 MA in total at the end of current quench, and this corresponds to about 95% of initial plasma current.

Moments induced in the shield blankets are shown in Tables 4.3-1 and 4.3-2. Figs. 4.3-27 and 4.3-28 show the time history of moment M_r and M_p on the modules, respectively. Figs. 4.3-29 and 4.3-30 show the poloidal distribution of M_r and M_p on modules. The maximum moment of each blanket module is shown in Fig. 4.3-31. Both moment of M_r and M_p are the largest in module #1 at the end of the disruption, the values of the moments are 970 kNm and 1470 kNm, respectively. Non-linear plasma current decay at the end of current quench as shown in Fig. 4.3-1 produces the higher moment comparing with linear decay. Maximum moment M_p for the linear current decay will be smaller than the calculated value of 1470 kNm.

Table 4.3-1 Moment M_r (kNm) on shield block for VDE/F-DIII
(Starting current quench is shown as 0 ms)

Module No.	3 ms	6 ms	9 ms	12 ms	15 ms	18 ms	21 ms	24 ms	27 ms	Max
1	-197	-287	-379	-646	-763	-832	-932	-968	-892	-968
2	-418	-597	-692	-774	-814	-805	-658	-589	-517	-814
3	-538	-767	-845	-709	-648	-593	-421	-338	-281	-845
4	-414	-593	-645	-478	-399	-347	-239	-185	-150	-645
5	-222	-323	-355	-258	-210	-180	-126	-98	-80	-355
6	-94	-141	-158	-119	-98	-85	-62	-49	-41	-158
7	-41	-64	-75	-60	-51	-45	-35	-29	-25	-75
8	-36	-57	-68	-56	-48	-43	-34	-28	-24	-68
9	-31	-46	-51	-37	-30	-25	-18	-14	-11	-51
10	-65	-96	-107	-79	-64	-54	-38	-30	-24	-107
11	-68	-100	-112	-82	-67	-56	-39	-30	-24	-112
12	-85	-127	-142	-106	-87	-74	-52	-39	-31	-142
13	-87	-129	-143	-108	-90	-77	-53	-40	-32	-143
14	-192	-287	-325	-262	-229	-204	-145	-112	-90	-325
15	-178	-259	-291	-261	-247	-229	-162	-128	-104	-291
16	-170	-248	-295	-349	-376	-375	-296	-258	-223	-376
17	-100	-145	-192	-335	-393	-422	-455	-460	-411	-460

Table 4.3-2 Moment M_p (kNm) on shield block for VDE/F-DIII
(Starting current quench is shown as 0 ms)

Module No.	3 ms	6 ms	9 ms	12 ms	15 ms	18 ms	21 ms	24 ms	27 ms	Max
1	-90	-152	-148	124	288	470	979	1324	1469	1469
2	-237	-398	-486	-327	-226	-135	39	168	238	-486
3	22	33	66	219	333	415	428	448	452	452
4	199	321	408	426	451	465	425	403	382	465
5	167	272	343	327	325	322	291	272	255	343
6	85	144	186	180	179	177	163	152	144	186
7	1	1	2	3	3	3	3	3	2	3
8	-20	-36	-49	-49	-49	-50	-47	-45	-43	-50
9	-20	-34	-43	-41	-40	-39	-36	-34	-32	-43
10	-30	-51	-66	-63	-63	-63	-58	-56	-53	-66
11	-17	-29	-38	-38	-39	-39	-36	-34	-32	-39
12	-23	-38	-48	-46	-47	-47	-43	-41	-39	-48
13	-3	-3	-5	-9	-14	-16	-16	-16	-16	-16
14	-63	-102	-131	-151	-172	-188	-179	-175	-171	-188
15	23	34	34	-9	-38	-59	-67	-73	-76	-76
16	49	83	97	28	-19	-57	-104	-142	-161	-161
17	39	68	70	-44	-104	-182	-436	-603	-668	-668

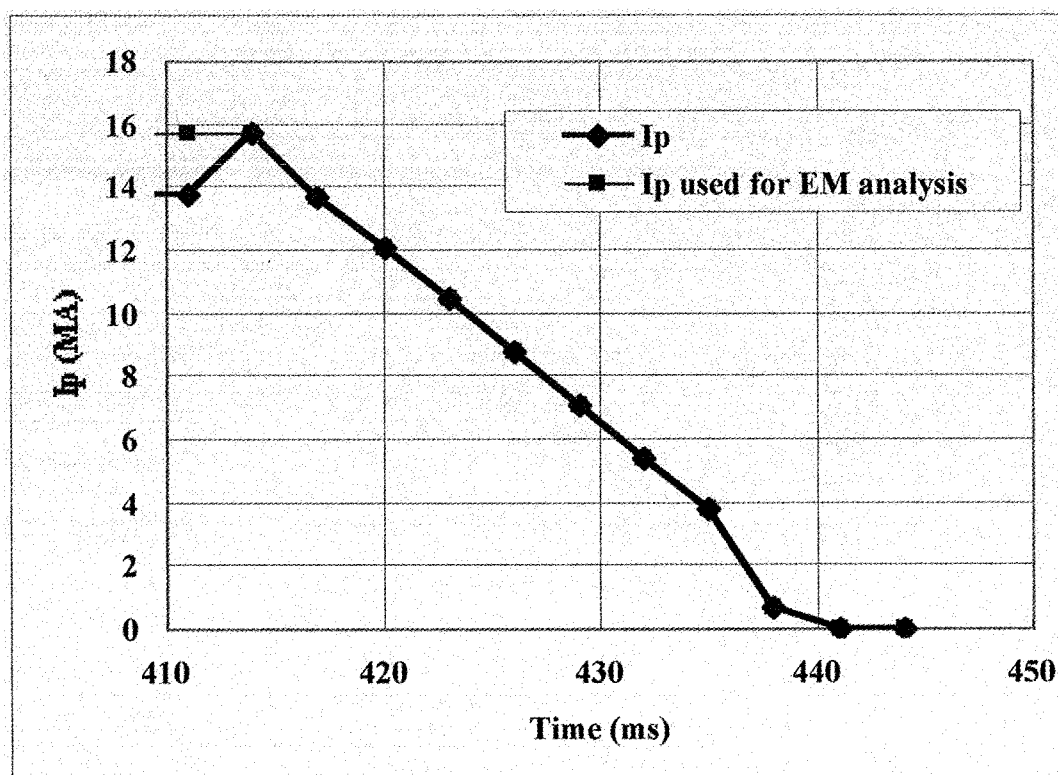


Fig. 4.3-1 Plasma current under VDE/F-DIII (Starting current quench is 414 ms)

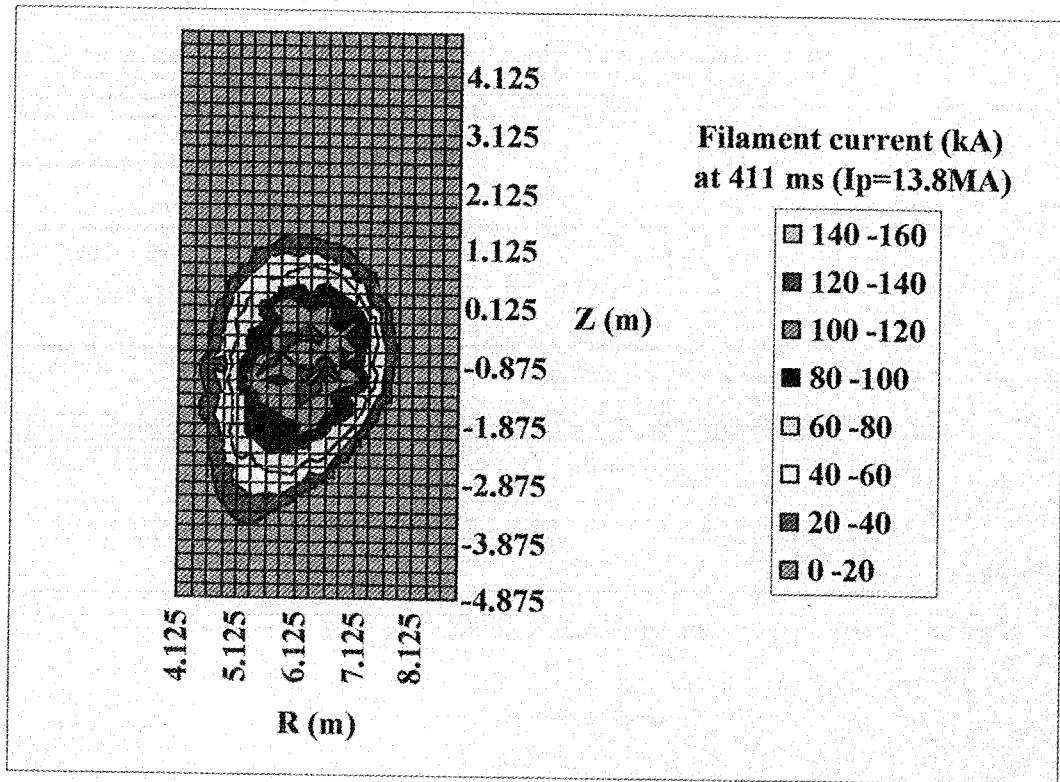


Fig. 4.3-2 Plasma current density before thermal quench under VDE/F-DIII

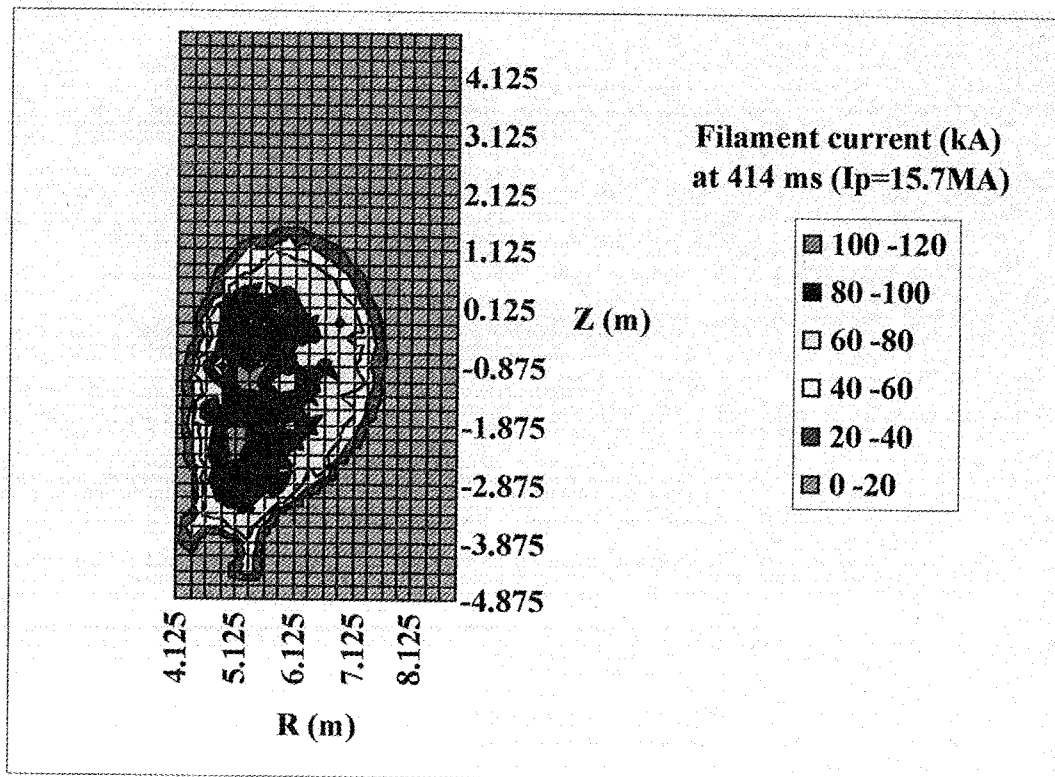


Fig. 4.3-3 Plasma current density just after thermal quench under VDE/F-DIII

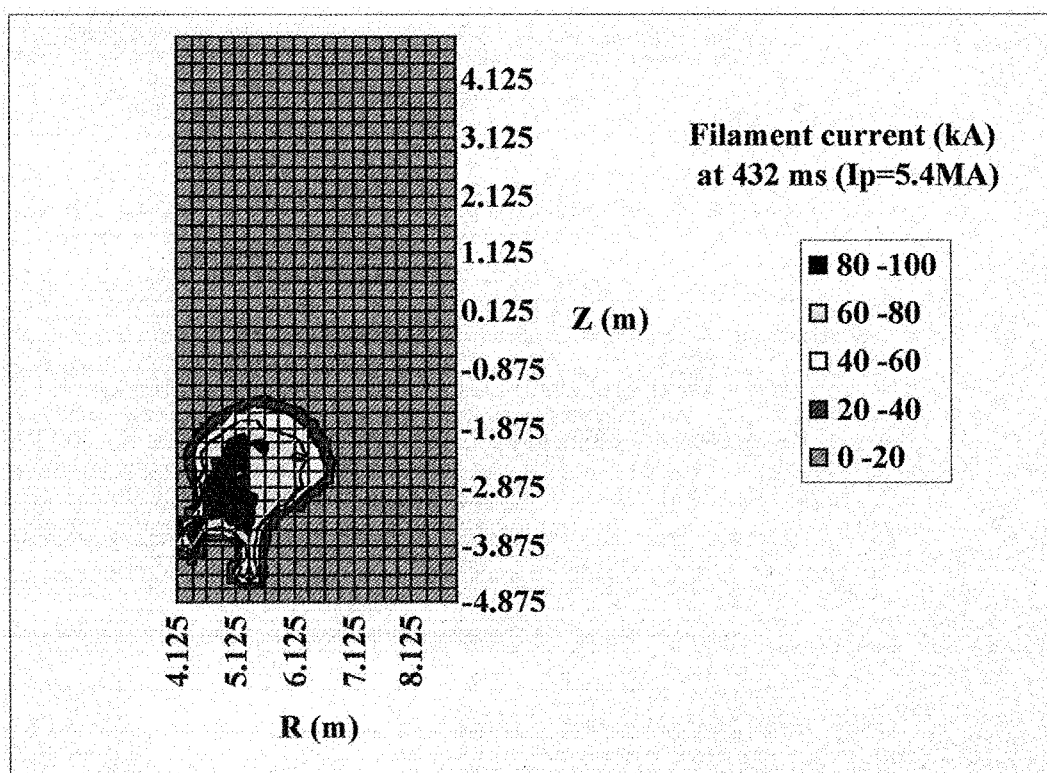


Fig. 4.3-4 Plasma current density at 18 ms during current quench under VDE/F-DIII

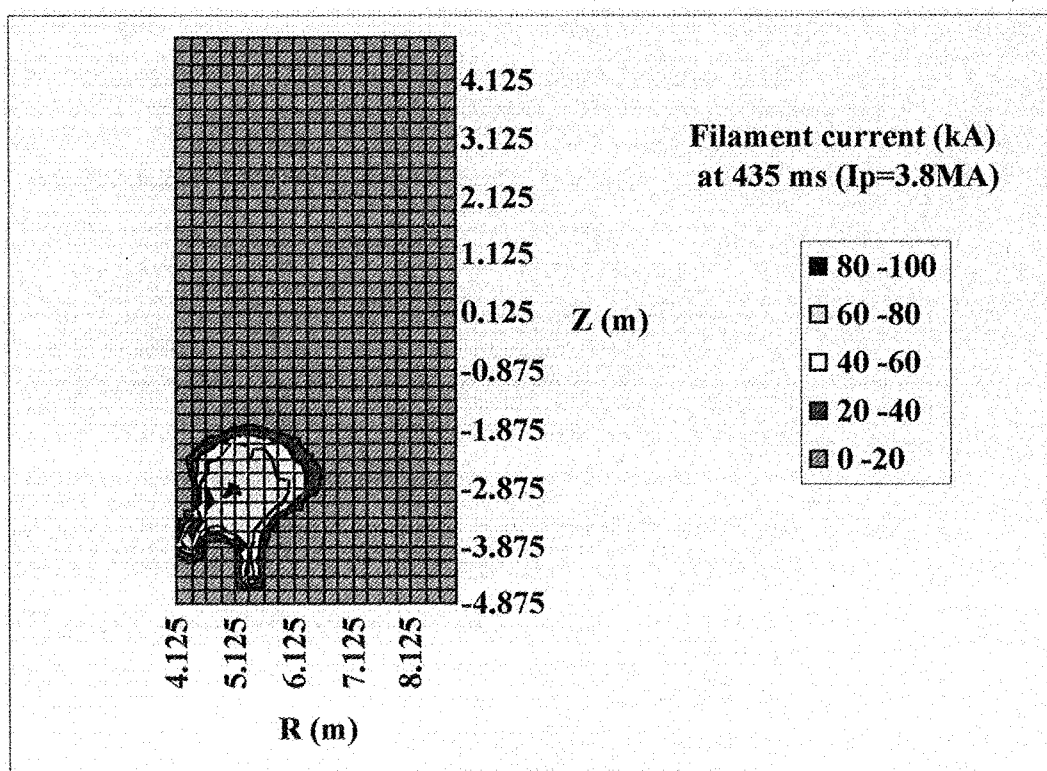


Fig. 4.3-5 Plasma current density at 21 ms during current quench under VDE/F-DIII

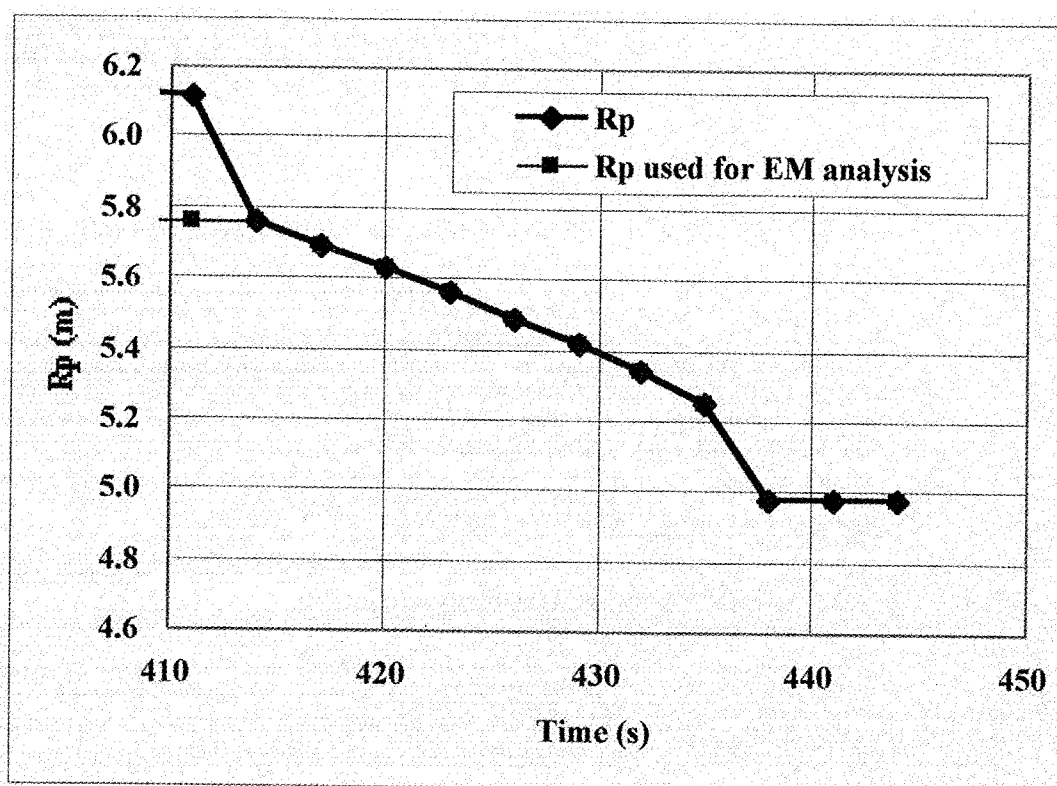


Fig. 4.3-6 Plasma position R_p under VDE/F-DIII (Starting current quench is 414 ms)

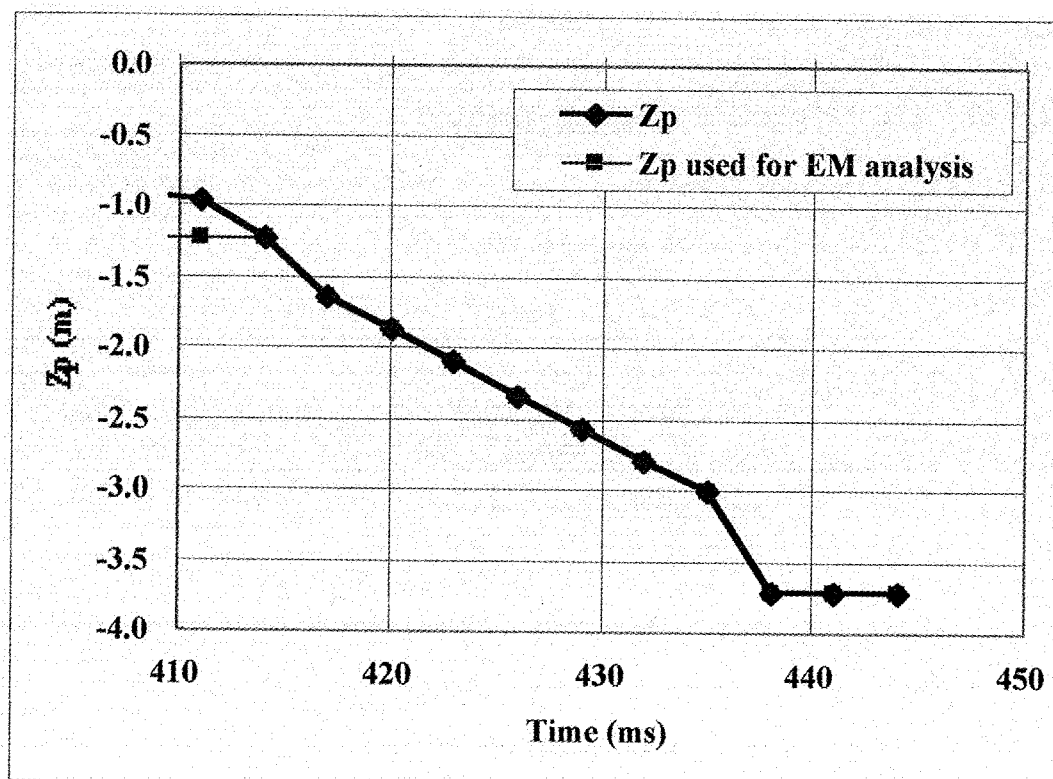


Fig. 4.3-7 Plasma position Z_p under VDE/F-DIII (Starting current quench is 414 ms)

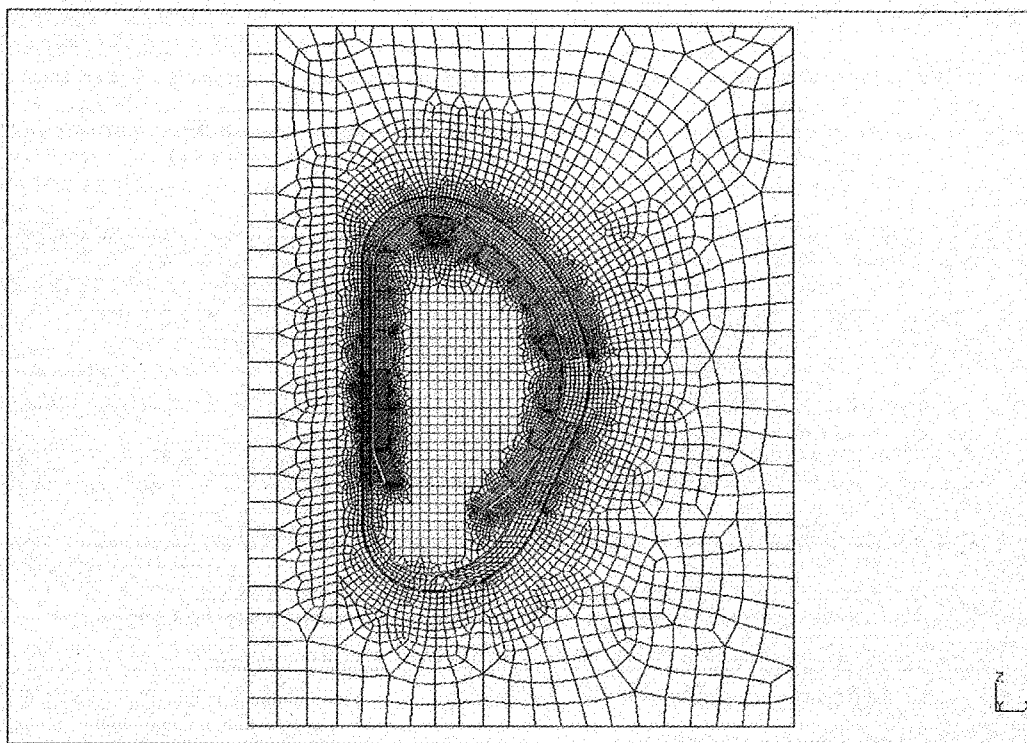


Fig. 4.3-8 Mesh model of VDE/F-D (Vertical cross section)

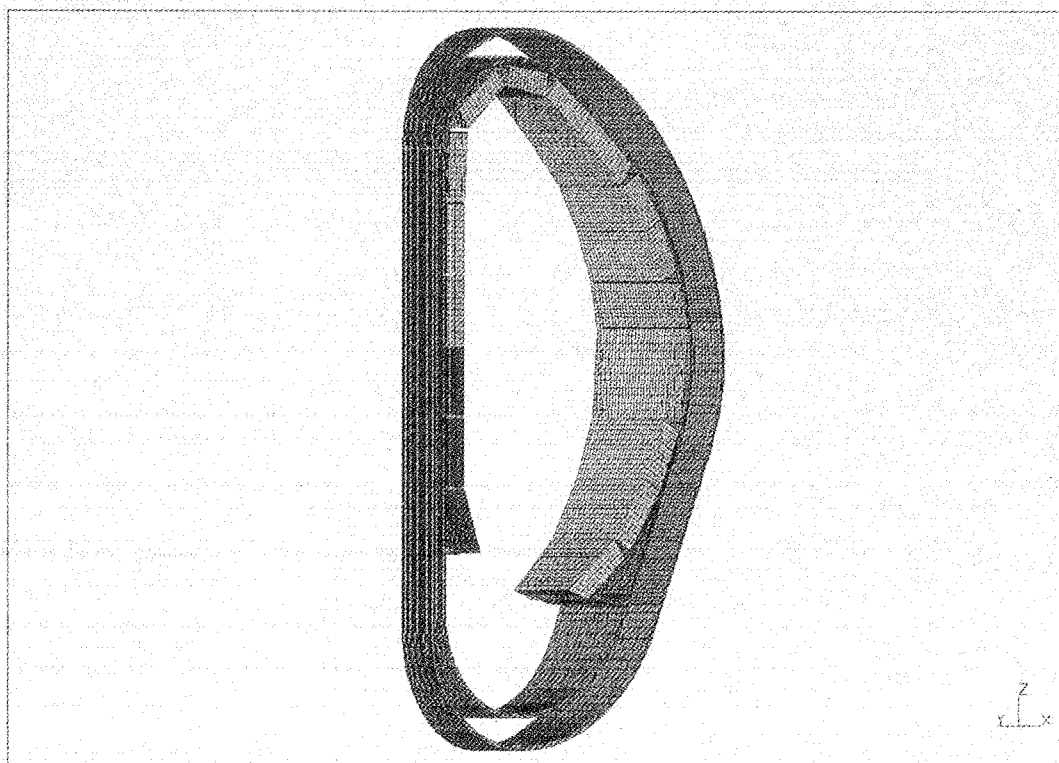


Fig. 4.3-9 Mesh model of VDE/F-D (Side view)

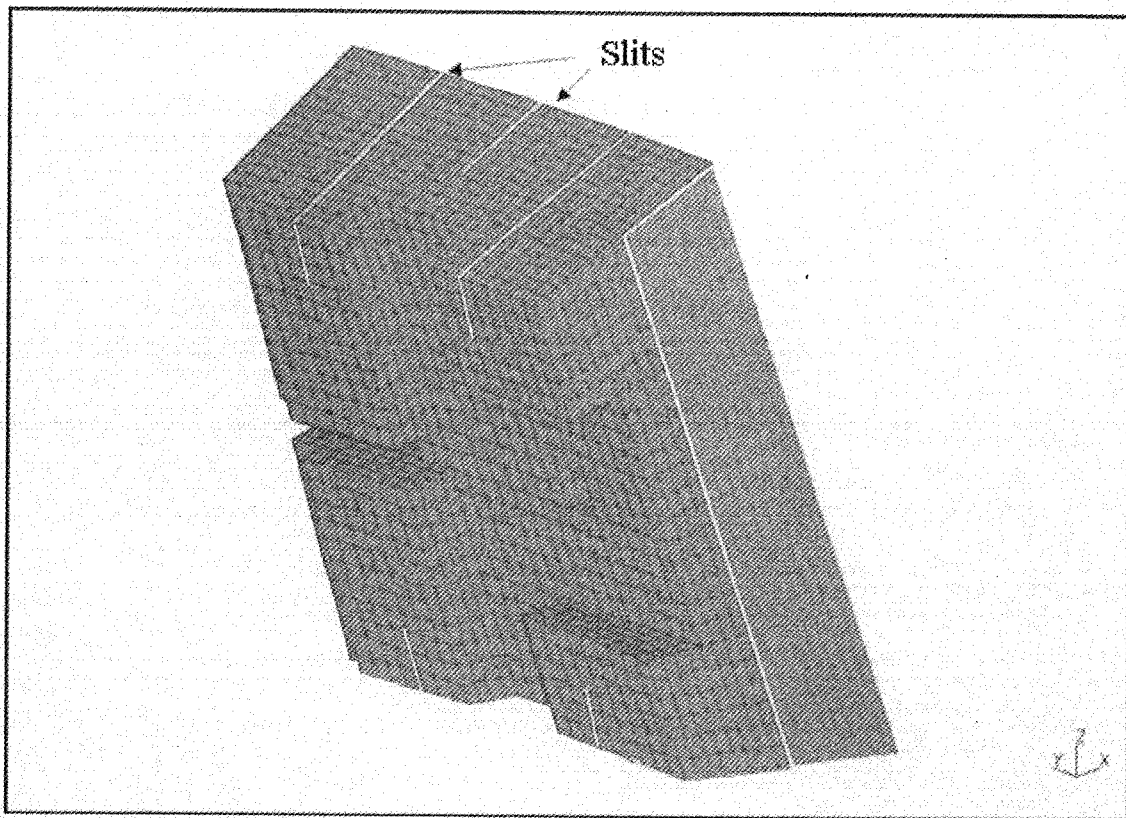


Fig. 4.3-10 Mesh model of module #1

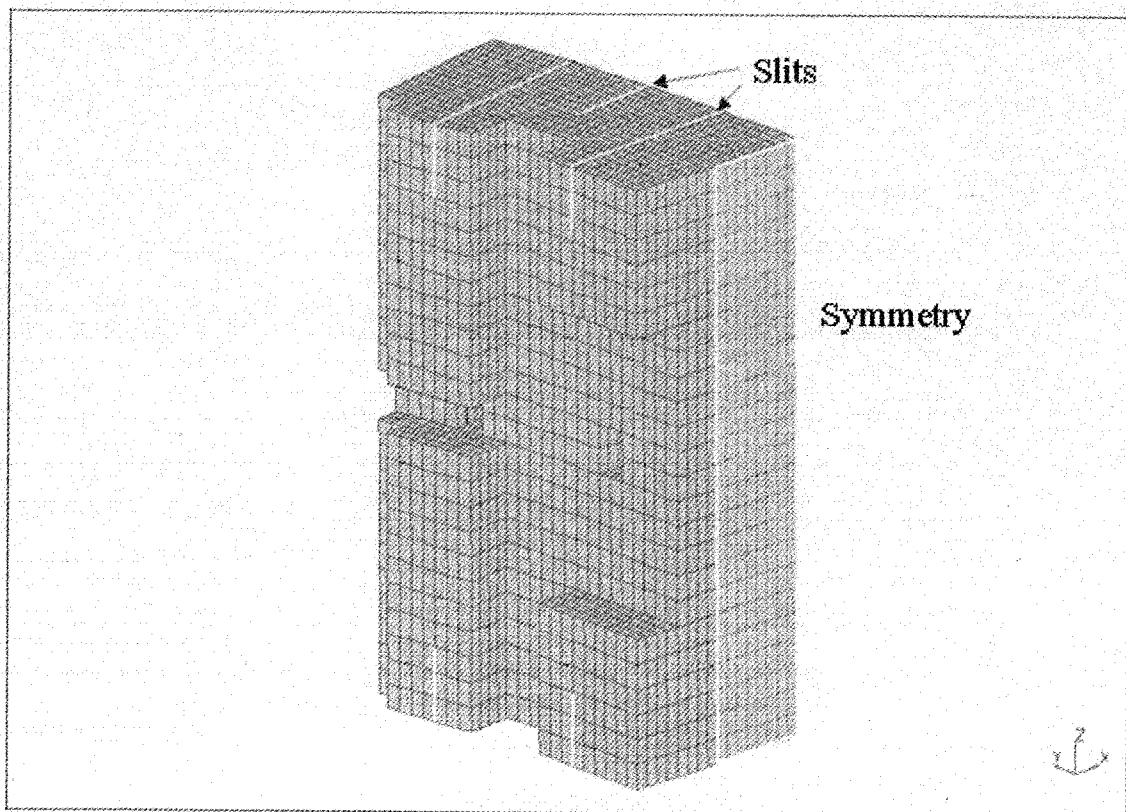


Fig. 4.3-11 Mesh model of module #3

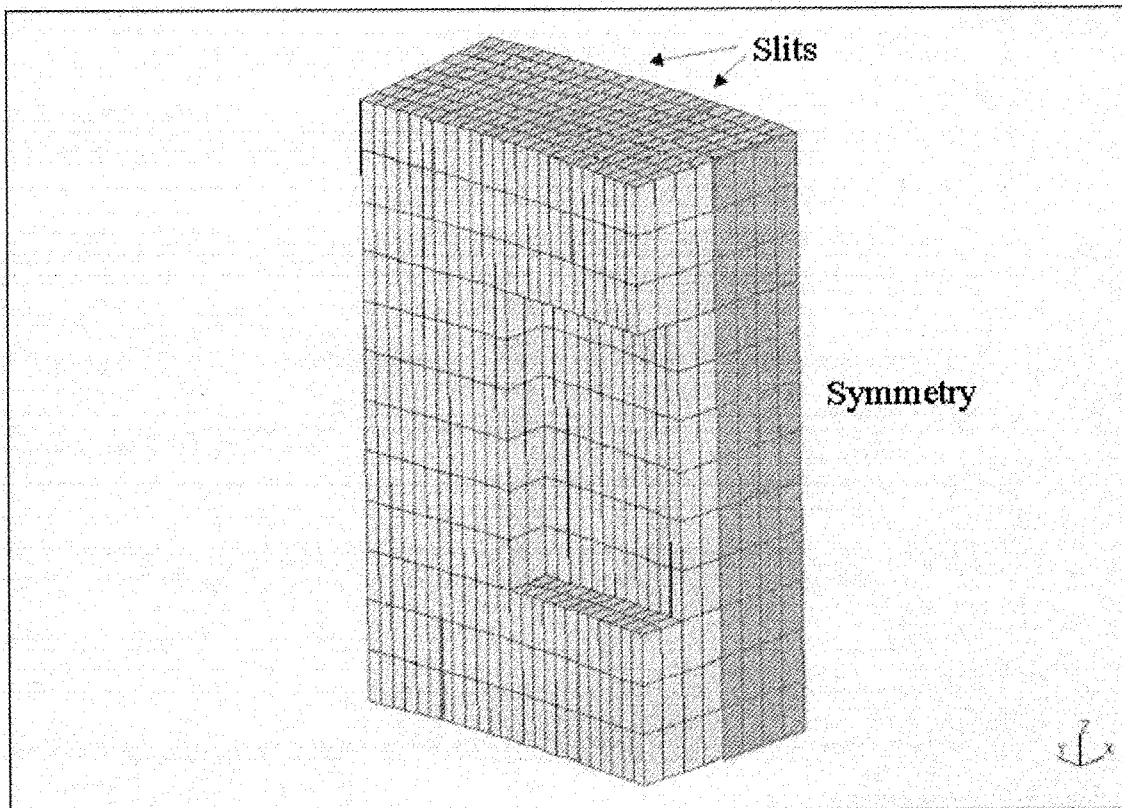


Fig. 4.3-12 Mesh model of inboard module except module #3

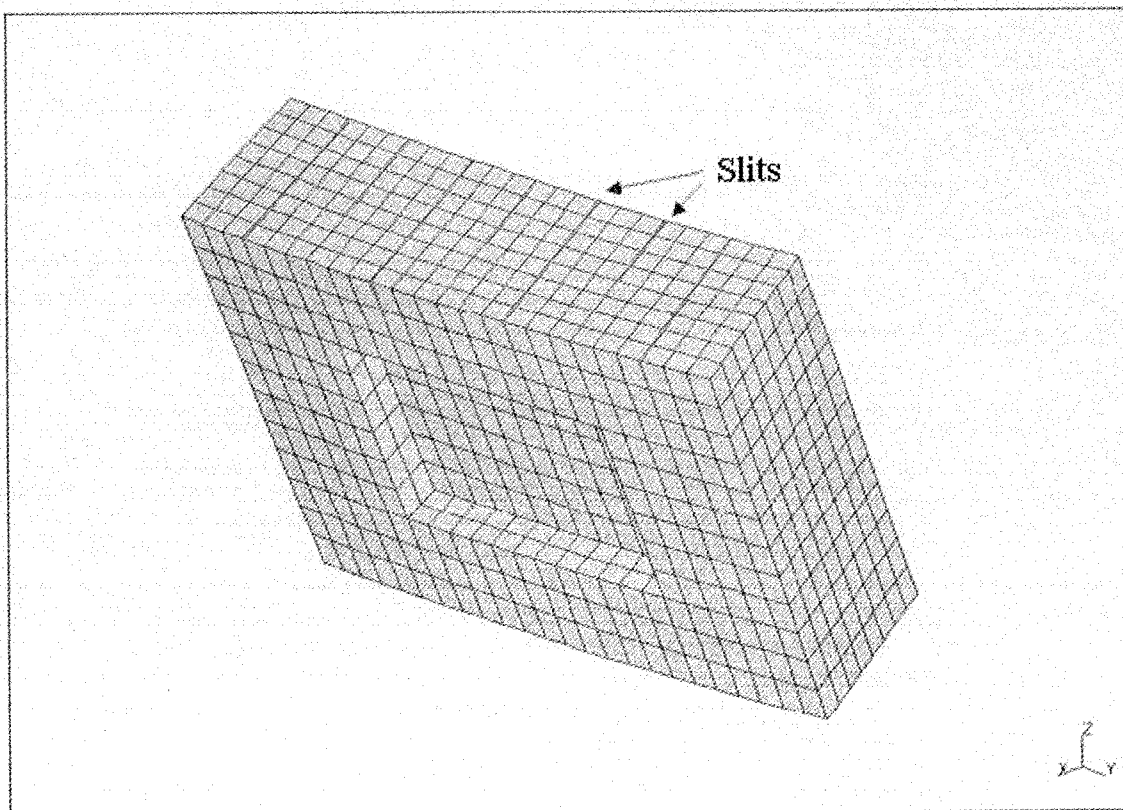


Fig. 4.3-13 Mesh model of outboard module #15

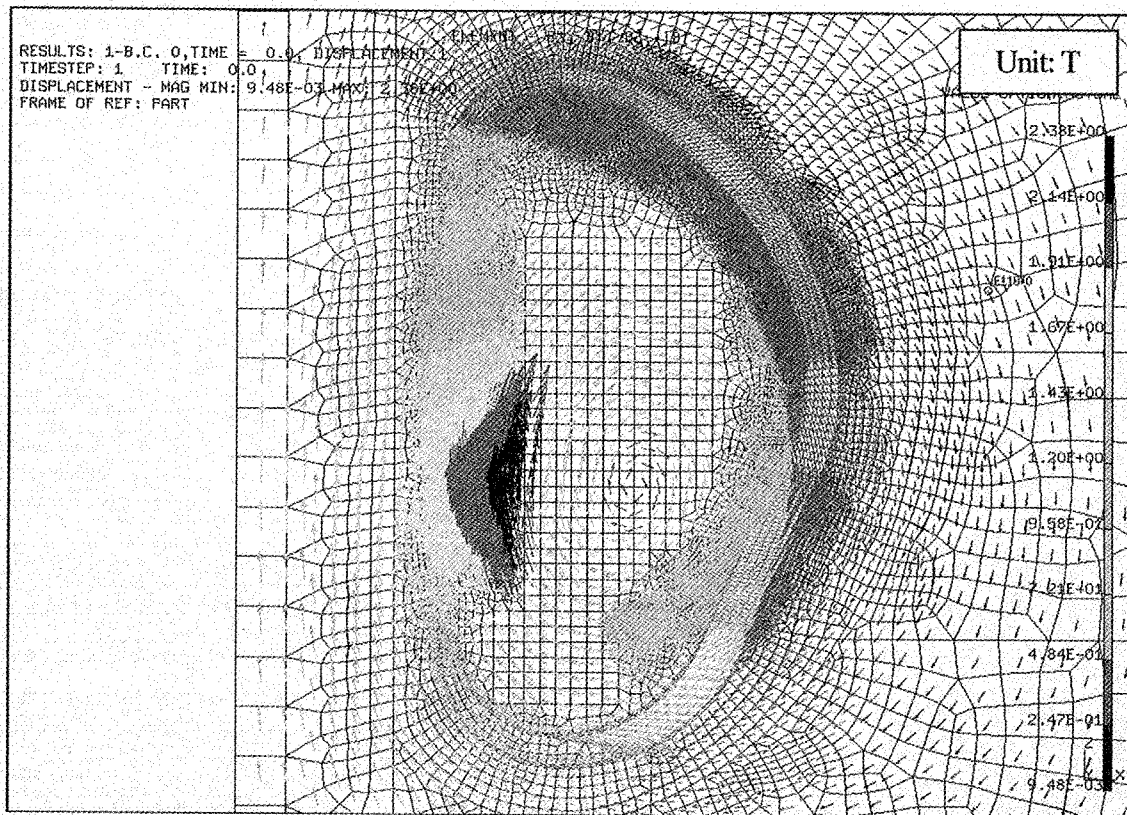


Fig. 4.3-14 Magnetic field due to plasma at the start of current quench under VDE/F-DIII

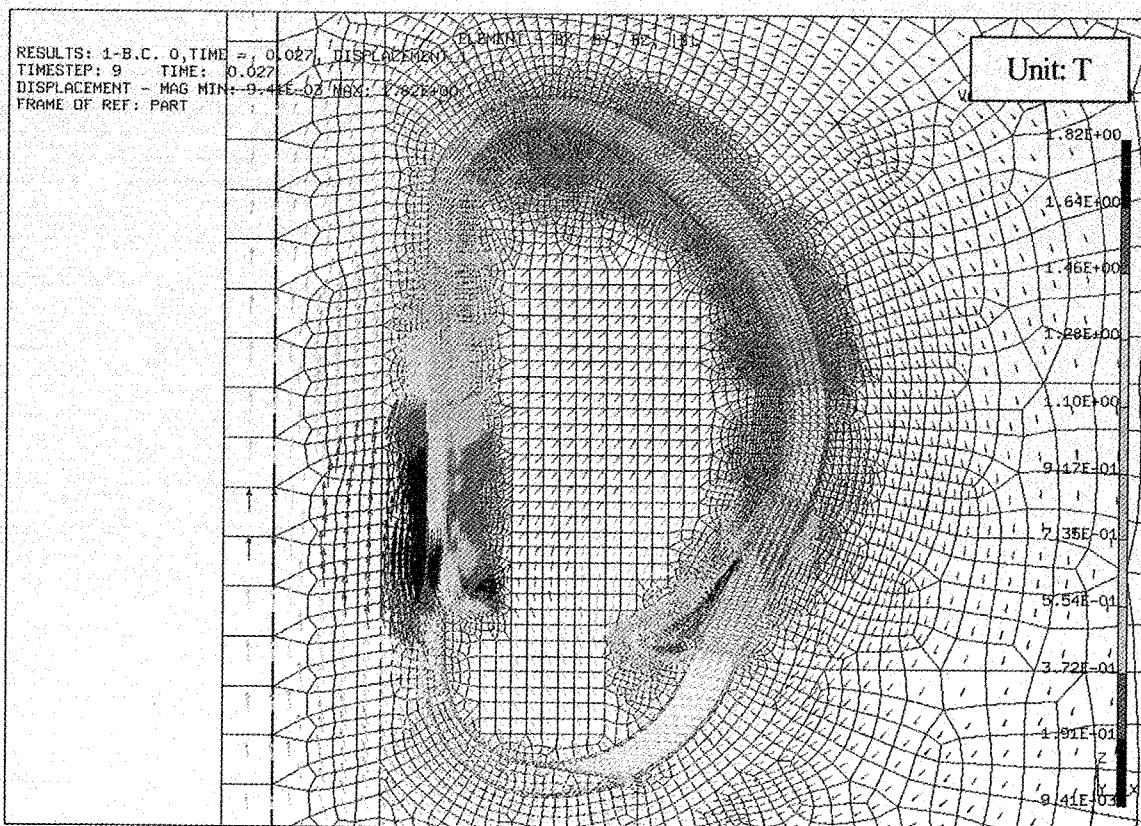


Fig. 4.3-15 Magnetic field due to eddy current at the end of current quench under VDE/F-DIII

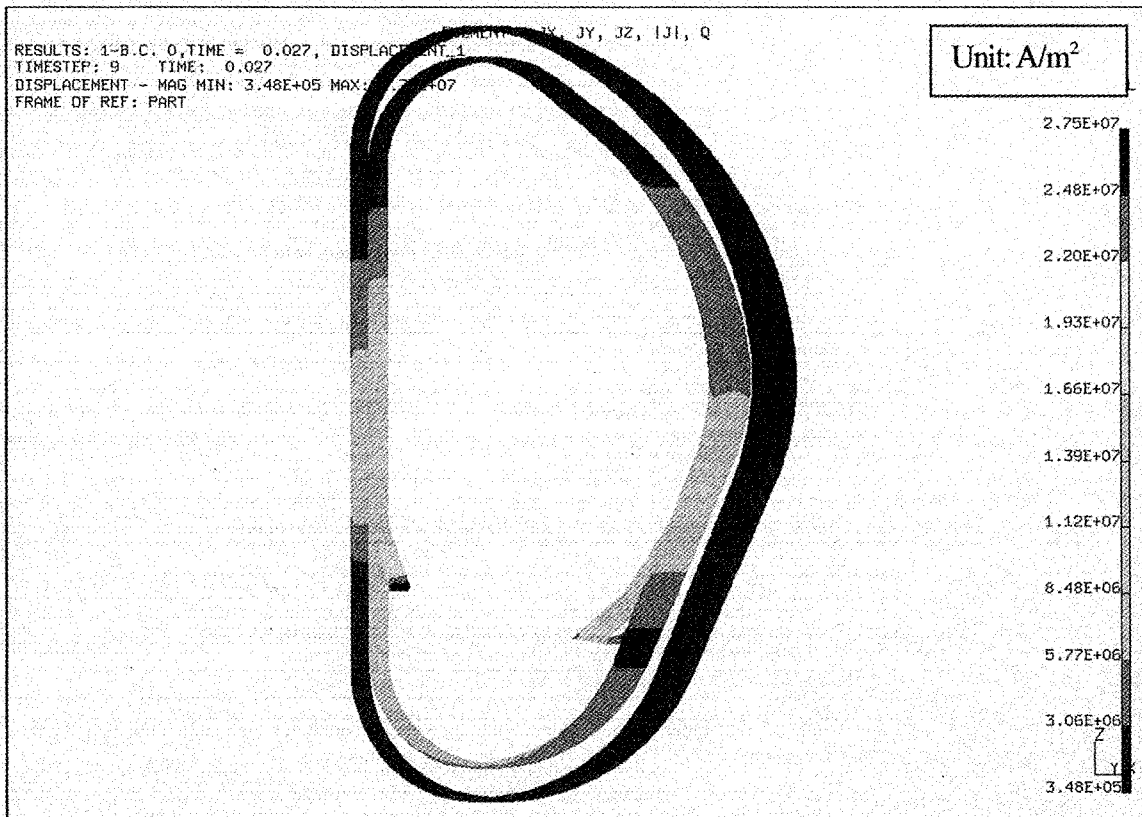


Fig. 4.3-16 Eddy current distribution on VV at the end of current quench under VDE/F-DIII

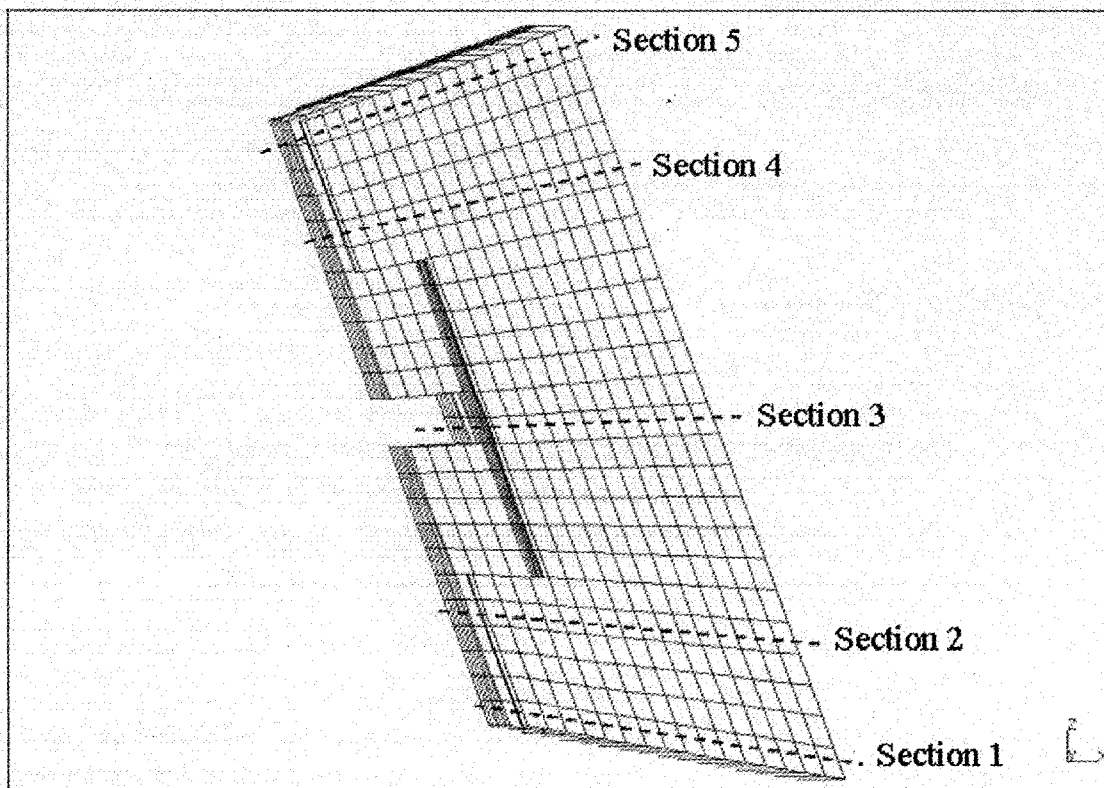


Fig. 4.3-17 Horizontal cross section of module #1 for showing eddy current distribution

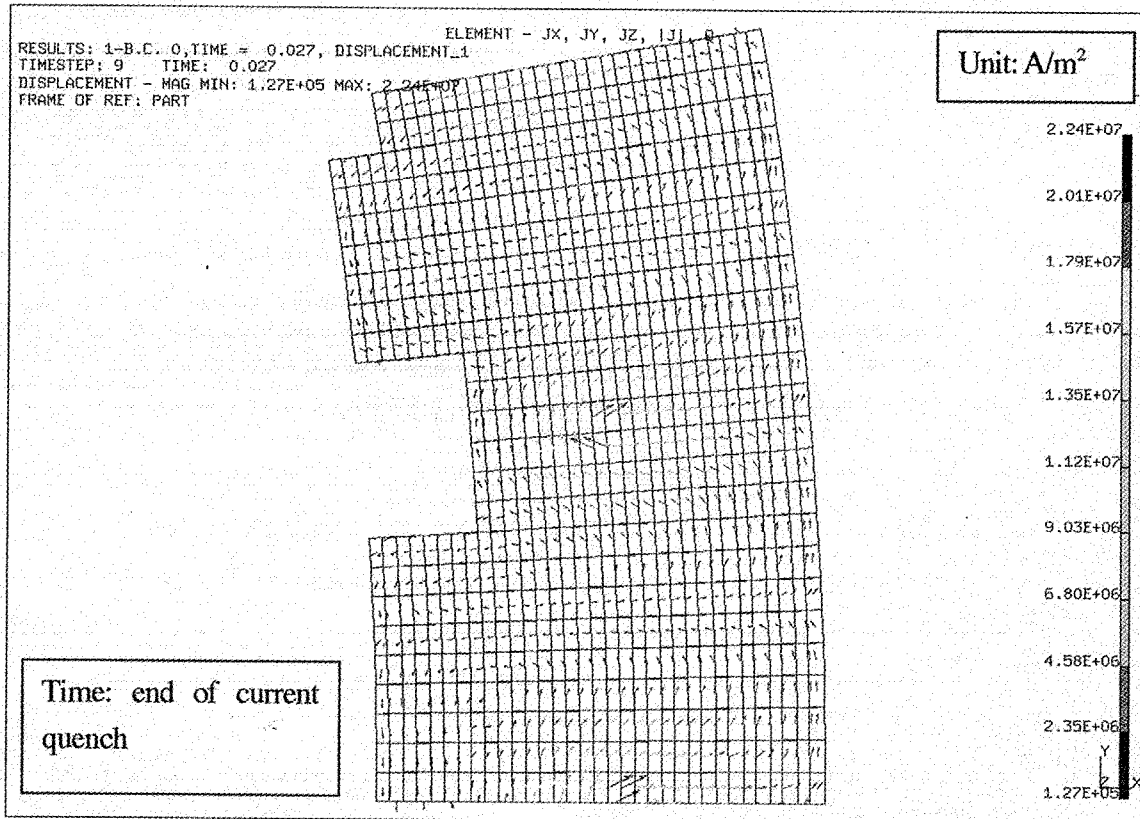


Fig. 4.3-18 Eddy current distribution on horizontal cross-section 1 of module #1

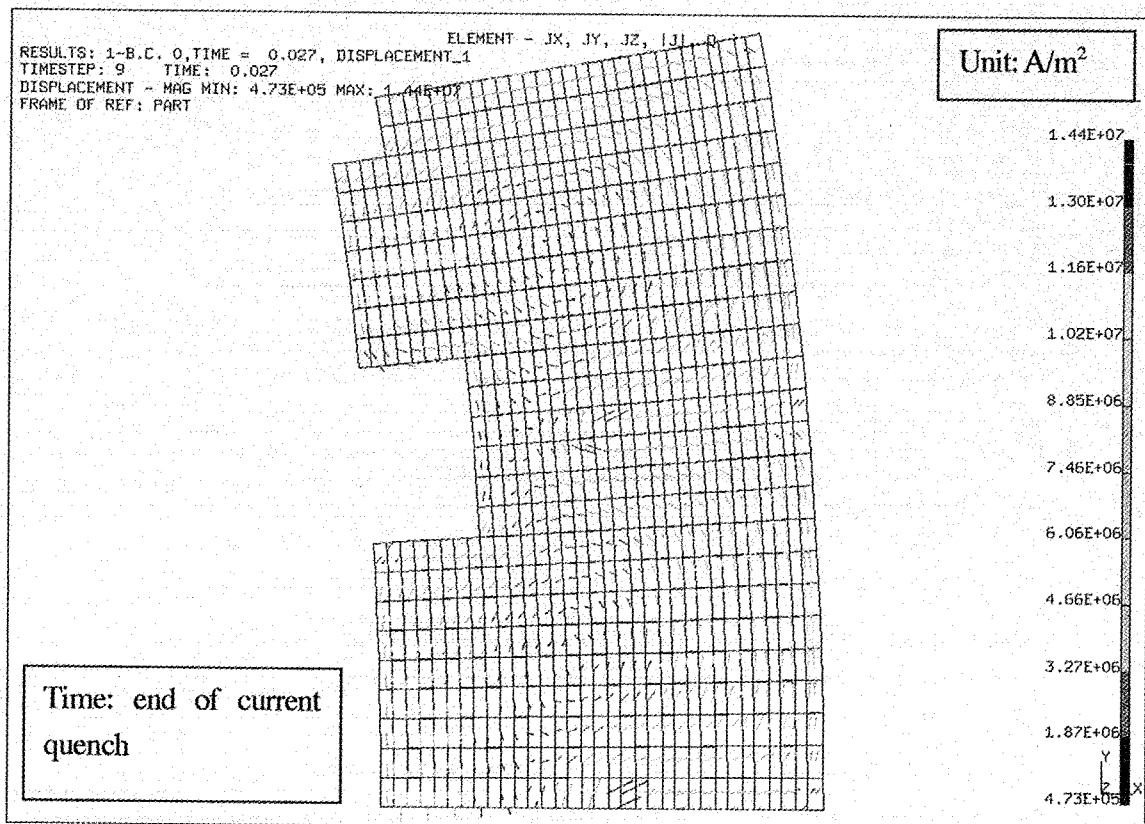


Fig. 4.3-19 Eddy current distribution on horizontal cross-section 2 of module #1

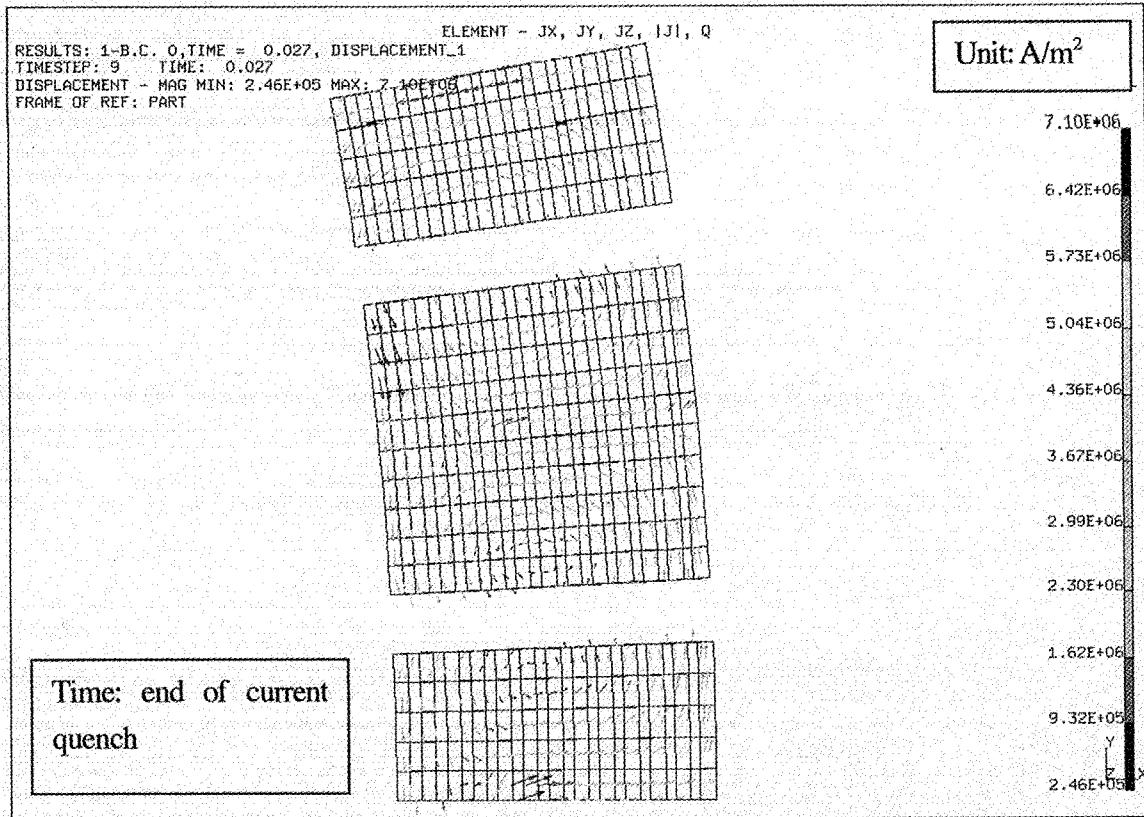


Fig. 4.3-20 Eddy current distribution on horizontal cross-section 3 of module #1

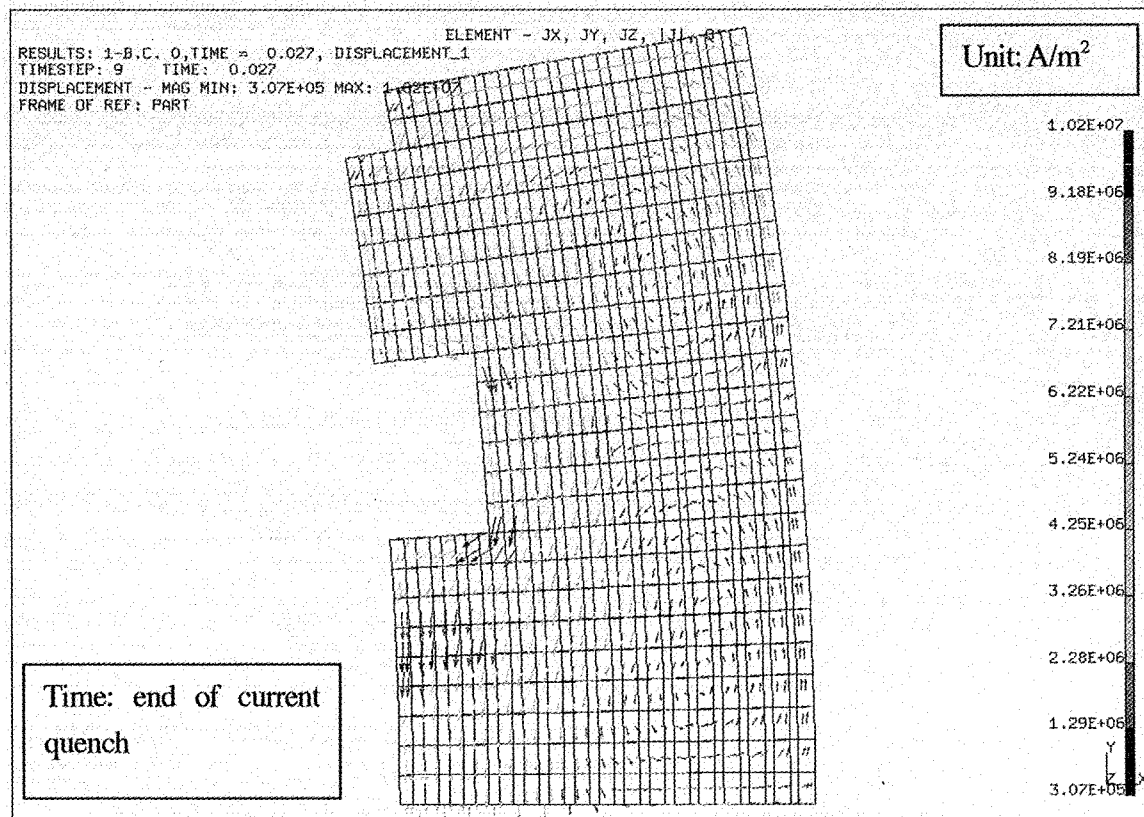


Fig. 4.3-21 Eddy current distribution on horizontal cross-section 4 of module #1

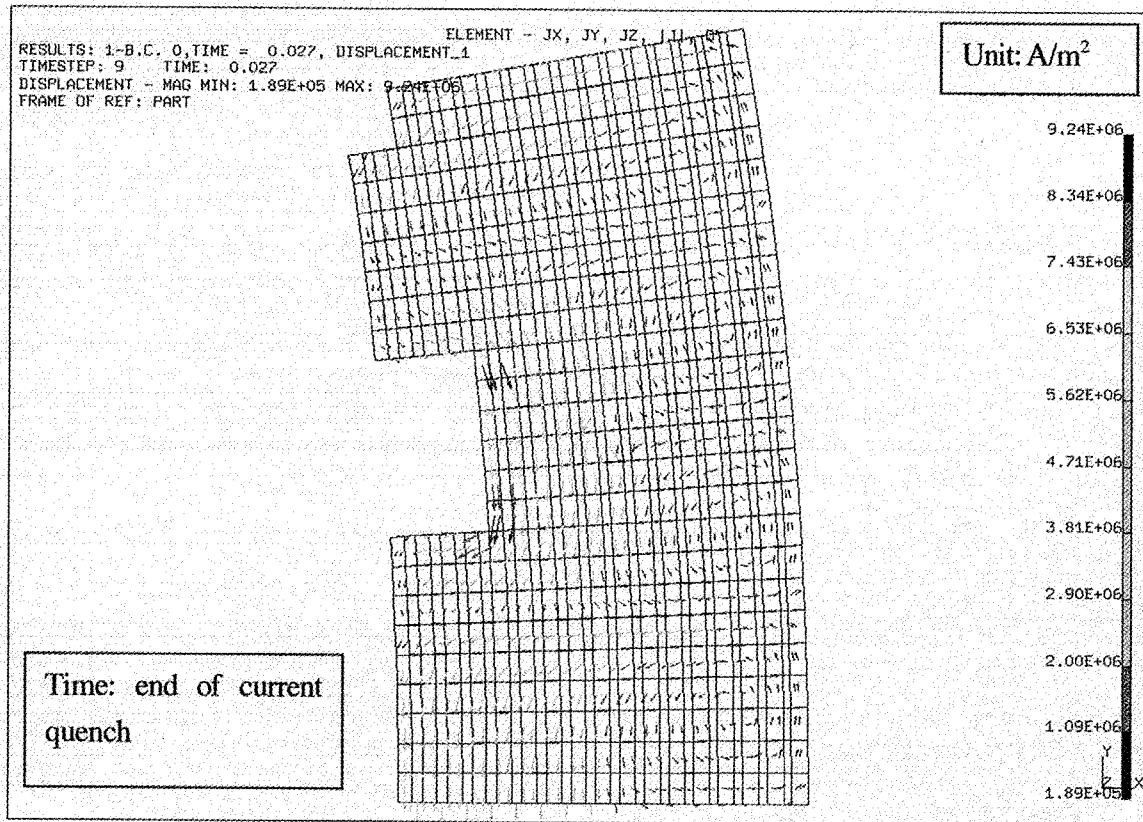


Fig. 4.3-22 Eddy current distribution on horizontal cross-section 5 of module #1

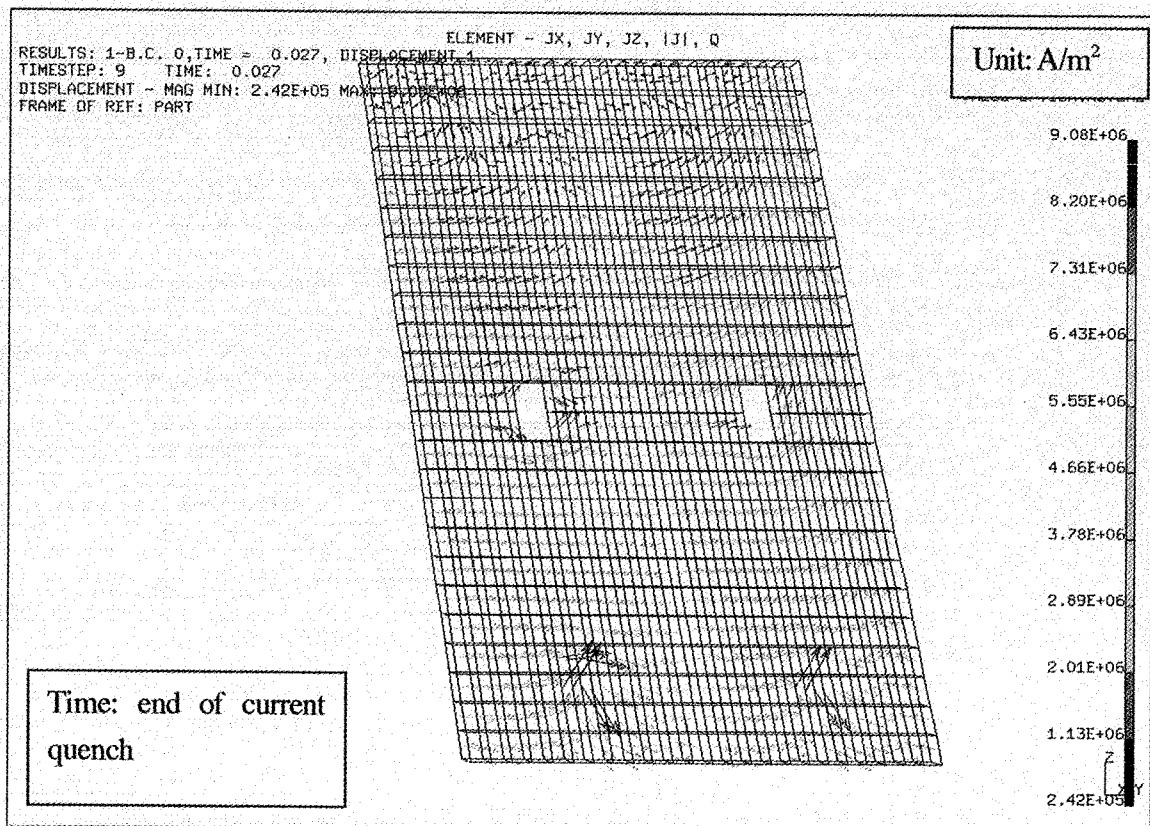


Fig. 4.3-23 Eddy current distribution on vertical cross-section 3 of module #1

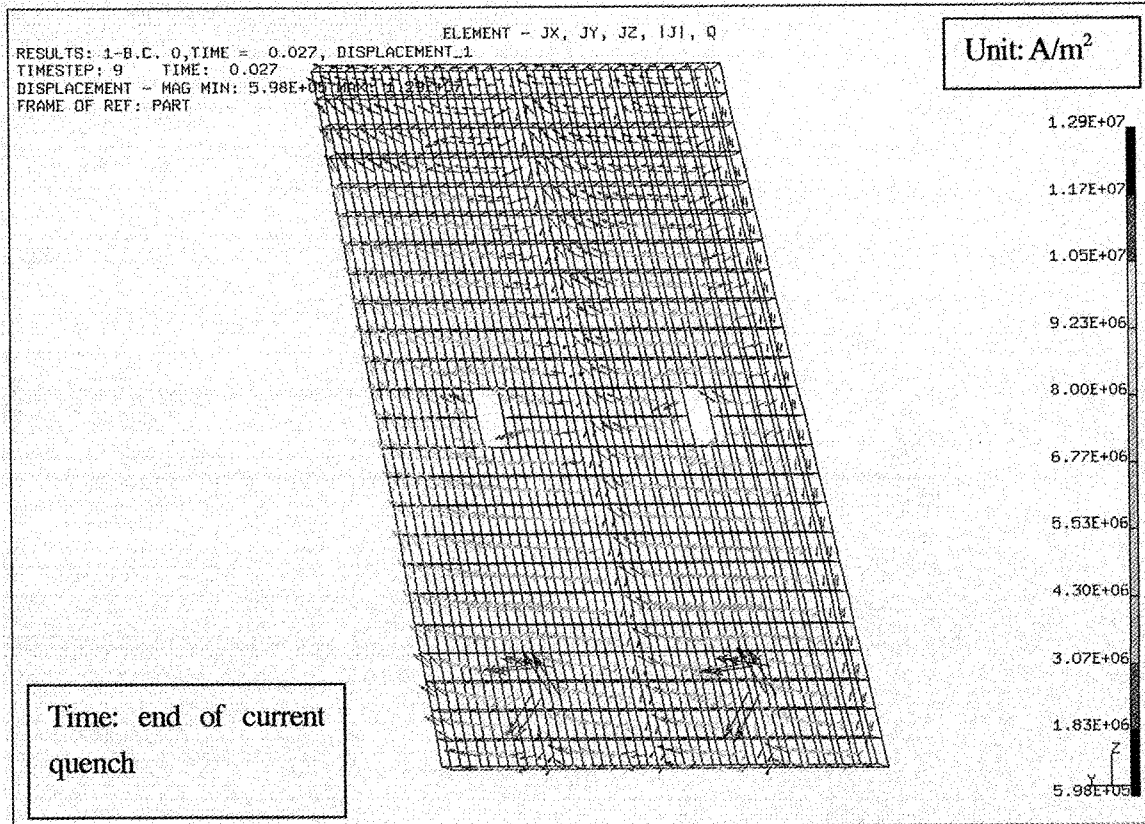


Fig. 4.3-24 Eddy current distribution on vertical cross-section 4 of module #1

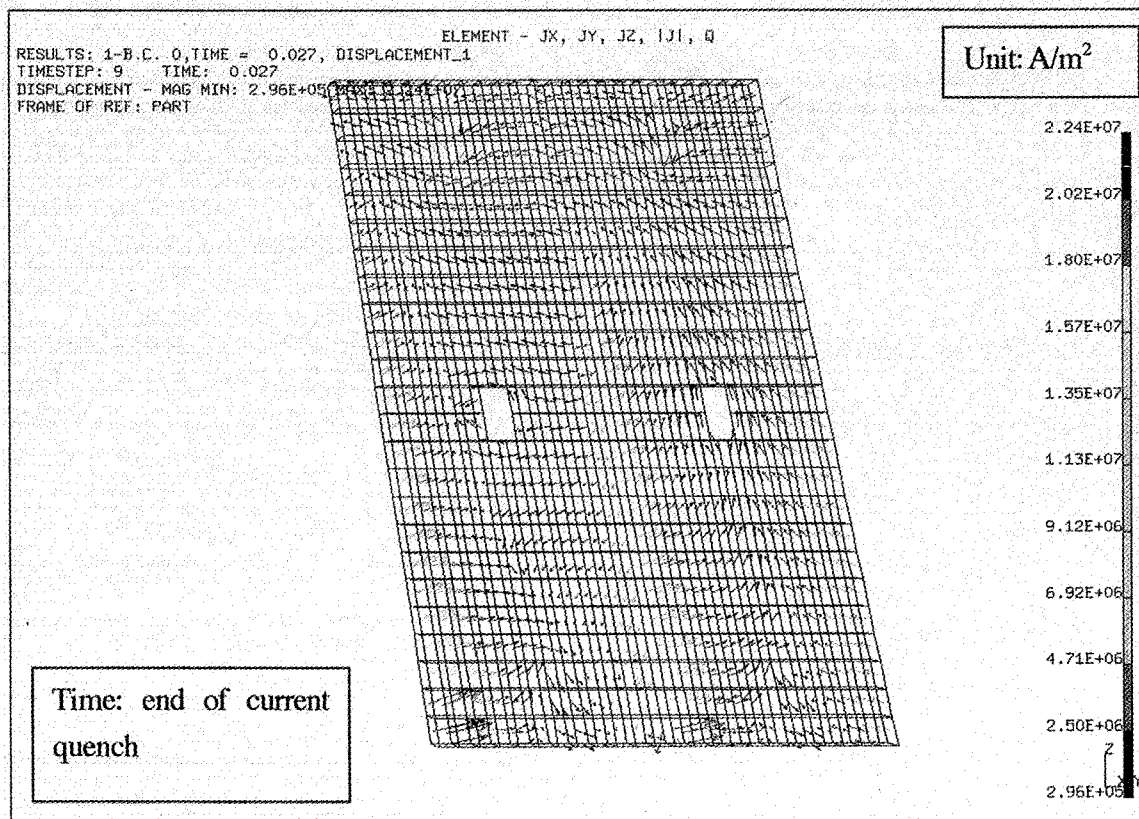


Fig. 4.3-25 Eddy current distribution on vertical cross-section 3 of module #1

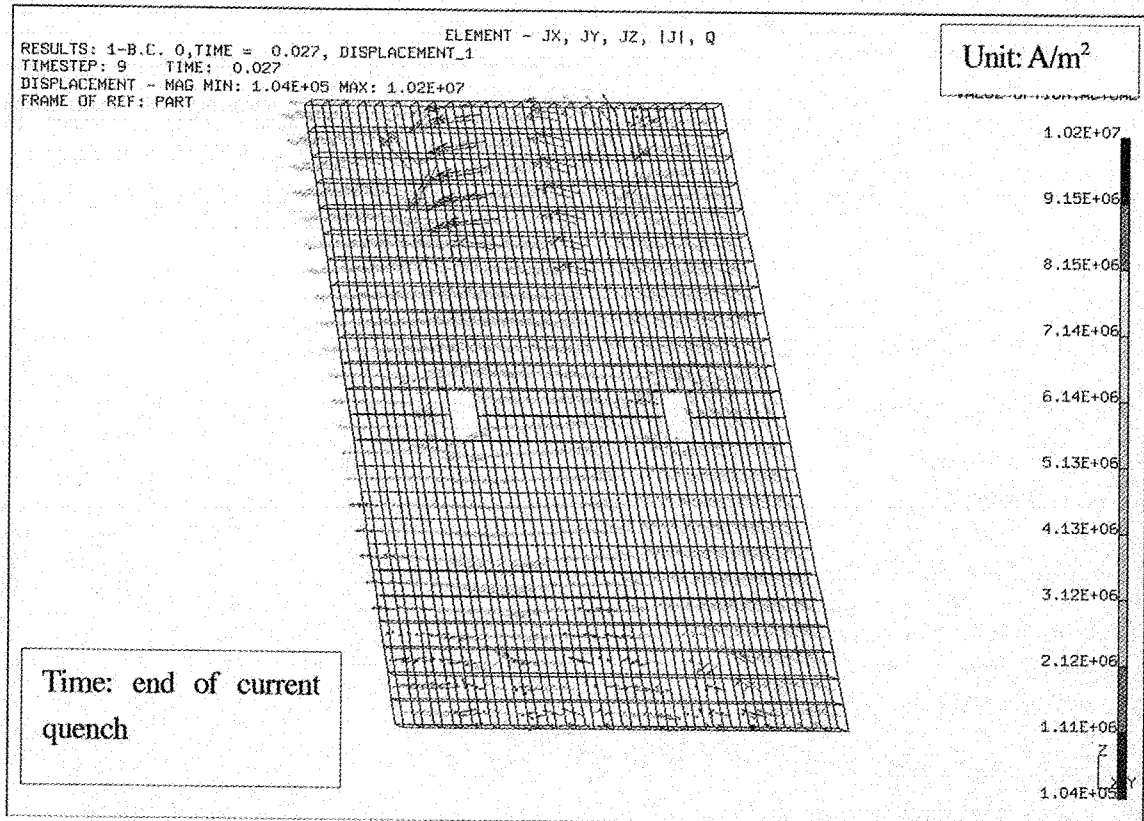


Fig. 4.3-26 Eddy current distribution on vertical cross-section 4 of module #1

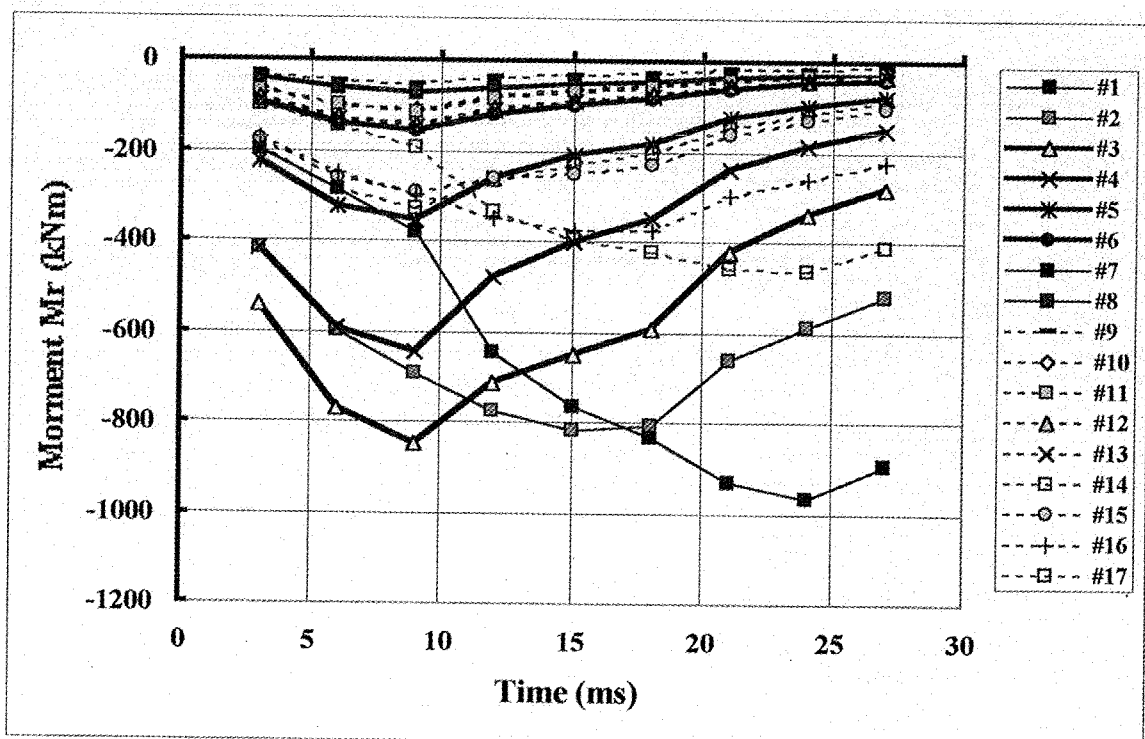


Fig. 4.3-27 Moment Mr on modules under VDE/F-DIII as a function of time
 (Starting current quench is shown as 0 ms)

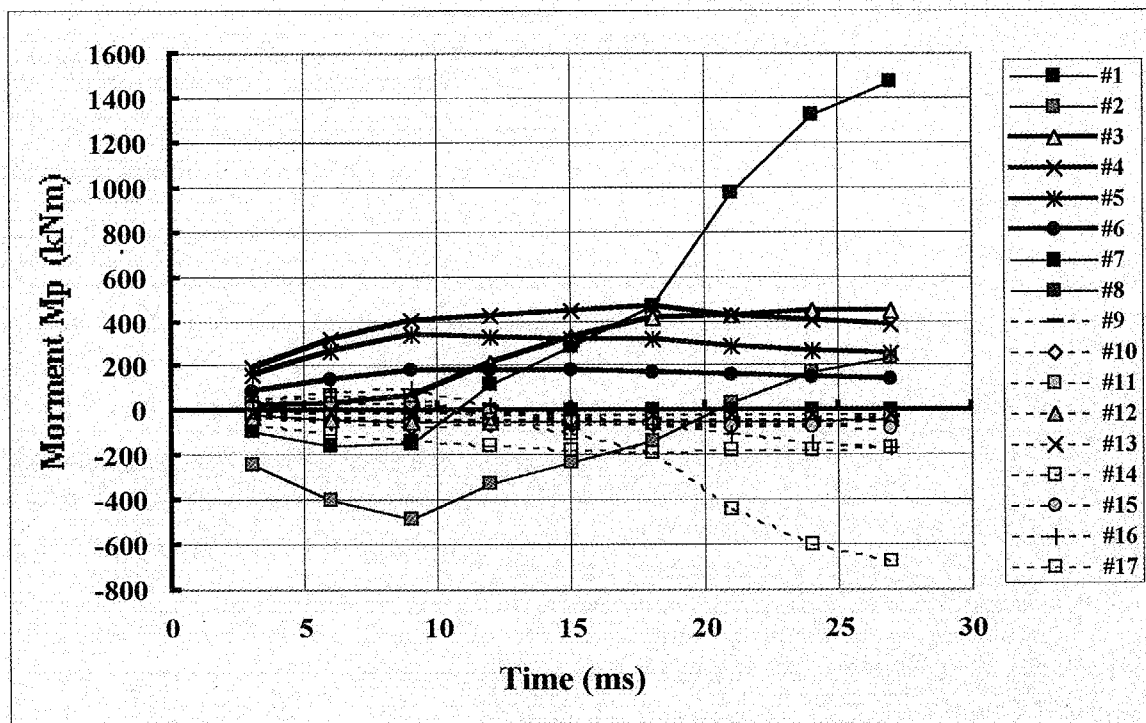


Fig. 4.3-28 Moment M_p on modules under VDE/F-DIII as a function of time
(Starting current quench is shown as 0 ms)

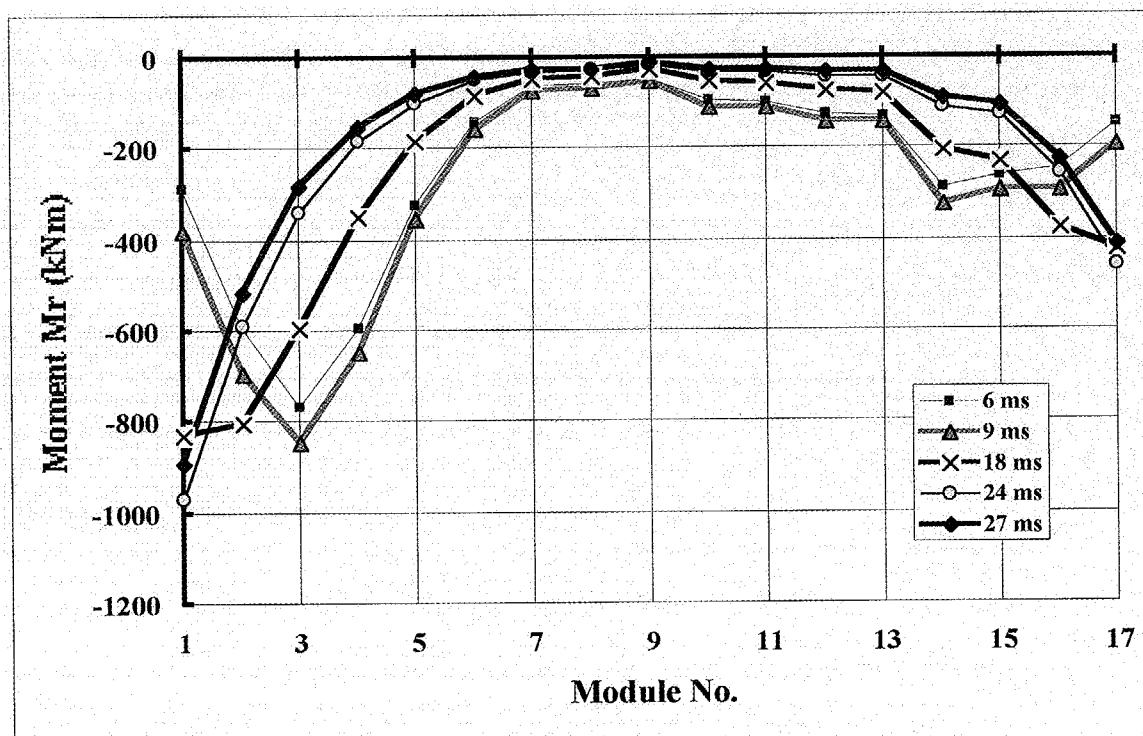


Fig. 4.3-29 Moment M_r on modules under VDE/F-DIII
(Starting current quench is shown as 0 ms)

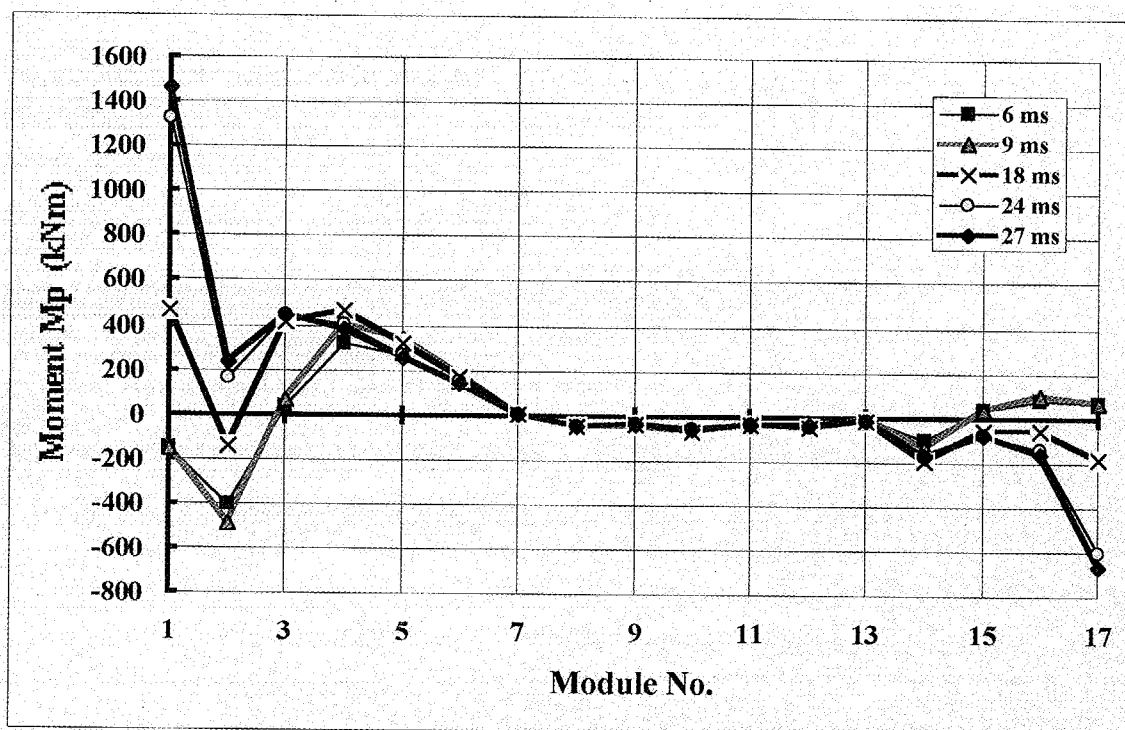


Fig. 4.3-30 Moment M_p on modules under VDE/F-DIII
(Starting current quench is shown as 0 ms)

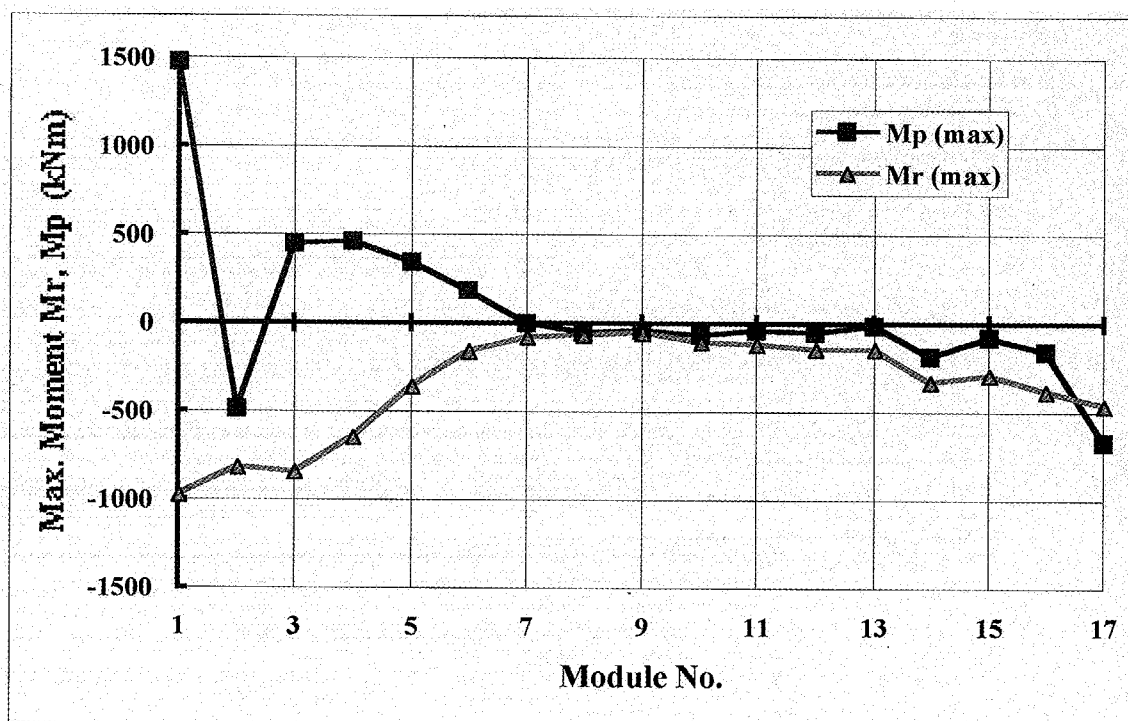


Fig. 4.3-31 Maximum moment on modules under VDE/F-DIII

4.4 Fast upward VDE (VDE/F-U)

4.4.1 Analysis method

4.4.1.1 Model of plasma movement

The plasma current of the fast upward VDE III (VDE/F-UIII) is shown in Fig. 4.4-1. According to the disruption scenario, the plasma starts to move upward, and then thermal quench occurs at 525 ms. The plasma current increases from 14.9 MA up to 17.3 MA at 528 ms due to thermal quench. The plasma current decreases to 0 MA at 555 ms. The plasma current densities during VDE/F-UIII are shown in Figs. 4.4-2 to 4.4-5. The plasma center position moves as shown in Figs. 4.4-6 and 4.4-7.

In the EM analysis, the plasma current change and movement during thermal and current quench are taken into account. Initial plasma current in the analysis is 14.9 MA at 525 ms before the thermal quench. The plasma movement is simulated using the filament current change in the plasma area.

4.4.1.2 Mesh model

Seventeen blankets in the poloidal cross section are modeled by the solid meshes same as the model for the centered disruption, as shown in Figs. 4.2.1-12 to 4.2.1-16. Some detail meshes are used for the blanket modules from #4 to #6 in this analysis in order to calculate the correct eddy current due to plasma upward movement.

4.4.2 Analysis results

Figure 4.4-8 shows magnetic flux density distribution due to eddy current at the end of current quench. Eddy current distribution in module #5 is shown in Fig. 4.4-9. EM force distribution on modules is shown in Fig. 4.4-10.

Moments induced in the shield blankets are shown in Tables 4.4-1 and 4.4-2. Figures 4.4-11 and 4.4-12 show the time history of moment M_r and M_p on the modules, respectively. Figures 4.4-13 and 4.4-14 show the poloidal distribution of M_r and M_p on modules. The maximum moment of each blanket module is shown in Fig. 4.4-15. Both moment of M_r and M_p are the largest at the end of current quench. The maximum moment M_r is 1360 kNm on module #5, and the maximum moment M_p is 660 kNm on module #6. Non-linear plasma current decay at the end of current quench as shown in Fig. 4.4-1 produces the higher moment comparing with linear decay. Maximum moment for the linear current decay will be smaller than the calculated value.

Table 4.4-1 Moment Mr (kNm) on shield block for VDE/F-UIII
(Starting current quench is shown as 0 ms)

Module No.	0 ms	6 ms	9 ms	12 ms	18 ms	24 ms	27 ms	Max
1	761	-251	-416	-379	-405	-256	-226	761
2	1001	-323	-554	-626	-681	-457	-410	1001
3	985	-330	-576	-825	-1005	-821	-768	-1005
4	551	-215	-360	-611	-798	-1019	-1014	-1019
5	427	-120	-223	-379	-542	-1302	-1361	-1361
6	427	-30	-104	-169	-271	-1090	-1165	-1165
7	262	-3	-49	-80	-140	-699	-765	-765
8	153	-22	-55	-79	-130	-653	-729	-729
9	-16	-46	-52	-62	-92	-404	-427	-427
10	-238	-125	-114	-134	-173	-522	-555	-555
11	-245	-130	-117	-146	-179	-346	-362	-362
12	-226	-151	-145	-190	-230	-291	-294	-294
13	-126	-124	-129	-169	-202	-195	-189	-202
14	-42	-191	-229	-290	-342	-276	-259	-342
15	128	-128	-178	-206	-227	-155	-139	-227
16	251	-124	-192	-201	-210	-136	-120	251
17	290	-121	-178	-161	-150	-87	-75	290

Table 4.4-2 Moment Mp (kNm) on shield block for VDE/F-UIII
(Starting current quench is shown as 0 ms)

Module No.	0 ms	6 ms	9 ms	12 ms	18 ms	24 ms	27 ms	Max
1	-236	80	125	90	57	10	-2	-236
2	181	4	-74	-237	-458	-528	-552	-552
3	-200	-18	30	-84	-227	-536	-622	-622
4	-253	21	112	199	286	-332	-490	-490
5	-24	124	185	332	493	136	50	493
6	-61	41	89	177	299	565	664	664
7	-22	-29	-27	-20	-19	-127	-149	-149
8	-75	-79	-86	-98	-126	-399	-492	-492
9	-157	-104	-97	-104	-118	-204	-231	-231
10	-184	-132	-126	-145	-168	-85	-58	-184
11	-16	-37	-44	-65	-87	1	24	-87
12	32	-7	-21	-41	-63	29	56	-63
13	96	52	44	52	63	104	117	117
14	235	105	70	78	91	158	182	235
15	100	66	59	79	104	116	121	121
16	66	40	39	61	94	103	108	108
17	135	-29	-51	-34	-19	4	9	135

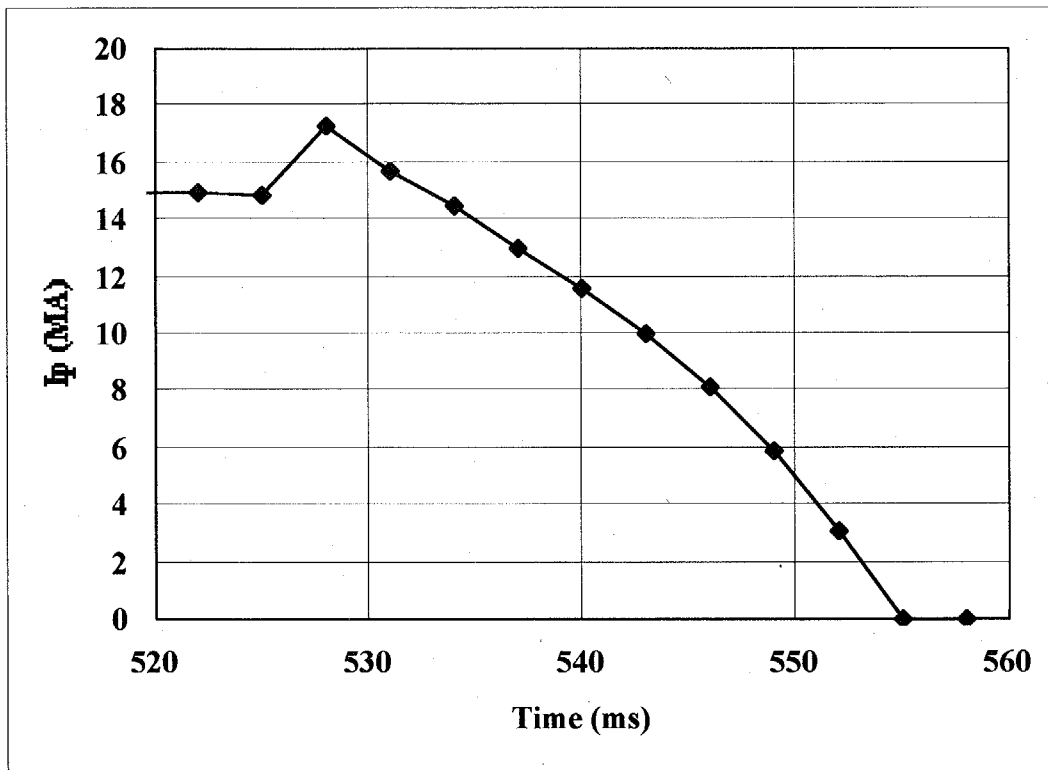


Fig. 4.4-1 Plasma current under VDE/F-UIII (Starting current quench is 528 ms)

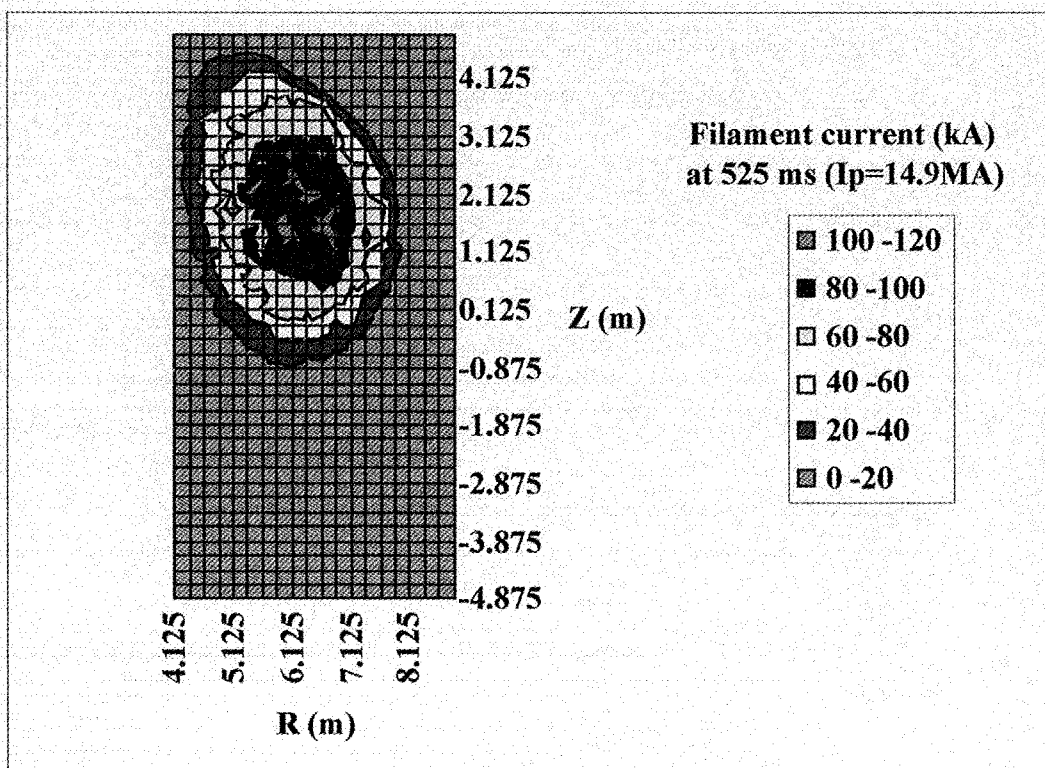


Fig. 4.4-2 Plasma current density before thermal quench under VDE/F-UIII

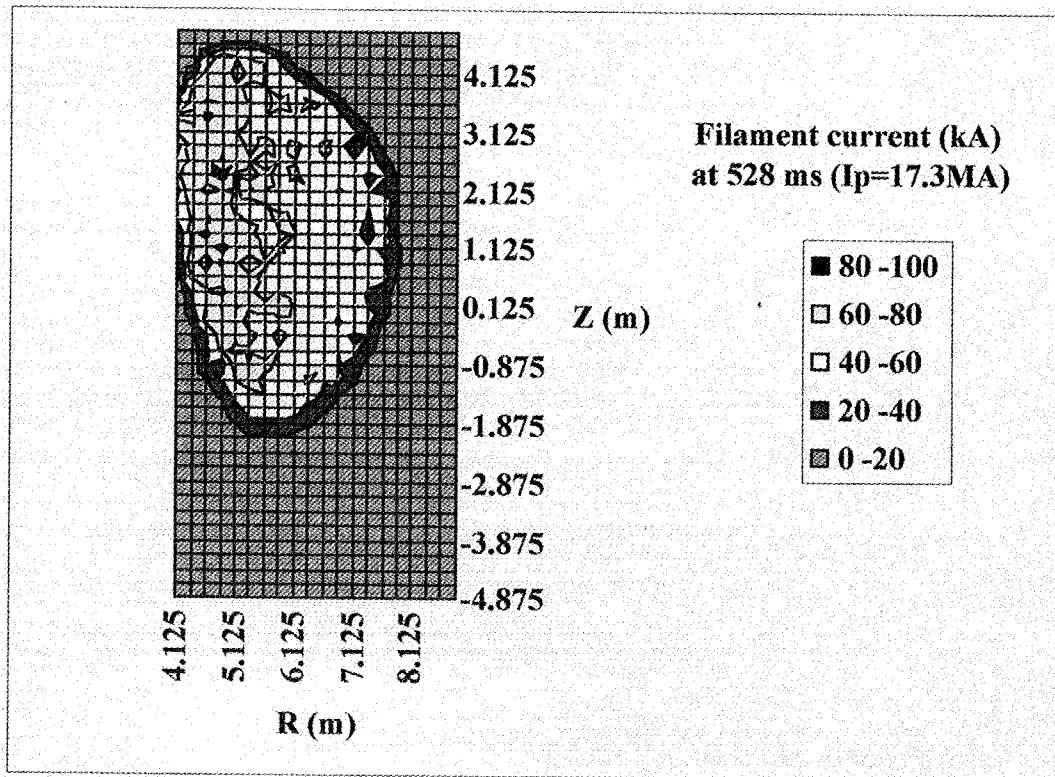


Fig. 4.4-3 Plasma current density just after thermal quench under VDE/F-UIII

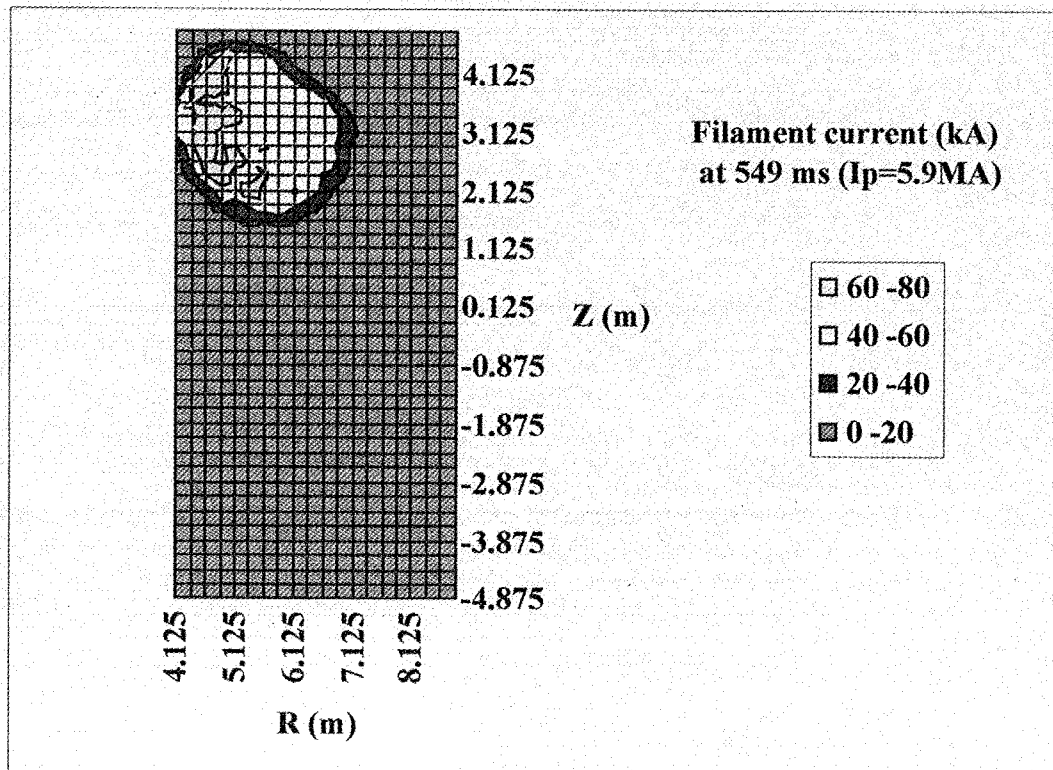


Fig. 4.4-4 Plasma current density at 21 ms during current quench under VDE/F-UIII

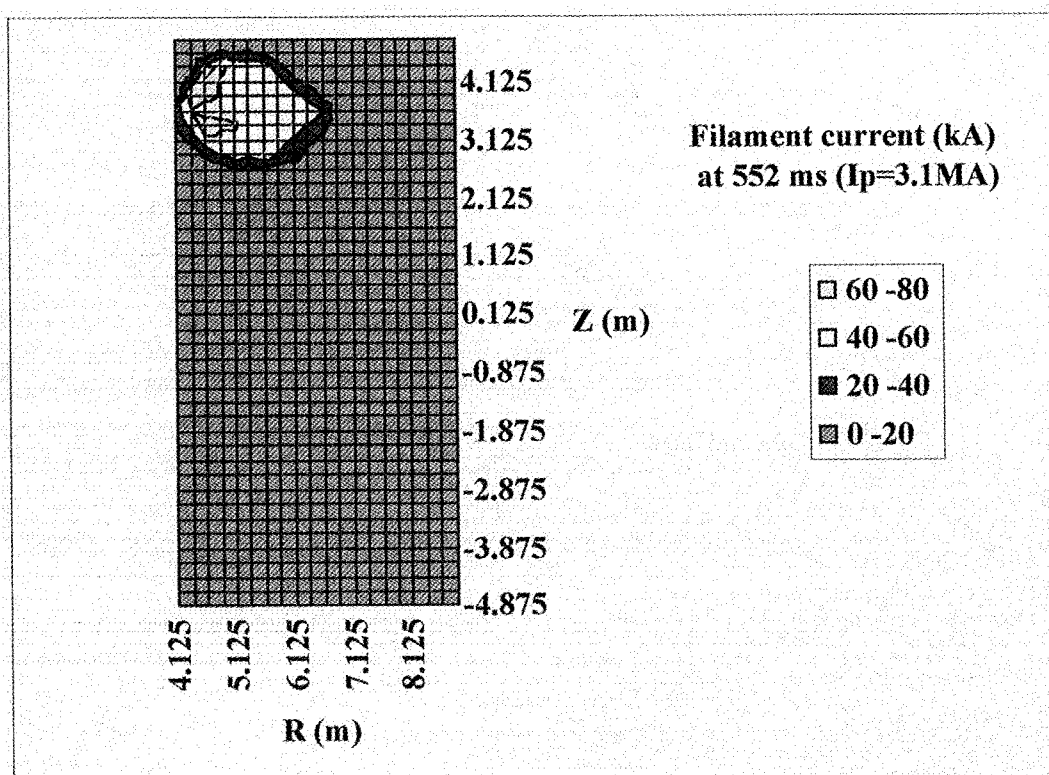


Fig. 4.4-5 Plasma current density at 24 ms during current quench under VDE/F-UIII

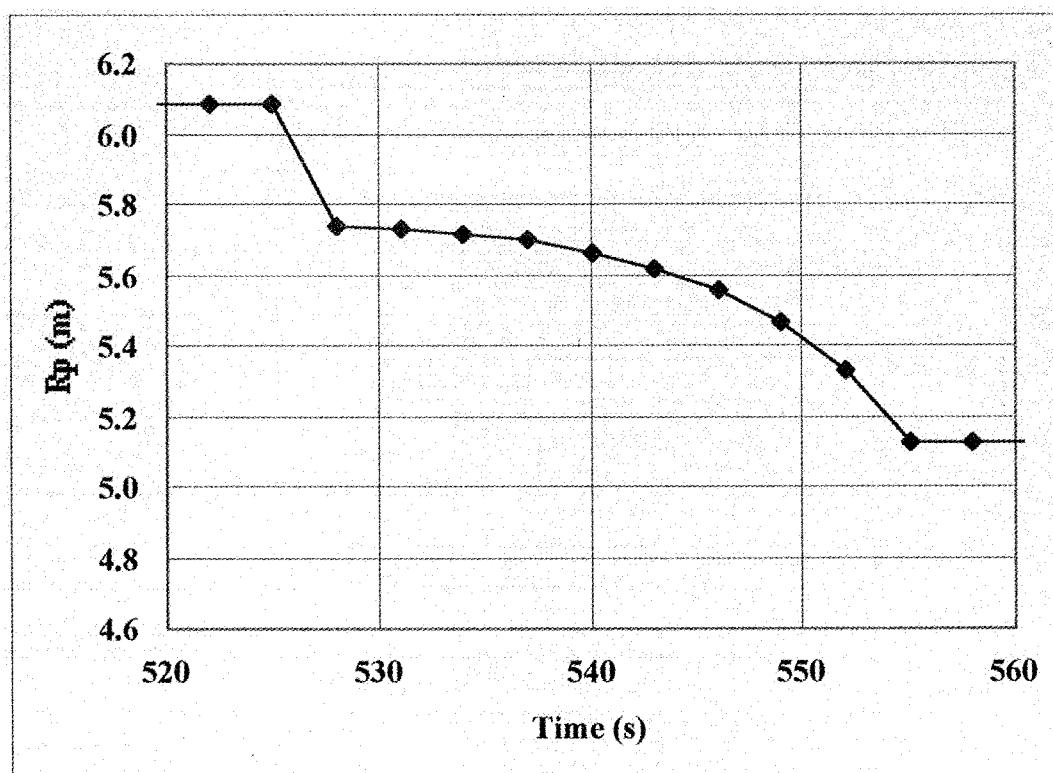


Fig. 4.4-6 Plasma position R_p under VDE/F-UIII (Starting current quench is 528 ms)

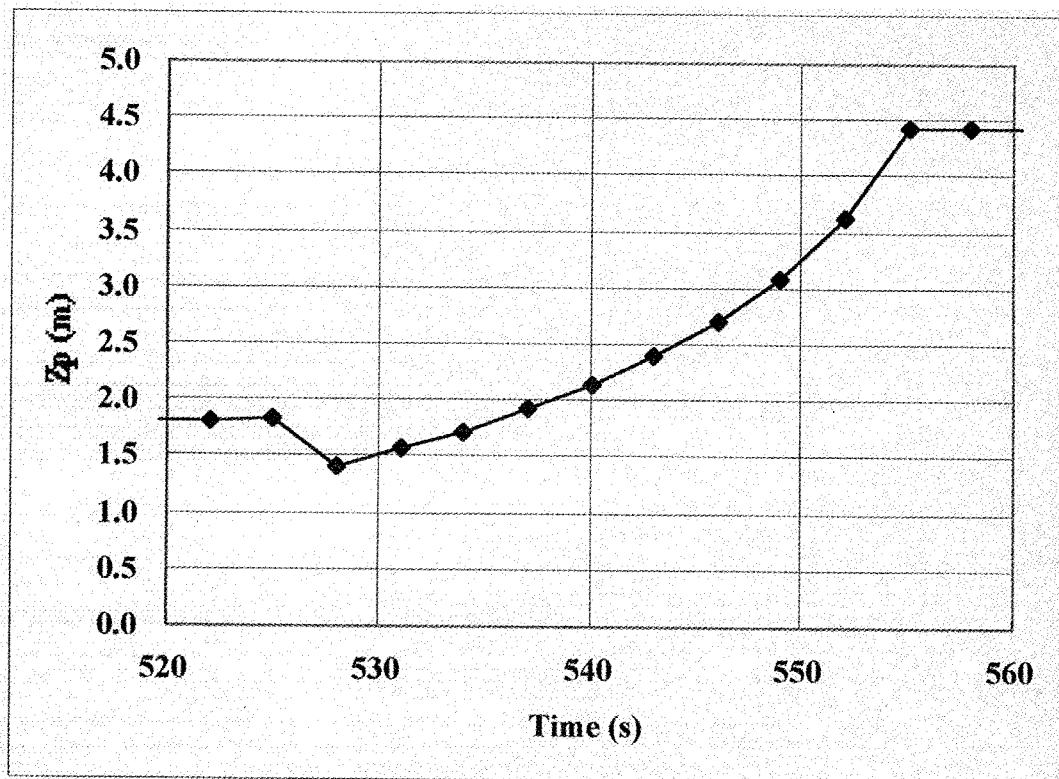


Fig. 4.4-7 Plasma position Z_p under VDE/F-UIII (Starting current quench is 528 ms)

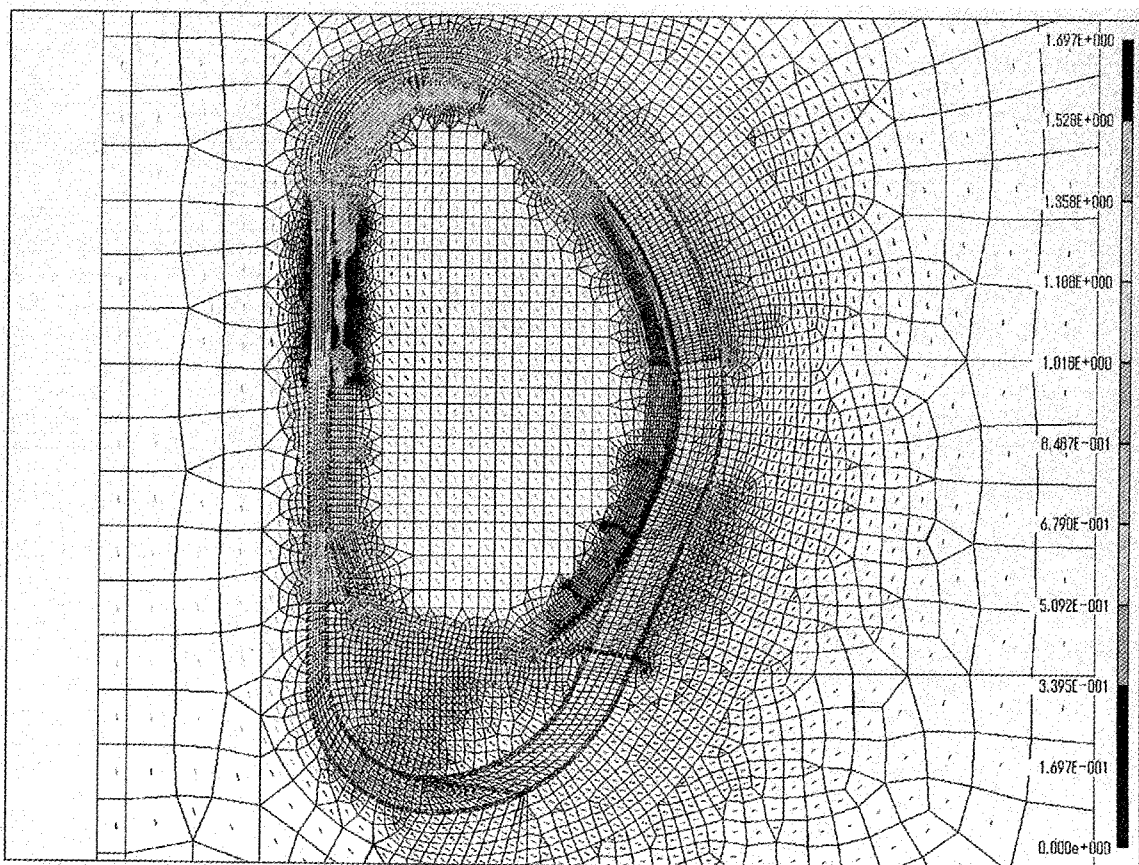


Fig. 4.4-8 Magnetic field due to eddy current at the end of current quench under VDE/F-UIII

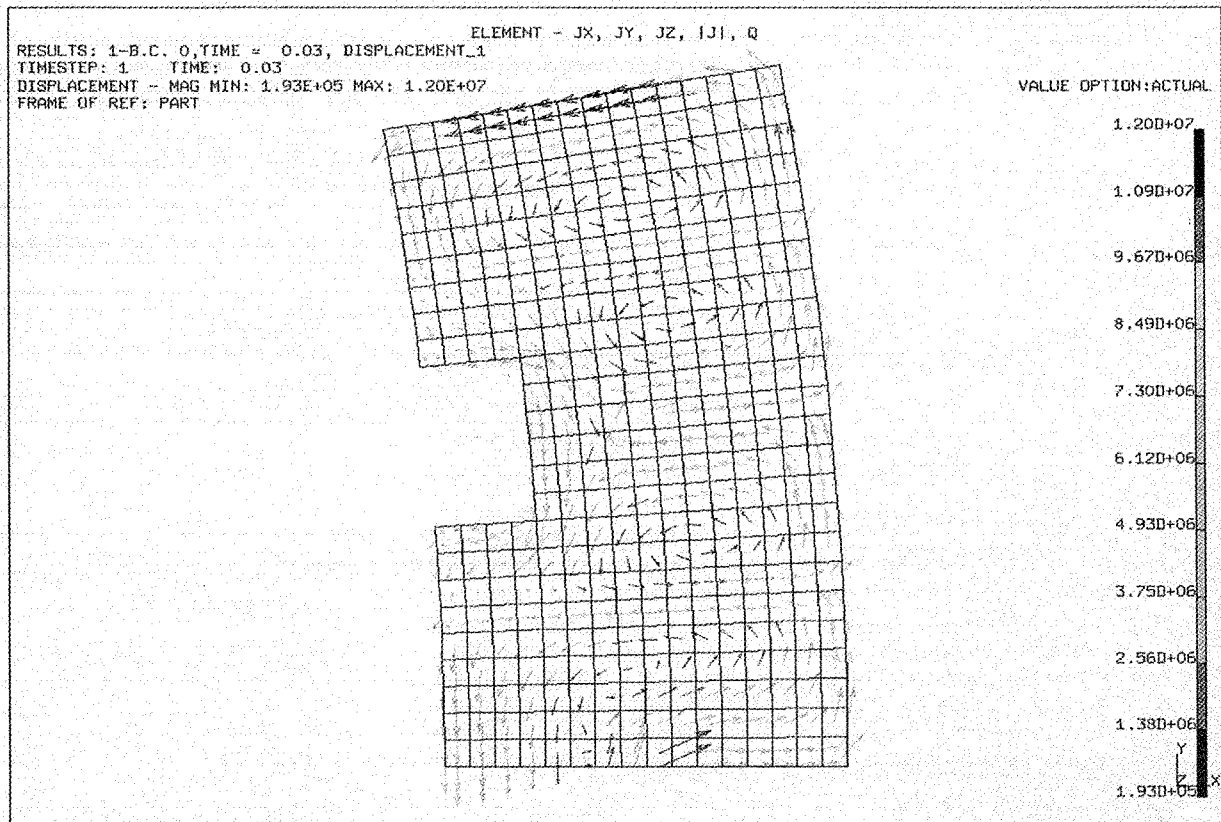


Fig. 4.4-9 Eddy current in module #5 at the end of current quench under VDE/F-UIM

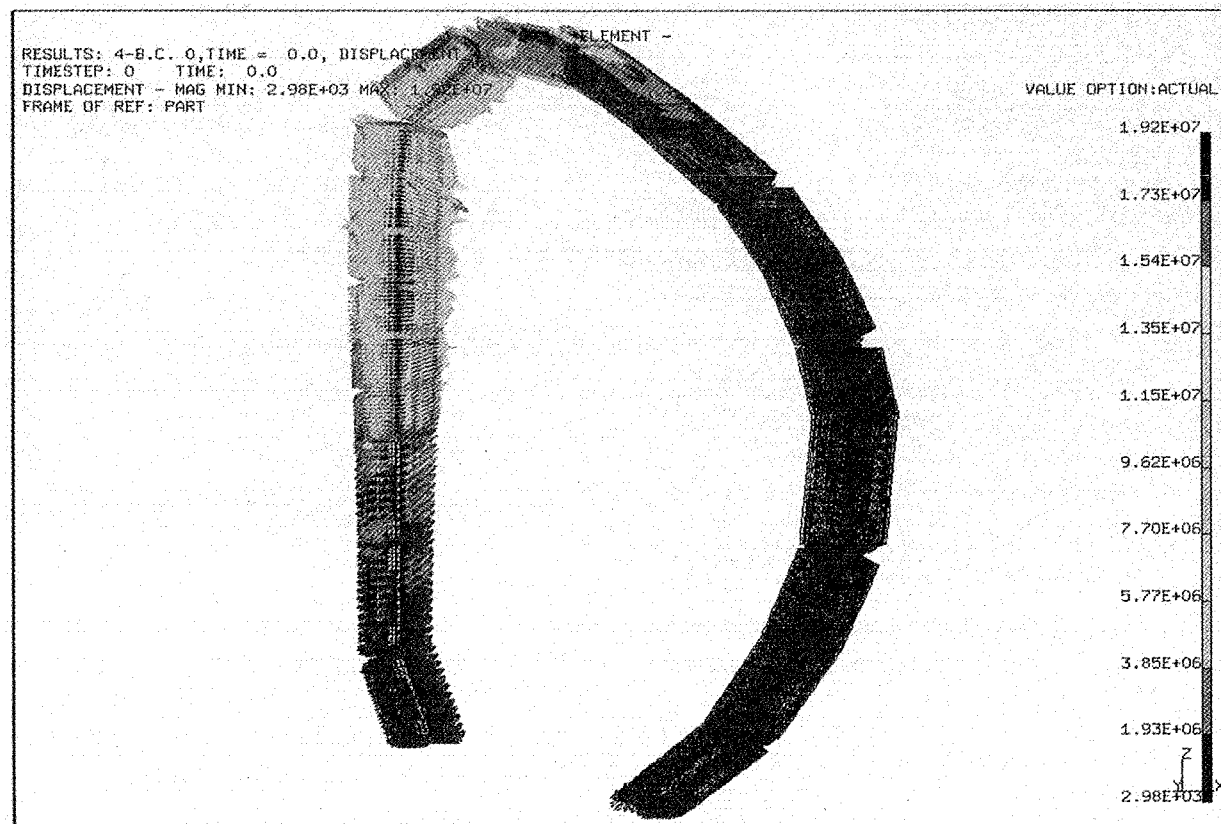


Fig. 4.4-10 EM force in modules at the end of current quench under VDE/F-UIM

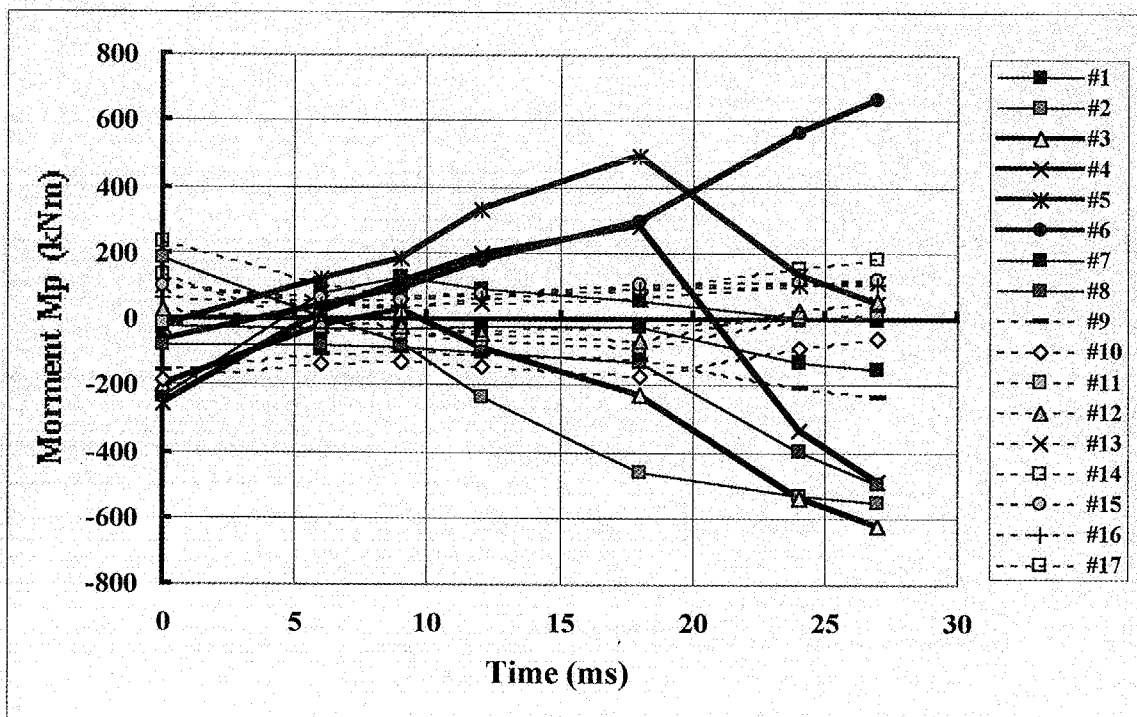
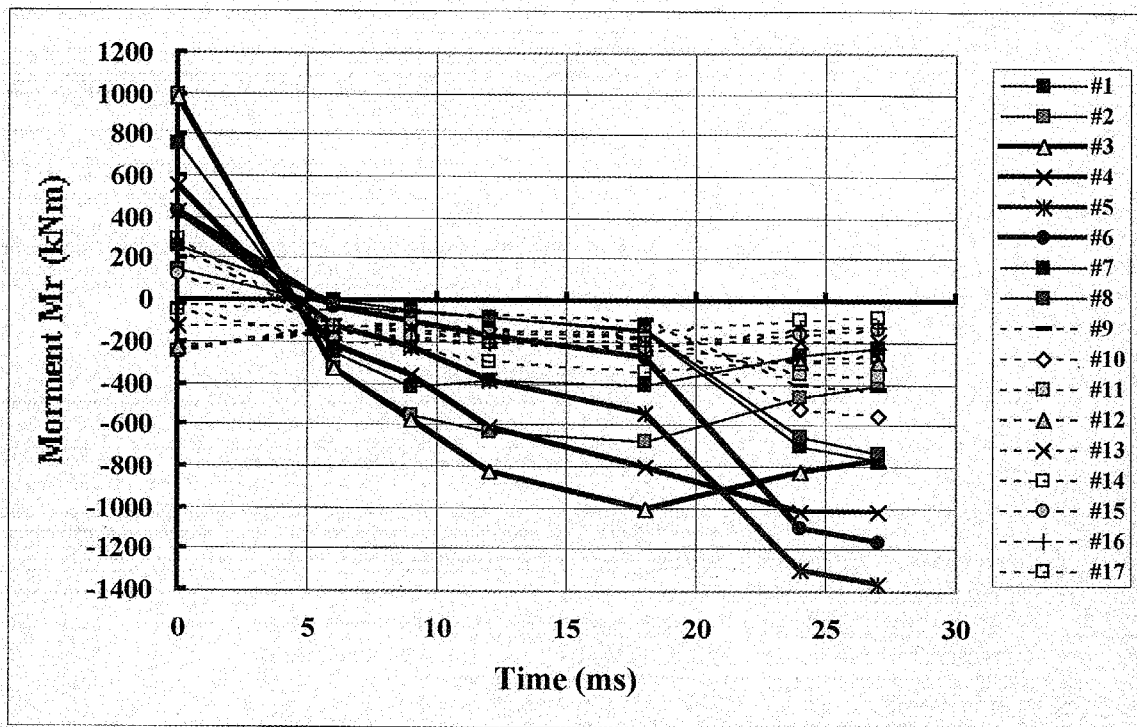


Fig. 4.4-12 Moment Mp on modules under VDE/F-UIII as a function of time
(Starting current quench is shown as 0 ms)

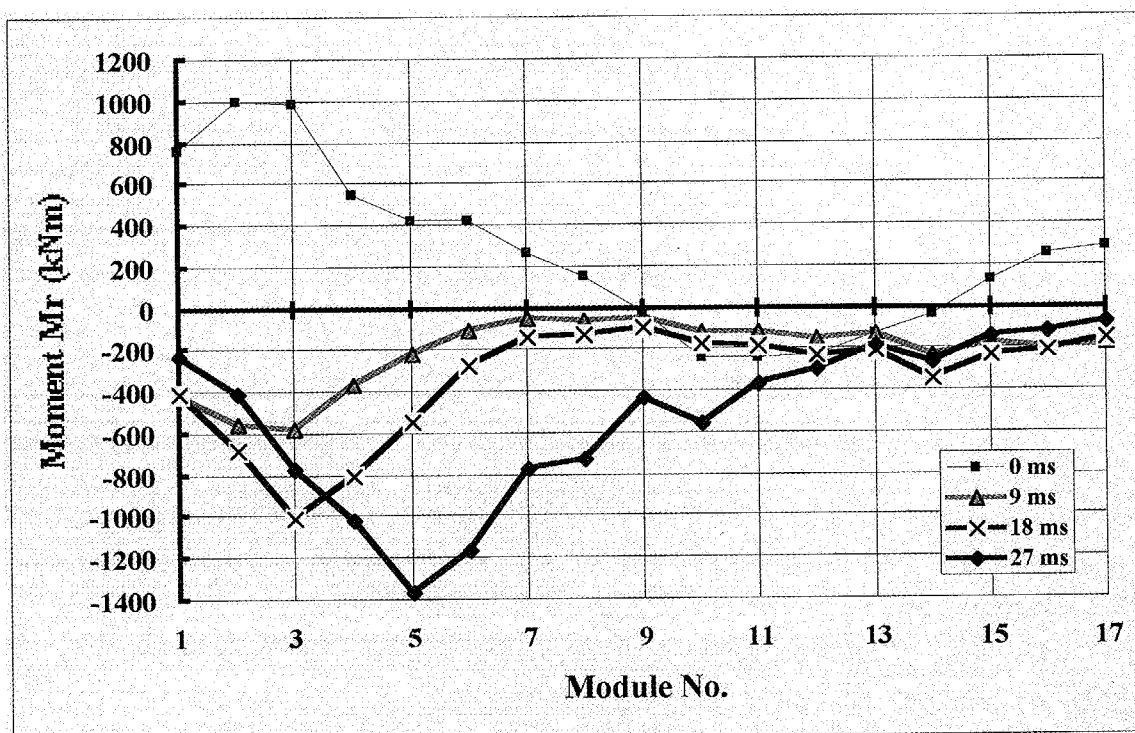


Fig. 4.4-13 Moment Mr on modules under VDE/F-UIII
(Starting current quench is shown as 0 ms)

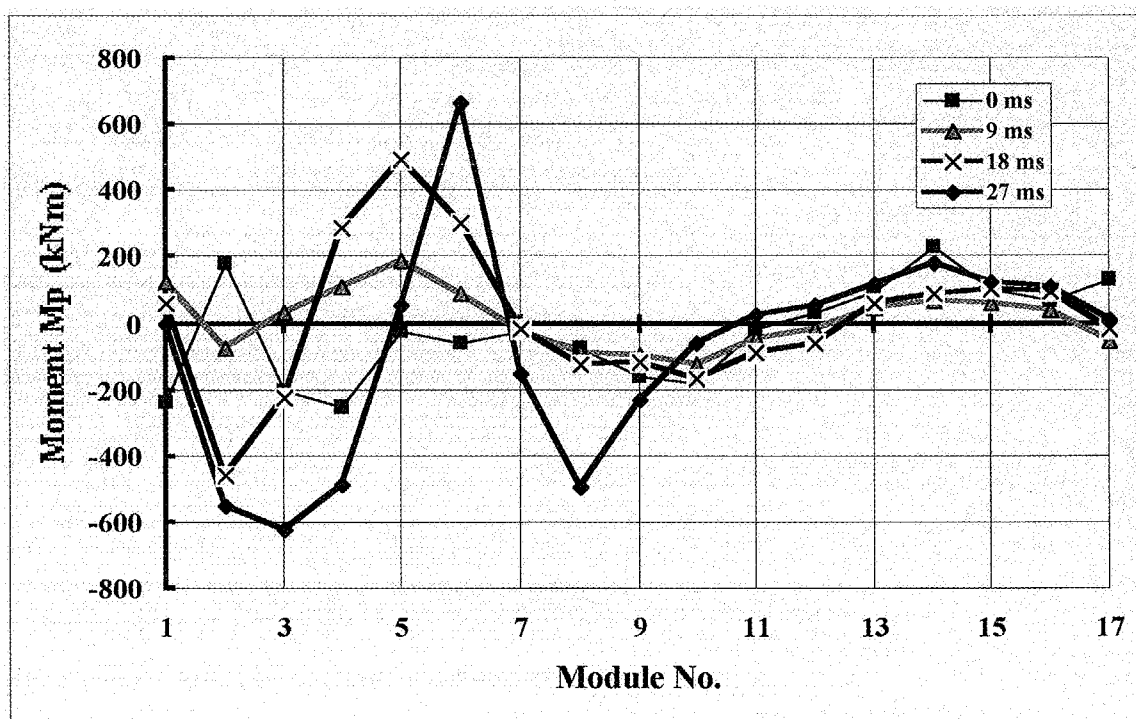


Fig. 4.4-14 Moment Mp on modules under VDE/F-UIII
(Starting current quench is shown as 0 ms)

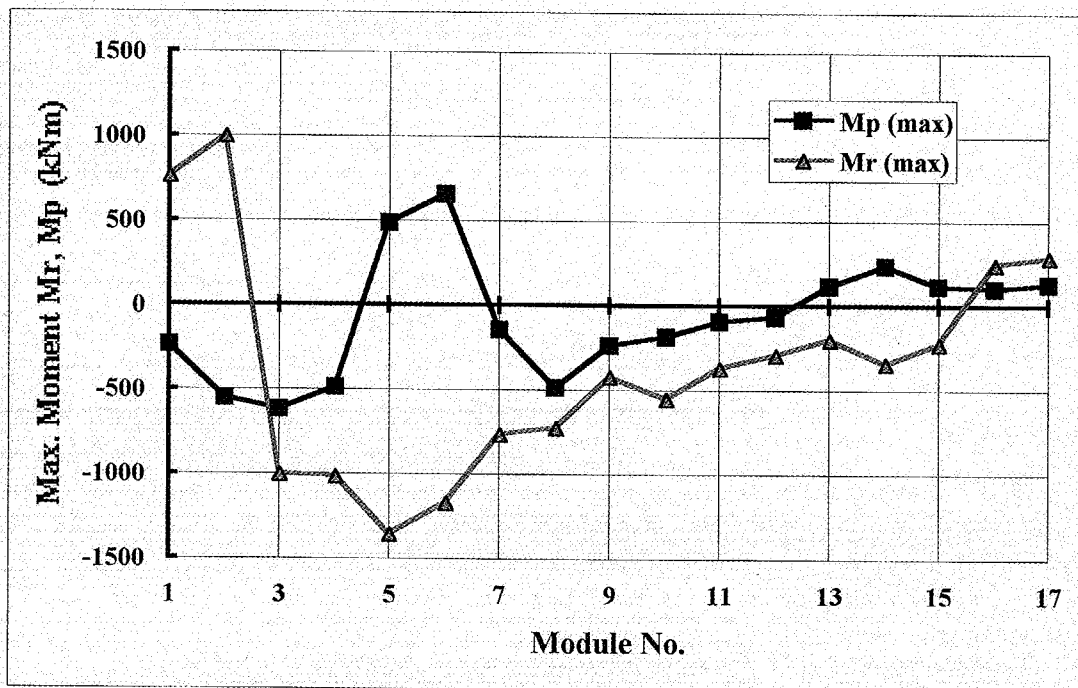


Fig. 4.4-15 Maximum moment on modules under VDE/F-UIII

4.5 Conclusions

The EM analyses for centered disruption II (CDII), fast downward VDE III (VDE/F-DIII), and fast upward VDE III (VDE/F-UIII) are conducted for all blankets in the poloidal cross section. The shield blocks are modeled by solid elements in order to consider the slit effect on the eddy current flow in the blanket structures. The cooling tubes in the shield blocks are modeled by equivalent material properties.

In order to confirm the validity of equivalent material properties, the analysis for a precise solid model of module #5 are performed under the CDII. The cooling tubes and slits are precisely modeled including first walls. The upper and lower blankets and VV walls are also included to consider the shielding effect of these structures. The analysis of the precise model shows the good agreement with the analysis results of equivalent property model, resulting in confirming the validity of the equivalent model.

The eddy current and EM force have been calculated under the disruption. The maximum loads on the module are summarized in Table 4.5-1. The maximum moment around radial axis (Mr) is -1.36 MNm under the VDE/F-UIII, and that around vertical axis (Mp) is 1.47 MNm under VDE/F-DIII.

Table 4.5-1 Maximum EM loads on the shield block

		Max. moment	Time after current quench	Module No.
CDII	Mr(ΔB_z)	-1.059 MNm	16.5 ms	3
	Mp(ΔB_r)	1.119 MNm	16.5 ms	5
VDE/F-DIII	Mr(ΔB_z)	-0.968 MNm	24 ms	1
	Mp(ΔB_r)	1.469 MNm	27 ms	1
VDE/F-UIII	Mr(ΔB_z)	-1.361 MNm	27 ms	5
	Mp(ΔB_r)	0.664 MNm	27 ms	6

5. Design and Structural Analysis on First Wall and Shield Block Attachments

5.1 First wall supporting beam

5.1.1 Supporting beam for separable first wall

A shielding blanket concept with separable first wall (FW) panels shown in Fig.5.1-1 has been proposed for ITER-FEAT. In this section, the FW attachment concepts with a supporting beam extruded from the back of the FW panel have been investigated taking into account withstanding against electromagnetic (EM) forces. The FW attachment structure design with a butt welding (full penetration) at the back of the shield block has been proposed. Simplified stress calculations for the welded joint have been performed to optimize the joint size. In addition, a basic layout of the welded FW attachment at the rear side of the module has been developed.

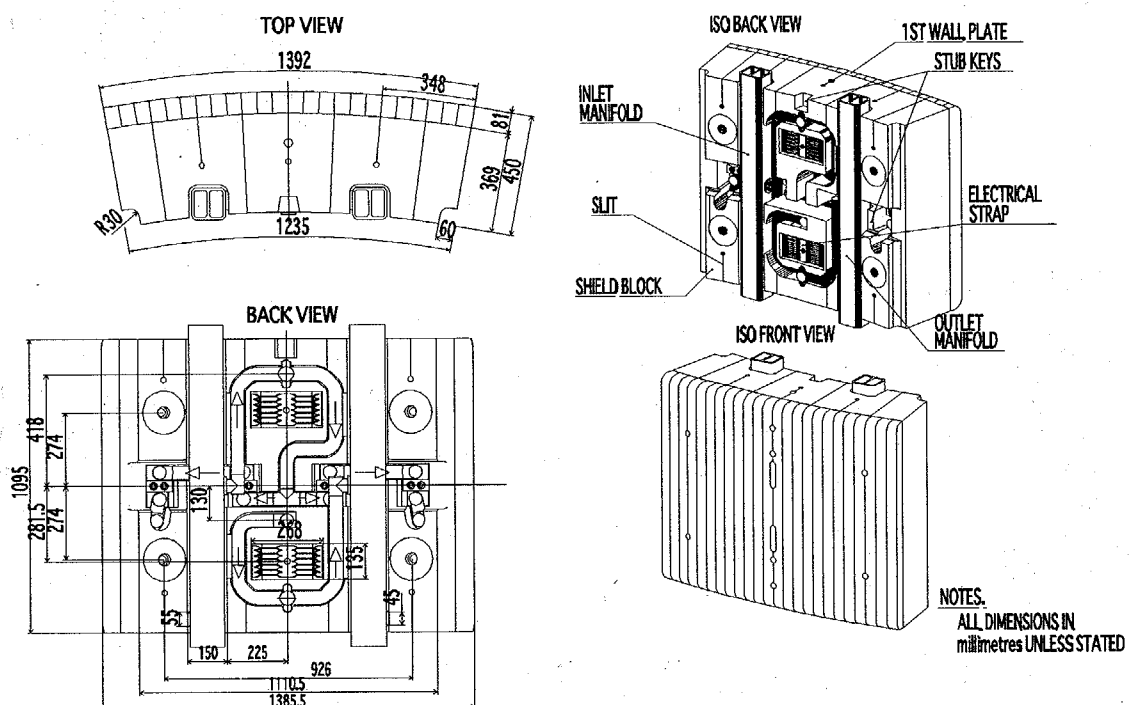


Fig. 5.1-1 Shielding blanket module with separable first wall

5.1.2 Basic design

The basic design for two attachment options, i.e., circular type welding and racetrack type welding for the butt welding attachment are shown in Fig.5.1-2. Both options have a stub structure at the end of the supporting beam. The cooling pipes for the FW are installed in these stub structures. Welding of the supporting beam to the shield block can be performed from inside the stub structure. Comparing with the circular welding option, the racetrack welding option seems better from the viewpoints of saving the space at the rear side of the module. Therefore, the racetrack welding option is mainly investigated here. Optimizations of the welding thickness and the supporting beam dimensions have been performed for 2 cases: i) radial length of the supporting beam = 180mm, ii) radial length of the supporting beam = 292mm

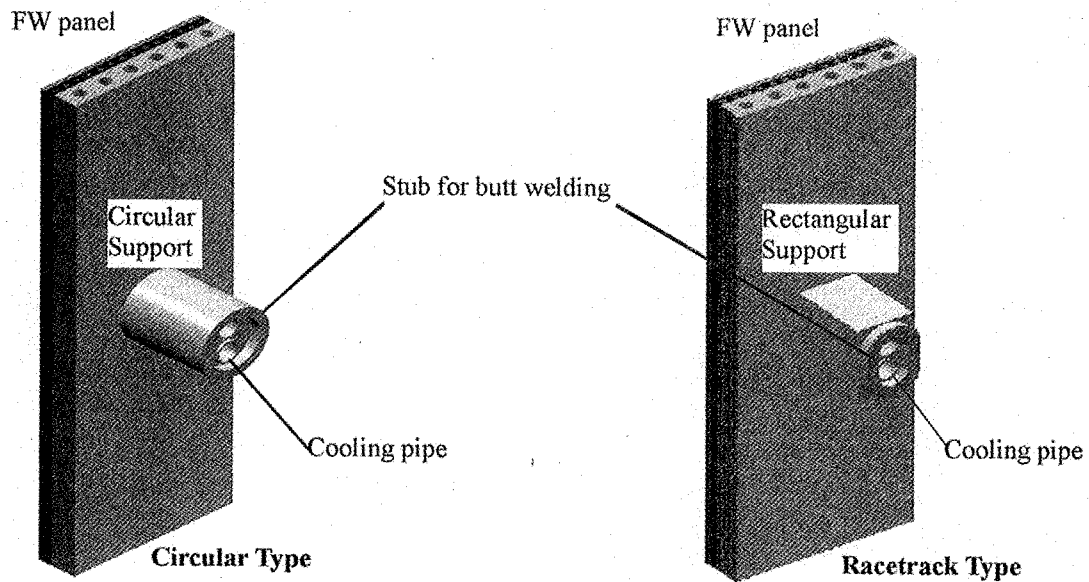


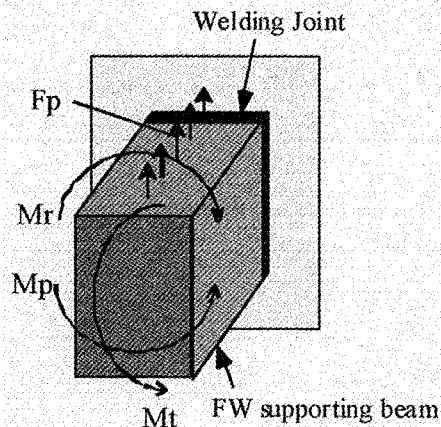
Fig. 5.1-2 Welding shapes of FW supporting beam

5.1.3 EM loads and calculation method

In this study, optimization of the welding thickness has been performed taking the EM loads under slow VDE and the fast VDE conditions into account. Estimated EM loads on the FW panel and the supporting beam are summarized in Table 5.1-1 [8]. EM Loads due to the slow VDE with halo current are severer for the design of the welded joint than that due to the fast VDE. Simplified stress calculation is performed as shown in Fig.5.1-3. Stresses on the welded joints due to the radial moment (M_r), poloidal moment (M_p), toroidal moment (M_t) and poloidal force (F_p) are calculated and compared with the allowable stress limit.

Table 5.1-1 EM loads on FW panle

EM Load Pattern	Fast VDE		Slow VDE with Halo Current	
	M_p due to ΔB_r Moment around poloidal axis	M_r due to ΔB_p Moment around radial axis	M_t/F_r due to I_{halo} Moment around toroidal axis	F_p due to I_{halo} Poloidal force
$L=0.18$ m	$M_p=5.6$ kNm	$M_r=7.6$ kNm	$M_t=28.5$ kNm $F_r=78$ kN	$F_p=560$ kN/m
$L=0.29$ m	$M_p=5.6$ kNm	$M_r=9.1$ kNm	$M_t=28.5$ kNm $F_r=78$ kN	$F_p=560$ kN/m



Notes

I_w : inertia moment of weld joint
 I_s : inertia moment of supporting beam
 Z_w : coefficient of section of welding joint
 Z_s : coefficient of section of support beam
 Z_p : polar modulus of section
 E : young's modulus

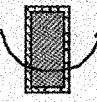
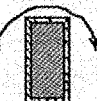
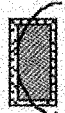
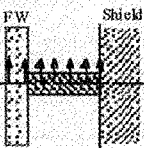
Stress Calculation	Deformation (Poloidal Direction)	Allowable Stress (MPa)
Bending Stress due to M_p $\sigma_{\text{bend}} = M_r / Z_p$ 	—	$S_m = 125 \text{ MPa}$ at 150°C
Shear Stress due to M_r $\tau = M_r / Z_p$ 	—	
Bending Stress due to M_t $\sigma_{\text{bend}} = M_t / Z_w$ 	$\delta = M_t L^2 / 2 E I_s$	Joint Effectiveness of welded joint: 0.85
Bending Stress due to F_p $M = F_p L^2 / 2$ $\sigma_{\text{bend}} = M / Z_w$ 	$\delta = F_p L^4 / 8 E I_s$	

Fig. 5.1-3 Stress calculations for FW supporting beam

The allowable stress intensity, S_m , for SS316LN is 147MPa at 150°C . The joint efficiency coefficient of 0.85 is applied to the butt welding with full penetration [9]. Therefore, the allowable stress intensity, S_m , for welded joint is assumed as 125 MPa ($=147 \times 0.85$) here. Based on this, the structural design criteria for the primary membrane + bending stress of $1.8 S_m = 225 \text{ MPa}$ (load category III [2]) is applied in the stress evaluations here.

5.1.4 Calculation results

5.1.4.1 Slow VDE case

5.1.4.1.1 Racetrack welding option

The maximum bending stresses in the welded joint as a function of welding thickness are shown in Fig. 5.1-4 (with 180 mm long supporting beam) and Fig. 5.1-5 (with 292 mm long supporting beam). In this calculation it is assumed that the EM loads are supported only by the weld at the beam end opposite to the FW panel. In addition, the severest constraint condition for the stress of the weld is assumed such that the poloidal movement of the supporting beam is free. As seen from Fig. 5.1-4, the welding thickness over 25 mm is needed to satisfy the allowable stress for 180 mm long supporting beam. On the other hand, 30-35 mm thick is needed for 292 mm long supporting beam, see Fig. 5.1-5. Considering the actual welding procedure, the required welding thickness for the latter (30-35 mm) is too thick to weld. The welding thickness should be reduced by adding another support structures, e.g., keys. Figure 5.1-6 shows the stresses on the welded joint in case the poloidal movement of the supporting beam is restrained, e.g., by touching the inner surface of the hole provided through the shield block to insert the supporting beam. In case the poloidal movement of the supporting beam is limited to be less than 0.3 mm, the welding thickness can be reduced to around 15 mm. Configurations of the FW support for the racetrack welding option are shown in Fig. 5.1-7 (180 mm long supporting beam) and Fig. 5.1-8 (292 mm long

supporting beam with additional keys at the root of the beam). As shown in Fig. 5.1-7, the minimum cross section of the supporting beam is expected to be around 110 mm x 165 mm for the 180 mm long beam. On the other hand, as shown in Fig. 5.1-8, the minimum cross section is reduced to be around 90 mm x 145 mm for the 292 mm long beam. In the latter case, the poloidal movement of the supporting beam is restrained by two keys, which are installed on both toroidal surfaces of the supporting beam.

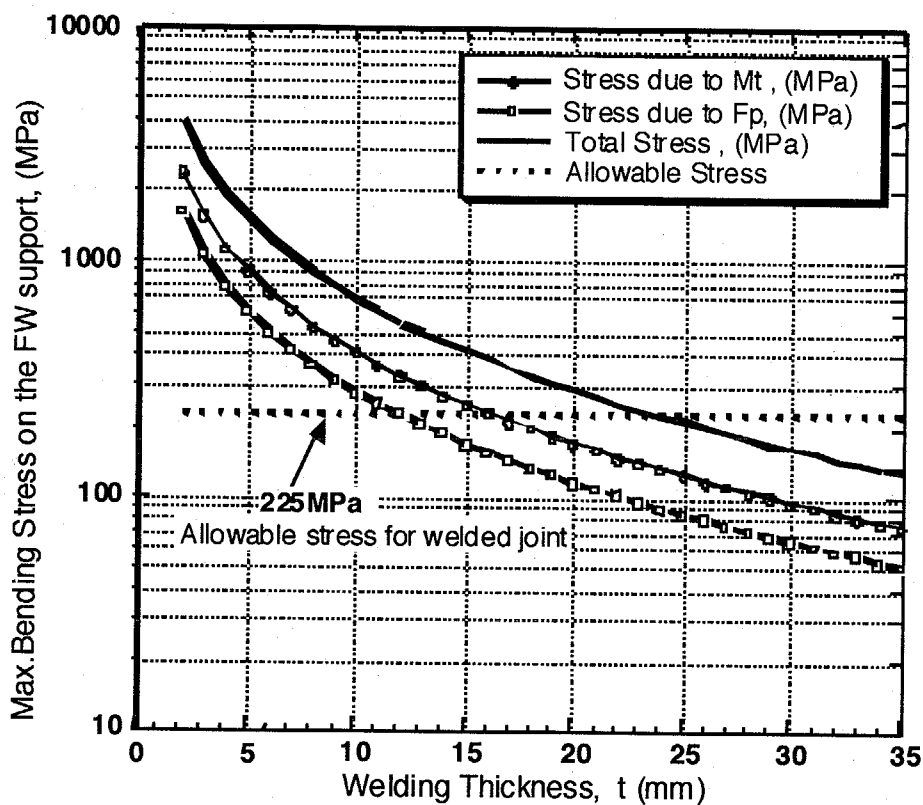


Fig. 5.1-4 Stress on the welded joint of FW supporting beam (slow VDE loads, racetrack welding, beam length 180 mm)

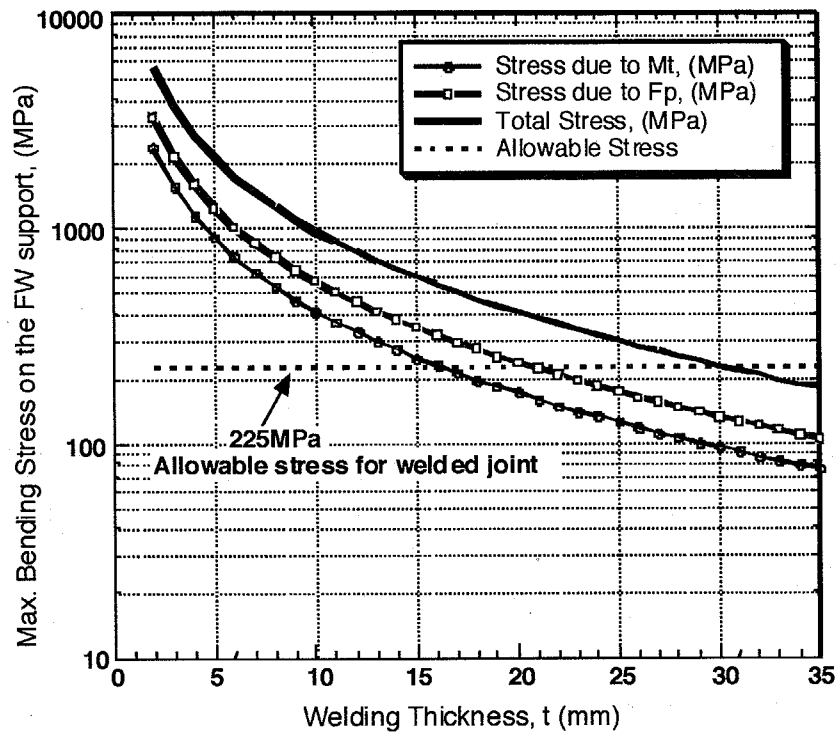


Fig. 5.1-5 Stress on the welded joint of FW supporting beam (slow VDE loads, racetrack welding, beam length 292 mm)

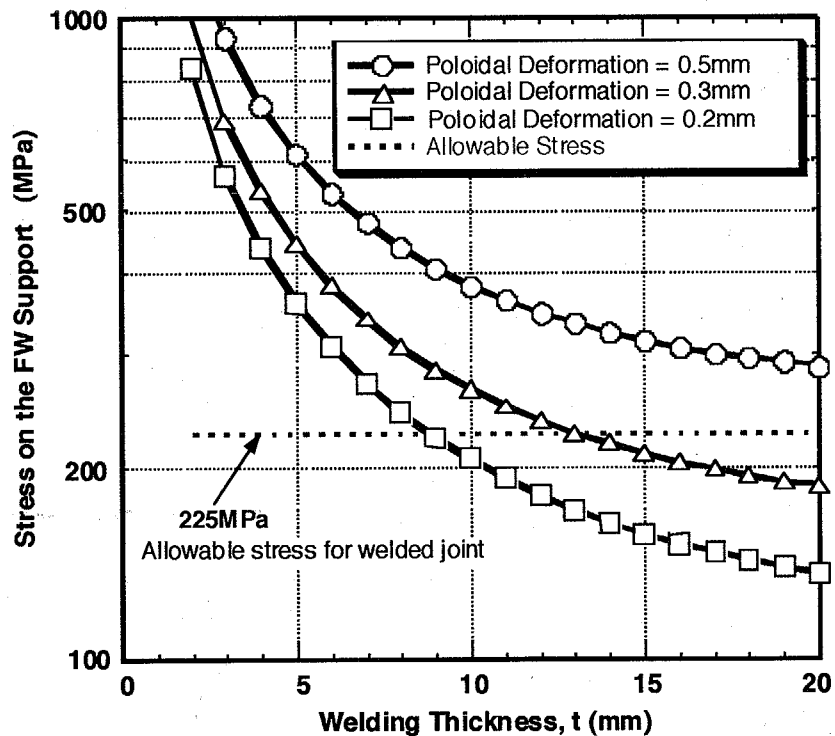


Fig. 5.1-6 Stress on the welded joint of FW supporting beam (slow VDE loads, racetrack welding, beam length 292 mm, poloidally restrained)

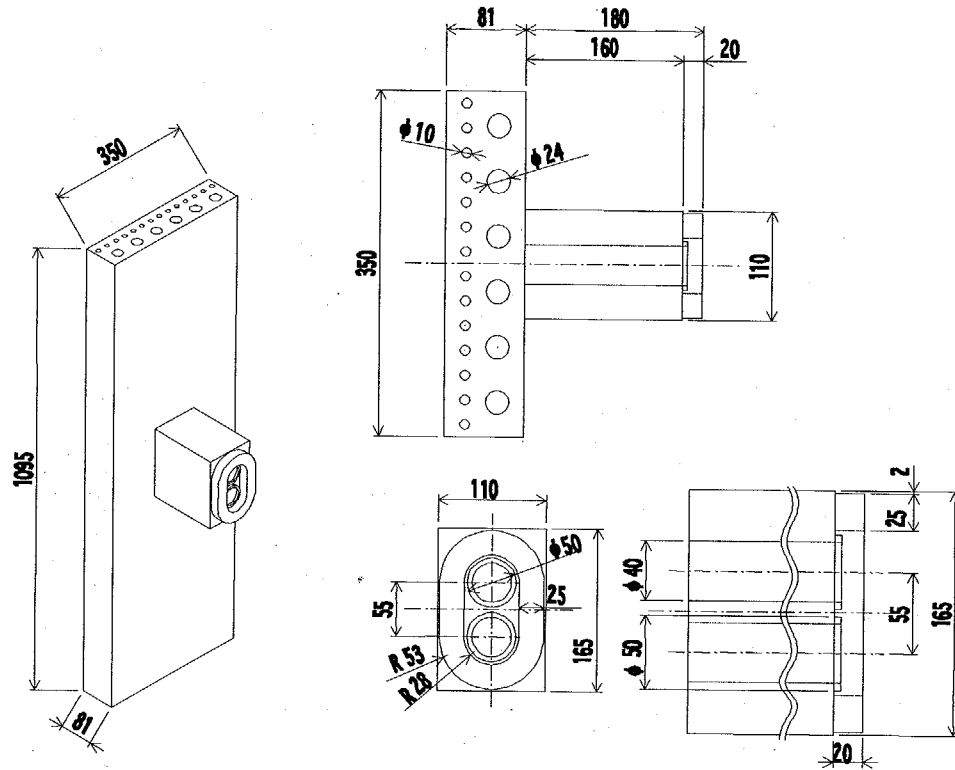


Fig. 5.1-7 FW supporting beam (racetrack welding, beam length 180 mm)

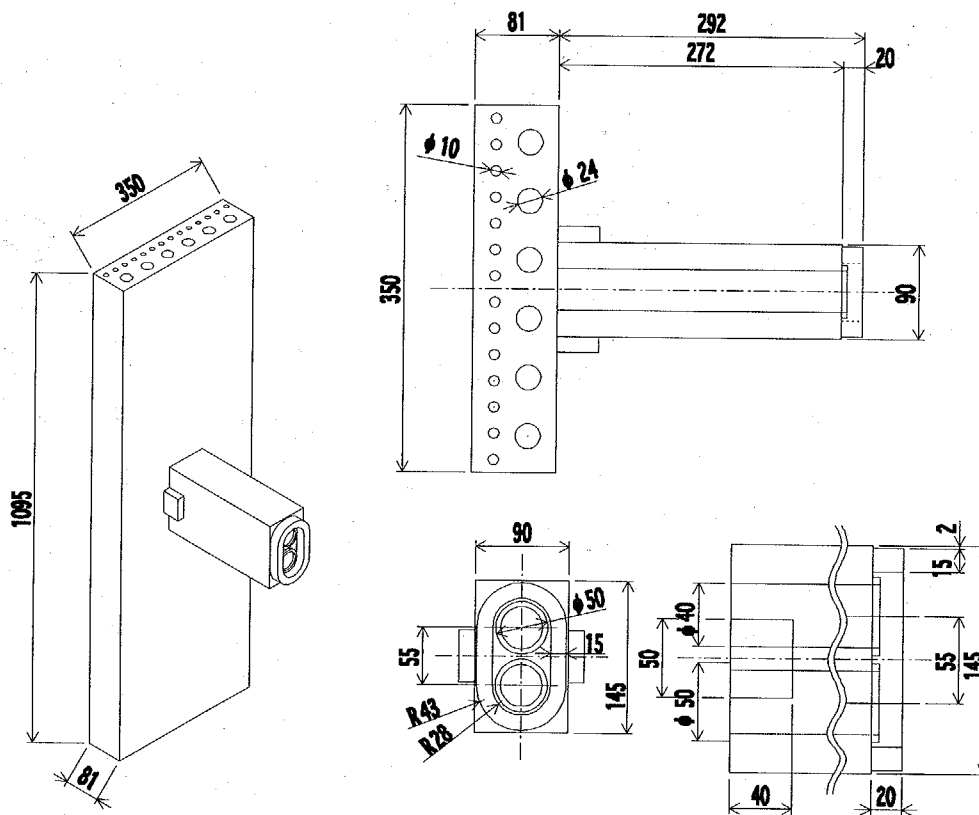


Fig. 5.1-8 FW supporting beam (racetrack welding, beam length 292 mm)

5.1.4.1.2 Circular welding option

The maximum bending stress in the circular welded joint are summarized in Fig.5.1-9 as a function of welding thickness. In this calculation, it is also assumed that the EM loads are supported only by the weld at the beam root. As the results, the welding thickness of 20 mm and 25 mm are necessary in order to satisfy the allowable stress limit for the beam length of 180 mm and 292mm, respectively. Figure 5.1-10 shows the stresses on the welded joint in case the poloidal movement of the supporting beam is restrained. If the poloidal movement of the supporting beam is limited less than 0.3 mm, the welding thickness can be reduced to around 15 mm. Configurations of the FW support for the circular welding option are shown in Fig.5.1-11 (180 mm long beam) and Fig.5.1-12 (292 mm long beam with additional support keys at the beam root). The diameters of the circular supporting beams are limited to be 151 mm and 135 mm or less in terms of the allowed space within the shield block for the former and the latter, respectively.

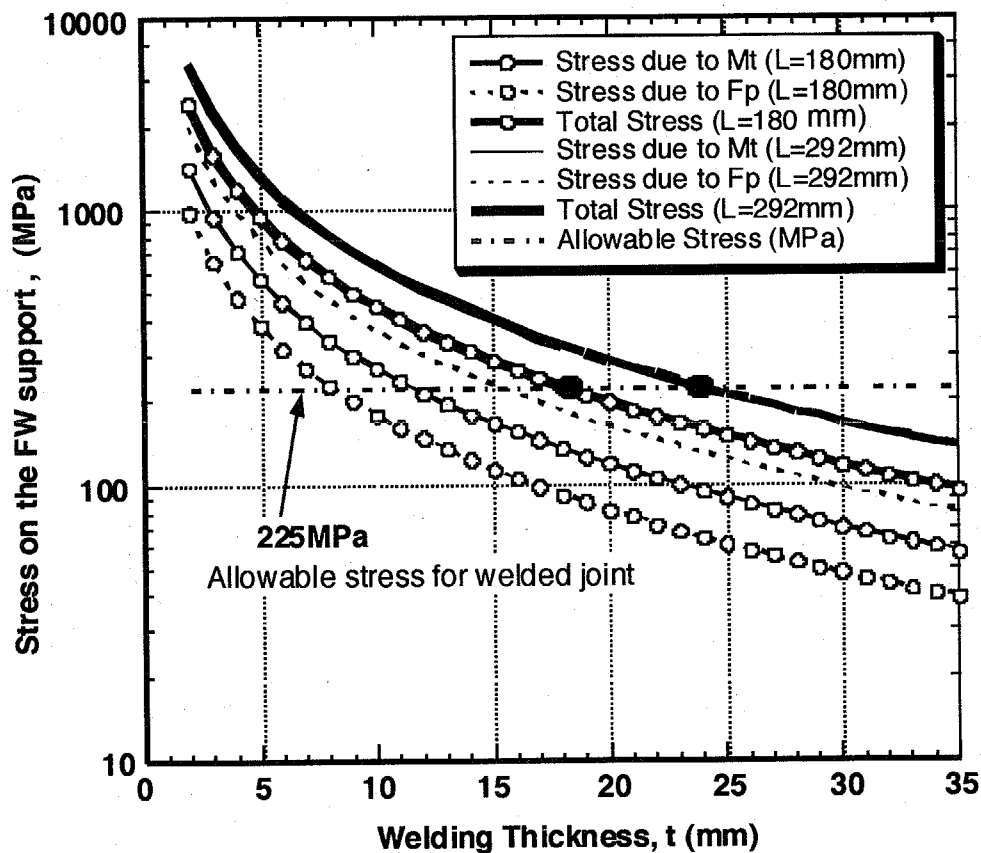


Fig. 5.1-9 Stress on the welded joint of FW supporting beam (slow VDE loads, circular welding, beam length 292 mm)

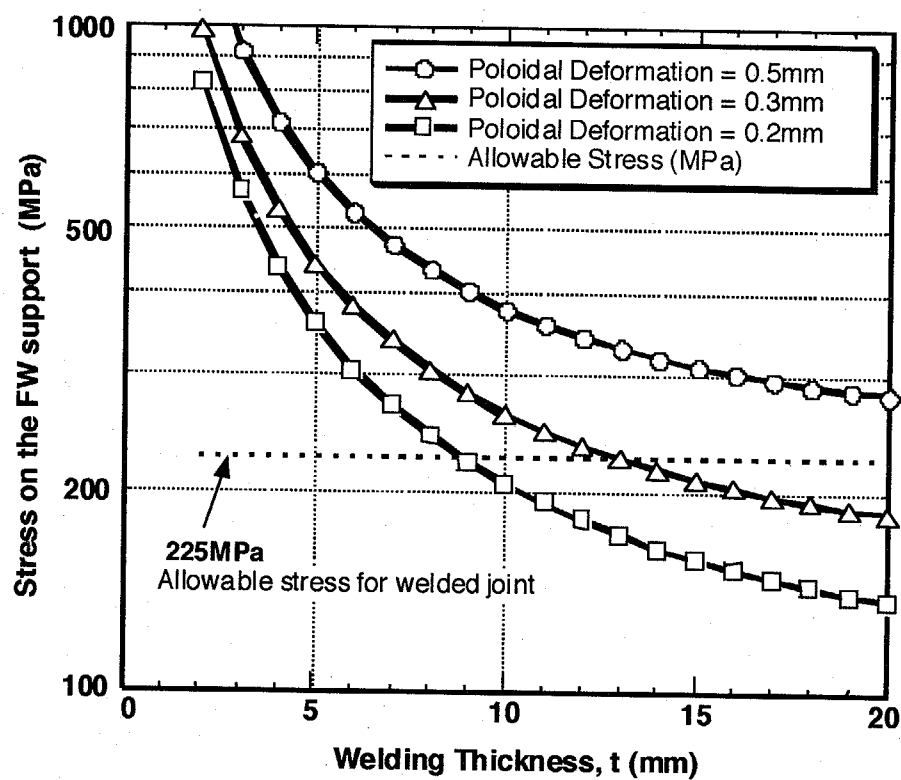


Fig. 5.1-10 Stress on the welded joint of FW supporting beam (slow VDE loads, circular welding, beam length 292 mm, poloidally restrained)

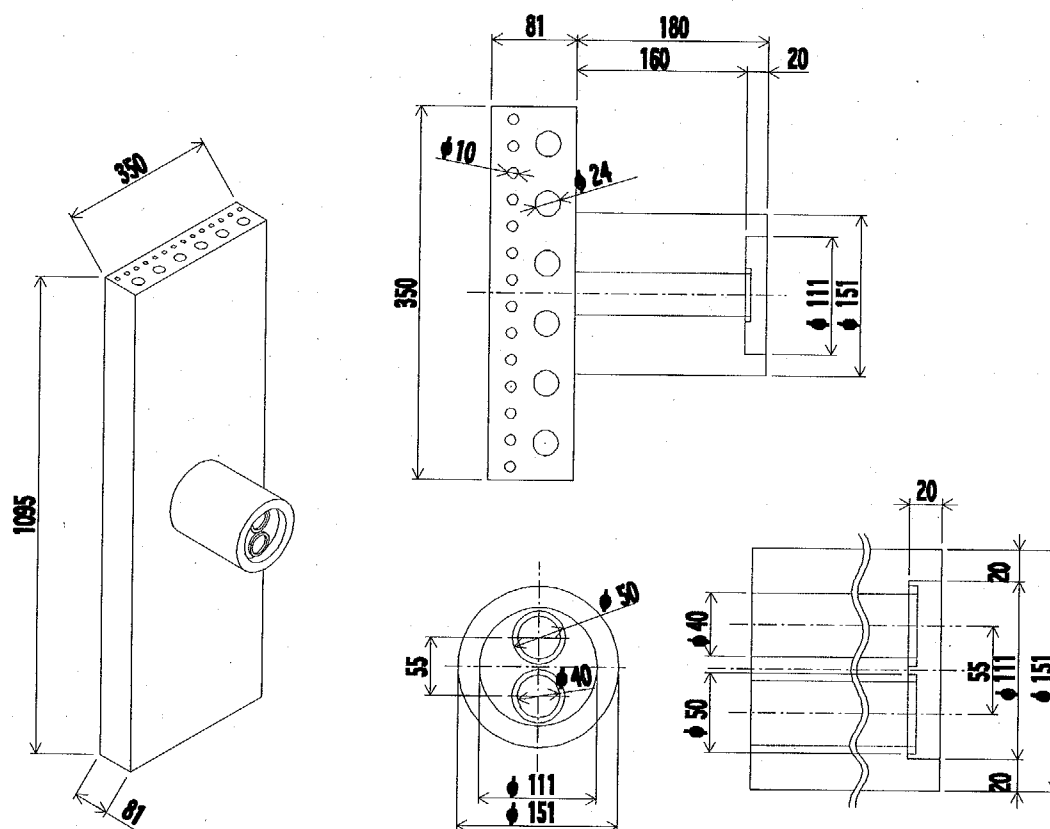


Fig. 5.1-11 FW supporting beam (circular welding, beam length 180 mm)

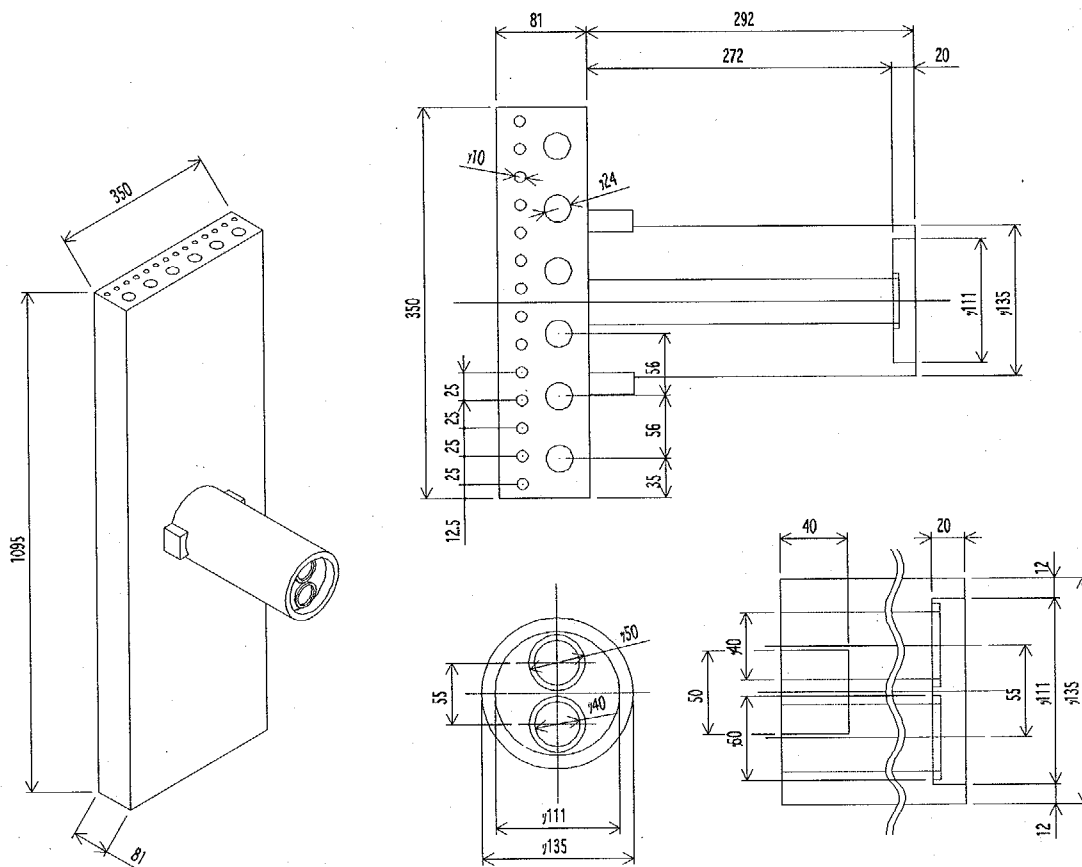


Fig. 5.1-12 FW supporting beam (circular welding, beam length 292 mm)

5.1.4.2 Fast VDE case

With the fast VDE load conditions shown in Table 5.1-1, a similar stress calculation for the racetrack welding option is performed. In this calculation the equivalent stress, σ_{eq} , is calculated by the following formula:

$$\sigma_{eq} = (\sigma^2 + 3\tau^2)^{1/2}$$

, where σ is the bending stress due to the poloidal moment (M_p) and τ is the shearing stress due to the radial moment (M_r).

The calculation results are shown in Figs. 5.1-13 and -14. As a result, the welding thickness of around 10 mm seems to be enough to withstand against the fast VDE loads.

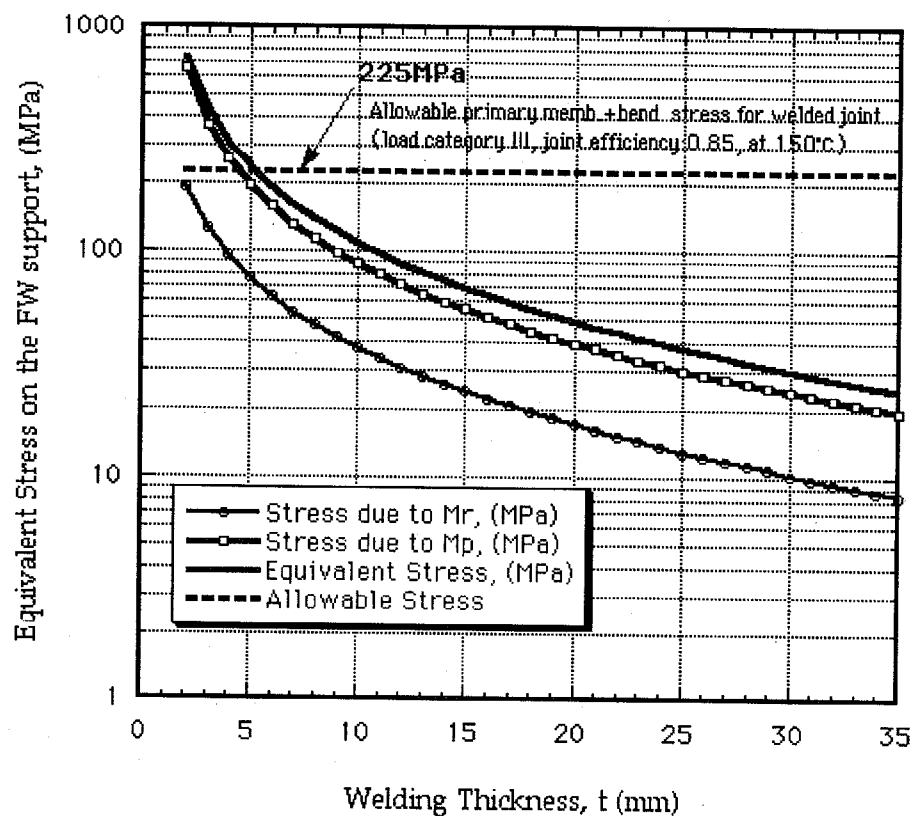


Fig. 5.1-13 Stress on the welded joint of FW supporting beam (fast VDE loads, racetrack welding, beam length 180 mm)

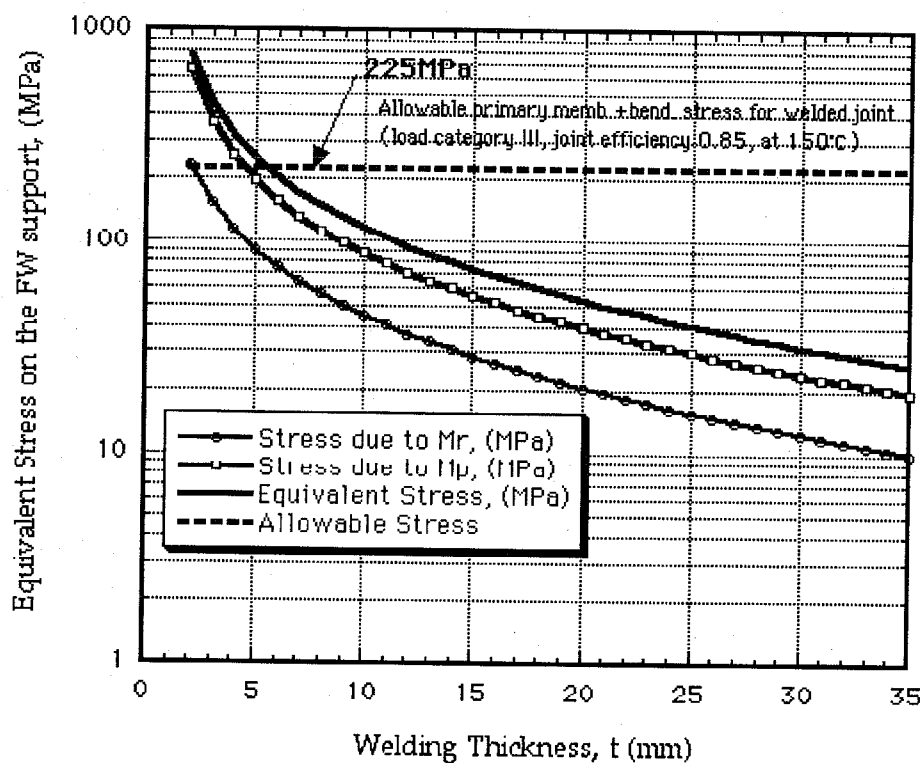
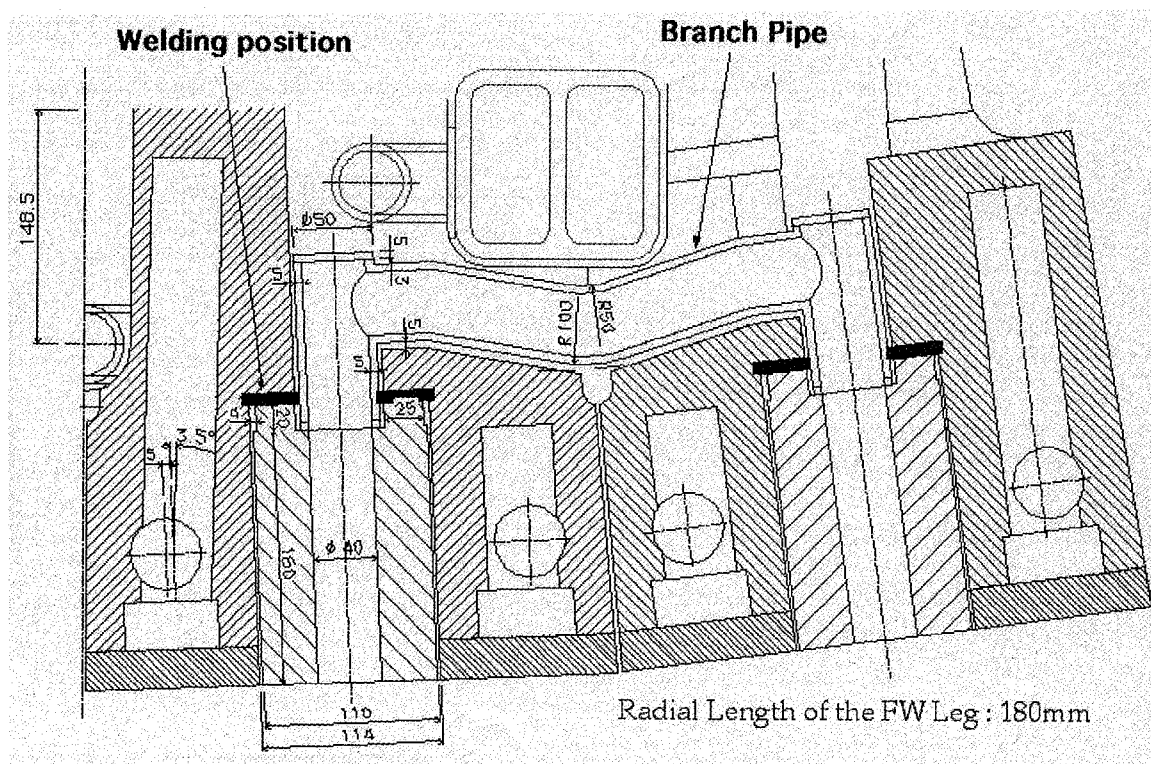


Fig. 5.1-14 Stress on the welded joint of FW supporting beam (fast VDE loads, racetrack welding, beam length 292 mm)

5.1.5 Basic layout of FW supporting beams

Figure 5.1-15 shows a horizontal cross-section of the inboard mid-plane module (toroidal half without FW panels). The basic layout of the supporting beams (racetrack welding option, 180 mm beam length, two beams for the half module) is also included in this figure. The branch pipe, which connects the coolant paths of adjacent FW panels, should be slightly bent in order to avoid the interference with the external manifold and maintain the stub thickness in the shield block. Fig.5.1-16 shows the basic layout for the longer supporting beams (racetrack welding option, 292 mm beam length with key structures). In this case, the branch pipe cannot be connected toroidally in the same plane between the two supporting beams. Therefore, as shown in Fig.5.1-17, some detours are needed to connect the branch pipes. Though the routing of the branch pipes seems possible, detailed arrangement of the pipes should be studied including the modification of the cooling paths in the shield block.



**Fig. 5.1-15 Cross-section of inboard mid-plane module
(toroidal half of the module, FW supporting beam length 180 mm)**

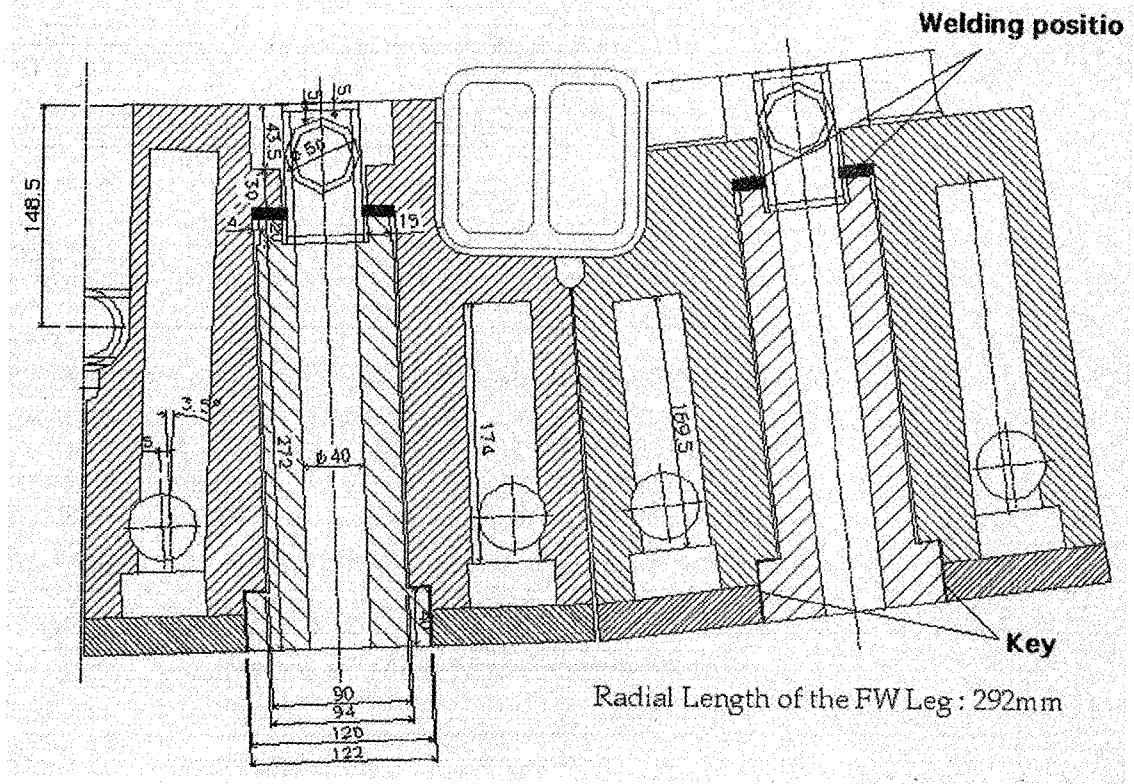


**Fig. 5.1-16 Cross-section of inboard mid-plane module
(toroidal half of the module, FW supporting beam length 292 mm)**

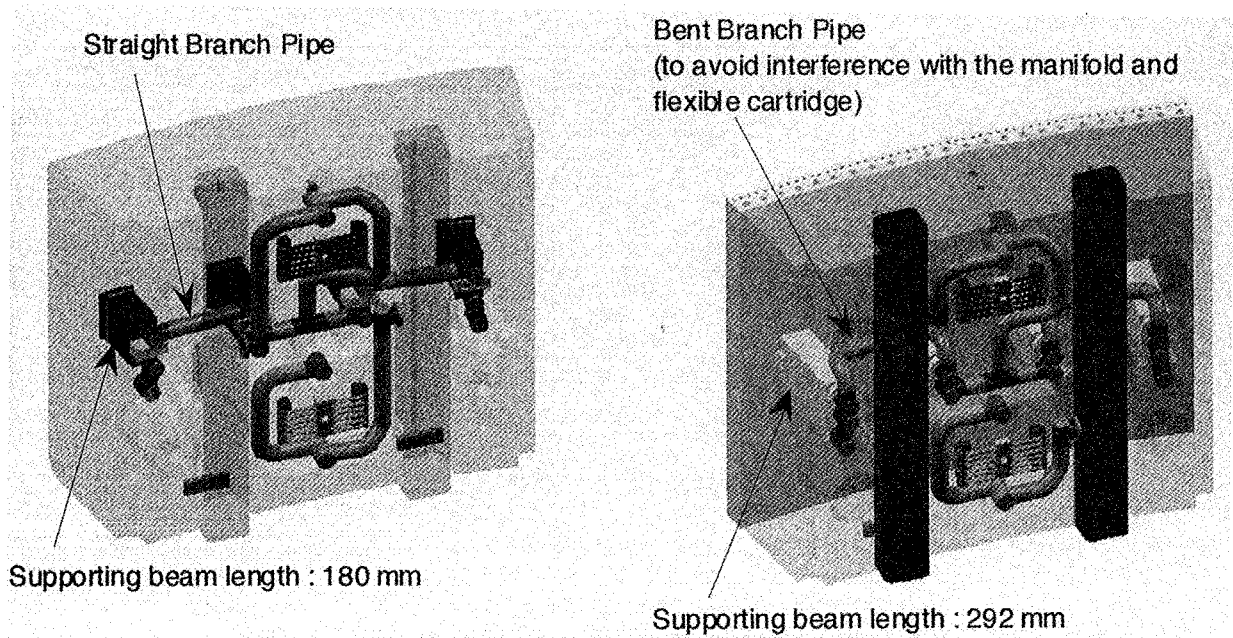


Fig. 5.1-17 Piping layout at the back of shield block

5.1.6 Conclusions

For the FW panel with a supporting beam from the back, a preliminary study for the welding attachment (racetrack welding option and circular welding option) has been performed. Following results are obtained for the racetrack welding option.

- 1) In the case of 180 mm long supporting beam, 25 mm thick welding will be needed if the poloidal movement are not constrained. For the 292 mm long supporting beam, 30-35mm thick welding will be needed.
- 2) In order to reduce the welding thickness, it is effective to add the key structure at the FW panel side and restrain the poloidal movement of the supporting beam. If the poloidal movement is limited to 0.3 mm, the welding thickness can be reduced to be around 15 mm for the longer supporting beam (292 mm).
- 3) For the longer supporting beam concept, the basic layout of the branch pipes at the back of the shield was studied. The routing of the branch pipes without the interference with the external manifold, slits, and flexible cartridges to fix the module to the vacuum vessel will be basically possible by some detours.

5.2 Strength evaluation of shield block region attached by flexible cartridge

5.2.1 EM pushing force

Due to the EM poloidal moment during plasma disruption, one side (either right or left) of the blanket module is pushed to the vacuum vessel via flexible cartridge as schematized in Fig. 5.2-1, a). In other words, the module back is pushed by the flexible cartridge. The area of the module back touched by the flexible cartridge is an annulus of 48 mm in inner diameter and 130 mm in outer diameter as shown in Fig. 5.2-1, b). As also shown in this figure, the area between the diameters 80 mm and 130 mm partly overlaps the region of the radial coolant channels. The minimum SS thickness of the module at the coolant channels is 30 mm.

For estimating the strength of the module (shield block) against the pushing force by the flexible cartridge, especially at the coolant channels, a calculation model shown in Fig. 5.2-1, c), i.e., a circular plate of 30 mm thickness with a circular hole at the center (uniformly distributed load, inner edge fixed, outer edge free), is used here. Since coolant channels occupy only a part of the annular region, this calculation model is very conservative.

Assumptions and calculation conditions are as follows:

- 1) The flexible cartridge is rigid.
- 2) Outer radius of the annular plate: $a = 65$ mm
- 3) Inner radius of the annular plate: $b = 40$ mm
- 4) Thickness of the annular plate: $h = 30$ mm
- 5) Total pushing force: 550 kN (=0.55 MN)
therefore, the distributed load: $p = 0.55 / \{\pi (0.13^2 - 0.048^2) / 4\} = 48$ MPa

The maximum stress, which is at the inner edge in this case, is given by the following formula [10]:

$$\sigma_{\max} = k p a^2 / h^2$$

where k is a coefficient calculated as a function of the ratio a/b and loading and constraint

conditions. For a/b of 1.6 ($=65/40$) and above loading and constraint conditions, the value of k is about 0.6 [10]. Therefore,

$$\sigma_{\max} = 0.6 \times 48 \times 0.065^2 / 0.03^2 = 135 \text{ MPa}$$

Since the stress intensity, S_m , of SS316L(N)-IG is 137 MPa (200 °C) [11], above stress is lower than the allowable stress, i.e., $1.5 S_m = 205 \text{ MPa}$.

5.2.2 EM pulling force

During plasma disruption, one side (either left or right) of the blanket module is pulled toward plasma as schematized in Fig. 5.2-2, a). This pulling force is concentrated around the bolt thread. For estimating the strength of the module (shield block) around the bolt thread against the pulling force, a calculation model shown in Fig. 5.2-2, c) is used. The model is an annular plate with concentrated load along the inner edge and constraint conditions of inner edge free and outer edge simply supported. The inner and outer diameters of the annular plate are 45 mm and 80 mm, respectively, and the plate thickness is 47.5 mm based on the dimensions indicated in Fig. 5.2-2, a) and b).

Assumptions and calculation conditions are summarized as follows:

- 1) The shield block and the bolt are firmly and uniformly connected at the thread.
- 2) Outer radius of the annular plate: $a = 40 \text{ mm}$
- 3) Inner radius of the annular plate: $b = 22.5 \text{ mm}$
- 4) Thickness of the annular plate: $h = 47.5 \text{ mm}$
- 5) Pulling force: $P = 550 \text{ kN} (=0.55 \text{ MN})$

The maximum stress, which is at the inner edge in this case, is given by the following formula [10]:

$$\sigma_{\max} = k P / h^2$$

The coefficient k calculated for a/b of 1.8 ($=40/22.5$) and above loading and constraint conditions is about 1.4 [9]. Therefore,

$$\sigma_{\max} = 1.4 \times 0.55 / 0.0475^2 = 341 \text{ MPa}$$

This stress exceeds the allowable stress of SS316L(N)-IG, i.e., $1.5 S_m = 205 \text{ MPa}$ (200 °C), while the bolt of Inconel 718 has sufficient strength. Though detail analysis would be needed, it can be preliminary concluded from the above calculation that the internal thread of the shield block could not withstand against the EM pulling force, then to reduce the stress to be lower than the allowable value, the thread length longer than 61.3 mm would be needed.

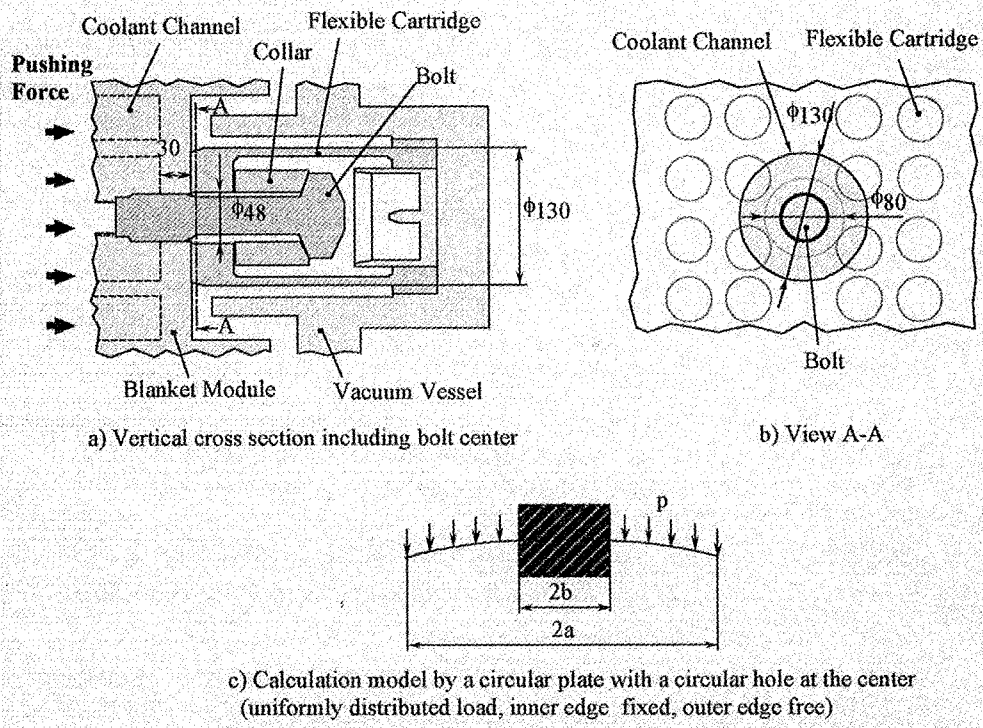


Fig. 5.2-1 Calculation model for strength evaluation of the shield block back region against EM pushing force

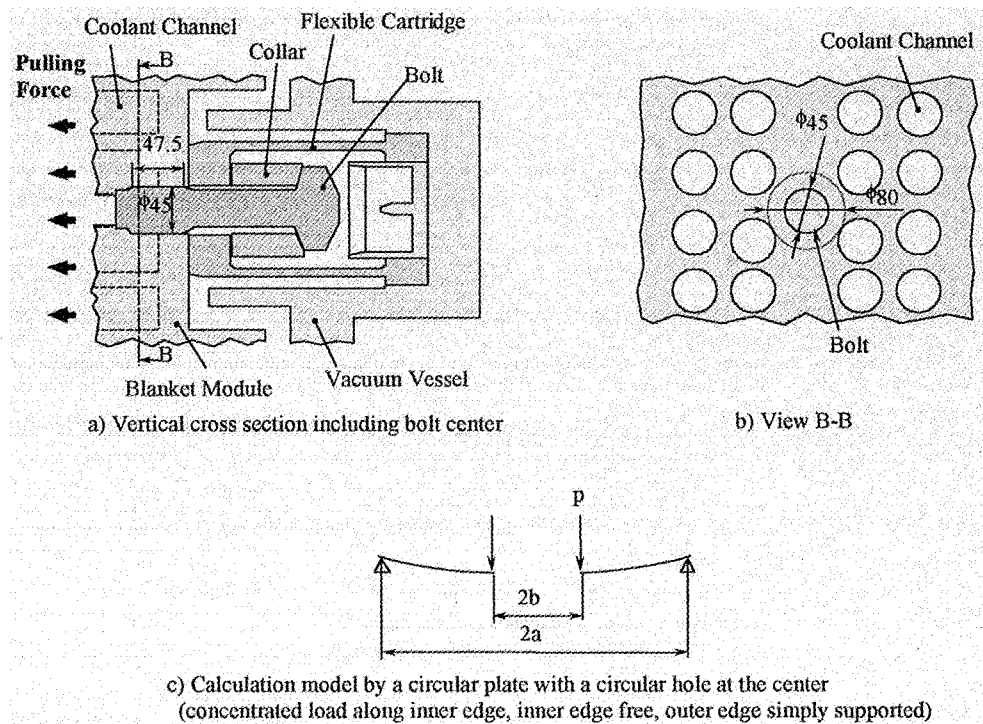


Fig. 5.2-2 Calculation model for strength evaluation of the shield block back region against EM pulling force

6. Design of Water-to-Water Leak Detection System for Integrated Cooling Manifold Concept

6.1 Background

The ITER engineering design activity (EDA) has successfully been terminated by editorial completion of the final design report (FDR) on the ITER-FEAT with many fruitful results. During the design of the ITER-FEAT, an optional design on the vacuum vessel (VV) was proposed for cost reductions, where a back plate for blanket modules was eliminated and the blanket modules were supported directly by the VV. In addition, an integrated cooling manifold concept was subsequently presented, where the blanket water cooling channels were recessed in the VV inner wall [12]. This means that the blanket cooling channels are integrated into the VV ones, although both the channels are structurally independent because of their different flow parameters. The most important consequence resulting from the integrated cooling manifold concept is the possibility of contamination (above acceptable levels) of the activated corrosion product (ACP) of the VV cooling loop by blanket cooling water. In this case, a water leak from a higher-pressure side (blanket) to a lower-pressure side (VV) is labeled as "water-to-water leak", in which the accidental water leak has to be detected within a reasonable time response and with sufficient sensitivity.

Since the ACP concentration of the blanket channel is 100 times higher than that of the VV channel, the maximum allowable water-to-water leak rate from the blanket channel to the VV one has been tentatively set at $8.68 \times 10^{-6} \text{ m}^3/\text{s}$ [13]. The ACP monitoring of the VV channel is not practical for the water-to-water leak detection, because in the early stage of the ITER operations, both the ACP concentrations of the blanket and VV channels will be far below the expectant levels. Based on the above background, we have assessed a tracer method as an ITER design task, in which some water soluble material is added periodically or semi-continuously to the blanket cooling channels as a tracer. When the accidental water-to-water leak occurs, the blanket dissolved tracer is leaked into the VV cooling channels and the VV leaked tracer is detected by a suitable method.

In this section, applicability of four candidate tracer materials, i.e. Na-24, heavy water and inert gases (He, Kr), for the ITER conditions is evaluated in view of detectable sensitivity of the water leakage and impact on ITER components. From the evaluation, the most suitable tracer is selected among them, and the water-to-water leak detection system by using the selected tracer is conceptually designed.

6.2 Design requirements

Major requirements were supplied by the ITER Joint Central Team (JCT).

6.2.1 Candidate tracer materials

- | | |
|-------------------------|------------------|
| 1) Radioactive isotope: | Na-24 |
| 2) Heavy water: | D ₂ O |
| 3) Inert gas: | He |
| 4) Inert gas: | Kr |

6.2.2 Target leak rate and sampling duration

Leak rate:	$>8.68 \times 10^{-6} \text{ m}^3/\text{sec}$
Sampling duration:	$< 30 \text{ min}$

6.2.3 Cooling water conditions

- 1) Vacuum vessel

Inlet temperature:	$120 \pm 10 \text{ }^\circ\text{C}$
Inlet pressure:	$1.6 \pm 0.2 \text{ MPa}$
Flow rate:	950 kg/sec
- 2) Shielding blanket

Inlet temperature:	$100 \pm 5 \text{ }^\circ\text{C}$
Inlet pressure:	$2.8 \pm 0.2 \text{ MPa}$
Flow rate:	1043 kg/sec

6.2.4 Other conditions

- 1) Tracer materials are introduced into the water cooling circuit of the shielding blanket due to its higher inlet pressure.
- 2) A water flow velocity of the vacuum vessel is 0.04 m/sec .
- 3) The Maximum distance from a water leakage to a detector is $<50 \text{ m}$.

6.3 Evaluation of lower detectable limit

6.3.1 Na-24

- 1) Assumption
 - a) An increase rate of the gamma-ray in the cooling circuit of the vacuum vessel is 1 Bq/sec for the minimum target leak rate of $8.68 \times 10^{-6} \text{ m}^3/\text{sec}$.
 - b) Na-24 is uniformly distributed in the water at a sampling point.
 - c) An overall measurement time required for detecting the gamma-ray using the Ge detector is 1000 seconds (17 min).
- 2) A radioactive concentration of the gamma-ray due to Na-24 in the cooling water of the shielding blanket

$$1 \text{ Bq/sec} / (8.68 \times 10^{-6} \text{ m}^3/\text{sec}) = 1.15 \times 10^5 \text{ Bq/m}^3.$$
- 3) An increase of the gamma-ray concentration in the vacuum vessel cooling water

An increase of the gamma-ray concentration due to the water leakage of $8.68 \times 10^{-6} \text{ m}^3/\text{sec}$ from the shielding blanket cooling circuit to the vacuum vessel cooling circuit is estimated as $1.05 \times 10^{-3} \text{ Bq/kg}$,

$$\text{where } 1.15 \times 10^5 \text{ Bq/m}^3 \times 8.68 \times 10^{-6} \text{ m}^3/\text{sec} / (950 \text{ kg/s}) = 1.05 \times 10^{-3} \text{ Bq/kg}.$$
- 4) Sensitivity of the gamma-ray detector

A lower detectable limit of the radioactivity method using the Ge detector for measuring radioactivity is, in general, about 5 Bq/kg at a water sample weight of 1 kg

and the overall measurement time of 1000 sec. Considering this actual sensitivity, it can be concluded that the minimum target leak rate of $8.68 \times 10^{-6} \text{ m}^3/\text{sec}$ is not detectable, because the concentration of $1.05 \times 10^{-3} \text{ Bq/kg}$ at the target leak rate is far below the detectable limit of 5 Bq/kg .

5) Influence of natural Na-23 in the water on detection of Na-24

A small amount of the natural Na-23 exists in the vacuum vessel water as an impurity, and a decay of Na-23 to Na-24 by the n- γ reaction will cause increase in the background gamma ray. Therefore, the Na-23 concentration in the vessel water has to be controlled so as to keep the level of the gamma ray less than $1.05 \times 10^{-3} \text{ Bq/kg}$. At present, it is too difficult technically to reduce the Na-23 decayed gamma ray within the value mentioned.

6.3.2 D₂O

1) Assumption

- a) D₂O is used as the cooling water of the shielding blanket.
- b) Light water is used as the cooling water of the vacuum vessel.
- c) A natural background concentration of D₂O in the light water is 0.015 wt% [14].
- d) A density of D₂O is $1.107 \times 10^3 \text{ kg/m}^3$.
- e) D₂O is uniformly distributed at a sampling point.

2) Concentration of D₂O in the vacuum vessel water channel

An increase in concentration of D₂O in the vessel water by the minimum target leak rate is estimated as 10.1 ppm,

$$\text{where } 8.68 \times 10^{-6} \text{ m}^3/\text{s} \times 1.107 \times 10^3 \text{ kg/m}^3 / (950 \text{ kg/s}) = 1.01 \times 10^{-5} \text{ (10.1 ppm)}.$$

3) Sensitivity of a Mass Spectrometer (MS) for D₂O

While a ppm level of D₂O is detectable with the MS, a molecular exchange reaction between the heavy and light water molecules will be occurred in the ionizer of the MS. Therefore, a lower detectable limit of the MS for D₂O is estimated as, in a practical use, roughly 100 ppm.

6) Influence of the background D₂O

A natural background concentration of D₂O in the vessel water is calculated as about 150 ppm,

$$\text{where } 950 \text{ kg/s} \times 0.015 \times 10^{-2} / 950 \text{ kg/s} = 1.5 \times 10^{-4} \text{ (150 ppm)}.$$

The natural background D₂O of 150 ppm is much larger than the increase in D₂O by leaks of 10.1 ppm. Hence, the minimum target leak rate of $8.68 \times 10^{-6} \text{ m}^3/\text{sec}$ cannot be detected by using the D₂O tracer.

6.3.3 He

1) Assumption

- a) A gaseous He is dissolved in the blanket water, and the solubility of He depends on

temperature and pressure of the water.

- b) The solute He in the water is uniformly distributed at the sampling point.

2) Solubility of He

The solubility of He in the water for the temperature range from 0 °C to 77 °C can be estimated by the following formula [14];

$$\ln(S) = A + B / (T/100) + C \times \ln(T/100),$$

where S : molar fraction (solubility)

T : temperature (K)

A : Specific constant for He, -41.4611

B : Specific constant for He, 42.5962

C : Specific constant for He, 14.0094

If the above formula is applicable at the temperature of 100 °C, the solubility of He is 9.17×10^{-6} (1.14×10^{-5} m³/kg) under an atmospheric pressure. The Solubility is directly proportional to the pressure, so that the solubility of He at the pressure of 2.8 MPa is 2.57×10^{-4} (3.19×10^{-4} m³/kg).

3) Leakage of the solute He into the vessel water

An increase in concentration of the solute He into the vessel water by the minimum target leak rate of 8.68×10^{-6} m³/sec is 2.9×10^{-9} m³/kg,

$$\text{where } 8.68 \times 10^{-6} \text{ m}^3/\text{sec} \times 1 \times 10^3 \text{ kg/m}^3 \times 3.19 \times 10^{-4} \text{ m}^3/\text{kg} / 950 \text{ kg/sec} \\ = 2.9 \times 10^{-9} \text{ m}^3/\text{kg}$$

4) Sensitivity of a He detector

A lower detectable concentration of the solute He by using a gas chromatography mass spectrometer (GC-MS) system is, in general, 0.1 ppm with a retention time of few minutes. In this case, the He concentration to be required for detecting the minimum target leak rate by using the GC-MS system is 29 ppm as below,

$$2.9 \times 10^{-9} \text{ m}^3/\text{kg} / (10^{-1} \times 10^{-3} \text{ m}^3/\text{kg}) = 2.9 \times 10^{-5} \text{ (29 ppm)},$$

at a condition, where the solute He in sampled water is extracted by an N₂ gas at 0.1 times the volume of the sampled water. This level of concentration can be detected by the GC-MS system.

5) Influence of background He

At the beginning of plasma operation, no amount of He solved in the vessel water exists. During the D-T operation, the 14 MeV neutrons produce some amount of He due to a reaction of neutrons with Oxygen in the water. Therefore, the background level of He rises with increasing the D-T operation time.

6.3.4 Kr

1) Assumption

- a) A gaseous Kr is dissolved in the blanket water, and the solubility of Kr depends on temperature and pressure of the water.
- b) The solute Kr in the water is uniformly distributed at the sampling point.

2) Solubility of Kr

The solubility of Kr at 2.8 MPa and 100 °C is estimated to be 6.27×10^{-4} (7.81×10^{-4} m³/kg).

3) Leakage of solute Kr into the vessel water

An increase in concentration of the solute Kr into the vessel water by the minimum target leak rate of 8.68×10^{-6} m³/sec is 7.1×10^{-9} m³/kg,

$$\text{where } 8.68 \times 10^{-6} \text{ m}^3/\text{sec} \times 1 \times 10^3 \text{ kg/m}^3 \times 7.81 \times 10^{-4} \text{ m}^3/\text{kg} / 950 \text{ kg/sec} \\ = 7.1 \times 10^{-9} \text{ m}^3/\text{kg}.$$

4) Sensitivity of a Kr detector

A lower detectable concentration of the solute Kr by using the GC-MS system is 0.1 ppm with a retention time of few minutes. In this case, the Kr concentration to be required for detecting the minimum target leak rate by using the GC-MS system is 71 ppm as below,

$$7.1 \times 10^{-9} \text{ m}^3/\text{kg} / (10^{-1} \times 10^{-3} \text{ m}^3/\text{kg}) = 7.1 \times 10^{-5} (71 \text{ ppm}),$$

at a condition, where the solute He in sampled water is extracted by a He gas at 0.1 times the volume of the sampled water. This level of concentration can be detected by the GC-MS system.

7) Influence of background

No amount of Kr solved in the vessel water exists at the beginning of plasma operation. The 14 MeV neutron radiation does not produce Kr during the D-T operation, so that no influence of the background is expected.

6.4 Impact of tracer materials on components and removal of tracers

6.4.1 Na-24

1) Impact on components

Na-24 is injected into water by the form of NaOH. Relation between concentration of NaOH and pH-index is summarized below.

Concentration of NaOH		pH
10	ppb	8.4
100	ppb	9.4
1	ppm	10.4
10	ppm	11.4

Since SS316LN-IG is used as the main structural material in the ITER, the influence of corrosion on SS316LN-IG will be not negligible over 1 ppm of NaOH. However, at the minimum target leak rate, presumable concentration of Na-24 in the blanket water is 10^{-9} ppm, so this level of the concentration has no effect on corrosion.

2) Removal of Na tracer

The Na-24 tracer can be removed from the vessel water by using the cation-exchange resin.

6.4.2 D₂O

1) Impact on components

Since it is no difference in chemical property between the heavy and light water, so there is no corrosion effect on the components.

2) Removal of D₂O

D₂O can be separated from the light water by condensing the vessel water with distillation, while a removal cost for D₂O will be rather higher than those for Na-24, He and Kr.

6.4.3 He

1) Impact on components

Since He is an inert gas, there is no corrosion effect on components. In case of an irregular change of the water pressure and temperature, the solubility of He gas will also change, and formation of He bubbles in the cooling circuit will be concerned at hydrodynamics of the cooling water.

2) Removal of He

The He tracer in the vessel water can be removed by a gas diffusion method under conditions of a high temperature and an atmospheric pressure.

6.4.4 Kr

1) Impact on components

Since Kr is an inert gas, there is no corrosion effect on components. In case of an irregular change of the water pressure and temperature, the solubility of Kr gas will also change, and formation of Kr bubbles in the cooling circuit will be concerned at hydrodynamics of the cooling water.

2) Removal of Kr

The Kr tracer in the vessel water can be removed by a gas diffusion method under conditions of a high temperature and an atmospheric pressure.

6.5 Assessment of candidate tracer materials

1) In case of the Na-24 tracer, the minimum target leak rate of 8.68×10^{-6} m³/sec from the blanket cooling water circuit cannot be detected by the existing Ge detector due to its poor sensitivity. Besides, it is technically difficult that an increase in concentration of the gamma ray caused by decay of the background Na-23, has to be suppressed below the increase in concentration of the gamma ray due to the Na-24 tracer.

2) As for the D₂O tracer, the minimum target leak rate of 8.68×10^{-6} m³/sec is not detectable by using the MS, because a molecular exchange reaction between the heavy water and light water in the MS itself reduces the detectable sensitivity for D₂O. Natural existence of D₂O in the vessel water affect the sensitivity of detector, and the ratio of amount of heavy water in the vessel water to the one in the blanket water is about 10. Besides, the increase in concentration of D₂O by the minimum target leak

rate is one order smaller than that of the natural D_2O in the vessel water, hence, the minimum target leak rate is not detectable.

- 3) As for the He tracer, if the concentration of background He produced by a neutron radiation in the vessel water can be reduced below the concentration of He by the minimum target leak rate from the blanket water, the water leakage will be detected by the GC-MS system. The minimum lower limit of the GC-MS system is about 0.1 ppm for He.
- 4) As for the Kr tracer, since no background of Kr exists in the vessel water, the water leakage from the blanket water can be detected by a combination of the gas diffusion system and GC-MS system.
- 5) Each tracer material will have no serious corrosion effect on the components at the minimum target leak rate.
- 6) The tracer materials can be removed or separated from the vessel water, for instance, the cation-exchange resin for Na-24, a gas diffusion method for He and Kr gas and a distillation method for D_2O . The distillation method will be the most expensive among them.

The evaluation of four candidate tracer materials is summarized in Table 6.5-1. In this preliminary study, the Kr gas is the most preferable tracer material among four materials.

Table 6.5-1 Assessment of tracer materials.

	Na-24	D_2O	He gas	Kr gas
Sensitivity	× Low detectability	Δ Moderate if exchange reaction in the MS is suppressed.	○ Detectable	○ Detectable
Background	Δ Moderate if reduction of Na-23 is possible in the water	× Issue on natural existence	Δ Moderate if removal of He generated is possible	○ No issue
Impact on components	○ No issue	○ No issue	○ No issue	○ No issue
Removal of tracer	○ Cation-exchange resin method	Δ Gas distillation method is high cost.	○ Gas diffusion method	○ Gas diffusion method
Assessment	×	×	Δ	○

6.6 Conceptual design of water-to-water leak detection system using Kr tracer

The water-to-water leak detection system proposed is mainly composed of a sampling system, diffusion column and MS-GC detector. In particular, the gas diffusion column is used for separation of gas dissolved in a fluid from the fluid to improve the sensitivity of the detection by the GC-MS analyzer. The diffusion column is generally used in the chemical plant and for measurement of the hydrogen content in the water in the power plant. A key parameter was the diffusion efficiency of Kr in diffusion column because it directly affects on sensitivity of Kr detection system, so the diffusion efficiency of Kr was determined by experiment.

6.6.1 Experiment on diffusion efficiency of Kr by diffusion column

Using experimental configuration shown in Fig. 6.6.1-1, the efficiency of transfer from liquid phase to gas phase for the Kr dissolved in the water has been investigated by using MS-GC analyzer (GC-MS-QP1000 of Shimadzu). Major experimental condition is shown in Table 6.6.1-1. Correlation between the diffusion efficiency and purge gas rate is indicated in Table 6.6.1-2. The ratio of liquid to gas rate (the ratio L/G) was varied. Table 6.6.1-3 indicates the dependency of the diffusion efficiency on the ratio L/G.

Table 6.6.1-1 Experimental condition.

Item	Condition
Dimension of diffusion column	ϕ 30 mm x H 1000 mm
Material of diffusion column	Plastic
Region filled with packing materials	850 mm in axial direction
Packing material	SUS (ϕ 6 mm x L 6 mm)
Packing factor	about 20 vol %
Purge gas species	Helium

Table 6.6.1-2 Correlation between diffusion efficiency and purge gas rate.

Purge gas rate (m^3/s)	Flow rate of sampled water (m^3/s)	L/G	Kr content in sampled water (ppb)	Kr content in purge gas (ppm)	Diffusion efficiency (%)
1×10^{-7}	1.75×10^{-6}	17.5	1000	2940	62.8
1.83×10^{-7}	1.63×10^{-6}	8.9	1000	1790	75.2
3×10^{-7}	1.75×10^{-6}	5.8	1000	1280	82.1

Table 6.6.1-3 Correlation between diffusion efficiency and L/G

Purge gas rate (m^3/s)	Flow rate of sampled water (m^3/s)	L/G	Kr content in sampled water (ppb)	Kr content in purge gas (ppm)	Diffusion efficiency (%)
1.83×10^{-7}	9.2×10^{-7}	5.0	1000	1160	86.8
1.83×10^{-7}	1.63×10^{-6}	8.9	1000	1790	75.2
1.83×10^{-7}	2.33×10^{-6}	12.7	1000	2340	68.8
1.83×10^{-7}	3.08×10^{-6}	16.8	1000	2820	62.7

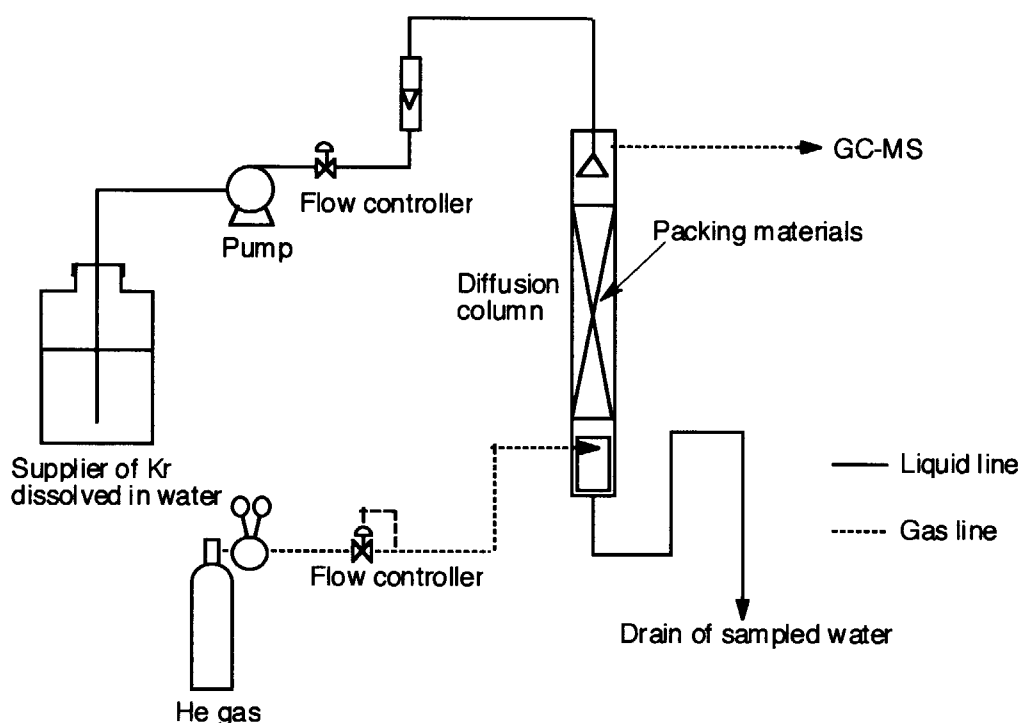


Fig. 6.6.1-1 Experimental configuration

From the above results, the ratio of L/G will be required in the range of 5 to 5.8 to obtain the diffusion efficiency more than 80 %. Considering a better response time, we have selected the design parameters for the diffusion column as shown in Table 6.6.1-4.

Table 6.6.1-4 Design parameters.

Item	Condition
Height of diffusion column	0.85 m
Carrier gas species	He
Flow rate of sample	$1.75 \times 10^{-6} \text{ m}^3/\text{s}$
Flow rate of carrier gas	$3 \times 10^{-7} \text{ m}^3/\text{s}$
Ratio of fluid to gas	5.8
Diffusion efficiency for Kr gas	82 %

Based on the above parameters, amount of Kr content in the water leak of $8.68 \times 10^{-6} \text{ m}^3/\text{s}$ can be evaluated to be 34 ppm in the carrier gas. At present, the lowest value measured in GC-MS analyzer is 0.6 ppm, so that this content of Kr gas in the carrier gas is measurable by the present GC-MC analyzer.

Increase of Kr in the vessel cooling water due to the leakage from the blanket cooling water is,

$$7.1 \times 10^{-6} \text{ m}^3/\text{m}^3 \text{ in the case of the water leakage of } 8.68 \times 10^{-6} \text{ m}^3/\text{s}.$$

The content of Kr gas dissolved in the water is,

$$7.1 \times 10^{-6} \text{ m}^3 / \text{m}^3 \times 1.75 \times 10^{-6} \text{ m}^3 / \text{s} = 1.24 \times 10^{-11} \text{ m}^3 / \text{s}$$

and then, Kr content in the carrier gas, considering the diffusion efficiency,

$$(1.24 \times 10^{-11} \text{ m}^3 / \text{s} \times 0.82 / 3.0 \times 10^{-7} \text{ m}^3 / \text{s}) \times 10^6 = 34 \text{ ppm.}$$

To improve the diffusion efficiency, the height of the diffusion column should be increased or the temperature should be increased.

6.6.2 Design of water-to-water leak detection system

The concept of the detection system is shown in Figs. 6.6.2-1 and 6.6.2-2. The sampling line is connected to the vessel cooling water circuit, and the sampled water is introduced to the detection system, which is mainly composed of the diffusion column and GC-MS analyzer. The flow rate introduced to the detection system is controlled by flow control valve.

At first, the sampled water goes through the diffusion column, and encounters the He carrier gas. At this moment, Kr gas dissolved in the water is transferred to the carrier gas, and the mixture of He and Kr gases is introduced to the gas analyzer through the cooling column. The cooling column is provided for removal of the excess water in the mixture gases. Finally, the He-Kr mixture gas goes into the GC-MS analyzer.

The flow velocity of the sampled water is assumed to be 1 m/sec, and a typical distance from the leak location to the detection system is assumed to be 50 m. Diameter and sampling rate are summarized in Table 6.6.2-1. The flow rate of the sampled water is less than $1.67 \times 10^{-5} \text{ m}^3 / \text{s}$ enough for the detection of Kr gas, so that the diameter of the sampling line will be 4 mm or less.

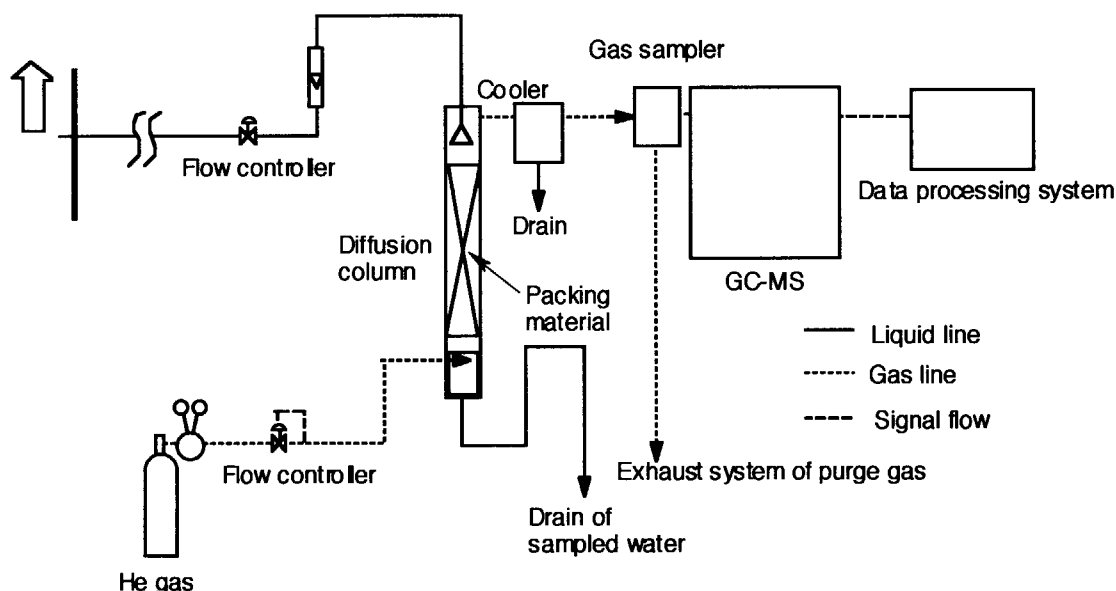


Fig. 6.6.2-1 Conceptual design of water-to-water detection system

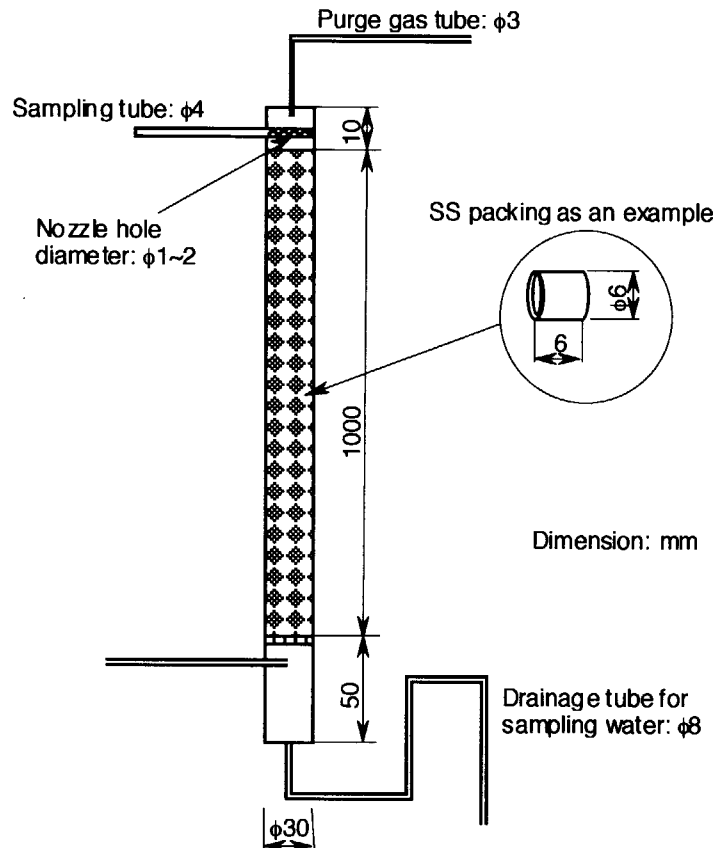


Fig. 6.6.2-2 Concept of diffusion column

Table 6.6.2-1 Summary of sampling conditions.

Diameter of sampling line (mm)	Time consuming from leakage to detection (sec)	Flow rate of sampled water (m ³ /s)
2	50	3.13×10^{-6}
4	50	1.26×10^{-5}
6	50	2.83×10^{-5}
8	50	5.03×10^{-5}
10	50	7.85×10^{-5}

The Kr gas contents in the vessel water is measured discontinuously. Sampling duration of the GC-MS is 5 minutes. Hence, the overall time delay of this system is estimated to about 30 min as shown in Table 6.6.2-2. To improve the response time of this system, porosity of packing materials is reduced and amount of the carrier gas increases keeping the ratio of fluid to gas.

Table 6.6.2-2 Estimated time delay.

Item	Time delay
Sampling line	About 1 min
Diffusion column	About 27 min
Diffusion column to sampler	About 1 min

6.7 Summary

- 1) Comparing several tracer materials for the water-to-water leak detection, Kr tracer was the most promising material for the ITER operation conditions.
- 2) To measure and detect Kr dissolved in the water, the system composed of the diffusion column and GC-MS analyzer was proposed, and typical design parameters to meet with the ITER condition were evaluated. The water-to-water leak rate less than 8.68×10^{-6} m³/sec can be detected by using the proposed system.

7. Conclusions

Design of the shielding blanket for ITER-FEAT employs the first wall of a separable structure from the shield block for radioactive waste reduction in case of unexpected excessive damage of the first wall and cost reduction in fabrication process. During the period of ITER EDA extension, the Japan Home Team has performed the design and analysis of the primary module of the shielding blanket, which has covered major critical design issues as follows:

- (1) Thermo-mechanical analysis of the separable first wall and shield block,
- (2) Thermal-hydraulic analysis of the shield block,
- (3) Electromagnetic analysis of the shielding blanket modules under the centered disruption and the upward and downward vertical displacement events
- (4) Design and structural analysis of the attachment of the separable first wall to the shield block,
- (5) Design of the coolant water leak detection method.

The results can be concluded as follows:

(1) Thermo-mechanical analysis

- Steady and transient analyses on the first wall strips with/without front access holes have been carried out by 2-D model.
- Maximum temperature is found acceptable in all regions at steady state and during the thermal cycle including plasma ramp-up, 400-sec flat top burning and ramp-down.
- Maximum stress is also shown within the allowable value.
- Three-dimensional analysis model for the shield block is generated for 1/4 block to evaluate the thermal stress due to the nuclear heating during the normal pulsed operation.
- The results indicate the peaking of marginal temperatures and excessive stresses at the front side corners. Based on this result, design modification such as the beveling of the corner edge and/or the decrease of the thickness of the header cover plate is suggested.

(2) Thermal-hydraulic analysis

- A 3-D model is generated for 1/2 shield block with all coaxial radial channels, poloidal/toroidal connectors and front manifolds.
- The results of flow distribution show that there are backward flows in the radial channels because of a flow obstruction in the poloidal connector by the inner tube of the radial channel.
- As shown in the above results, the maximum temperature of the structural material is 428 °C at the top/bottom edge region of the front side.

(3) Electromagnetic analysis

- Three-dimensional models are generated with solid elements for one detail blanket module and a sector including blanket modules and the vacuum vessel.
 - The maximum moment around radial axis (M_r) is 1.36 MNm on module #5 under the fast upward VDE III and that around vertical axis (M_z) is 1.47 MNm on module #1 under the fast downward VDE III.
- (4) Design and structural analysis of the attachment of the separable first wall to the shield block
- Welding attachment of the supporting beam of the first wall panel is proposed.
 - To withstand the electromagnetic force, the welding thickness of 25 mm is needed in the case of 180-mm-long supporting beam when the poloidal movement of the supporting beam is free. For 292-mm-long supporting beam, 30- to 35-mm-thick welding is required.
 - When the poloidal movement of the supporting beam is limited to 0.3 mm at the root of the supporting beam to the first wall, e.g. by a limited gap width between the supporting beam and the hole wall of the shield block, the welding thickness can be reduced to be around 15 mm for the longer supporting beam.
 - Strength evaluation of the shield block region attached by the flexible connector can be preliminary concluded that the internal thread of the shield block would need more integrity against the electromagnetic pulling force. To reduce the stress to satisfy the allowable value, the thread length longer than 61.3 mm would be needed.
- (5) Design of the coolant water leak detection method
- For the detection of water-to-water leak in case of the integrated manifold (i.e. the leak of blanket water to vacuum vessel water loop), four candidate tracer materials, Na-24, heavy water, He and Kr are evaluated on the view points of the detection sensitivity of the water leakage and the impact on ITER components.
 - Each tracer material will have no serious corrosion effect on the components at the minimum target leak rate.
 - The tracer materials can be removed or separated from the vacuum vessel water, for instance by the cation-exchange resin for Na-24, a gas diffusion method for He and Kr gas and a distillation method for D_2O .
 - Among the candidates, Kr would be most appropriate as the tracer since no background of Kr exists in the vacuum vessel water. The blanket water leakage into the vacuum vessel water can be detected by a combination of the gas diffusion system and GC-MS system.

It should be noted that the design of the shielding blanket of ITER-FEAT has been investigated in more detail and improved based on above results before its finalization.

Acknowledgement

The authors wish to express their gratitude to Drs. M. Seki H. Takatsu and S. Seki for their support and encouragement. This work has been performed as one of the design tasks within the framework of ITER Engineering Design Activities (EDA) Extension Period. The authors would like to thank the members of the Blanket Group of the ITER Joint Central Team for their guidance and discussion.

References

- [1] ITER Plant Description Document, G A0 FDR 1 01-07-13 R1.0, (2001)
- [2] ITER Material Properties Handbook, IdoMS No G A1 DDD 1 98-05-28 W 0.3, Garching, Germany.
- [3] Fushiki Matsuoka, Calculation of a Three Dimensional Eddy Current by the FEM-BEM Coupling Method, Proc. Electromagnetomechanical Interaction in Deformable Solid and Structures (1987), 169-174
- [4] N.Miki, Blanket Group of ITER Joint Central Team, private communication.
- [5] ITER-FEAT Outline Design Report (ODR), (1999)
- [6] M. Verrecchia, Design Integration Group of ITER Joint Central Team, private communication ("FEAT type I and type II plasma disruption simulation", G 73 MD 27 00-03-06 W 0.1 (2000)).
- [7] A. Kameari and R. C. Popa, "EMSolution: A program for three-dimensional electromagnetic analysis", presented at 2nd Japanese-Bulgarian-Macedonian Joint Seminar on Applied Electromagnetics, November 1-3, 1999, Sapporo.
- [8] N.Miki, Blanket Group of ITER Joint Central Team, private communication.
- [9] Summary of ITER Structural Design Criteria, S 74 FDR 1 97-12-03 W 0.2 (1997).
- [10] S. P. Timoshenko and S. Woinowsky-Krieger, Theory of Plates and Shells, McGraw-Hill (1981).
- [11] ITER Structural Design Criteria for In-vessel Components, G 74 MA 8 01-05-28 W0.2 (2001).
- [12] M. Onozuka, K. Ioki, G. Johnson et al, Design and analysis of the vacuum vessel for RTO/RC-ITER, Fusion Eng. Des. 51-52 (2000) 249.
- [13] ITER Task Force Report, Chapter VI, ITER Garching JCT (1999).
- [14] CRC Handbook of Chemistry and Physics, 80th ed. (D. R. Lide, editor) (CRC Press, New York, 1999).

国際単位系 (SI) と換算表

表1 SI基本単位および補助単位

量	名称	記号
長さ	メートル	m
質量	キログラム	kg
時間	秒	s
電流	アンペア	A
熱力学温度	ケルビン	K
物質の量	モル	mol
光度	カンデラ	cd
平面角	ラジアン	rad
立体角	ステラジアン	sr

表3 固有の名称をもつSI組立単位

量	名称	記号	他のSI単位による表現
周波数	ヘルツ	Hz	s ⁻¹
力	ニュートン	N	m·kg/s ²
圧力, 応力	パスカル	Pa	N/m ²
エネルギー, 仕事, 熱量	ジュール	J	N·m
工率, 放射束	ワット	W	J/s
電気量, 電荷	クーロン	C	A·s
電位, 電圧, 起電力	ボルト	V	W/A
静電容量	ファラド	F	C/V
電気抵抗	オーム	Ω	V/A
コンダクタンス	ジーメン	S	A/V
磁束	ウェーバ	Wb	V·s
磁束密度	テスラ	T	Wb/m ²
インダクタンス	ヘンリー	H	Wb/A
セルシウス温度	セルシウス度	°C	
光束	ルーメン	lm	cd·sr
照射	ルクス	lx	lm/m ²
放射能	ベクレル	Bq	s ⁻¹
吸収線量	グレイ	Gy	J/kg
線量当量	シーベルト	Sv	J/kg

表2 SIと併用される単位

名称	記号
分, 時, 日	min, h, d
度, 分, 秒	°, ', "
リットル	l, L
トン	t
電子ボルト	eV
原子質量単位	u

$$1 \text{ eV} = 1.60218 \times 10^{-19} \text{ J}$$

$$1 \text{ u} = 1.66054 \times 10^{-27} \text{ kg}$$

表4 SIと共に暫定的に維持される単位

名称	記号
オングストローム	Å
バー	b
バール	bar
ガリ	Gal
キュリー	Ci
レントゲン	R
ラド	rad
レム	rem

$$1 \text{ Å} = 0.1 \text{ nm} = 10^{-10} \text{ m}$$

$$1 \text{ b} = 100 \text{ fm} = 10^{-28} \text{ m}^2$$

$$1 \text{ bar} = 0.1 \text{ MPa} = 10^5 \text{ Pa}$$

$$1 \text{ Gal} = 1 \text{ cm/s}^2 = 10^{-2} \text{ m/s}^2$$

$$1 \text{ Ci} = 3.7 \times 10^{10} \text{ Bq}$$

$$1 \text{ R} = 2.58 \times 10^{-4} \text{ C/kg}$$

$$1 \text{ rad} = 1 \text{ cGy} = 10^{-2} \text{ Gy}$$

$$1 \text{ rem} = 1 \text{ cSv} = 10^{-2} \text{ Sv}$$

表5 SI接頭語

倍数	接頭語	記号
10 ¹⁸	エクサ	E
10 ¹⁵	ペタ	P
10 ¹²	テラ	T
10 ⁹	ギガ	G
10 ⁶	メガ	M
10 ³	キロ	k
10 ²	ヘクト	h
10 ¹	デカ	da
10 ⁻¹	デシ	d
10 ⁻²	センチ	c
10 ⁻³	ミリ	m
10 ⁻⁶	マイクロ	μ
10 ⁻⁹	ナノ	n
10 ⁻¹²	ピコ	p
10 ⁻¹⁵	フェムト	f
10 ⁻¹⁸	アト	a

(注)

- 表1-5は「国際単位系」第5版, 国際度量衡局 1985年刊行による。ただし, 1 eV および 1 uの値は CODATA の1986年推奨値によった。
- 表4には海里, ノット, アール, ヘクタールも含まれているが日常の単位なのでここでは省略した。
- barは, JISでは流体の圧力を表わす場合に限り表2のカテゴリーに分類されている。
- EC閣僚理事会指令では bar, barnおよび「血圧の単位」mmHgを表2のカテゴリーに入れている。

換算表

力	N (=10 ⁵ dyn)	kgf	lbf
	1	0.101972	0.224809
	9.80665	1	2.20462
	4.44822	0.453592	1

$$\text{粘度 } 1 \text{ Pa} \cdot \text{s} (\text{N} \cdot \text{s} / \text{m}^2) = 10 \text{ P (ポアズ)} (\text{g} / (\text{cm} \cdot \text{s}))$$

$$\text{動粘度 } 1 \text{ m}^2 / \text{s} = 10^4 \text{ St (ストークス)} (\text{cm}^2 / \text{s})$$

圧	MPa (=10 bar)	kgf/cm ²	atm	mmHg (Torr)	lbf/in ² (psi)
	1	10.1972	9.86923	7.50062 × 10 ³	145.038
力	0.0980665	1	0.967841	735.559	14.2233
	0.101325	1.03323	1	760	14.6959
	1.33322 × 10 ⁻⁴	1.35951 × 10 ⁻³	1.31579 × 10 ⁻³	1	1.93368 × 10 ⁻²
	6.89476 × 10 ⁻³	7.03070 × 10 ⁻²	6.80460 × 10 ⁻²	51.7149	1

エネルギー・仕事・熱量	J (=10 ⁷ erg)	kgf·m	kW·h	cal (計量法)	Btu	ft·lbf	eV
	1	0.101972	2.77778 × 10 ⁻⁷	0.238889	9.47813 × 10 ⁻⁴	0.737562	6.24150 × 10 ¹⁸
	9.80665	1	2.72407 × 10 ⁻⁶	2.34270	9.29487 × 10 ⁻³	7.23301	6.12082 × 10 ¹⁹
	3.6 × 10 ⁶	3.67098 × 10 ⁵	1	8.59999 × 10 ⁵	3412.13	2.65522 × 10 ⁶	2.24694 × 10 ²⁵
	4.18605	0.426858	1.16279 × 10 ⁻⁶	1	3.96759 × 10 ⁻³	3.08747	2.61272 × 10 ¹⁹
	1055.06	107.586	2.93072 × 10 ⁻⁴	252.042	1	778.172	6.58515 × 10 ²¹
	1.35582	0.138255	3.76616 × 10 ⁻⁷	0.323890	1.28506 × 10 ⁻³	1	8.46233 × 10 ¹⁸
	1.60218 × 10 ⁻¹⁹	1.63377 × 10 ⁻²⁰	4.45050 × 10 ⁻²⁶	3.82743 × 10 ⁻²⁰	1.51857 × 10 ⁻²²	1.18171 × 10 ⁻¹⁹	1

$$1 \text{ cal} = 4.18605 \text{ J (計量法)}$$

$$= 4.184 \text{ J (熱化学)}$$

$$= 4.1855 \text{ J (15 °C)}$$

$$= 4.1868 \text{ J (国際蒸気表)}$$

$$\text{仕事率 } 1 \text{ PS (仏馬力)}$$

$$= 75 \text{ kgf} \cdot \text{m/s}$$

$$= 735.499 \text{ W}$$

放射能	Bq	Ci
	1	2.70270 × 10 ⁻¹¹
	3.7 × 10 ¹⁰	1

吸収線量	Gy	rad
	1	100
	0.01	1

照射線量	C/kg	R
	1	3876
	2.58 × 10 ⁻⁴	1

線量当量	Sv	rem
	1	100
	0.01	1

(86年12月26日現在)

